Neutron Scattering Studies of Correlated Electron Systems

Lucy Helme

Thesis submitted for the degree
of Doctor of Philosophy

Linacre College
University of Oxford
Trinity Term 2006

Neutron Scattering Studies of Correlated Electron Systems

Lucy Helme
Linacre College, University of Oxford

Thesis submitted for the Degree of Doctor of Philosophy, Trinity Term 2006

This thesis presents neutron scattering studies of three correlated electron systems, each of which exhibit different competing interactions. These include charge order, magnetic order and lattice degrees of freedom. The main focus is on magnetic excitations within the systems. In all cases the experimental data have been analysed through comparison with theoretical models.

Chapter 3 presents an investigation into the Jahn-Teller effect in the rare earth oxide PrO_2, through inelastic neutron scattering studies of the crystal field transitions above and below a static structural distortion temperature. The data are compared with a point-charge model of the crystal field levels. We conclude that the observed temperature evolution of the crystal field levels originates from the structural distortion due to the Jahn-Teller effect.

Chapter 4 describes studies of magnetic excitations in the layered charge-ordered transition-metal oxide $La_{1.5}Sr_{0.5}CoO_4$ through inelastic neutron scattering studies, and subsequent comparison with spin-wave dispersion models. It was found that the spin-wave excitations were decoupled from the charge order. Inclusion of the strong crystal anisotropy was necessary in order to successfully describe the data.

Chapters 5 and 6 present studies of the magnetically ordered phase of Na_xCoO_2 with $x \sim 0.75$, a metallic layered transition-metal oxide. Chapter 5 describes investigations into the magnetic excitations in the compound, which were successfully modelled by linear spin-wave theory, including terms for the anisotropy. The excitations were found to be highly three dimensional despite the layered nature of the crystal structure. Chapter 6 presents a diffraction study of a spin-flop transition in an applied magnetic field, which confirmed the magnetic order. The transition field was found to be in excellent agreement with the exchange and anisotropy parameters extracted in chapter 5.

ACKNOWLEDGEMENTS

CONTENTS

LIST OF FIGURES

LIST OF TABLES

CHAPTER 1

Introduction to Correlated Electron Systems

In this thesis various complex behaviours in strongly correlated metal oxides are studied using neutron scattering techniques and complementary theoretical modelling. Traditionally, many compounds in condensed matter physics have been successfully modelled by ignoring interactions between electrons. In many metals the electrons can be treated as fully delocalized and electrons are 'nearly-free' while, at the opposite extreme, in many insulators the electrons can be modelled as tightly bound to the ions, and again interactions between them are neglected [1]. The behaviours of these compounds are relatively simple to understand. When the electrons in a system are instead highly correlated, complex phenomena are observed, sometimes including strongly enhanced physical properties.

Materials in which the electrons are strongly correlated provide some of the most challenging and exciting problems in condensed matter physics today. The discovery in 1986 of high critical temperature (high–T_c) superconductivity in layered copper oxides [2] took the physics community by surprise, and triggered a massive surge of interest in the field. Since then a whole host of new compounds have been discovered which exhibit fundamentally new behaviour that cannot be described by conventional ideas of metals and insulators, and many new theories have been put forward to model them.

In strongly correlated electron systems the interactions between electrons are significant relative to the kinetic energy of the electrons, and no model based on the idea of free electrons can successfully describe their physical properties. Experimentally, the collective electronic behaviour results in a broad range of interesting pheneomena, ranging from superconductivity to colossal magnetoresistance (CMR) and heavy-fermion effects. While great progress has been made in understanding these phenomena, there remain a large number of unanswered questions. The mechanism of high-T_c superconductivity, for example, is still under debate twenty years on. One important idea that has emerged is that these exciting physical properties are a result of competition, or synergy, between several coexisting types of order, including magnetic, charge and orbital order, as well as lattice effects. The interplay between these states is thought to be crucial to understanding the complex phase diagrams of strongly correlated electron systems. In the following sections we will describe the types of order relevant to the work in this thesis.

1.1 Ordered States

1.1.1 Superconductivity

Superconducting materials can be divided into two classes: *conventional super-conductors*, which can be described by the Bardeen-Cooper-Schrieffer (BCS) theory [3], and *unconventional superconductors*, which cannot. The term unconventional superconductor covers several families of compounds, all of which display unusual properties, and are prime examples of correlated electron systems. We concentrate here on superconducting transition metal oxides, a category dominated by cuprate materials, which are described briefly below.

High-temperature superconductors: the cuprates

Since the unexpected discovery of high-temperature superconductivity in a cuprate material in 1986 [2] hundreds of high-T_c compounds have been discovered, and all share a layered structure made up of one or more copper-oxygen planes. The parent compound is an antiferromagnetic insulator, La_2CuO_4, which is shown in fig. 1.1b. One method of producing a superconducting state is by doping excess holes into the material by replacing some of the trivalent La by divalent Sr ions [1]. The resulting compound $La_{2-x}Sr_xCuO_4$ has x holes added to the Cu–O plane, and by tuning the

---

[1]There are many other hole-doped cuprate superconductors with slightly different layered structures, such as $YBa_2Cu_3O_{6+y}$ (YBCO), and it is also possible to achieve superconductivity by electron-doping [4].
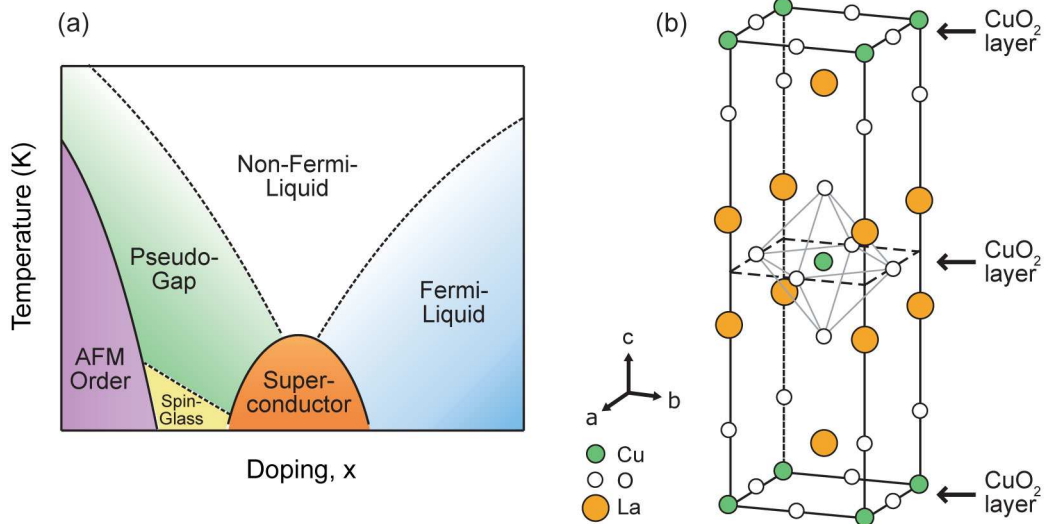
Figure 1.1: (a) General cuprate phase diagram. AFM denotes the antiferromagnetically ordered phase. (b) The structure of the parent compound La_2CuO_4: layers of CuO_2 spaced by La ions.

value of x a superconducting state can be achieved [5]. Figure 1.1a shows a generic phase diagram for the cuprate superconductors. The superconducting region is dome-shaped, and ranges from $x \approx 0.06$ to 0.25 in $La_{2-x}Sr_xCuO_4$. At an optimal doping level x_0 the superconducting critical temperature is highest, approximately 40 K in $La_{2-x}Sr_xCuO_4$, but up to 93 K and higher in other cuprates [2]. T_c drops at higher and lower values of x within the superconducting region, and the superconductor is said to be overdoped or underdoped respectively.

There is still much theoretical debate over the nature of superconductivity in the cuprates, and we will not go into it here. A recent review can be found in reference [4]. Mounting evidence suggests that the pairing is spin singlet, and d-wave [3]. From the phase diagram (fig. 1.1a) it is clear that there are a rich variety of other phases present in these compounds, and physicists agree that understanding the phase diagram as a whole is key to understanding the superconducting region.

Sodium cobaltate

After the discovery of high-T_c superconductivity in the layered cuprates, many searches were made for superconductivity in other transition metal oxides. Success came in 1994 with the discovery of the superconducting state of strontium ruthenate, Sr_2RuO_4. Although the T_c is much lower, Sr_2RuO_4 has an almost identical structure to the cuprates, and was hoped to shed further light on the superconductivity mechanism in these layered compounds. However, it was soon discovered that the superconductivity in Sr_2RuO_4 is very different from the cuprates, exhibiting p-wave triplet pairing, and is in fact much more similar to the superfluidity in ^{3}He [7].

The next breakthrough came in 2003 when Takada *et al.* succeeded in synthesising a superconducting layered cobaltate, with a T_c of about 5 K [8], triggering an explosion of research activity. The compound, $Na_xCoO_2 \cdot yH_2O$ ($x \approx 0.35$, $y \approx 1.3$), consists of two dimensional layers of CoO_2 which are separated by thick layers of sodium ions and water molecules. Figure 1.2 shows the structure of Na_xCoO_2 (b) before and (c) after intercalation with water. Hydrating the compound increases the spacing between the CoO_2 layers, almost doubling the c–axis lattice constant.

There are clearly similarities between $Na_xCoO_2 \cdot yH_2O$ and the cuprate superconductors. Like the cuprates, sodium cobaltate is a layered transition metal oxide, with the layers consisting of CoO_2 rather than CuO_2. Similarly, these layers are separated by insulating spacer layers. However, in the cuprates the CuO_2 layers have a square lattice, and in sodium cobaltate the CoO_2 layers are hexagonal, as shown in fig. 1.2b. A drawing of the phase diagram of sodium cobaltate is shown in fig. 1.2a, plotted as a function of sodium doping x. Clearly the superconducting region is much smaller than in the cuprates: superconductivity is achieved in a small region around $x \approx 0.3$, and only when the compound is also hydrated. As in the cuprates, and in contrast to the ruthenates, the superconductivity arises out of a highly complex normal state. There are magnetically ordered phases close to the superconducting

---

[2]Such as $YBa_2Cu_3O_{6+y}$ (YBCO) and $Ba_2Sr_2CaCu_2O_{8+y}$ (Bi-2212) [4].
[3]This means that the Cooper pairs are in a spin-singlet state with $l = 2$ [6].
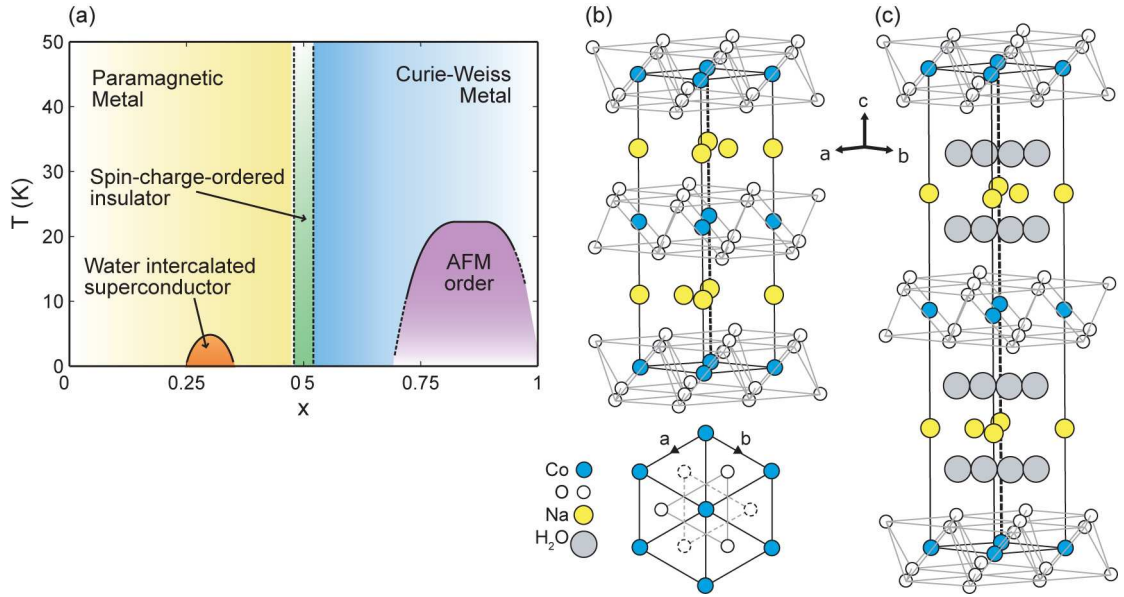
Figure 1.2: (a) The phase diagram of Na_xCoO_2. (b) The hexagonal structure of non-superconducting sodium cobaltate. (c) The superconducting compound $Na_xCoO_2 \cdot yH_2O$, after hydration.

phase: at $x \approx 0.5$ there is a spin-charge-ordered state [9], and above $x \approx 0.7$ there is an antiferromagnetically ordered state, with a ordering temperature of ~ 22 K [10].

1.1.2 Magnetic Order

Magnetic order is an important degree of freedom to understand: magnetically ordered phases are present in high-T_c compounds and their presence is thought to be intimately connected with the superconductivity. The majority of this thesis is devoted to studying magnetic order and excitations. This section briefly describes the mechanisms of magnetic order, which are often connected to charge order, orbital order and crystal lattice effects. These are discussed in the following sections.

Magnetic moments

There are two types of magnetic moment: in a diamagnetic substance the application of a magnetic field induces a magnetic moment which opposes the field that caused it, while in a paramagnetic substance the applied magnetic field induces a magnetic moment which aligns parallel with the field.

The paramagnetic moment of an ion comes from the spin $\boldsymbol{s}$ (where $|\boldsymbol{s}| = 1/2$) and orbital angular momentum $\boldsymbol{l}$ of the electrons in unfilled electronic shells. The total spin and orbital angular momentum are calculated from the vector sums over all individual electrons: $\boldsymbol{S} = \sum_i \boldsymbol{s}_i$ and $\boldsymbol{L} = \sum_i \boldsymbol{l}_i$. Over one full shell these sum to zero because of spherical symmetry so electrons in filled shells do not contribute

to the paramagnetic moment. The electrons in partially filled shells do contribute, and the resulting spin $\boldsymbol{S}$ and orbital angular $\boldsymbol{L}$ momentum can combine together in $(2L+1)(2S+1)$ ways to give the total angular momentum $\boldsymbol{J}$. In an isolated ion the ground state, the most energetically favourable state, is calculated by Hund's rules, which say that S and L must be maximised in order to minimise the Coulomb repulsion between electrons [11]. In this case the magnetic moment is calculated from the spin-orbit interaction, and we can write an effective moment

$$\mu_{\text{eff}} = g_J \mu_B \sqrt{J(J+1)} \ , \tag{1.1}$$

where μ_B is the Bohr magneton and g_J is the Landé g-value given by

$$g_J = \frac{3}{2} + \frac{S(S+1) - L(L+1)}{2J(J+1)} \ . \tag{1.2}$$

However, in a crystal lattice the crystal field may alter the ground state, as will be discussed later. In $3d$ ions the crystal field often serves to quench the orbital angular momentum, and allows the ion to be modelled with a pure spin magnetic moment

$$\mu_{\text{eff}} = g \mu_B \sqrt{S(S+1)} \ , \tag{1.3}$$

where $g = 2$ for pure spin. The spin-orbit interaction can be included as a weak perturbation by altering the value of g.

Exchange interactions

Magnetic order occurs in a compound when interactions between the moments of neighbouring magnetic ions are such that it is energetically favourable for them to order in a periodic arrangement. Possible interactions include the magnetic dipolar interaction and magnetic exchange interactions. The magnetic dipolar interaction is generally too weak to account for the ordering of magnetic materials [11], and in systems such as those studied in this thesis the magnetic order is determined by the exchange couplings between ions.

The exchange interaction between two ions originates from differences in the electrostatic energy of possible relative orientations of the magnetic moments of the ions such that an energy gain can be made by choosing a certain configuration over others. As an example we consider the simple case of the exchange interaction between two electrons at positions $\boldsymbol{r}_1$ and $\boldsymbol{r}_2$. Either electron can be in a spatial state ψ_a or ψ_b, so that the joint wave function contains the terms $\psi_a(\boldsymbol{r}_1)\psi_b(\boldsymbol{r}_2)$ and $\psi_a(\boldsymbol{r}_2)\psi_b(\boldsymbol{r}_1)$. The Pauli exclusion principle requires the overall wavefunction Ψ to be antisymmetric, and by including both spin and spatial states this can be achieved in two ways: an antisymmetric (singlet) spin state χ_S (S=0) with a symmetric spatial state, or a symmetric (triplet) spin state χ_T (S=1) with an antisymmetric spatial state. The total wavefunction for the singlet (Ψ_S) or triplet (Ψ_T) case is then

$$\Psi_S = \frac{1}{\sqrt{2}} \left[\psi_a(\boldsymbol{r}_1)\psi_b(\boldsymbol{r}_2) + \psi_a(\boldsymbol{r}_2)\psi_b(\boldsymbol{r}_1) \right] \chi_S \tag{1.4}$$

$$\Psi_T = \frac{1}{\sqrt{2}} \left[\psi_a(\boldsymbol{r}_1)\psi_b(\boldsymbol{r}_2) - \psi_a(\boldsymbol{r}_2)\psi_b(\boldsymbol{r}_1) \right] \chi_T \ .$$

By assuming that the spin parts of the wavefunction are normalized we can write the difference in energies between the singlet and triplet state as

$$J = E_T - E_S \;\; = \;\; \int \Psi_T^* \mathcal{H} \Psi_T \, \mathrm{d}\boldsymbol{r}_1 \mathrm{d}\boldsymbol{r}_2 - \int \Psi_S^* \mathcal{H} \Psi_S \, \mathrm{d}\boldsymbol{r}_1 \mathrm{d}\boldsymbol{r}_2 \tag{1.5}$$

$$= \;\; -2 \int \psi_a^*(\boldsymbol{r}_1)\psi_b^*(\boldsymbol{r}_2) \, \mathcal{H} \, \psi_a(\boldsymbol{r}_2)\psi_b(\boldsymbol{r}_1) \, \mathrm{d}\boldsymbol{r}_1 \mathrm{d}\boldsymbol{r}_2 \;\; .$$

and this defines the *exchange constant* (or exchange integral), J. It is straightforward to show that we can write an effective spin Hamiltonian [11]

$$\mathcal{H} = (E_T - E_S)\boldsymbol{S}_1 \cdot \boldsymbol{S}_2 = J\boldsymbol{S}_1 \cdot \boldsymbol{S}_2 \;\; , \tag{1.6}$$

so J is a measure of the interaction between the two spins. If $J < 0$, $E_T < E_S$ and the triplet state $S = 1$ is favoured; if $J > 0$, $E_T > E_S$ and the singlet state $S = 0$ is favoured.

Generalizing these ideas to a many-body system is a complicated problem, but it was recognised early on by Heisenberg that equation 1.6 could be generalized to provide a good description of the interactions between magnetic moments on all neighbouring ions in a compound. The result is known as the Heisenberg Hamiltonian:

$$\mathcal{H} = \sum_{i,j} J_{ij}\boldsymbol{S}_i \cdot \boldsymbol{S}_j \;\; , \tag{1.7}$$

where the sum is over all pairs of spins i, j (each pair is counted only once), and J_{ij} is the exchange constant describing the interaction between i and j. In this notation $J > 0$ favours antiparallel alignment of moments (*antiferromagnetic* alignment) and $J < 0$ favours parallel alignment of moments (*ferromagnetic* alignment).

When electrons on neighbouring ions interact directly, with no intermediary, the exchange interaction is known as *direct exchange*. The strength of this interaction is strongly dependent on the overlap of the electron shells of the two ions. There is often insufficient overlap for a strong direct exchange interaction, either because the wavefunctions lie very close to the nucleus (*e.g.* in rare earth $4f$ electrons), or because the ions are too far apart (*e.g.* in transition metal oxides where the magnetic ions are separated by oxygen). In these cases an *indirect exchange* interaction may be important. In ionic solids the most important interaction is known as *superexchange*, an indirect exchange interaction between two non-neighbouring magnetic ions which is mediated by a non-magnetic ion between them. Figure 1.3 represents the superexchange interaction in a magnetic oxide between two magnetic ions M mediated by an oxygen ion. The M ions are represented by one type of d orbital, and vertical arrows represent the spins of electrons distributed over the bond in the antiferromagnetic and ferromagnetic interactions. The antiferromagnetic arrangement is more favourable to electron hopping, and therefore allows the electrons to become delocalized over the structure, lowering the kinetic energy. Superexchange therefore generally favours an antiferromagnetic alignment, with $J > 0$.[4]

---

[4]Ferromagnetic superexchange is possible, see ref. [11], but the interaction is weaker and less common.
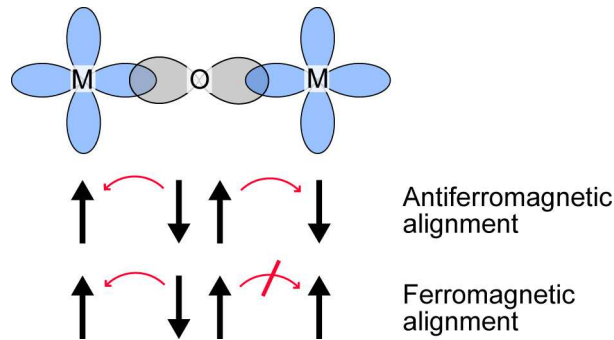
Figure 1.3: Superexchange in a magnetic oxide over the M–O–M bond. The M ions are represented by one type of d orbital. Vertical arrows represent the spins of electrons distributed over the bond, while thin arrows represent electron hopping. It is clear that the antiferromagnetic arrangement is more favourable to electron hopping.
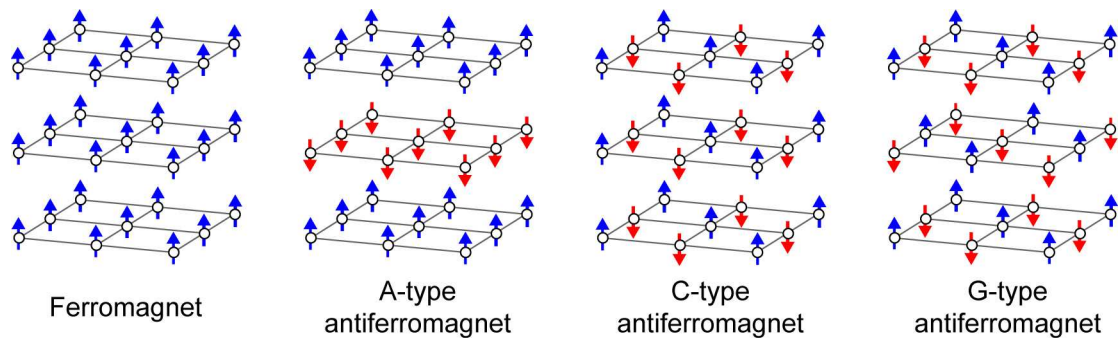
Figure 1.4: Schematic diagram showing the spin directions in an ordered ferromagnet and A-type, C-type and G-type antiferromagnets.

Antiferromagnetism

The sign of the exchange constant J determines whether the exchange interaction favours parallel or antiparallel alignments of the magnetic moments in a compound. When J is negative the lowest energy is achieved by aligning all spins in parallel resulting in *ferromagnetism*, as shown in fig. 1.4. However, in magnetic oxides, which are the focus of this thesis, interactions often favour antiparallel alignment of spins, leading to *antiferromagnetic* ground states. Figure 1.4 shows some types of layered antiferromagnets: A-type, where alignment is ferromagnetic within layers and antiferromagnetic between them; C-type, where alignment is antiferromagnetic within layers and ferromagnetic between them; G-type, where all interactions are antiferromagnetic.
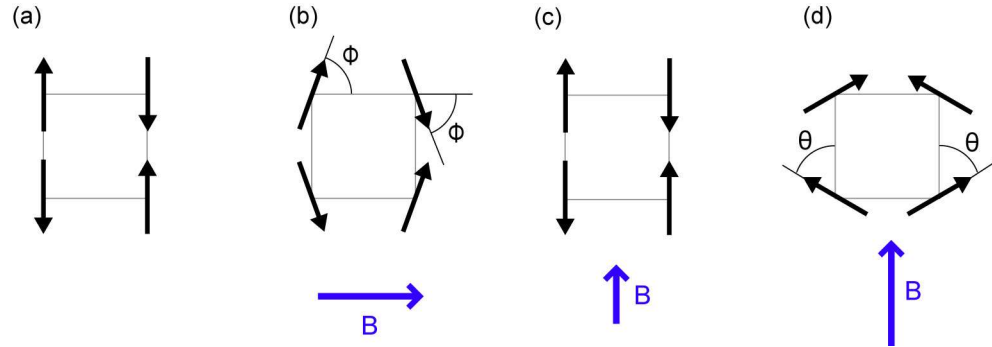
Figure 1.5: The effect of an external applied field on an antiferromagnet. (a) No applied field. (b) Field B perpendicular to ordered moments. (c) Weak field parallel to ordered moments. (d) Strong field B parallel to ordered moments (Spin-flop).

In general an antiferromagnet can usually be considered as two interlocking sublattices of spins: one of 'up' spins and one of 'down' spins. In zero field the magnetic moments of the two sublattices cancel so the net magnetization is zero. To make a measurement of the magnetization a small magnetic field is applied along a particular direction. If the field is applied perpendicular to the ordered moment direction (see fig. 1.5b) then both 'up' and 'down' spins tilt slightly towards the field and a component of magnetization is measured along the field direction. If the small field is applied parallel to the ordered moment direction of one sublattice, and antiparallel to the other (see fig. 1.5c), the net effect on the two sublattices is zero and no magnetization component is measured. This gives rise to large anisotropies in magnetization measurements of antiferromagnets in the ordered phase.

If a strong magnetic field is applied perpendicular to the moment direction the spins tilt in the same way, see fig. 1.5b. As the field increases ϕ decreases until the spins are finally parallel. However, if a strong magnetic field is applied parallel to the ordered moments the effect is more interesting. As the field is increased the spins remain as shown in fig. 1.5c until at a critical field they suddenly flip into the configuration shown in fig. 1.5d. This is known as a *spin-flop transition*.

1.1.3 Charge Order

In a doped material, the replacement of one ion by another ion of different valence introduces excess holes (or electrons) into the material. At high temperatures the excess holes are generally randomly distributed, but on cooling they may form a periodic arrangement due to the repulsive Coulomb interaction between them. This ordered state of localized charge is known as charge order (CO).

Charge ordering occurs in slightly different ways in different layered materials, but the pattern of ordering is highly dependent on doping level. As an example we
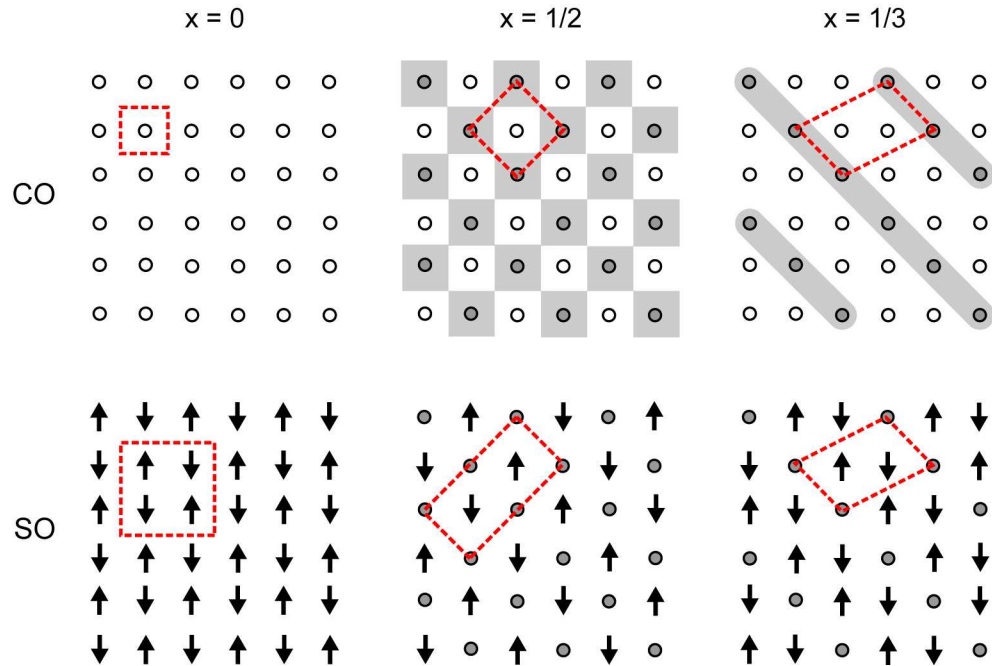
Figure 1.6: Top row: Example 2D charge ordering (CO) patterns on a square lattice for three values of doping. Dark circles show positions of extra holes. Bottom row: Effect of charge ordering on antiferromagnetic spin ordering (SO) in the case when an extra hole on a magnetic ion changes the valence so that it no longer has a moment, or does not order. Red dashed boxes mark unit cells.

can consider materials with a layered structure, such as $La_{2-x}Sr_xMO_4$ (M=metal, Cu, Mn, Ni, Co), where the holes reside on the conduction layers (MO_2). The metal ions M in the conduction layers form a square lattice. In a 'half-doped' material with $x = 1/2$ there is one extra hole per two M ions, and charge ordering naturally forms a checkerboard pattern consisting of two different M valences , see fig. 1.6. When $x \neq 1/2$, charges often order instead into periodically spaced lines of charge known as 'stripes'. An example striped arrangement for $x = 1/3$, as seen in the nickelates, is also shown in fig. 1.6. Charge stripes have come into focus recently because of their effect on high-T_c superconductivity. Static charge order is thought to destroy superconductivity, while many theories suggest that dynamic charge stripes are in fact essential components in the superconducting phase [12].

Charge ordering is often accompanied by slight lattice distortions, which alter the lattice periodicity and allow direct observation of charge ordering. Its effects can also be detected by transport and magnetic susceptibility measurements, because the transfer of conduction holes is disturbed by the ordered pattern. In antiferromagnetic materials the presence of charge ordering has a dramatic effect on the magnetic

ordering pattern. This is demonstrated in the lower row of fig. 1.6 which shows antiferromagnetic order on a square lattice with three different charge orders (red dashed boxes show the magnetic unit cells). Although these diagrams illustrate charge and magnetic order that is commensurate with the crystal lattice, incommensurate charge order is also observed. The incommensurability can be due to charge density waves, wave-like modulations in the charge which can have a periodicity incommensurate with the lattice, or due to discommensurations in the charge order.

1.1.4   Orbital Order and Lattice Effects

Magnetic ions in strongly correlated electron systems are often transition metals or rare earths with valence electrons in the 3d or 4f shells. These orbitals are not spherically symmetric so the symmetry of the local environment of the magnetic ion can determine which orbitals are favoured as the ground-state, and can affect the orientation of the orbitals within the crystal structure.

As an example, figure 1.7 shows a magnetic 3d ion in an octahedral environment of surrounding oxygen ions. We consider the two d-orbitals with four-fold angular dependence in the xy plane: d_{xy} and $d_{x^2+y^2}$, shown in fig. 1.7(b, c). It is clear that the d_{xy} orbital has a much lower overlap with the p orbitals of the neighbouring oxygen ions than the $d_{x^2+y^2}$ orbital, and hence will have lower energy. This leads to a splitting between the levels known as t_{2g} (which include d_{xy}, d_{xz} and d_{yz}), and the e_g levels (d_{z^2} and $d_{x^2+y^2}$).

Effects like these can lead to the orbitals aligning into a periodic pattern in the crystal lattice in order to minimize the energy of the configuration: this is known as *orbital ordering*. One example is the manganate compound $La_{1-x}Sr_{1+x}MnO_4$, which is isostructural to the high-T_c cuprates discussed earlier. The phase diagram of $La_{1-x}Sr_{1+x}MnO_4$ is shown in fig. 1.8a [13]. At half doping ($x = 0.5$) the compound exhibits charge, magnetic and orbital ordering within the layers, as shown
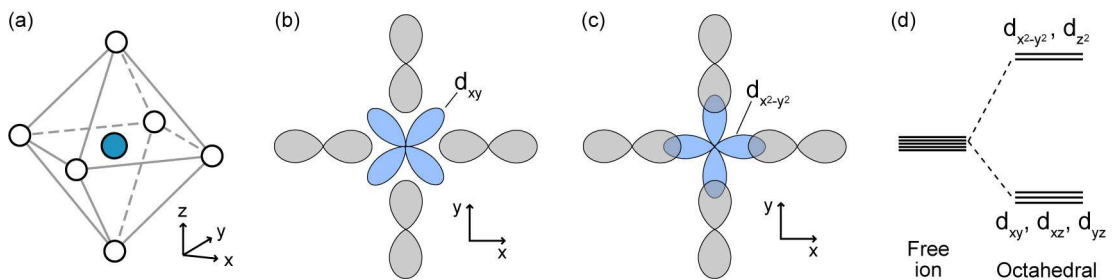
Figure 1.7: (a) A magnetic ion surrounded by oxygen ions forming an octahedron. (b) d_{xy} orbital of the magnetic ion surrounded by the p orbitals of the oxygens. The d_{xy} orbital is lower in energy than the $d_{x^2+y^2}$ orbital (c). (d) The resulting splitting in energy levels.
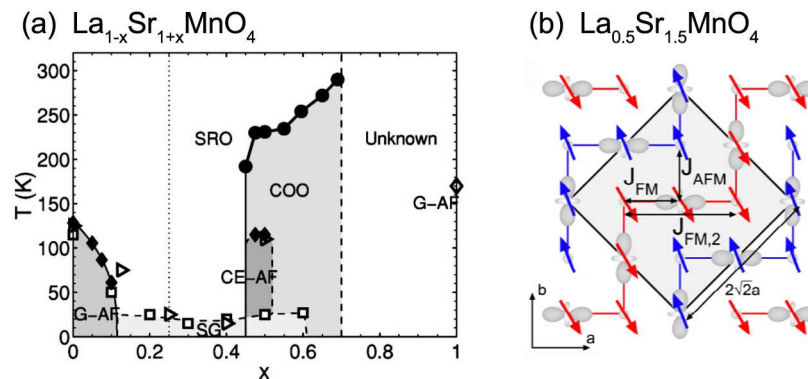
Figure 1.8: (a) The phase diagram of the manganate $La_{1-x}Sr_{1+x}MnO_4$ [13]. (b) At $x = 0.5$ there is orbital ordering in the layers [14, 15].

in fig. 1.8b. At this doping level the orbitals order to produce zig-zag chains [14], followed at low temperature by magnetic order along the chains [15]. Orbitals are fundamental in determining the nature of magnetic exchange interactions between ions, as discussed above, and so orbital order strongly affects the magnetic ordering in a compound. The Goodenough-Kanamori rules [16] specify how the ions' orbitals, and the bond directions, determine whether interactions between ions are likely to be antiferromagnetic or ferromagnetic.

The crystal field

The concept of a crystal field has long been used to describe the effect of neighbouring ions (ligands) on the properties of a central magnetic ion [17], with varying degrees of sophistication, and varying degrees of success. In its simplest form crystal field theory calculates the orbital splittings of energy levels of the magnetic ion due to the electrostatic potential exerted by the ligands through Coulomb repulsion. The resulting energy levels, such as those shown in figure 1.7d, are known as *crystal field levels*.

Crystal field perturbations are found to be roughly two orders of magnitude greater for the d–electrons of the transition ions than for the f–electrons of the lanthanide ions. This is because f orbitals are close to the nucleus, and are partially shielded from the effect of the crystal field by s and p shells that lie further out. The relative importance of the crystal field in comparison to the spin-orbit coupling, for instance, determines how the calculations are performed. Crystal field theory is discussed further in chapter 4.

The Jahn-Teller effect

The Jahn-Teller theorem states that a high symmetry state with orbitally degenerate levels is unstable with respect to a spontaneous distortion, which lifts the

degeneracy and therefore lowers the energy of the ground state. This spontaneous distortion is known as the *Jahn-Teller effect*. The lifting of degeneracy is limited only by Kramers' theorem which states that in an ion with an odd number of valence electrons two-fold spin-degeneracy must remain in the absence of a magnetic field.

In a periodic lattice the distortion can occur throughout the structure, leading to a structural phase transition to a reduced symmetry state (*cooperative Jahn-Teller effect*). The lowering of symmetry, and therefore orbital degeneracy, implies an occupation of particular orbitals, simultaneous with orbital ordering. In some cases at higher temperatures the distortion can switch back and forth from one axis to another, and this is known as the *dynamic Jahn-Teller effect*.

1.2 Excitations

In an ordered array of atoms, *i.e.* a crystal lattice, the order can be disrupted by thermally excited lattice vibrations. These are quantized as phonons and their behaviour is described by a dispersion relation, which determines the relationship between the energy of the phonon and wavevector (or momentum). In a magnetically ordered compound the ordered spins can similarly be disrupted by excitations called spin waves which are quantized as magnons. These can be conceptualized as flipped spins that propagate through the material like a wave. Their behaviour is similarly described by a dispersion relation.

The measurement of excitations in a system is useful as it provides information on the interatomic forces within the system. Often it can be experimentally difficult to distinguish spin-wave scattering from scattering due to phonons.

Spin-wave dispersion relations

Mapping out spin-wave dispersion relations is valuable as it gives quantitative information on the exchange interactions in the compound. As a simple example we consider the case of a one dimensional spin-1/2 ferromagnet, with a ground state containing N spins all pointing 'up'. This is represented as state $|0\rangle$ shown in fig. 1.9. The Hamiltonian for the Heisenberg model (eqn. 1.7) can be written:

$$\mathcal{H} = J \sum_i \boldsymbol{S}_i \cdot \boldsymbol{S}_{i+1} = J \sum \left[S_i^z S_{i+1}^z + \frac{1}{2} \left(S_i^+ S_{i+1}^- + S_i^- S_{i+1}^+ \right) \right] \ , \qquad (1.8)$$

where J is negative for a ferromagnet and $\boldsymbol{S}_i$ is the spin-operator acting on a site i. S_i^- and S_i^+ are operators that create or destroy a flipped spin on site i. The Hamiltonian acting on the ground state $|0\rangle$ defines the ground state energy E_0 by $\mathcal{H}|0\rangle = E_0|0\rangle$, and we find $E_0 = NS^2J$. An excitation is created by flipping one of the spins, say spin j, to give an excited state $|j\rangle = S_j^-|0\rangle$, also depicted in fig. 1.9. Applying the Hamiltonian to the excited state $|j\rangle$ gives:

$$\mathcal{H}|j\rangle = (NS^2J - 2SJ)|j\rangle + SJ|j+1\rangle + SJ|j-1\rangle \ , \qquad (1.9)$$
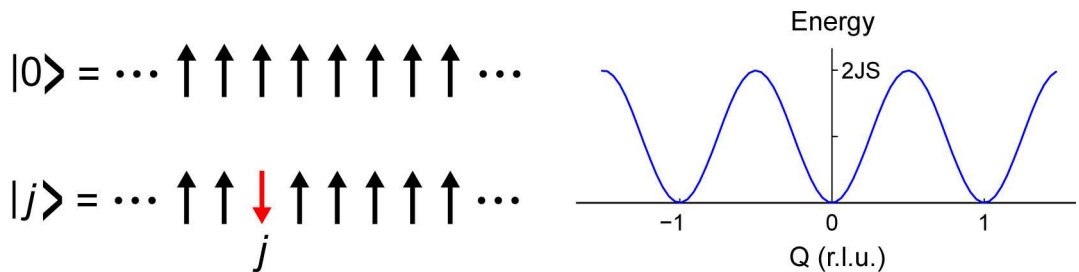
Figure 1.9: Left: ground state $|0\rangle$ and excited state $|j\rangle$ of a 1D S=1/2 ferromagnet. Right: Spin-wave dispersion of the system.

which can be diagonalized using the Fourier transform $|q\rangle = \sum_j \exp(iqr_j)|j\rangle$, where r_j is the position of spin j. This gives

$$\mathcal{H}|q\rangle = (E_0 + \hbar\omega)|q\rangle = NS^2 J - 2JS(1 - \cos(qa)) \ , \tag{1.10}$$

where a is the spacing between spins in the chain. The dispersion relation for the 1D ferromagnet is therefore given by the expression $\hbar\omega = -2JS(1 - \cos(qa))$. This is plotted in fig. 1.9 for $J = -1$. It is clear that by fitting the dispersion to data the exchange constant J can be extracted.

The calculation above is for a very simple problem, with an easy solution to diagonalizing the Hamiltonian. For more complicated problems, such as 2D or 3D antiferromagnets, linear spin-wave theory is used, employing the operator technique first proposed by Holstein and Primakoff [18]. This technique will be explained further within this thesis, but a general description of the method is found in reference [19].

Crystal field excitations

Another type of magnetic excitation that will be studied in this thesis are excitations between crystal field levels. Crystal field excitations are *local* excitations, as opposed to spin waves, which propagate through the lattice. Excitations from the ground state to excited crystal field levels are observed as peaks in the energy spectrum of an inelastic neutron scattering measurement, and these peaks give an accurate picture of the crystal field splitting. Changes in the crystal field, due to lattice distortions for example, alter the crystal field splittings and this is detected as movement of peak positions in the energy spectrum or changes in the number of peaks observed.

1.3   Scope of this Thesis

Within this thesis three different correlated electron systems have been studied, each of which display a different combination of the competing types of order described in section 1.1. A large part of the thesis is dedicated to experimental measurements of magnetic excitations in these compounds, and the development of theoretical models which describe the data. Neutron scattering is a valuable tool for probing correlated electron systems, especially the spin correlations and excitations [20], and the majority of the experimental measurements reported in this thesis were made using neutrons. Chapter 2 presents the theoretical basis and experimental techniques of neutron scatting. The following four results chapters each focus on one of the three compounds studied:

Chapter 3: PrO_2

> The first system, PrO_2, is a rare-earth oxide which exhibits magnetic ordering. The main interest here, however, is the competition between orbital and lattice degrees of freedom which results in an interesting type of cooperative Jahn-Teller distortion. In chapter 3 we present measurements of the crystal field excitations above and below the static Jahn-Teller distortion temperature, which probe the splittings of the crystal field levels due to the lattice distortion. The experimental observations are interpreted with the help of a simple point-charge model to simulate the effect of the Jahn-Teller distortion on the crystal field at the Pr site, and hence on the energy levels in the system.

Chapter 4: $La_{1.5}Sr_{0.5}CoO_4$

> The second system studied is the doped transition metal oxide $La_{1.5}Sr_{0.5}CoO_4$. This compound is an insulator which exhibits stable charge ordering. At low temperatures the charge order coexists with magnetic ordering within the two-dimensional CoO_2 layers. Chapter 4 presents a characterization of the magnetic excitations in $La_{1.5}Sr_{0.5}CoO_4$, which are highly two-dimensional. Through comparison with models of the excitations we investigate the magnetic interactions and the anisotropy in the compound, and ask whether the magnetic and charge degrees of freedom are coupled. We find that it is necessary to include the effect of the crystal-field and spin-orbit interactions on the ground state in order to model the system successfully.

Chapters 5 and 6: Na_xCoO_2

> The subject of chapters 5 and 6 is the magnetic phase of Na_xCoO_2 with $x \approx 0.75$. In this unhydrated phase there is no superconductivity, and the compound is good metal. Chapter 5 investigates the magnetic excitations in $Na_{0.75}CoO_2$, which are found to be highly three-dimensional despite the layered structure of the compound. Evidence for itinerant effects is discussed. In chapter 6 we present a study of the spin-flop transition in $Na_{0.8}CoO_2$, which confirms the magnetic ordering pattern with spins lying along the c axis, and gives further information on the magnetic interactions in the system.

Finally, in chapter 7, we present the main conclusions of the results chapters, and discuss further work that might be undertaken to extend the studies presented in this thesis.

1.4 Publications

A number of publications have arisen from the work presented in this thesis, and these are listed below.

Chapter 3:

Influence of static Jahn-Teller distortion on the magnetic excitation spectrum of PrO_2,
C. H. Webster, L. M. Helme, A. T. Boothroyd, D. F. McMorrow, S. B. Wilkins, C. Detlefs, B. Janoušová, and M. J. McKelvy, in preparation.

Chapter 4:

Magnetic excitations in $La_{1.5}Sr_{0.5}CoO_4$,
L.M. Helme, A.T. Boothroyd, D. Prabhakaran, F.R. Wondre, C.D. Frost and J. Kulda, Physica B **350**, e273 (2004).

Chapters 5 and 6:

Spin gaps and magnetic structure of Na_xCoO_2,
L. M. Helme, A. T. Boothroyd, R. Coldea, D. Prabhakaran, A. Stunault, G. J. McIntyre and N. Kernavanois, Phys. Rev. B **73**, 054405 (2006).

Three-Dimensional Spin Fluctuations in $Na_{0.75}CoO_2$,
L. M. Helme, A. T. Boothroyd, R. Coldea, D. Prabhakaran, D. A. Tennant, A. Hiess, and J. Kulda, Phys. Rev. Lett. **94**, 157206 (2005).

Ferromagnetic In-Plane Spin Fluctuations in Na_xCoO_2 Observed by Neutron Inelastic Scattering,
A.T. Boothroyd, R. Coldea, D. A. Tennant, D. Prabhakaran, L.M. Helme and C. D. Frost, Phys. Rev. Lett. **92**, 197201 (2004).

References

[1] J. Singleton, *Band Theory and Electronic Properties of Solids* (Oxford University Press, Oxford, U.K., 2001).

[2] J. G. Bednorz and K. A. Müller, Z. Phys. B **64**, 189 (1986).

[3] J. Bardeen, L. N. Cooper, and J. R. Schrieffer, Phys. Rev. **108**, 1175 (1957).

[4] P. A. Lee, N. Nagosa and X-G. Wen, Rev. Mod. Phys. **78**, 17 (2006).

[5] B. Batlogg and C. Varma, Physics World, February 2000, p33.

[6] J. F. Annett, *Superconductivity, Superfluids and Condensates* (Oxford University Press, Oxford, U.K., 2004).

[7] Y. Maeno, T. M. Rice and M. Sigrist, Physics today **54**, 42 (2001).

[8] K. Takada, H. Sakurai, E. Takayama-Muromachi, F. Izumi, R. A. Dilanian and T. Sasaki, Nature **422**, 53 (2003).

[9] G. Gašparović, R. A. Ott, J.-H. Cho, F. C. Chou, Y. Chu, J. W. Lynn, and Y. S. Lee, Phys. Rev. Lett. **96**, 046403 (2006); T. Imai, F. L. Ning, M. Van Dyken, F. C. Chou, A. P. Reyes and P. L. Kuhns, cond-mat/0607625 (2006); J. Wooldridge, G. Balakrishnan, D. McK. Paul, C. Frost, P. Bourges, and M. R. Lees, cond-mat/0608196 (2006).

[10] T. Motohashi, R. Ueda, E. Naujalis, T. Tojo, I. Terasaki, T. Atake, M. Karppinnen and H. Yamauchi, Phys. Rev. B **67**, 064406 (2003); D. Prabhakaran, A. T. Boothroyd, R. Coldea and N. R. Charnley, J. Crystal Growth **271**, 74 (2004); A. T. Boothroyd, R. Coldea, D. A. Tennant, D. Prabhakaran, L. M. Helme and C. D. Frost, Phys. Rev. Lett. **92**, 197201 (2004); L. M. Helme, A. T. Boothroyd, R. Coldea, D. Prabhakaran, D. A. Tennant, A. Hiess, and J. Kulda, Phys. Rev. Lett. **94**, 157206 (2005); S. P. Bayrakci, I. Mirebeau, P. Bourges, Y. Sidis, M. Enderle, J. Mesot, D. P. Chen, C. T. Lin, and B. Keimer, Phys. Rev. Lett. **94**, 157205 (2005).

[11] S. J. Blundell, *Magnetism in Condensed Matter* (Oxford University Press, Oxford, U.K., 2001).

[12] See for example: V. J. Emery, S. A. Kivelson and O. Zachar, Phys. Rev. B **56**, 6120 (1997); H. Johannesson and I. Japaridze, Phys. Rev. B **68**, 214507 (2003).

[13] S. Larochelle, A. Mehta, L. Lu, P. K. Mang, O. P. Vajk, N. Kaneko, J. W. Lynn, L. Zhou and M. Greven, Phys. Rev. B **71**, 024435 (2005).

[14] S. B.Wilkins, P. D. Spencer, P. D. Hatton, S. P. Collins, M. D. Roper, D. Prabhakaran and A.T. Boothroyd, Phys. Rev. B **91**, 167205 (2003).

[15] D. Senff, F. Krüger, S. Scheidl, M Benomar, Y. Sidis, F. Demmel and M. Braden, Phys. Rev. Lett. **96**, 257201 (2006).

[16] J. Kanamori, J. Phys. Chem. Solids **10**, 87 (1959).

[17] B. N. Figgis and M. A. Hitchman, *Ligand Field Theory and Its Applications* (Wiley-VCH, New York, U.S.A., 2000).

[18] T. Holstein and H. Primakoff, Phys. Rev. **58**, 1098 (1940).

[19] C. Kittel, *Quantum Theory of Solids* (Wiley, New York, U.S.A., 1963).

[20] G. Aeppli, S. Hayden and T. Perring, *Seeing the spins in solids*, Physics World, December 1997, p33.

CHAPTER 2

Neutron Scattering

2.1 Introduction

Neutron scattering is a versatile technique that is particularly well suited to studying the properties of strongly correlated electron systems, described in the last chapter. This is due in large part to the basic properties of the neutron, combined with technology that allows production of high neutron fluxes, and instumentation designed specifically for the study of condensed matter systems.

The de Broglie wavelength of thermal neutrons is very similar to interatomic spacings in solids ($\sim$ Å), allowing diffraction measurements to be performed to study the structure of solids. In addition, the energy spectrum of neutrons produced by research sources is of the same order as that of many excitations in condensed matter systems. Inelastic neutron scattering processes which create excitations therefore cause a large relative change in the neutron's energy, and so are an accurate method of measuring the excitations in a system.

There are several important differences between neutrons and x-rays, which are similarly used to study condensed matter. One major advantage of neutrons over x-rays is that neutrons possess a magnetic moment and so can interact with magnetic dipole moments, allowing neutron scattering to directly probe magnetic order and excitations in condensed matter systems. Secondly, the strength of neutron scattering from an atom varies randomly across the periodic table, while x-ray scattering depends solely on the number of electrons. Neutrons therefore have the advantage that they can 'see' light atoms in solids that also contain heavy atoms. Finally, neutrons scatter weakly, so they can penetrate several centimeters into a material and therefore probe the bulk of the sample, rather than the surface properties.

2.2   Neutron scattering theory

Neutron scattering is a well established technique, and the theory of neutron scattering is covered in detail in textbooks [1, 2]. The following sections briefly present the main concepts and results that will be used within this thesis.

In a neutron scattering experiment a collimated (usually monochromatic) beam of neutrons is incident on a target sample, scatters through some interaction with the sample, and the energy spectrum of the scattered neutrons is measured using detectors in one or a range of directions.

We first consider a neutron with an initial wavevector $\boldsymbol{k}_i$ incident on a sample and which is then scattered by the sample into a state with a final wavevector $\boldsymbol{k}_f$. The angle between $\boldsymbol{k}_i$ and $\boldsymbol{k}_f$ through which the neutron is scattered is labelled 2θ. This event is shown in figure 2.1. The transfer of momentum to the sample is then $\hbar\boldsymbol{Q}$, where $\boldsymbol{Q}$ is known as the *scattering vector* and is defined as

$$\boldsymbol{Q} = \boldsymbol{k}_i - \boldsymbol{k}_f \ . \tag{2.1}$$

These three vectors ($\boldsymbol{k}_i$, $\boldsymbol{k}_f$, $\boldsymbol{Q}$) together form the scattering triangle, also shown in fig. 2.1. In an inelastic scattering event the neutron loses (or gains) energy during the process, and the energy transfer is given by

$$E_T = \hbar\omega = E_i - E_f = \frac{\hbar^2}{2m_n}(\boldsymbol{k}_i^2 - \boldsymbol{k}_f^2) \ , \tag{2.2}$$

where E_i and E_f are the initial and final energies of the neutron, and m_n is the mass of the neutron.

In an experiment a neutron is detected if it hits the detector, which subtends a solid angle $\Delta\Omega$, and has an energy within the acceptable range ΔE_f around the
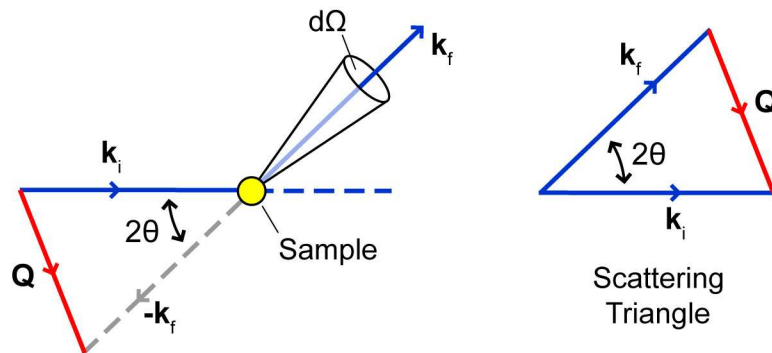
Figure 2.1: Schematic diagram of the geometry of a neutron scattering experiment. Incident neutrons with wavevector $\boldsymbol{k}_i$ are scattered by the sample into a final state $\boldsymbol{k}_f$. The scattering triangle defines the scattering wavevector $\boldsymbol{Q} = \boldsymbol{k}_i - \boldsymbol{k}_f$. $d\Omega$ is the unit of solid angle subtended by the detector.

nominal value E_f. If the incident neutron flux is Φ_0 and the detector has an efficiency η then the neutron count rate is

$$\eta \; \Phi_0 \frac{d^2\sigma}{d\Omega dE_f} \; \Delta\Omega \; \Delta E_f \;\; . \tag{2.3}$$

The quantity $d^2\sigma/d\Omega dE_f$ is the partial differential cross-section. This is the basic quantity measured during a neutron scattering experiment and depends on the details of the interaction between the neutron and the sample, and it is this quantity which can be related to theoretical models. Since the neutron can interact with either the nuclei within the sample, or with unpaired electrons in magnetic atoms we examine the form of the cross section for both nuclear and magnetic scattering in the following sections.

2.2.1 Neutron Scattering Cross-Section

First we define what is meant by the term cross section. The *total scattering cross-section*, counting neutrons scattered in any direction, is defined by the equation

$$\sigma_{tot} = (\text{total number of neutrons scattered per second})/\Phi_0 \;, \tag{2.4}$$

where Φ_0 is the flux of the incident neutrons, as before. The *differential cross-section* is then the number of neutrons that are scattered into a certain direction per second, and can be defined as

$$\frac{d\sigma}{d\Omega} = \frac{\left(\begin{array}{c}\text{number of neutrons scattered per second into}\\\text{the solid angle } \mathrm{d}\Omega \text{ in the direction } \theta, \phi\end{array}\right)}{\Phi \, \mathrm{d}\Omega} \;, \tag{2.5}$$

where $d\Omega$ is the unit of solid angle as shown in fig. 2.1 and (θ, ϕ) are polar coordinates defining the direction of the scattered beam. The *partial* or *double differential cross-section* is the number of neutrons that are scattered per second into a certain direction with a certain range of energy values, and corresponds to the probability of the collision having a certain range of outcomes defined by these values. The *partial differential cross-section* is defined as

$$\frac{d^2\sigma}{d\Omega \, dE_f} = \frac{\left(\begin{array}{c}\text{number of neutrons scattered per second into}\\\text{the solid angle } \mathrm{d}\Omega \text{ in the direction } \theta, \phi\\\text{with final energy between } E_f \text{ and } E_f + \mathrm{d}E_f\end{array}\right)}{\Phi \, \mathrm{d}\Omega \, \mathrm{d}E_f} \;\; . \tag{2.6}$$

To obtain an expression for the *partial differential cross-section* we consider the probability of a transition of the neutron-target system from an initial state λ_i to a final state λ_f. Since neutron scattering is shown experimentally to be a very weak process the interacting potential between neutron and target can be treated as a perturbation and Fermi's Golden Rule can be applied to calculate the transition probability. In scattering theory this is equivalent to the Born approximation which

assumes that both the incoming and scattered beam are plane waves. The neutron is described by a plane wave state characterized by its wavevector λ, and the scattering cross section between λ_i and λ_f can be written in the Born approximation as

$$\left(\frac{d^2\sigma}{d\Omega\,dE_f}\right)^{\lambda_i}_{\lambda_f} = \frac{k_f}{k_i}\left(\frac{m_n}{2\pi\hbar^2}\right)^2 |\langle\lambda_f|V(\boldsymbol{Q})|\lambda_i\rangle|^2 \delta(E_{\lambda_f} - E_{\lambda_i} - \hbar\omega) \ , \qquad (2.7)$$

where $V(\boldsymbol{Q})$ is the Fourier transform of the neutron-matter interaction potential $V(\boldsymbol{r})$:

$$V(\boldsymbol{Q}) = \int V(\boldsymbol{r})\exp(i\boldsymbol{Q}\cdot\boldsymbol{r})d^3\boldsymbol{r} \ . \qquad (2.8)$$

The scattering cross-section for whole process is a sum of equation 2.7 over all possible initial and final states of the system, and over all possible initial and final spin-states of the neutron:

$$\frac{d^2\sigma}{d\Omega\,dE_f} = \frac{k_f}{k_i}\left(\frac{m_n}{2\pi\hbar^2}\right)^2 \sum_{\sigma_i,\sigma_f} p_{\sigma_i} \sum_{\lambda_i,\lambda_f} p_{\lambda_i} |\langle\sigma_f\lambda_f|V(\boldsymbol{Q})|\sigma_i\lambda_i\rangle|^2 \delta(E_{\lambda_f} - E_{\lambda_i} - \hbar\omega) \ , \ (2.9)$$

where p_{λ_i} is the probability distribution for initial states λ_i and p_{σ_i} is the probability distribution for the initial spin-states of the neutron σ_i. The spin-states of the neutron are considered again in section 2.2.4 when we discuss polarized neutron scattering.

The scattering cross-section is therefore dependent on the type of interaction between the neutron and the matter it scatters from, and hence the interaction potential $V(\boldsymbol{r})$ (eqn. 2.8). The derivations of this potential and the corresponding scattering cross-sections for different interactions are covered in depth in texts by Squires, Lovesey and others [1, 2, 3]. Here we will briefly discuss some results that will be used later.

2.2.2 The Nuclear Interaction

In any neutron scattering experiment the dominant contribution to the total scattering will come from nuclear elastic scattering which arises from the neutron interacting with nuclei in the sample through the strong nuclear force. Neutrons interact with nuclei j at positions $\boldsymbol{r}_j$ through an interaction potential which can be approximated by

$$V_N(\boldsymbol{r}) = \frac{2\pi\hbar^2}{m_n}\sum_j \bar{b}_j\,\delta(\boldsymbol{r} - \boldsymbol{r}_j) \ , \qquad (2.10)$$

where $\bar{b}_j$ are the scattering lengths of each atomic nucleus [1].

For unpolarized neutrons it is possible to express the partial differential cross-section as a sum of a coherent and incoherent term:

$$\frac{d^2\sigma}{d\Omega\,dE_f} = \frac{d^2\sigma_{\text{coh}}}{d\Omega\,dE_f} + \frac{d^2\sigma_{\text{incoh}}}{d\Omega\,dE_f} \ . \qquad (2.11)$$

---

[1]$\bar{b}_j$ are determined experimentally and have been tabulated [4].

The coherent scattering results from interference effects between the nuclei and in a neutron scattering experiment is observed as elastic Bragg scattering and inelastic phonon scattering. The incoherent scattering is observed as an isotropic background, and is usually subtracted before analysis of the coherent scattering, so we neglect this term.

Nuclear coherent elastic scattering cross-section

In crystalline samples the interference of neutrons scattering from periodic planes of atoms in the lattice gives rise to *Bragg* peaks in the intensity of the elastically scattered neutrons ($E_i = E_f$). These occur when the scattering wavevector $\boldsymbol{Q}$ is perpendicular to a set of crystal planes and is equal to one of the reciprocal lattice vectors $\boldsymbol{\tau}$ of the reciprocal nuclear unit cell. The scattering cross-section for nuclear elastic scattering is given by

$$\left(\frac{d^2\sigma}{d\Omega\, dE_f}\right)^{\text{nuclear}}_{\text{elastic}} = \delta(\hbar\omega)\, \frac{\mathrm{d}\sigma_N}{\mathrm{d}\Omega}(\boldsymbol{Q}) \tag{2.12}$$

$$= \frac{N(2\pi)^3}{V_0}\, |F_N(\boldsymbol{Q})|^2\, \delta(\boldsymbol{Q} - \boldsymbol{\tau})\, \delta(\hbar\omega) \ ,$$

where

$$F_N(\boldsymbol{Q}) = \sum_j \bar{b}_j\, \exp(i\boldsymbol{Q}\cdot\boldsymbol{r}_j)\, \exp(-W_j(Q, T)) \tag{2.13}$$

is the *nuclear structure factor* and the sum over j extends over all nuclei at positions $\boldsymbol{r}_j$ within one unit cell. $\bar{b}_j$ are the scattering lengths of each atom and the Debye-Waller factor $\exp(-W_j(Q, T))$ arises from the thermal motion of atoms about their nominal positions.

2.2.3 The Magnetic Interaction

Magnetic scattering of neutrons occurs due to an interaction between the magnetic dipole moment of the incident neutron and the electromagnetic field due to the intrinsic spin and orbital momentum of unpaired electrons in magnetic ions in the sample. The neutron magnetic moment is

$$\boldsymbol{\mu}_n = -\gamma\mu_N\boldsymbol{\sigma} \ , \tag{2.14}$$

where μ_N is the nuclear magneton, $\gamma \approx 1.913$ is the gyromagnetic ratio and $\boldsymbol{\sigma}$ is the Pauli spin operator with eigenvalues of ± 1. The interaction potential for magnetic scattering takes the form

$$V_M(\boldsymbol{r}) = -\boldsymbol{\mu}_n \cdot \boldsymbol{B}(\boldsymbol{r}) \ , \tag{2.15}$$

where $\boldsymbol{B}$ represents the local magnetic flux density from the unpaired electrons of the magnetic ions, due to both their intrinsic spin and orbital motion (angular momentum). It is the Fourier transform of the interaction potential, $V_M(\boldsymbol{Q})$, that is needed to determine the cross section. Using Maxwell's equations, $\boldsymbol{B}$ can be related

to the magnetization $\boldsymbol{M}$, so that the Fourier transform of the interaction potential can be written:

$$V_M(\boldsymbol{Q}) = -\boldsymbol{\mu}_n \cdot \boldsymbol{B}(\boldsymbol{Q}) = -\mu_0 \boldsymbol{\mu}_n \cdot \boldsymbol{M}_\perp(\boldsymbol{Q}) \ , \tag{2.16}$$

where $\boldsymbol{M}_\perp(\boldsymbol{Q})$ is the component of the magnetization perpendicular to the scattering vector $\boldsymbol{Q}$: [2]

$$\boldsymbol{M}_\perp(\boldsymbol{Q}) = \hat{\boldsymbol{Q}} \times \{\boldsymbol{M}(\boldsymbol{Q}) \times \hat{\boldsymbol{Q}}\} \ . \tag{2.17}$$

The Dipole Approximation

The general expression for $\boldsymbol{M}_\perp(\boldsymbol{Q})$ is complicated, and for most purposes it is sufficient to use an approximation known as the *dipole approximation*. This is employed in slightly different ways for $3d$ compounds (transition metals) and $4f$ compounds (rare earths), as outlined below. More detail is given in references [2] and [1].

For $3d$ ions J is not a good quantum number. The orbital angular momentum $\boldsymbol{L}$ is often quenched, but the spin-orbit interaction can induce a small component of $\boldsymbol{L}$ in a direction parallel or antiparallel to the spin $\boldsymbol{S}$. In this case $\boldsymbol{L}$ is replaced by $(g-2)\boldsymbol{S}$, and it can be shown that in the dipole approximation the magnetization can be written

$$\boldsymbol{M}(\boldsymbol{Q}) = -g\mu_B f(\boldsymbol{Q})\boldsymbol{S} = f(\boldsymbol{Q})\boldsymbol{\mu} \ , \tag{2.18}$$

where $\boldsymbol{\mu} = -g\mu_B \boldsymbol{S}$ is the moment, $f(\boldsymbol{Q})$ is the magnetic form factor, and can be calculated from tables,[3] and g is a function of spin and orbital angular momentum ($g = 2$ for spin-only angular momentum; $g \neq 2$ if there is an orbital component).

$4f$ ions in general have both spin and unquenched orbital angular momentum, and J is a good quantum number. In this case it can be shown that the magnetization can be written

$$\boldsymbol{M}(\boldsymbol{Q}) = -g_J\mu_B f(\boldsymbol{Q})\boldsymbol{J} = f(\boldsymbol{Q})\boldsymbol{\mu} \ , \tag{2.19}$$

where this time $\boldsymbol{\mu} = -g_J\mu_B \boldsymbol{J}$, $f(\boldsymbol{Q})$ takes a different form for $4f$ ions (see [1]), and g_J is the Landé splitting factor.

Using either 2.18 or 2.19 allows the cross section for magnetic scattering to be written in various useful forms. In the following sections we present some results that will be used within this thesis.

Magnetic elastic scattering cross-section

In ordered magnetic systems magnetic elastic scattering is observed as magnetic Bragg peaks, in an analogous way to nuclear Bragg peaks. Magnetic Bragg peaks arise from scattering from the average magnetic lattice, occurring when the scattering vector $\boldsymbol{Q}$ coincides with a reciprocal magnetic lattice vector $\boldsymbol{\tau}_M$. For example, in

---

[2]Note that the two texts that we reference (Lovesey [2] and Squires [1]) define an interaction vector $\mathbf{Q}$ which in the notation used here is equal to $-\boldsymbol{M}/(2\mu_B)$. This is confusing since we use the symbol $\boldsymbol{Q}$ for the scattering wavevector, so here we use the magnetization $\boldsymbol{M}$ throughout.

[3]For $3d$ ions the form factor can be caluclated in the dipole approximation (see [5]) or by using an exact spin-only form when $L = 0$.

a simple antiferromagnetically ordered structure, where the magnetic unit cell is doubled compared to the nuclear unit cell, Bragg peaks would be observed at half-integer wavevectors.

The scattering cross-section for magnetic elastic scattering in the dipole approximation is given by

$$
\begin{aligned}
\left(\frac{d^2\sigma}{d\Omega \, dE_f}\right)^{\text{magnetic}}_{\text{elastic}} &= \delta(\hbar\omega) \frac{\mathrm{d}\sigma_M}{\mathrm{d}\Omega}(\boldsymbol{Q}) \\
&= \frac{N_m(2\pi)^3}{V_{0m}} \left(\frac{\gamma r_0}{2}\right)^2 \sum_{\alpha\beta} \left\langle \left(\delta_{\alpha,\beta} - \hat{Q}_\alpha \hat{Q}_\beta\right) F^\alpha(\boldsymbol{Q}) F^{\beta*}(\boldsymbol{Q}) \right\rangle \\
&\qquad\qquad \times \, \delta(\boldsymbol{Q} - \boldsymbol{\tau}_M) \, \delta(\hbar\omega) \;,
\end{aligned}
\tag{2.20}
$$

where $\boldsymbol{\tau}_M$ is a reciprocal magnetic lattice vector and the sum is over $\alpha, \beta = x, y, z$. $\langle ... \rangle$ represents an average over domains, and the magnetic structure factor is given by

$$
F^\alpha(\boldsymbol{Q} = \boldsymbol{\tau}_M) = \sum_j \mu_j^\alpha f_j(\boldsymbol{Q}) \exp(i\boldsymbol{Q} \cdot \boldsymbol{r}_j) \exp(-W_j(Q, T)) \;,
\tag{2.21}
$$

where μ_j^α is the α-component of the magnetic moment of the jth ion, $\boldsymbol{r}_j$ is its position within the magnetic unit cell and f_j is the magnetic form factor (see eqns. 2.18 and 2.19). $\exp(-W_j(Q, T))$ is the Debye-Waller factor as before.

Magnetic inelastic scattering cross section

A large part of this thesis will concentrate on inelastic scattering measurements made to observe magnetic excitations, such as crystal field transitions (chapter 4) and spin waves (chapters 5, 6). The cross section for magnetic inelastic neutron scattering can be written:

$$
\left(\frac{d^2\sigma}{d\Omega \, dE_f}\right)^{\text{magnetic}}_{\text{inelastic}} = \left(\frac{\gamma r_0}{2}\right)^2 f^2(\boldsymbol{Q}) \, \mathrm{e}^{-2W(Q,T)} \frac{k_f}{k_i} S(\boldsymbol{Q}, \omega) \;,
\tag{2.22}
$$

where $S(\boldsymbol{Q}, \omega)$ is known as the response function, and is written as

$$
S(\boldsymbol{Q}, \omega) = \sum_{\alpha\beta} \left\langle \left(\delta_{\alpha,\beta} - \hat{Q}_\alpha \hat{Q}_\beta\right) S^{\alpha\beta}(\boldsymbol{Q}, \omega) \right\rangle \;.
\tag{2.23}
$$

$S^{\alpha\beta}(\boldsymbol{Q}, \omega)$ are the space and time Fourier transforms of the time-dependent spin-spin correlation functions:

$$
S^{\alpha\beta}(\boldsymbol{Q}, \omega) = \frac{1}{2\pi\hbar} \int_{-\infty}^{+\infty} \sum_{j,j'} \mathrm{e}^{i\boldsymbol{Q}\cdot(\boldsymbol{r}_j - \boldsymbol{r}_{j'})} \mathrm{e}^{-i\omega t} \left\langle S_{j'}^\alpha(0) S_j^\beta(t) \right\rangle dt \;,
\tag{2.24}
$$

where $S_j^\beta(t)$ is the β-component of the spin at site j and at time t, and $\langle ... \rangle$ denotes a statistical average over the initial states of the system. A simplified expression

for the correlation functions can be written for excitations measured at low ('zero') temperatures, where only the ground state $|0\rangle$ with energy E_0 is populated:

$$S^{\alpha\alpha}(\boldsymbol{Q},\omega) = \sum_\lambda |\langle\lambda|S^\alpha(\boldsymbol{Q})|0\rangle|^2 \, \delta(\hbar\omega + E_0 - E_\lambda) \ , \qquad (2.25)$$

where the sum is over all eigenstates $|\lambda\rangle$ of the system with energy E_λ. $S^\alpha(\boldsymbol{Q})$ is the of the Fourier transform of the α-component of the spin density, S_j^α.

The notation above assumes $3d$ ions, which are the focus of the spin-wave calculations in this thesis. Chapter 3 presents studies of crystal field excitations in a $4f$ material. In this case it is useful to write the response function, for localized excitations, in the form:

$$S(\boldsymbol{Q},\omega) = \sum_{ij} \rho_i |\langle j|\hat{\mu}_\perp|i\rangle|^2 \delta(E_i - E_j - \hbar\omega) \ , \qquad (2.26)$$

where the excitations occur between states $|M_J\rangle = |i\rangle$ and $|j\rangle$, ρ_i is the population of $|i\rangle$ and $\hat{\mu}_\perp$ is the component of the magnetic moment perpendicular to $\boldsymbol{Q}$.

2.2.4   Polarized neutrons

The previous sections have concentrated on unpolarized neutrons, considering only the scattering of neutrons from one momentum state to another. Polarized neutron scattering makes use of the spin-states of the neutrons to gain further information on the state of the system. We now consider the effect on the cross section of using polarized neutrons. From equation 2.9 we see that the cross section depends on the initial and final spin states of the neutron, σ_i and σ_f:

$$\left(\frac{d^2\sigma}{d\Omega\, dE_f}\right)_{\lambda_i\to\lambda_f} \propto |\langle\sigma_f\lambda_f|V(\boldsymbol{Q})|\sigma_i\lambda_i\rangle|^2 \ . \qquad (2.27)$$

Previously we neglected the neutron spin-states for unpolarized neutron scattering, but for polarized neutrons we need to take them into account.

Spin-states of the neutron

We will consider only longitudinal polarization analysis. A neutron is a spin-1/2 fermion, and in a magnetic field the spin lies parallel ('up', $|\uparrow\rangle$, eigenvalue $+1$) or antiparallel ('down', $|\downarrow\rangle$, eigenvalue -1) to the field, or *polarization direction*. Neutrons polarized by a field can scatter in four possible scattering processes:

$$
\left.
\begin{array}{l}
|\uparrow\rangle \to |\uparrow\rangle \\
|\downarrow\rangle \to |\downarrow\rangle
\end{array}
\right\}
\quad
\begin{array}{l}
\text{Non Spin Flip} \\
\text{(NSF)}
\end{array}
\qquad (2.28)
$$

$$
\left.
\begin{array}{l}
|\uparrow\rangle \to |\downarrow\rangle \\
|\downarrow\rangle \to |\uparrow\rangle
\end{array}
\right\}
\quad
\begin{array}{l}
\text{Spin Flip} \\
\text{(SF)}
\end{array}
$$

In two processes the neutrons' spin-state remains unchanged (non-spin-flip), while in the other two the neutrons' spin-state is 'flipped' (spin-flip processes).

Nuclear coherent scattering

For nuclear coherent scattering the matrix elements in equation 2.27 can be written

$$\langle \sigma_f | V_N(\boldsymbol{Q}) | \sigma_i \rangle = V_N(\boldsymbol{Q}) \langle \sigma_f | \sigma_i \rangle \ . \tag{2.29}$$

For the four possible scattering processes we then get:

$$\langle \sigma_f | \sigma_i \rangle = \begin{cases} 1 \begin{cases} | \uparrow \rangle \to | \uparrow \rangle \\ | \downarrow \rangle \to | \downarrow \rangle \end{cases} & \text{Non Spin Flip (NSF)} \\ 0 \begin{cases} | \uparrow \rangle \to | \downarrow \rangle \\ | \downarrow \rangle \to | \uparrow \rangle \end{cases} & \text{Spin Flip (SF)} \end{cases} \tag{2.30}$$

This means that all coherent nuclear scattering is measured in the non-spin-flip channel.

Magnetic scattering

The expression for the Fourier transform of the interaction potential for magnetic neutron scattering given in equation 2.16:

$$V_M(\boldsymbol{Q}) = -\gamma r_0 \boldsymbol{\sigma} \cdot \boldsymbol{M}_\perp(\boldsymbol{Q}) = -\gamma r_0 \sum_\alpha \sigma_\alpha M_\perp^\alpha(\boldsymbol{Q}) \ , \tag{2.31}$$

where $\boldsymbol{\sigma}$ is the Pauli spin operator (the spin of the neutron is $\boldsymbol{s}_n = \boldsymbol{\sigma}/2$), and $M_\perp^\alpha(\boldsymbol{Q})$ are the components of the Fourier transform of the sample magnetization perpendicular to the scattering vector $\boldsymbol{Q}$ given by eqn. 2.17. With z as the neutron spin quantization direction (polarization direction) the matrix elements of V_M for the four scattering processes are given by [4]:

$$\langle \sigma_f | V_M(\boldsymbol{Q}) | \sigma_i \rangle = -\gamma r_0 \times \begin{cases} M_\perp^z(\boldsymbol{Q}) & | \uparrow \rangle \to | \uparrow \rangle \\ -M_\perp^z(\boldsymbol{Q}) & | \downarrow \rangle \to | \downarrow \rangle \end{cases} \left. \right\} \text{(NSF)} \\ \begin{cases} M_\perp^x(\boldsymbol{Q}) + i M_\perp^y(\boldsymbol{Q}) & | \uparrow \rangle \to | \downarrow \rangle \\ M_\perp^x(\boldsymbol{Q}) - i M_\perp^y(\boldsymbol{Q}) & | \downarrow \rangle \to | \uparrow \rangle \end{cases} \left. \right\} \text{(SF)} \tag{2.32}$$

Considered together, equations 2.27, 2.31 and 2.32 allow us to conclude that:

- magnetic neutron scattering measures components of the magnetic moment perpendicular to $\boldsymbol{Q}$;

- the component of the magnetic moment perpendicular to the polarization contributes to spin-flip scattering;

- the component of the magnetic moment parallel to the polarization $\boldsymbol{P}$ contributes to non-spin-flip scattering.

---

[4]See for example Squires [1], chapter 9, section 9.3.

Distinguishing magnetic scattering from non-magnetic scattering

Performing a neutron scattering experiment using polarized neutrons allows us to determine whether or not a signal is magnetic. If the polarization direction is set parallel to the scattering vector $\boldsymbol{Q}$ then all magnetic scattering will be spin-flip, and all non-magnetic (all nuclear coherent) scattering will be non-spin-flip. A feature that appears in the spin-flip channel only is then shown to be magnetic in origin. However, we note that if the sample's magnetic moment is also parallel to $\boldsymbol{Q}$ then the scattering cannot be observed.

A description of using polarization analysis to determine the direction of ordered moments is given in appendix A.

Flipping ratio

Although we will not go into the details of how to polarize a neutron beam here, it is important to note that in practice a beam will never be 100% polarized either up ($|\uparrow\rangle$) or down ($|\downarrow\rangle$). The *flipping ratio*, f, is introduced to allow polarized neutron data to be corrected for the imperfect experimental polarization of the beam.

With the polarization parallel to the scattering wavevector ($\boldsymbol{P} \parallel \boldsymbol{Q}$), a measurement of a nuclear Bragg peak should see all scattering in the non-spin-flip (NSF) channel. Any scattering in the spin-flip channel is therefore due to the imperfect polarization, and the flipping ratio can be defined as

$$f = \frac{c_{\mathrm{NSF}}}{c_{\mathrm{SF}}} \quad , \tag{2.33}$$

where c_{NSF}, c_{SF} are the counts measured experimentally in the non-spin-flip and spin-flip channels respectively [5]. f is determined experimentally in this way, and both non-spin-flip and spin-flip measurements can be corrected:

$$I_{\mathrm{SF}} = \frac{f}{f-1}c_{\mathrm{SF}} - \frac{1}{f-1}c_{\mathrm{NSF}} \quad \text{and} \quad I_{\mathrm{NSF}} = \frac{f}{f-1}c_{\mathrm{NSF}} - \frac{1}{f-1}c_{\mathrm{SF}} \quad , \tag{2.34}$$

where I_{NSF} and I_{SF} are the corrected intensities. This correction is important when accurate ratios of the intensities measured in each channel are needed (see appendix A) but will not be applied in general for qualitative measurements using polarized neutrons.

2.2.5 The Response Function $S(\boldsymbol{Q},\omega)$

It is often convenient to express the cross section in general in terms of the response function $S(\boldsymbol{Q},\omega)$, which depends only on $\boldsymbol{Q}$ and ω:

$$\frac{d^2\sigma}{d\Omega dE_f} = \frac{k_f}{k_i} S(\boldsymbol{Q},\omega) \quad , \tag{2.35}$$

---

[5]A magnetic Bragg peak can be used to define the flipping ratio in similar manner, only in this case $f = c_{\mathrm{SF}}/c_{\mathrm{NSF}}$.

where $S(\boldsymbol{Q}, \omega)$ is defined so as to absorb all the factors that appear before it in eqn. B.10, except for (k_f/k_i). The advantage of this is that it factorizes the cross section into a part that depends on the setup of the experiment (k_f/k_i), and a function that depends only on the properties of the system $S(\boldsymbol{Q}, \omega)$.

The response function can therefore easily be compared with theory. In many cases it is possible to calculate the response function directly from a model, using the results in previous sections. However, in cases where the exact form of $S(\boldsymbol{Q}, \omega)$ is unknown it is useful to create an approximate function with which to fit the data. This function must obey general properties of the response function, which can be derived from linear response theory. We will simply state them below, but the proofs can be found in textbooks by Squires [1] and Lovesey [2].

Principle of detailed balance

The principle of detailed balance states that for any neutron inelastic scattering process a general property of the response function $S(\boldsymbol{Q}, \omega)$ is that

$$S(\boldsymbol{Q}, \omega) = \exp(\hbar\omega/k_B T) \times S(-\boldsymbol{Q}, -\omega) \; , \tag{2.36}$$

i.e. the probability that the scattering process takes place through the system initially being in the higher energy state and losing energy to the neutron is $\exp(\hbar\omega/k_B T)$ less likely than the system initially being in the ground state and taking energy from the neutron.

Fluctuation-dissipation theorem

The fluctuation dissipation theorem states that the dynamic part of the response function ($\tilde{S}(\boldsymbol{Q}, \omega)$) can be related to the imaginary part of the susceptibility by

$$\tilde{S}(\boldsymbol{Q}, \omega) = \{1 + n(\omega)\} \frac{1}{\pi} \chi''(\boldsymbol{Q}, \omega) \; , \tag{2.37}$$

where χ'' is the imaginary part of the generalized susceptibility $\chi(\boldsymbol{Q}, \omega) = \chi'(\boldsymbol{Q}, \omega) - i\chi''(\boldsymbol{Q}, \omega)$. $n(\omega)$ is known a the *temperature factor* or *detailed balance factor*, and is given by

$$n(\omega) = \frac{1}{\exp(\hbar\omega/k_B T) - 1} \; . \tag{2.38}$$

The dynamic part of the response function can also be written in terms of the spectral-weight function:

$$\tilde{S}(\boldsymbol{Q}, \omega) = \omega \left\{1 + n(\omega)\right\} \frac{1}{\pi} \chi'(\boldsymbol{Q}, 0) F(\boldsymbol{Q}, \omega) \; , \tag{2.39}$$

where the spectral weight function is normalised to unity:

$$\int_{-\infty}^{\infty} F(\boldsymbol{Q}, \omega) \, \mathrm{d}\omega = 1 \; . \tag{2.40}$$

Since $\chi'(\boldsymbol{Q}, 0)$ is independent of ω and $F(\boldsymbol{Q}, \omega)$ is a function normalised to unity the form of eqn. 2.39 can be used to construct lineshapes to fit energy spectra.

2.3   Instrumentation

Neutron scattering measurements performed for this thesis were undertaken at two neutron sources: the Institut Laue-Langevin (ILL) in Grenoble, France, which is a reactor source, and at ISIS at the Rutherford Appleton Laboratory in the UK, which is a spallation source.

A reactor source uses a controlled nuclear fission reaction to produce a steady flux of neutrons. At a spallation source, on the other hand, proton pulses produced in a synchrotron are fired into a heavy metal target, and this results in the emission of pulses of neutrons. Both sources use a moderator to control the velocity of the neutrons. The temperature of the moderator determines whether the resultant neutron beam contains thermal neutrons ($T \sim 300$ K), cold neutrons ($T \sim 25$ K), or hot neutrons ($T \sim 2400$ K). The distribution of neutron energies in the beam is related to temperature by $E_n = k_B T$.

A wide range of instrumentation has been developed to apply neutron scattering to various different problems. Here we describe briefly the types of instruments employed within this thesis. Further information on the instruments used here can be found on the ILL and ISIS websites [6], and a more comprehensive discussion of neutron scattering using triple-axis spectrometers can be found in the textbook by Shirane *et al.* [7]. The particular experimental setups for this thesis are covered in more detail in the results chapters 3, 4, 5 and 6.

2.3.1   Triple-axis Spectrometers

The triple-axis spectrometer is one of the most versatile instruments for inelastic studies, particularly well suited to studies of magnetic excitations and phonons. It is also well suited to reactor sources, which have a constant neutron flux, and the triple-axis spectrometers used in this thesis were at the ILL.

A schematic diagram of a triple-axis spectrometer is shown in figure 2.2. The name 'triple-axis' refers to the three axes of the monochromator, sample and analyser which can be rotated independently to fix the angles $2\theta_M$, 2θ and $2\theta_A$ respectively.

The incoming polychromatic neutron beam is incident on a single crystal monochromator which selects a narrow band of energies by Bragg reflection. Filters may be placed in the beam after the monochromator to remove higher order harmonics which also satisfy the Bragg condition of the monochromator, but which would contaminate the measurements. The now monochromatic beam is incident on the sample, and the neutrons are generally scattered by the sample in many directions. The analyser is positioned to select scattering along a particular direction to be measured. Varying the angle of Bragg reflection from the analyser allows neutrons of a particular energy to hit the detector and be counted. Figure 2.2 also shows the scattering vector $\boldsymbol{Q}$ in relation to the scattering angle 2θ. In effect, by varying the three angles $2\theta_M$, 2θ and $2\theta_A$ it is possible to choose $\boldsymbol{k}_i$, $\boldsymbol{k}_f$ and 2θ, and therefore to specify the scattering vector $\boldsymbol{Q}$ and energy transfer E of a particular point to be measured.
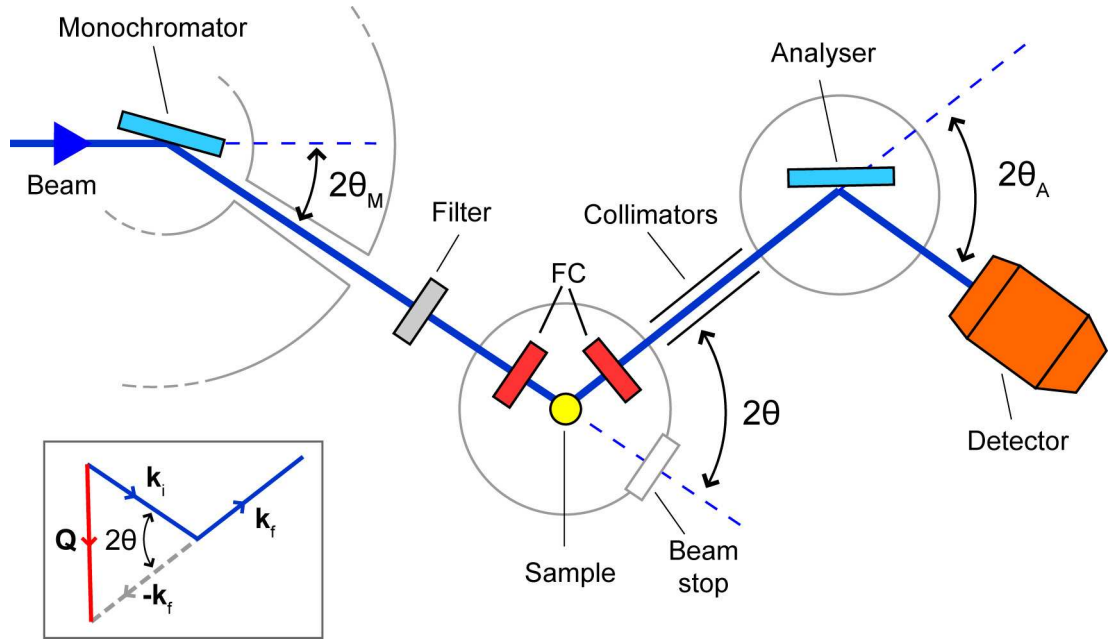
Figure 2.2: Schematic diagram of a triple-axis spectrometer. FC show the positions of flipper coils if the spectrometer is set up to use polarized neutrons; these are not present for normal unpolarized measurements. The inset shows the scattering triangle for this configuration.

Scans are usually made by choosing a series of $(\mathbf{Q}, E)$ points along one particular direction, usually either along a direction in $\mathbf{Q}$ at one fixed energy, or along the energy axis at a fixed point in $\mathbf{Q}$. We refer to these as constant-E and constant-$\mathbf{Q}$ scans respectively. In a standard setup as shown in fig. 2.2 all components of the spectrometer lie in the horizontal plane, so it is only possible to choose scattering wavevectors $\mathbf{Q}$ that lie in the horizontal plane. The sample must therefore be mounted to place the wavevectors of interest within the horizontal scattering plane.

In practice scans are made with either a fixed incident wavevector $\mathbf{k}_i$ or a fixed final wavevector $\mathbf{k}_f$, while varying the other. With fixed $\mathbf{k}_i$ the monochromator axis $(2\theta_M)$ is fixed, so the sample position is unchanged throughout the scan: the angles 2θ and $2\theta_A$ move to perform the scan. Working with fixed $\mathbf{k}_f$ requires all components of the instrument to move during the scan. This second setup is more commonly used.

2.3.2 Triple-axis Spectrometers with Polarized Neutrons

When the triple-axis spectrometer is used with polarized neutrons the setup is similar to the unpolarized setup shown in fig. 2.2. The same process is used to choose the $\mathbf{Q}$–E points to measure, and to perform scans. However, to include one-

dimensional polarization analysis there are some important differences.

The main difference is the addition of two flipper coils (the positions of which are marked 'FC' in fig. 2.2), an electromagnetic guide field around the sample position and the replacement of both monochromator and analyser by Heusler crystals (Cu_2MnAl). The Heusler monochromator both monochromates the neutron beam and polarizes it. This is achieved by magnetizing the Heusler crystal in the direction of the required polarization. The Heusler crystal has a cross-section such that neutrons of one polarization (say, $|\uparrow\rangle$) are preferentially Bragg scattered, while the cross-section for the other polarization ($|\downarrow\rangle$) is almost zero. The polarization direction is maintained through the experiment using the guide field. On scattering within the sample, a combination of spin-flip and non-spin-flip processes will occur, so that the beam reaching the analyser will contain a combination of the two polarizations, the proportion of which gives information about the sample (see section 2.2.4). The Heusler analyser again preferentially Bragg scatters one of these polarizations (say, $|\uparrow\rangle$), and the number of neutrons with this polarization is measured by the detector. In order to measure the other polarization ($|\downarrow\rangle$) the flipper coils must be used. These flip the polarization of all the neutrons in the beam, and by turning one or both flippers on it is possible to measure all four processes described in section 2.2.4. Specifically, it is possible to measure the scattering from processes that flip the neutrons' spins (spin-flip processes) separately from the scattering from processes that do not (non-spin-flip processes).

2.3.3 Time-of-Flight Chopper Spectrometers

Time-of-flight chopper spectrometers are also used to probe excitations using inelastic neutron scattering. While triple-axis spectrometers measure one point in $\boldsymbol{Q}$-E space at a time, time-of-flight chopper spectrometers allow a large coverage of $\boldsymbol{Q}$-E space to be studied in a single measurement.

In a chopper spectrometer a chopper is used to monochromate the beam, rather than a single crystal monochromator. The Fermi chopper is a rotating drum made, for example, of curved layers of alternating aluminium (transparent to neutrons) and boron (a neutron absorber). A pulse of incident neutrons spreads out in time as it travels, and the fastest (highest energy) neutrons reach the chopper first. As it rotates the chopper allows through a section of the pulse containing neutrons with the desired energy; faster or slower neutrons are blocked by the absorbing strips. The energy range and width is determined by the phase and frequency of the chopper rotation. Chopper spectrometers can be used at steady-flux reactor sources, but the beam must be chopped into pulses before it reaches the Fermi chopper, and this wastes a large proportion of flux. Chopper spectrometers are therefore ideally suited to pulsed spallation sources, and the experiments performed on chopper spectrometers for this thesis were all performed at ISIS.

Figure 2.3 (top) shows a schematic diagram of a time-of-flight chopper spectrometer. Before the Fermi chopper is a background chopper which reduces background contamination by cutting away the edges of the pulse. The monochromatic pulse of
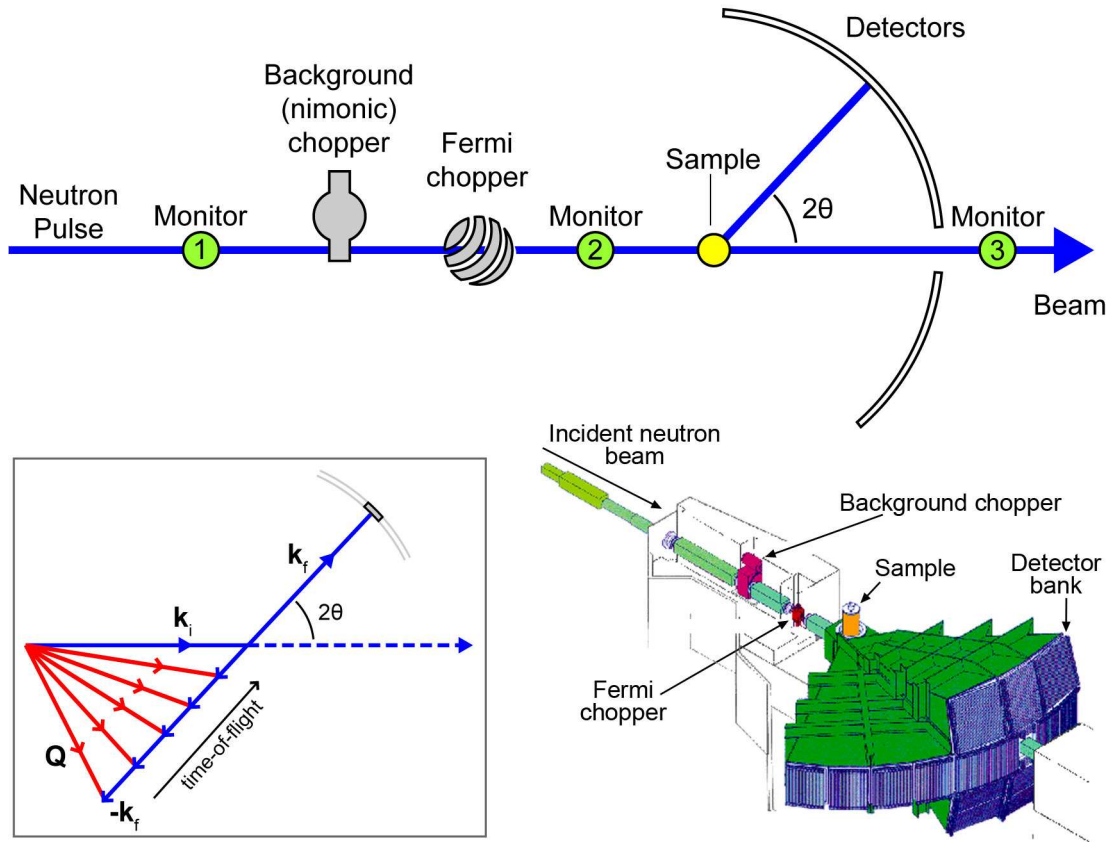
Figure 2.3: Top: schematic diagram of a time-of-flight chopper spectrometer. Bottom left: scattering triangle showing that the scattering vector $\boldsymbol{Q}$ varies with time-of-flight. Bottom right: the MAPS chopper spectrometer at ISIS, showing the large pixelated detector bank.

neutrons scatters from the sample in a range of directions, and neutrons hit the large pixellated detector bank. The detectors record both the neutrons' position and the time at which they are counted. From the time-of-flight, and accurate measurements of the distance travelled, it is possible to calculate how fast the neutrons travelled from the sample, and from this the energy transfer during scattering (see below). One measurement therefore records a large area of $\boldsymbol{Q}$-space over a range of energies.

Time-of-flight analysis

We first consider the calculation of the energy transfer, given in any neutron scattering process by

$$E = \hbar\omega = E_i - E_f \quad , \tag{2.41}$$

where E_i and E_f are the incident and final energies. In a time-of-flight experiment E_i is chosen by the chopper frequency and phase. Instead of directly measuring E_f the time-of-flight of the neutrons from sample to detector, t, is recorded. Substituting

the equations $E_f = m_n v^2/2$ and $v = D/t$, where m_n is the mass of the neutron, v is its velocity and D is the distance from sample to detectors, into eqn. 2.41 leads to an expression for the energy transfer:

$$E = \hbar\omega = E_i - \frac{m_n D^2}{2t^2} \quad . \tag{2.42}$$

The initial wavevector $\boldsymbol{k}_i$ is known, and the scattered wavevector $\boldsymbol{k}_f$ is now fully defined by E_f and the position the neutron hit the detector. The scattering vector $\boldsymbol{Q}$ can be calculated from $\boldsymbol{k}_i$ and $\boldsymbol{k}_f$ using the standard scattering triangle, shown in the bottom left corner of fig. 2.3. $\boldsymbol{Q}$ is shown to be dependent on the time-of-flight, and is therefore coupled to the energy transfer.

The chopper experiments reported in this thesis were performed on two spectrometers called MAPS and HET at ISIS. On these instruments the data set is recorded in time-position binning, and a program called *Homer* [8] converts the data into an array in $\boldsymbol{Q}$-E space. The *Homer* program also converts the data to absolute units using the sample mass, and by comparing the data measured to similar measurements made on a standard vanadium sample. The final intensities are

$$Intensity = \frac{k_i}{k_f} \frac{d^2\sigma}{d\Omega dE_f} \quad \text{in} \quad \text{mb sr}^{-1}\text{meV}^{-1}\text{f.u.}^{-1} \quad , \tag{2.43}$$

where f.u. stands for one formula unit of the sample. These units are referred to as *absolute units* when presenting time-of-flight data taken on MAPS and HET.

Interpreting MAPS data

Two experiments in this thesis were performed on single crystals using the MAPS chopper spectrometer at ISIS, a diagram of which is shown in the bottom right of fig. 2.3. MAPS has a large detector banks approximately perpendicular to the incident beam. This makes it ideally suited to the study of compounds with two-dimensional excitations. When the scattering of interest shows no dependence on one $\boldsymbol{Q}$–direction, say l, this direction is placed parallel to the incoming beam. Data is recorded over a large range of $\boldsymbol{Q}$ in the ab plane, but the value of l varies both over the detector bank, and with energy. However, since the scattering has no l-dependence the data may be projected into the ab plane with no loss of information. Interpreting data from three-dimensional compounds is more complicated, involving careful choice of crystal orientation and incident energy to make the wavevector of interest coincide with the energy of interest.

2.3.4   Powder Diffractometers

Powder diffractometers are used for accurate structure determination. Figure 2.4 shows a schematic diagram of a constant angle powder diffractometer. This type of instrument uses the whole polychromatic ('white') neutron beam, and is usually used at pulsed sources. The polychromatic beam scatters from the sample and neutrons
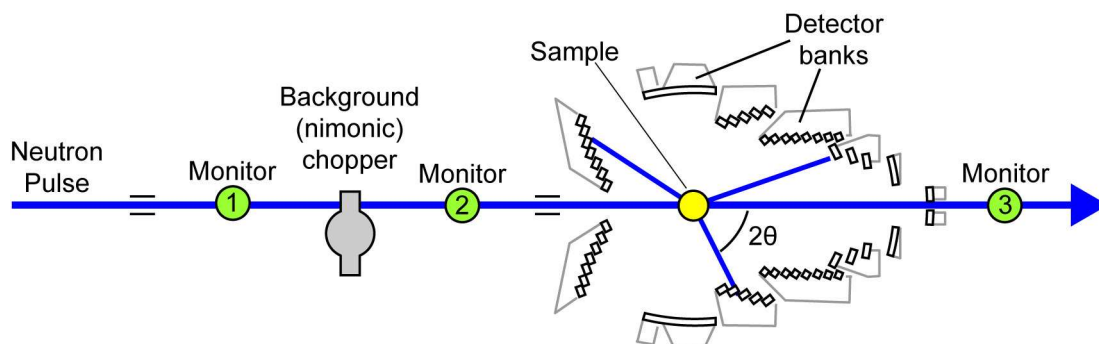
Figure 2.4: Schematic diagram of a constant angle diffractometer, based on the diffractometer GEM at ISIS.

are detected in detector banks at specific angles covering a large range of 2θ. Time-of-flight analysis is used to convert the neutron arrival time to lattice spacing. The spectra recorded in the data banks show a large number of peaks over a wide range of lattice spacing, and the structure is refined using Rietveld refinement on these spectra. The resolution of the instrument is best at large scattering angles, so often only banks at large 2θ are included in the refinement.

2.3.5 Single Crystal Diffractometers

Single crystal diffractometers are also used for accurate structure determination, for both crystallographic and magnetic structures. A standard double axis diffractometer looks much like the triple-axis spectrometer shown in fig. 2.2, but without the analyser, and is used in much the same way, but for elastic scattering only.

References

[1] G.L. Squires, *Introduction to the Theory of Thermal Neutron Scattering* (Cambridge University Press, Cambridge, U.K., 1978).

[2] S. W. Lovesesy, *Theory of neutron scattering from consdensed matter*, vol. 2, Clarendon Press, Oxford, (1984).

[3] E. Balcar and S. W. Lovesey, *Theory of Magnetic Neutron and Photon Scattering* (Clarendon Press, Oxford, U.K., 1989).

[4] Scattering lengths are listed at http://www.ncnr.nist.gov/resources/n-lengths/, taken from Neutron News, **3**, No. 3, 29-37 (1992).

[5] Information on magnetic form factors: http://www.ill.fr/dif/ccsl/ffacts/

[6] Institute Laue-Langevin, Grenonble, France, http://www.ill.fr/; ISIS, Rutherford Appleton Laboratory, U.K., http://www.isis.rl.ac.uk/.

[7] G. Shirane, S. M. Shapiro and J. M. Tranquada, *Neutron Scattering with a Triple-Axis Spectrometer: Basic Techniques* (Cambridge University Press, Cambridge, U.K., 2006).

[8] For information on *Homer* see for example the HET manual, found at http://www.isis.rl.ac.uk/excitations/.

CHAPTER 3

Jahn-Teller Effect in PrO$_2$

3.1 Introduction

This chapter presents calculations of the crystal-field energy levels in PrO$_2$ using a simple point-charge model. These calculations were motivated by recent studies that revealed evidence of a low-temperature static structural distortion below a Jahn-Teller distortion temperature T_D. The calculations described in section 3.2 predict splitting of the orbitally degenerate ground state in the distorted phase. Neutron inelastic-scattering measurements are presented in section 3.3. These studies reveal the temperature dependence of the crystal-field levels, in particular confirming the splitting of the ground-state below T_D. The results are discussed with reference to the calculations.

At room temperature PrO$_2$ is paramagnetic, and forms the cubic *fluorite* structure shown in figure 3.1, with lattice spacing $a = 5.392$ Å. Each Pr^{4+} ion is surrounded by a cube of eight oxygen ions. The Pr^{4+} $4f^1$ configuration consists of two Russell-Saunders terms: $^2F_{5/2}$ and $^2F_{7/2}$, of which the $J = 5/2$ multiplet is lower. Group theory dictates that the cubic crystal field due to the surrounding oxygen ions would split the ground state into a four-fold degenerate Γ_8 and doublet Γ_7 state. Furthermore, both phenomenological point-charge calculations for a cubic crystal field, and susceptibility measurements point to a Γ_8 ground-state [1] (see fig. 3.1, right).

Early neutron measurements on powder samples by Kern *et al.* revealed that below a temperature of $T_N \approx 14$ K the Pr spins order antiferromagnetically [2]. They also measured the Γ_8–Γ_7 crystal-field splitting at 30 K to be ≈ 130 meV within the $J = 5/2$ ground state manifold. However, the ordered magnetic moment per Pr ion was measured to be $0.6 \pm 0.1\mu_B$, far too small to agree with calculated moments for a Γ_8 ground-state. This lead Kern *et al.* to propose a dynamic Jahn-Teller effect in PrO$_2$, which would allow lifting of the ground-state degeneracy and reduction of the calculated moment.

Recent work by Boothroyd *et al.* has provided further evidence for a dynamic Jahn-Teller effect in the Γ_8 electronic ground state [3]. Neutron inelastic measurements on a polycrystalline sample of PrO$_2$ revealed two distinct features in the low-temperature energy spectrum: (1) sharp peaks above 100 meV characteristic of crystal-field transitions between the $4f^1$ states of Pr, both within the $J = 5/2$ multiplet and intermultiplet transitions between $^2F_{5/2}$ and $^2F_{7/2}$, and (2) a broad band of scattering between approximately 10–100 meV. Some of these results are

reproduced in figure 3.2, measured with incident neutron energies between 30 and
1200 meV.

Figure 3.2a clearly shows the Γ_8–Γ_7 crystal-field transition at 131 meV previously
reported by Kern *et al.*, and the broad band of scattering centred on ~ 30 meV
but extending from 10 to 100 meV. Figures 3.2b and c show peaks interpreted as
intermultiplet transitions between crystal field levels with $J = 5/2$ and $J = 7/2$.
In fig. 3.2a we also observe a peak centred at 3 meV, which was found to shift to
lower energies as the temperature was increased, becoming quasielastic above the
magnetic ordering temperature ($T_N \approx 14$ K), and which was therefore attributed to
splitting of the ground-state multiplet due to the static exchange field present in the
antiferromagnetically ordered phase.

Although the sharp peaks at higher energies were readily explained as crystal-field
levels, the broad scattering feature does not fit into the same scheme. Boothroyd *et
al.* proposed that the effects were the result of strong coupling between $4f^1$ electronic
states and local lattice distortions, leading to the dynamic Jahn-Teller effect (DJTE).
To investigate this coupling between electronic and vibrational degrees of freedom
they proposed a model with a *vibronic* Hamiltonian, based on the cubic crystal-
field splittings but coupling a single phonon mode to the lowest crystal-field levels.
Although simplistic, calculations with this model produced vibronic levels in the right
region of the spectrum [3], supporting the above interpretation of the data.

Following these measurements on the energy spectrum of PrO₂ further studies
were made of the structure by Gardiner *et al.* [4]. Neutron diffraction data on a single
crystal of PrO₂ revealed a cooperative Jahn-Teller distortion at $T_D = 120\pm2$ K. Below
this temperature the existence of half-integer reflections gave evidence for a doubling
of the unit cell along one crystallographic direction. These reflections satisfied the
selection rules $h = n + 1/2$, $k =$ odd, $l =$ even, where n, k and l are integers, and
h, k and l can be permuted. Reflections with $l = 0$ were only present below $T = 20$
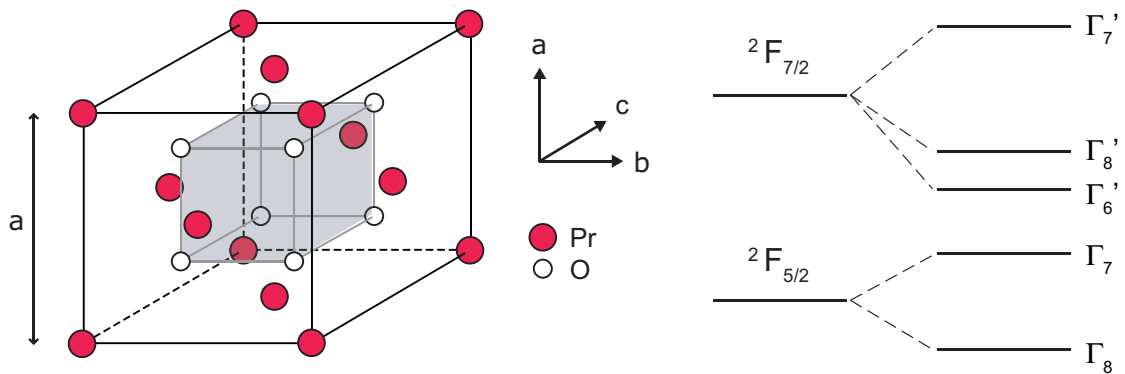
Figure 3.1: Left: The face-centred cubic *fluorite* structure of PrO₂ at high
temperature. Right: Schematic diagram of the splitting of the
free ion multiplets for the Pr⁴⁺ ion in a cubic crystal electric field.
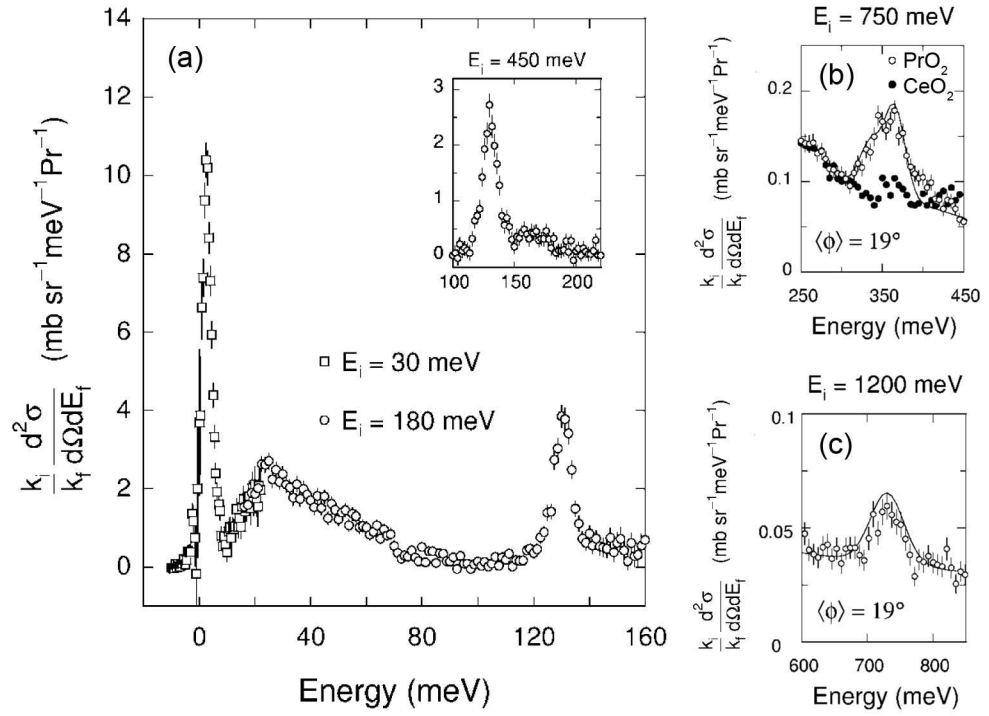
Figure 3.2: Low-temperature neutron inelastic data on PrO_2 and CeO_2 measured by Boothroyd *et al.* [3]. (a) PrO_2 spectrum corrected for the non-magnetic background by subtraction of CeO_2 data. (b, c) Intermultiplet ($^2F_{5/2}$–$^2F_{7/2}$) transitions in PrO_2.
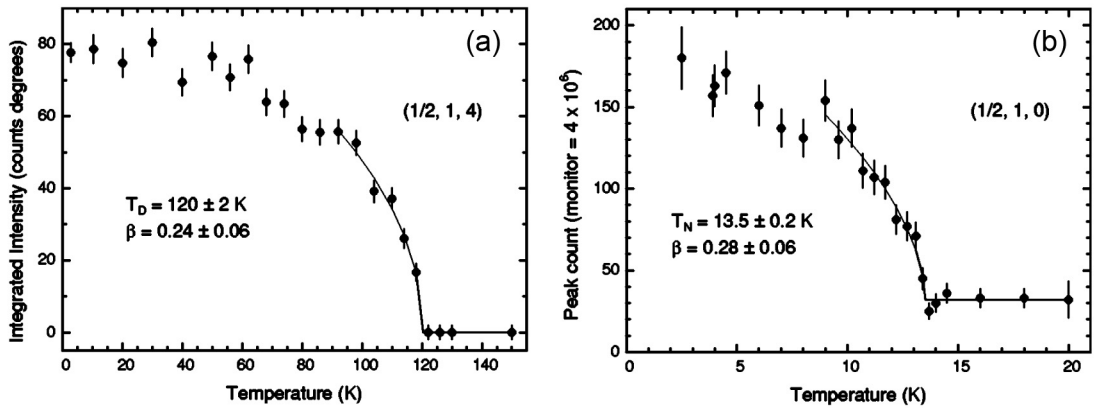
Figure 3.3: Temperature dependences of the (a) $(1/2, 1, 4)$ and (b) $(1/2, 1, 0)$ peaks from Gardiner *et al.* [4]. Solid lines are fits of the form $I \propto (T_\alpha - T)^{2\beta}$, where T_α is T_D or T_N as indicated.

K. The temperature dependence of two such reflections are shown in fig. 3.3. Figure 3.3a shows a structural reflection with $l \neq 0$, from which T_D was determined. Figure 3.3b is an example of a reflection with $l = 0$, which shows the intensity falling to zero within experimental error at $T_N = 13.5$ K, the same ordering temperature found for stronger integer magnetic order reflections. Gardiner *et al.* therefore concluded that the half-integer reflections with $l = 0$ belong to the magnetic phase, revealing that a component of the magnetic unit cell is also doubled along one crystal axis, i.e. the displacement of oxygen ions due to the Jahn-Teller distortion affects the magnetic ordering of the Pr sublattice.

Gardiner *et al.* performed detailed analysis of the intensities of a set of integer and half-integer structural and magnetic reflections at low temperatures in order to identify the structure produced by the Jahn-Teller distortion below $T_D = 120 \pm 2$ K, and the refined magnetic structure. The analysis gave two possible patterns of oxygen displacements, displayed in figures 3.4 b and c. Blue arrows represent the direction of the oxygen ion displacements, calculated to be $d = 0.07$ Å for either structure. In the first structure, labelled the *sheared* structure (fig. 3.4b), oxygen cubes in the two halves of the doubled unit cell are sheared in opposite directions. In the second structure (fig. 3.4c) the two sides of each cube are sheared in rotated directions, and we label this the *chiral* structure [1]. After averaging over domains it proved impossible to distinguish between the two possibilities for the doubled structural unit cell. However, consideration of both crystal-field and Jahn-Teller energies found the chiral structure to be more energetically favourable [5]. Possibilities for the doubled magnetic structure are given in reference [4], but again could not be definitively distinguished between using the neutron data.

Very recent x-ray diffraction measurements made by Gardiner *et al.* [6] have in fact ruled out the sheared structure, and confirmed the chiral displacement of oxygen ions as the correct structure below the Jahn-Teller distortion ($T_D = 120$ K). Since previous analysis of the energy spectra by Boothroyd *et al.* and others has assumed a cubic crystal field, and resulting four-fold orbitally degenerate Γ_8 ground state, there is clearly scope for further modelling. The newly confirmed chiral structure lowers the crystal-field symmetry at the Pr site, and must therefore split the Γ_8 ground state. With accurate measurements of the oxygen displacements in the chiral structure it is valuable to calculate the effect of the crystal-field on the energy levels, and to see if the ground state splitting might contribute to the intensity around 30 meV shown in fig. 3.2a. Detailed measurements of the spectra in this region at higher temperatures are needed to establish whether this level disappears above $T_D = 120$ K. Since these calculations also model the effect of the Jahn-Teller distortion on the Γ_7 excitation at 130 meV there is motivation to perform measurements of the temperature dependence of this level.

The rest of this chapter presents the results of a first-principles simple point-charge calculation of the crystal field levels in PrO$_2$. This is followed by a report on further neutron scattering measurements of the energy spectrum of PrO$_2$ made

---

[1]This structure is not truly chiral because the sense of rotation of the displacement vector is mirrored in the two halves of the unit cell, but we use the label for convenience.
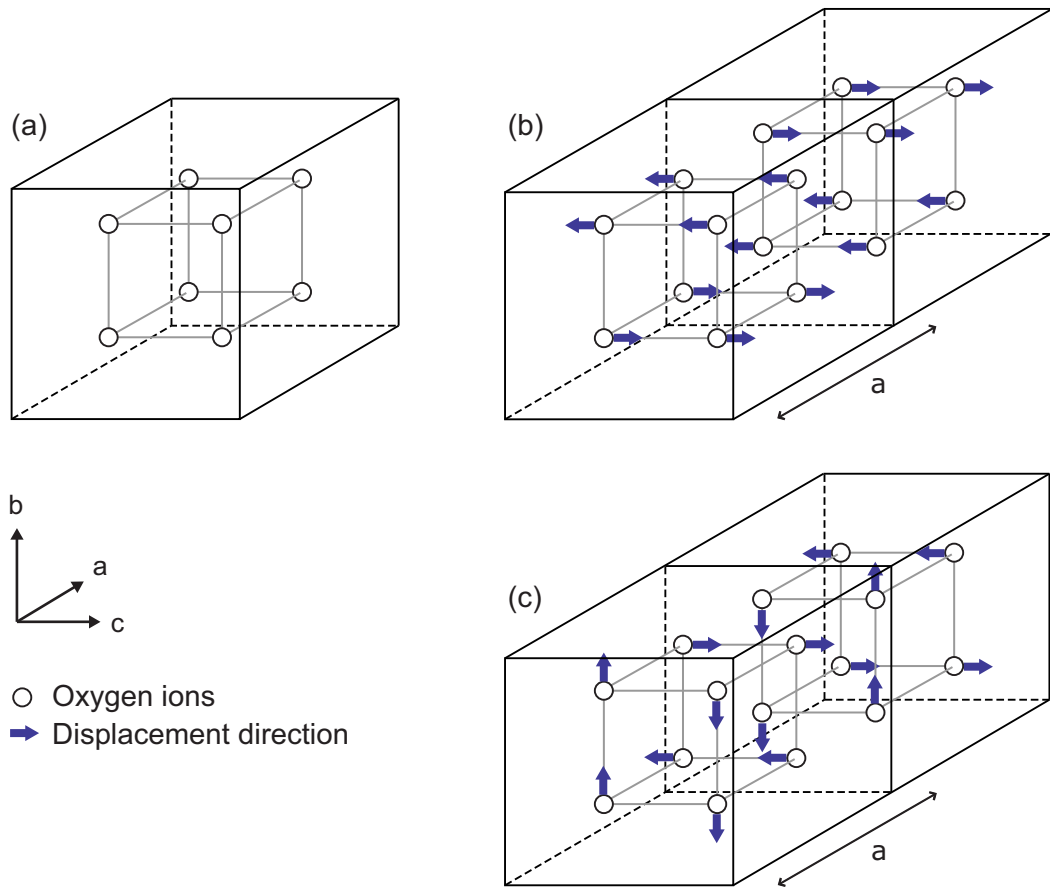
Figure 3.4: The structure of PrO$_2$ showing oxygen ions only. (a) Fluorite structure at high temperatures, as in fig. 3.1. Possible distorted structures are shown in (b) *Sheared structure* and (c) *Chiral structure*, with arrows showing the direction oxygen ion displacements. Both (b) and (c) double the unit cell in one direction.

to study the crystal-field levels in more detail, and in particular their temperature dependence. The results of the neutron scattering experiments are discussed in comparison with those of the crystal field calculation.

3.2   Crystal Field Calculation

3.2.1   Crystal Field Theory versus Ligand Field Theory

The concept of a crystal field was first developed by Bethe in 1929 to study the effect of surrounding ions on the electron distribution of a single magnetic ion on a lattice. The ion and its surrounding neighbouring ions (ligands) were modelled as uniform spheres, their charges located at a point in the centre, with no overlapping of the charge distributions. The crystal field was then defined as the effect of those charges on the central ion, calculated solely from the Coulomb interaction between the central and surrounding ions, and *crystal field theory* the method of calculating its effect on physical properties of the system.

Many effects are neglected in this simple theory. A more general model of the field due to the surrounding ions might include, among other things, covalency effects, spatial distribution of charge allowing for charge distribution overlap, and ligand bond strengths. The term *ligand field theory* has been coined to describe the manner in which the physical properties of an ion in a compound are influenced by all effects of the surrounding ions. Crystal field theory is then a limiting case of ligand field theory which considers only electrostatic interactions.

3.2.2   Point-Charge Model

Many attempts have been made to improve calculations of the crystal field by introducing more of these effects, with limited success [7]. In fact it has been found that many results of ligand field theory depend largely on the symmetry of the distribution of the ligand surrounding the central ions, and far less on the details of the model. Useful information can therefore be obtained from a simple point-charge model using crystal field theory which, although neglecting many effects, does include all the information on the symmetry of the surrounding ligands. Including only the electrostatic interaction between the central and nearest-neighbouring ions has the advantage that the effect of the crystal field on the energy spectrum of the ion in question can be calculated from first principles. This is the approach we take for PrO₂. However, because it disregards the overlap between charge distributions the point-charge model is known to underestimate the crystal field splittings of energy levels.

If we assume that the crystal electric field effects are small [2] they can be calculated as a perturbation on the free-ion wavefunctions and energy levels of the Pr ions. The problem then becomes one of finding the perturbing Hamiltonian and its matrix elements between free-ion states of the Pr ions. This matrix can then be diagonalized to find the energy levels and eigenfunctions of the Pr ion in the crystal electric field.

---

[2]This is a valid approximation for $4f$ electrons which are shielded from the crystal field by outer s and p shells.

3.2.3 Determining the Perturbing Hamiltonian

We consider the effect on the Pr ion due to its immediate surroundings: each nearest-neighbouring oxygen ion (ligand) is modelled as a point charge, and affects the electrons of the Pr ion via the Coulomb interaction. The electrostatic potential at a point (r, θ, ϕ) near the origin at the Pr ion is then given by:

$$V(r, \theta, \phi) = \frac{1}{4\pi\varepsilon_0} \sum_j \frac{q_j}{|(\boldsymbol{R}_j - \boldsymbol{r})|} \quad , \tag{3.1}$$

where q_j is the charge at the jth neighboring ion, a distance R_j from the origin. We make the approximation that the crystal electric field affects only electrons in unfilled shells of the Pr ion, since closed shells would be affected only in a higher order of perturbation. If the Pr ion has i electrons in unfilled shells at positions (r_i, θ_i, ϕ_i), and with charges $-|e|$, then classically the perturbing potential energy due to the crystal electric field (CEF) can be written:

$$W_{CEF} = \sum_i -|e|\, V_i = \frac{1}{4\pi\varepsilon_0} \sum_i \sum_j \frac{-|e|\, q_j}{|(\boldsymbol{R}_j - \boldsymbol{r}_i)|} \quad . \tag{3.2}$$

The crystal electric field (CEF) perturbing Hamiltonian operator $\mathcal{H}_{CEF}$ is effectively this classical potential energy rewritten in terms of operators, i.e.

$$\mathcal{H}_{CEF} = W_{CEF} = \sum_i -|e|\, V(r_i, \theta_i, \phi_i) \quad . \tag{3.3}$$

3.2.4 Tensor Operators

In order to facilitate the calculation we make use of operator equivalents. The calculation of the matrix elements of these operators is discussed in the literature [3]. Standard tensor operators $C_q{}^k$ are defined as:

$$C_m{}^n = \left(\frac{4\pi}{2n+1}\right)^{\frac{1}{2}} Y_n{}^m \quad , \tag{3.4}$$

where $Y_n{}^m$ are spherical harmonic functions [9]. We then introduce *Crystal Field Parameters*, B_{nm}, in order to write a generalised CEF Hamiltonian in terms of the

---

[3]The tensor operators used here are fully described by Wybourne [8], although some errors are contained within the text. For a simple explanation of the method of calculation, which uses the same point-charge set-up but a different operator technique (Stevens' operators), see Hutchings [9]. This technique was not followed since the use of Stevens' operators restricts the basis states to those in the lowest J multiplet. We note that the crystal field parameters are defined slightly differently in the two operator methods, with a simple conversion between the two notations [10], although the final eigenvalues and eigenvectors will differ because of the truncation of basis states in the Stevens' operator method.

tensor operators [4]:

$$\mathcal{H}_{CEF} = \sum_n B_{n0} C_0{}^n + \sum_n \sum_{m=1}^n B_{nm}^c \left[C_{-m}{}^n + (-1)^m C_m{}^n \right]$$ (3.5)

$$+ \sum_n \sum_{m=1}^n i B_{nm}^s \left[-C_{-m}{}^n + (-1)^m C_m{}^n \right] ,$$

Since the matrix elements of the tensor operators $C_m{}^n$ are known, the energy levels and eigenvectors are easily found by calculating the crystal field parameters B_{nm}. Expressions for these are derived by equating the generalised Hamiltonian above with that derived from the point charge model (eqn. 3.3).

In order to simplify the calculations that follow by avoiding imaginary quantities it is useful to introduce tesseral harmonic functions (Z_{nm}), which are related to the spherical harmonics $Y_n{}^m$:

$$Z_{n0} = Y_n{}^0$$ (3.6)

$$\left. \begin{array}{l} Z^c{}_{nm} = (1/\sqrt{2})[Y_n{}^{-m} + (-1)^m Y_n{}^m] \\ Z^s{}_{nm} = (i/\sqrt{2})[Y_n{}^{-m} - (-1)^m Y_n{}^m] \end{array} \right\} \quad m > 0 .$$

Using the definition of the tensor operators (eqn. 3.4) along with eqn. 3.6 we can rewrite the tensor operators in terms of tesseral harmonics. The expression for the generalised CEF Hamiltonian (eqn. 3.5) then becomes:

$$\mathcal{H}_{CEF} = \sum_n B_{n0} \left(\frac{4\pi}{2n+1} \right)^{\frac{1}{2}} Z_{n0}$$ (3.7)

$$+ \sum_n \sum_{m=1}^n B_{nm}^c \sqrt{2} \left(\frac{4\pi}{2n+1} \right)^{\frac{1}{2}} Z_{nm}^c$$

$$- \sum_n \sum_{m=1}^n B_{nm}^s \sqrt{2} \left(\frac{4\pi}{2n+1} \right)^{\frac{1}{2}} Z_{nm}^s .$$

3.2.5 Crystal Field Parameters, B_{nm}

It can be shown (see reference [9]) that

$$\frac{1}{|(\boldsymbol{R}_j - \boldsymbol{r})|} = \sum_{n=0}^\infty \frac{r^n}{R^{(n+1)}} \left[\sum_\alpha \frac{4\pi}{(2n+1)} Z_{n\alpha}(\theta_j, \phi_j) Z_{n\alpha}(\theta, \phi) \right] ,$$ (3.8)

where the sum over α includes $m = 0$ and both c and s terms for all $m \neq 0$ (i.e. Z_{n0} as well as Z_{nm}^c and Z_{nm}^s for all m). Inserting this into eqn. 3.1, and using eqn. 3.3

---

[4]The superscripts c and s on the B_{nm} refer to the operator functions they multiply: when written out fully in terms of Legendre functions B^c and B^s coefficients multiply functions of the form $\cos(m\phi)$ and $\sin(m\phi)$, respectively.

we can rewrite the CEF Hamiltonian due to the surrounding point charges as:

$$
\begin{aligned}
\mathcal{H}_{CEF} &= -\frac{|e|}{4\pi\varepsilon_0}\sum_j q_j \sum_n \frac{r^n}{R_j^{(n+1)}}\frac{4\pi}{(2n+1)}Z_{n0}(\theta_j,\phi_j)Z_{n0}(\theta,\phi) \qquad (3.9)\\
&\quad -\frac{|e|}{4\pi\varepsilon_0}\sum_j q_j \sum_n \sum_m \frac{r^n}{R_j^{(n+1)}}\frac{4\pi}{(2n+1)}Z_{nm}^c(\theta_j,\phi_j)Z_{nm}^c(\theta,\phi)\\
&\quad -\frac{|e|}{4\pi\varepsilon_0}\sum_j q_j \sum_n \sum_m \frac{r^n}{R_j^{(n+1)}}\frac{4\pi}{(2n+1)}Z_{nm}^s(\theta_j,\phi_j)Z_{nm}^s(\theta,\phi)
\end{aligned}
$$

By directly comparing this expression for the Hamiltonian derived from the point-charge model (eqn. 3.9) with the expression defining the crystal field parameters (eqn. 3.7) we find expressions for the crystal field parameters in the point-charge model:

$$
\begin{aligned}
B_{n0} &= -\frac{|e|}{4\pi\varepsilon_0}\langle r^n\rangle\left(\frac{4\pi}{2n+1}\right)^{\frac{1}{2}}\sum_j \frac{q_j}{R_j^{(n+1)}}Z_{n0}(\theta_j,\phi_j) \qquad (3.10)\\
B_{nm}^c &= -\frac{|e|}{4\pi\varepsilon_0}\frac{\langle r^n\rangle}{\sqrt{2}}\left(\frac{4\pi}{2n+1}\right)^{\frac{1}{2}}\sum_j \frac{q_j}{R_j^{(n+1)}}Z_{nm}^c(\theta_j,\phi_j)\\
B_{nm}^s &= +\frac{|e|}{4\pi\varepsilon_0}\frac{\langle r^n\rangle}{\sqrt{2}}\left(\frac{4\pi}{2n+1}\right)^{\frac{1}{2}}\sum_j \frac{q_j}{R_j^{(n+1)}}Z_{nm}^s(\theta_j,\phi_j) \quad ,
\end{aligned}
$$

where the sum over j is over the nearest-neighbouring ions. $\langle r^n\rangle$ is the nth radial moment of the charge distribution [5].

The crystal field parameters derived above fully define the perturbing Hamiltonian in the point-charge model and, with eqn. 3.5, allow easy calculation of the matrix elements of $\mathcal{H}_{CEF}$ and subsequent diagonalization to find energy levels and eigenvectors. These last steps were performed using the program *SPECTRE* [11].

3.2.6 Matrix Elements

Matrix elements of the crystal field Hamiltonian are calculated between basis states of the free Pr^{4+} ion. A full set of 14 basis states of the two multiplets $^2F_{5/2}$ and $^2F_{7/2}$ is included, with states labelled $|\psi\rangle = |J,M\rangle$, where $M = -J\cdots J$. The initial splitting between the six-fold degenerate $|\frac{5}{2},M\rangle$ and eight-fold degenerate $|\frac{7}{2},M\rangle$ levels is given by the spin-orbit splitting ζ for a free Pr ion.

The perturbing Hamiltonian, $\mathcal{H}_{CEF}$ is diagonalized in this basis to give the eigenfunctions and eigenvalues of the new crystal electric field energy levels. The CEF eigenfunctions are then used to calculate the matrix elements between the new

---

[5]The radial moments $\langle r^n\rangle$ are tabulated by Freeman and Desclaux [12]. However, the values for Pr^{4+} are not tabulated, were taken from an older and less reliable source [13], and scaled. The scaling factors were calculated by comparing values for the radial functions of Ce^{3+} which appear in both sources.

ground state and excited levels in the dipole approximation:

$$|\langle j|\hat{\mu}_\perp|i\rangle|^2 \tag{3.11}$$

where $|i\rangle$ and $|j\rangle$ are the initial and final CEF eigenfunctions (having corresponding eigenvalues E_i, E_j), and $\hat{\mu}_\perp$ is the component of the magnetic moment operator perpendicular to $\boldsymbol{Q}$. If we assume that the energy levels are sharp, we can write the response function, $S(\boldsymbol{Q},\omega)$ (see chapter 2, section 2.2.3):

$$S(\boldsymbol{Q},\omega) = \sum_{i,j} \rho_i |\langle j|\hat{\mu}_\perp|i\rangle|^2 \delta(E_i - E_j - \hbar\omega) \quad , \tag{3.12}$$

where ρ_i is the thermal population factor of the initial state. $S(\boldsymbol{Q},\omega)$ can be directly compared to neutron scattering data.

3.2.7   Results

Figure 3.5 shows the Pr ions and their nearest-neighbouring oxygen ions, in the cubic and 'chiral' structures (as defined in fig. 3.4(b,c)). In the chiral structure the oxygen octahedra are distorted by small displacements of the oxygen ions in the directions marked by the arrows, measured by Gardiner *et al.* to be 0.07Å [4].

Using equation 3.10 the crystal field parameters were calculated for the Pr sites in both the cubic structure and distorted chiral structure. The parameters are given in table 3.1. The displacements of the oxygen ions in the distorted structures lower the symmetry of the Pr site, and therefore the symmetry of the crystal electric field, so more B_{nm} parameters are needed to define the CEF Hamiltonian. In particular we see that the cubic structure (which has four-fold symmetry) needs only B_{nm} where n, m are multiples of four, while the chiral structure (which has two-fold rotational symmetry only) includes other n, m, restricted only to multiples of two.
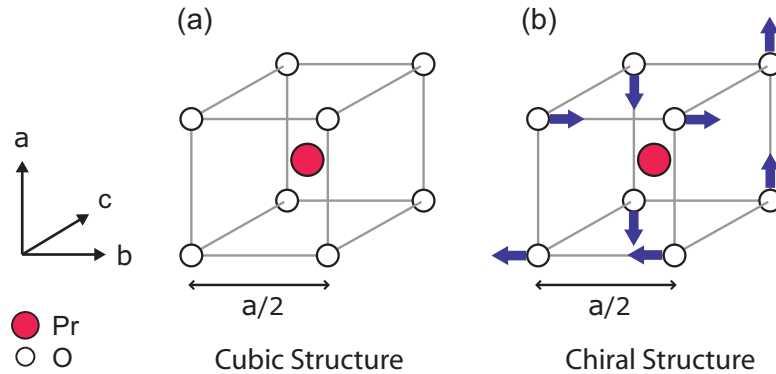
Figure 3.5: Pr environments in the (a) cubic and (b) chiral structures: nearest neighbouring oxygen ion positions only. Blue arrows indicate the displacement directions of oxygen ions in the distorted structure.

Cubic	$B_{20} = 0$	$B_{22}^c = 0$	$B_{22}^s = 0$
	$B_{40} = -197.16$	$B_{42}^c = 0$	$B_{42}^s = 0$
	$B_{60} = 20.87$	$B_{44}^c = -117.82$	$B_{44}^s = 0$
		$B_{62}^c = 0$	$B_{62}^s = 0$
		$B_{64}^c = -39.04$	$B_{64}^s = 0$
		$B_{66}^c = 0$	$B_{66}^s = 0$
Chiral	$B_{20} = 5.18$	$B_{22}^c = 0$	$B_{22}^s = 69.45$
	$B_{40} = -197.92$	$B_{42}^c = 0$	$B_{42}^s = 23.11$
	$B_{60} = 20.69$	$B_{44}^c = -117.18$	$B_{44}^s = 0$
		$B_{62}^c = 0$	$B_{62}^s = -1.83$
		$B_{64}^c = -39.08$	$B_{64}^s = 0$
		$B_{66}^c = 0$	$B_{66}^s = -0.90$

Table 3.1: Crystal field parameters for the two structures, in meV.

Calculation of the matrix elements of the crystal field Hamiltonian and subsequent diagonalization were performed using *SPECTRE* to give the energy levels and eigenfunctions of the new crystal field states. The results are given in figure 3.6 and table 3.2, which displays the lowest calculated energy levels, largest two components of each associated eigenvector, and $\sum |\langle j|\hat{\mu}_\perp|i\rangle|^2$ (eqn. 3.11) which indicates the relative intensities of the levels.

We see that for the cubic structure the point-charge model predicts a four-fold orbitally degenerate ground-state (Γ_8), and a doublet at 52.0 meV (Γ_7), in agreement with the experimental evidence discussed in the introduction. As discussed earlier, the point charge model is known to underestimate energy levels, so the 52.0 meV level predicted here corresponds to the peak at ≈ 130 meV measured by neutron scattering. In the chiral structure the calculations predict a further splitting of the ground state, resulting in a crystal field level 8.9 meV above the new ground state. Assuming a similar re-scaling of the energy levels this splitting might be expected to be ~ 20 meV in reality. The chiral distortion also shifts the 52.0 meV level up to 71.7 meV, and as well as moving to higher energies this level is predicted to reduce in intensity in the chiral phase: table 3.2 shows a reduction in $\sum |\langle j|\hat{\mu}_\perp|0\rangle|^2$ of 42%.

Structure	j	Energy E_j	Eigenvector $\lvert J, M \rangle$	$\sum \lvert \langle j \lvert \hat{\mu}_\perp \lvert 0 \rangle \rvert^2$
Cubic	0	0.0 meV	$1.00\lvert\frac{5}{2},+\frac{1}{2}\rangle - 0.04\lvert\frac{7}{2},-\frac{7}{2}\rangle \ldots$	2.546
		0.0 meV	$1.00\lvert\frac{5}{2},-\frac{1}{2}\rangle + 0.04\lvert\frac{7}{2},+\frac{7}{2}\rangle \ldots$	
		0.0 meV	$0.88\lvert\frac{5}{2},+\frac{5}{2}\rangle + 0.40\lvert\frac{5}{2},-\frac{3}{2}\rangle \ldots$	
		0.0 meV	$0.88\lvert\frac{5}{2},-\frac{5}{2}\rangle + 0.40\lvert\frac{5}{2},+\frac{3}{2}\rangle \ldots$	
	1	52.0 meV	$0.91\lvert\frac{5}{2},-\frac{3}{2}\rangle - 0.41\lvert\frac{5}{2},+\frac{5}{2}\rangle \ldots$	1.615
		52.0 meV	$0.91\lvert\frac{5}{2},+\frac{3}{2}\rangle - 0.41\lvert\frac{5}{2},-\frac{5}{2}\rangle \ldots$	
Chiral	0	0.0 meV	$0.92\lvert\frac{5}{2},+\frac{1}{2}\rangle + 0.03\lvert\frac{7}{2},+\frac{1}{2}\rangle \ldots$	2.618
		0.0 meV	$0.92\lvert\frac{5}{2},-\frac{1}{2}\rangle - 0.03\lvert\frac{7}{2},-\frac{1}{2}\rangle \ldots$	
	1	8.9 meV	$0.89\lvert\frac{5}{2},-\frac{5}{2}\rangle + 0.44\lvert\frac{5}{2},+\frac{3}{2}\rangle \ldots$	0.619
		8.9 meV	$0.89\lvert\frac{5}{2},+\frac{5}{2}\rangle + 0.44\lvert\frac{5}{2},-\frac{3}{2}\rangle \ldots$	
	2	71.7 meV	$0.84\lvert\frac{5}{2},-\frac{3}{2}\rangle - 0.37\lvert\frac{5}{2},+\frac{5}{2}\rangle \ldots$	0.939
		71.7 meV	$0.84\lvert\frac{5}{2},+\frac{3}{2}\rangle - 0.37\lvert\frac{5}{2},-\frac{5}{2}\rangle \ldots$	

Table 3.2: Lower crystal field levels for the two structures, calculated using the crystal field parameters in table 3.1: energy levels and largest components of eigenvectors. Also listed are the sum of the squares of matrix elements between each level and the ground state, $\sum \lvert \langle j \lvert \hat{\mu}_\perp \lvert 0 \rangle \rvert^2$, see eqn. 3.11.
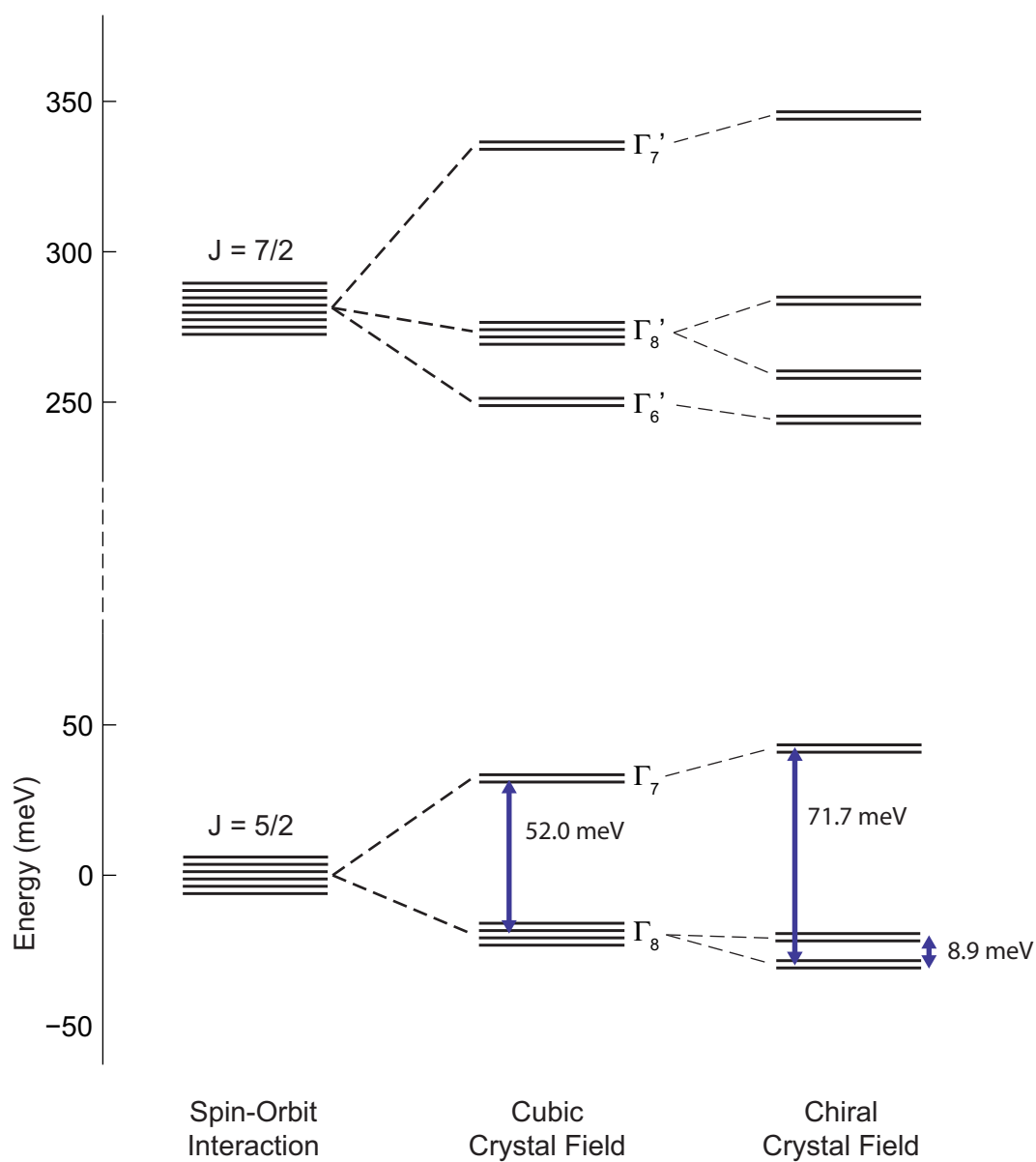
Figure 3.6: Results of the point-charge crystal-field calculation for PrO$_2$: energy levels of free-ions split by the spin-orbit interaction; splitting of these levels in the cubic structure; splitting of the same levels in the chiral structure.

3.3 Neutron Scattering Measurements

3.3.1 Experimental Details

Neutron scattering measurements were made on a powder sample of PrO$_2$ using the HET (High Energy Transfer) spectrometer at the ISIS facility at the Rutherford Appleton Laboratory. HET is a time-of-flight spectrometer optimised for studies of high-energy magnetic excitations. An outline of time-of-flight spectrometers is given in chapter 2. The banks of detectors surrounding the sample, and 2.5 m away, are almost continuous at low angles ($\phi = 2\theta = 9.31 - 28.69°$), with an additional bank at higher angles ($\phi = 2\theta = 125.44 - 138.72°$) [6].

In order to estimate the background scattering due to non-magnetic processes, such as phonon scattering or multiple-scattering events, measurements were also made on a sample of CeO$_2$. CeO$_2$ was chosen as it is isostructural to PrO$_2$ at room temperature, it has a very similar lattice constant (5.411 Å compared to 5.3856 Å for PrO$_2$), and Pr and Ce have very similar nuclear scattering lengths [14]. For these reasons the non-magnetic scattering from CeO$_2$ has been shown to be very similar to that from PrO$_2$ [3], but because the Ce^{4+} ion is non-magnetic there is no magnetic scattering from CeO$_2$.

Sample Preparation

The sample of polycrystalline PrO$_2$ was prepared by oxidation of a starting material of commercially available Pr$_6$O$_{11}$ by D. Prabhakaran. The Pr$_6$O$_{11}$ was first baked in air at 1020ºC for 10 hours in order to remove any excess oxygen or moisture absorbed from the atmosphere. The pure Pr$_6$O$_{11}$ powder was then cooled to 280ºC and annealed at this temperature under oxygen flow for a week with daily regrinding in order to produce PrO$_2$. The CeO$_2$ powder sample was prepared from commercially available CeO$_2$ by baking at ~ 1000ºC for approximately 10 hours to remove any moisture absorbed from the atmosphere.

For this experiment a sample of PrO$_2$ of mass 25.83 g was sealed in an aluminium foil packet measuring approximately 4.0 by 3.8 cm with a depth of 0.8 cm. A sample of CeO$_2$ of mass 25.98 g was prepared in a similar way. Each sample was mounted in a top-loading closed-cycle-refrigerator (CCR) by clamping the top of the foil packet with an aluminium fixture, and positioned with the incident beam centred on and perpendicular to the largest face of the packet.

3.3.2 Measurements

The spectrum was measured at 7 K, 50 K, 80 K 100 K, 110 K, 115 K, 120 K, 130 K, 165 K and 200 K, using two different incident energies at each temperature: $E_i = 80$ meV (chopper frequency 350 Hz) and $E_i = 250$ meV (chopper frequency 500 Hz)[7].

---

[6]There are also banks at 4 m from the sample which were neglected in this experiment.

[7]The measurements at 165 K were made only with $E_i = 250$ meV

An identical set of measurements were made on the sample of CeO$_2$, at a reduced set of temperatures (7 K, 80 K, 120 K and 165 K).

Vanadium spectra were used to calibrate the detectors. The *Homer* program [15] was used to do this, and to convert the intensities into absolute units (see chapter 2):

$$Intensity = \frac{k_i}{k_f} \frac{d^2\sigma}{d\Omega dE_f} \quad \text{in} \quad \text{mb sr}^{-1}\text{meV}^{-1}\text{Pr}^{-1} \ . \tag{3.13}$$

These units are referred to as *absolute units* hereafter. Any magnetic signal is strongest at low angles in $\phi = 2\theta$ (small $\boldsymbol{Q}$), while the non-magnetic background intensity due to phonons will be strongest at high angles (large $\boldsymbol{Q}$). We therefore averaged data over two regions of interest for each measurement:

$$\text{Low angle bank (LA)}: \quad 9.31° \leq \phi \leq 19.31° \quad \langle\phi\rangle = \langle2\theta\rangle = 14.31° \tag{3.14}$$
$$\text{High angle bank (HA)}: \quad 125.44° \leq \phi \leq 138.72° \quad \langle\phi\rangle = \langle2\theta\rangle = 132.08° \ .$$

3.3.3 Absorption and self-shielding corrections

Absorption and self-shielding corrections compensate for absorption of neutrons by the sample and neutrons that scatter more than once and thus miss the detector. Both processes lower the total transmission of neutrons and a correction is applied to the raw detector count to account for this. The following correction is valid for small-angle scattering only.

The total correction cross-section σ is given by the sum of the absorption and self-shielding cross-sections:

$$\sigma(E) = \sigma_a(E) + \sigma_{ss} \ . \tag{3.15}$$

Figure 3.7 shows the experimental setup, with neutrons incident perpendicular to the largest face of the foil package, which has width x_0. We consider a single scattering event taking place over a distance dx at a distance x into the sample, changing the neutron energy from E_i to E_f. The transmission T is then given by the integral:

$$T = \frac{1}{x_0} \int_0^{x_0} \exp\left(-n\sigma(E_i)x\right) \times \exp\left(-n\sigma(E_f)(x_0 - x)\right) \ dx \tag{3.16}$$

$$= \exp\left(-n\left[\sigma_a(E_f) + \sigma_{ss}\right]x_0\right) \left[\frac{1 - \exp\left(-n\left[\sigma_a(E_i) - \sigma_a(E_f)\right]x_0\right)}{n\left[\sigma_a(E_i) - \sigma_a(E_f)\right]x_0}\right] \ ,$$

where n is the number of scattering units per unit volume, x and x_0 are defined in figure 3.7 and σ_a and σ_{ss} are the absorption and self-shielding cross-sections.

The coherent and incoherent scattering cross-sections (σ_{coh}, σ_{incoh}) for Pr and Ce are tabulated, as are the absorption cross-sections for incident neutrons with $E_i = 25$ meV [16]. For large incident energies $\sigma_{ss} \simeq \sigma_{incoh} + \sigma_{coh}$, and by making the assumption that the absorption cross-section is inversely proportional to the neutron velocity, and therefore proportional to $1/\sqrt{(E)}$, the transmission was evaluated for the incident energies $E_i = 80$, 250 meV. The data was corrected accordingly. Average values for the transmission were 91% and 92% for $E_i = 80$ and 250 meV respectively.
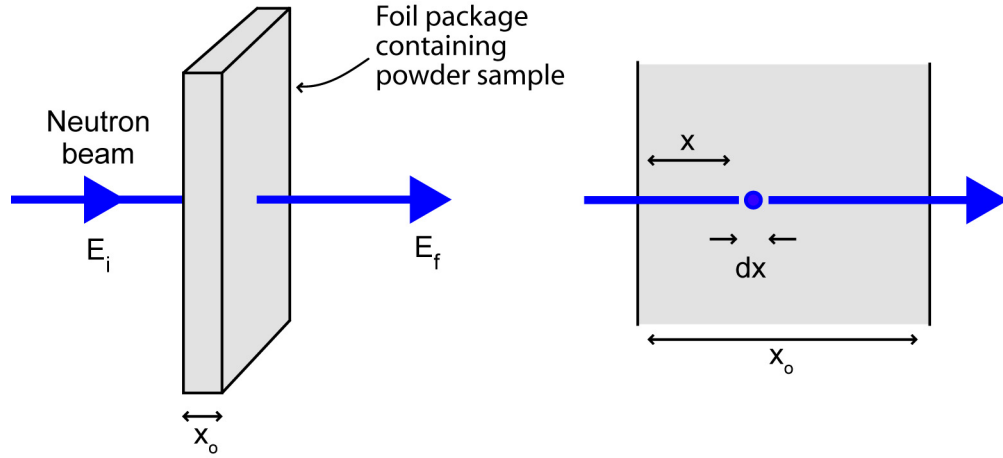
Figure 3.7: The experimental setup for powder neutron inelastic scattering. Neutrons of incident energy E_i enter the sample. They are assumed to travel for a distance x with this energy, then scatter once within a distance dx, and travel the remaining distance until exiting the sample with an energy E_f. These quantities are used to define the sample transmission (eqn. 3.16).

3.3.4 Results

Figure 3.8 shows the data from measurements made at low temperature (7 K) using each of the two incident energies ($E_i = 80, 250$ meV) on both the PrO$_2$ and CeO$_2$ samples. Data are shown as a function of energy, averaged over either the low angle (LA) or high angle (HA) detector banks, as described previously.

To study the magnetic features we look at the low-angle (LA) PrO$_2$ spectra at both incident energies. The data clearly show the features reported previously by Boothroyd *et al.* [3], and reproduced in figure 3.2. There is a sharp peak at approximately 130 meV shown in the low-angle PrO$_2$ data measured at $E_i = 250$ meV (fig. 3.8ai). This spectrum also shows the broad band of scattering between about 10–100 meV, which is measured in more detail with $E_i = 80$ meV (fig. 3.8bi). The fact that the intensity in these features is present in the PrO$_2$ measurements but not in the corresponding CeO$_2$ spectra confirms that they are magnetic in origin.

The high-angle (HA) data give information on the non-magnetic signals in both compounds, from phonons and multiple-scattering processes. Looking at figures 3.8aii and bii we see that generally the same features are present in both the PrO$_2$ and CeO$_2$ spectra. This validates the use of CeO$_2$ as a good measure of the non-magnetic scattering for PrO$_2$.
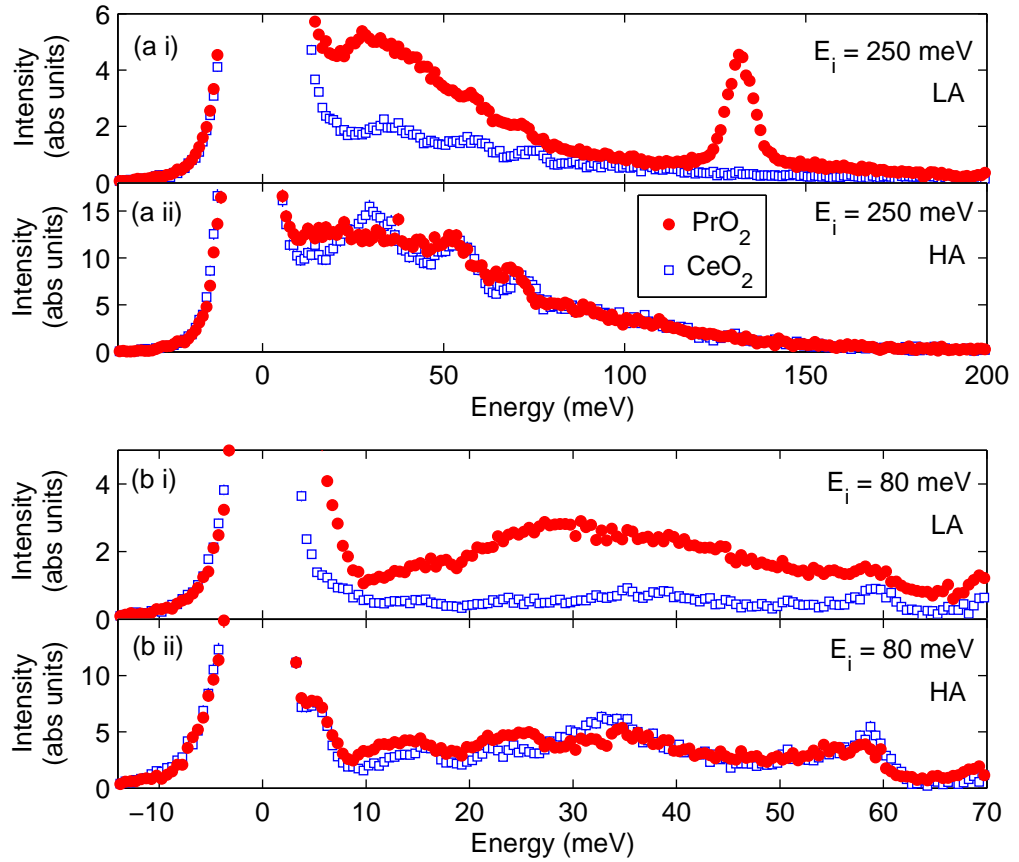
Figure 3.8: Energy spectra of PrO$_2$ and CeO$_2$ measured at 7 K on HET: raw data averaged over low-angle (LA) and high-angle (HA) detector banks, measured using two incident energies (E_i = 80 meV and 250 meV as marked).

3.3.5 Background Subtraction

In the data with E_i = 250 meV there are no background features in the region of interest around 120 meV. Above 100 meV both the PrO$_2$ and CeO$_2$ high-angle spectra, as well as the CeO$_2$ low-angle spectrum, show a smooth gradient. It is therefore unnecessary to subtract the non-magnetic background in order to analyse the data.

However, the high-angle data measured with E_i = 80 meV show a series of features that are associated with the phonon density of states. The low-angle CeO$_2$ data measured with E_i = 80 meV contains small features that correspond to the features of the high-angle spectrum. In order to isolate the magnetic signal in PrO$_2$ it was therefore necessary to subtract the non-magnetic background from the low-angle PrO$_2$ spectrum.

Two methods of subtraction are presented. The first is a simple subtraction of
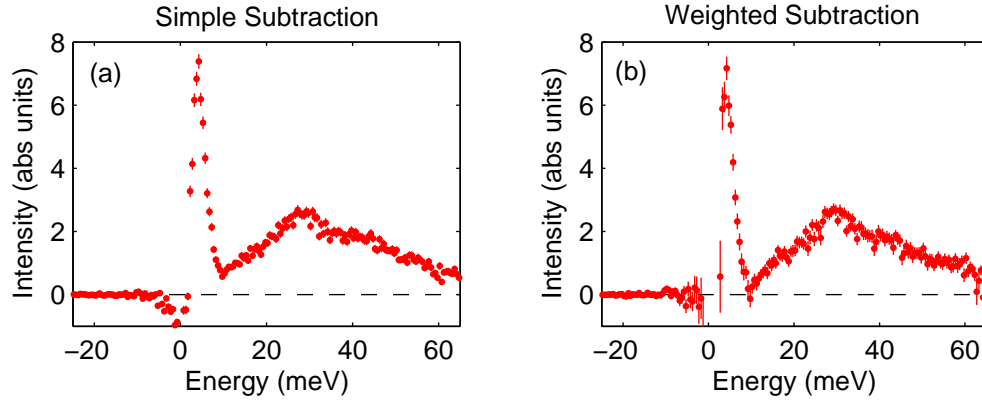
Figure 3.9: PrO$_2$ low-angle spectra at 7K measured with $E_i = 80$ meV. The non-magnetic background has been subtracted using (a) the simple subtraction (eqn. 3.17), and (b) the weighted subtraction (eqn. 3.18).

the low-angle CeO$_2$ spectra from the low-angle PrO$_2$ spectra:

$$I'_{\text{PrO}_2(\text{LA})} = I_{\text{PrO}_2(\text{LA})} - I_{\text{CeO}_2(\text{LA})} \quad , \tag{3.17}$$

where I represents the intensity in each original spectrum, and I' is the magnetic intensity after background subtraction.

Since the phonon peaks in PrO$_2$ and CeO$_2$ (fig. 3.8bii) occur in slightly different positions a second method was also used (labelled the *weighted* subtraction for reference):

$$I'_{\text{PrO}_2(\text{LA})} = I_{\text{PrO}_2(\text{LA})} - \frac{I_{\text{PrO}_2(\text{HA})}}{I_{\text{CeO}_2(\text{HA})}} \times I_{\text{CeO}_2(\text{LA})} \quad . \tag{3.18}$$

Both subtraction methods were employed for $E_i = 80$ meV data at all temperatures. Linear interpolation was used to generate CeO$_2$ spectra for those temperatures not measured, and standard error analysis was used to generate error bars for the subtracted data.

Figure 3.9 shows results of the two subtraction methods for 7 K data. Both spectra show the same features, but the error bars are greatly increased by using the second method of subtraction. We therefore employed simple subtraction of the low-angle spectra for the following analysis.

3.3.6 Analysis of $E_i = 250$ meV Data

Figure 3.10a shows data averaged over the low-angle bank measured with an incident energy of 250 meV on PrO$_2$ at 10 temperatures between 7 and 200 K. The data have been corrected for absorption and self-shielding effects. Data taken at different temperatures have been offset vertically by 2 meV from each previous
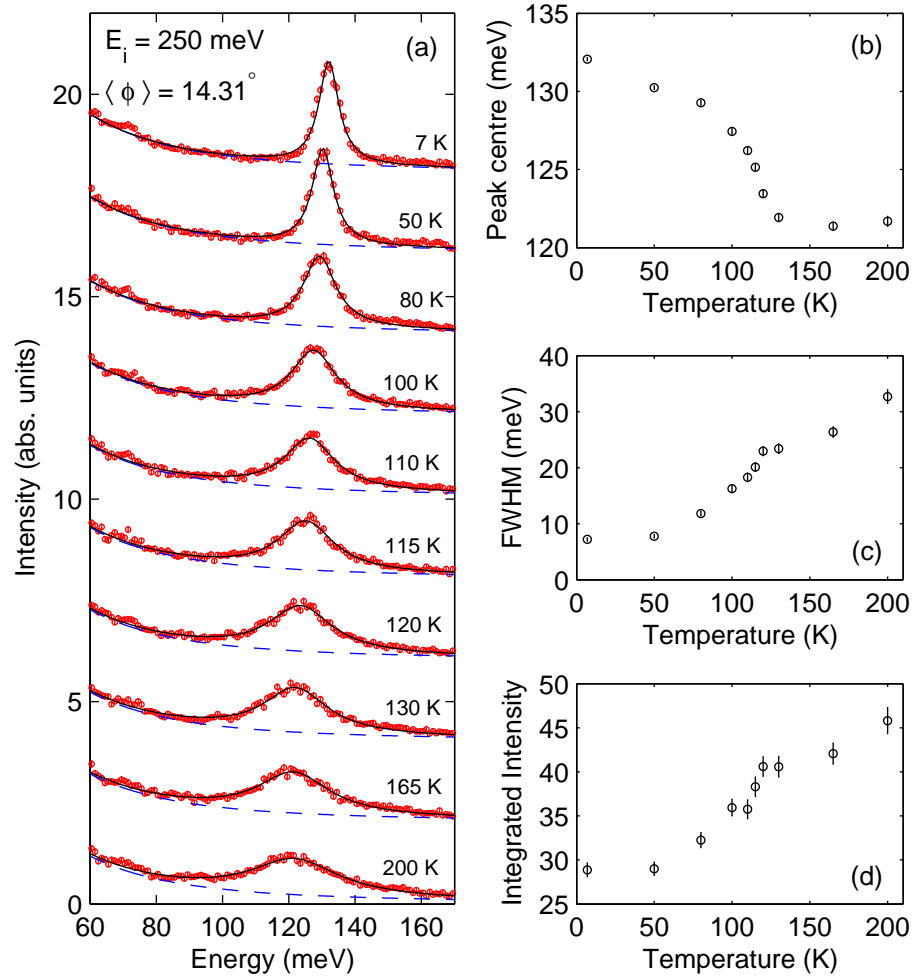
Figure 3.10: (a) Low-angle PrO$_2$ data, showing the crystal field transition to
the Γ_7 excited state. Data taken at different temperatures have
been offset vertically by 2 meV from the previous temperature.
Black lines are fits to the data using a Lorentzian profile on
a sloping background. (b-d) Variation of the peak centre, full
width at half maximum (FWHM) and integrated intensity with
temperature.

temperature for clarity. There is a clear peak at each temperature, corresponding
to the crystal field transition from the ground state to the Γ_7 excited state. As
the temperature increases the intensity of the peak increases, and the peak centre is
seen to move lower in energy. To analyse this trend quantitatively the data at each
temperature were fitted with a Lorentzian lineshape on a background, represented
as solid lines in figure 3.10a. The background was modelled as the tail of a second
Lorentzian, the centre and width of which were fixed to the value fitted at 7 K for
all other fits, but the amplitude of which was allowed to vary. The background

contribution is marked on 3.10a as a dashed line for each temperature. Data between 40 meV and 200 meV were included in each fit. Parameters from these fits are shown in fig.s 3.10(b–d).

Figure 3.10b shows the centre of the Γ_7 peak as a function of temperature. As the temperature increases from 7 K to 200 K the peak centre moves from 132.1 ± 0.1 meV to 121.9 ± 0.3 meV. The points follow an order parameter shape, suggesting a transition at ~ 120 K. This is consistent with the known Jahn-Teller distortion temperature at $T_D = 120 \pm 2$ K [4]. The width of the Γ_7 peak increases as the temperature increases, with a distinct change in gradient around $T_D = 120 \pm 2$ K (fig. 3.10c).

Comparison to the Point Charge Calculation

The point-charge crystal field calculation presented in section 3.2 estimated a value of 52.0 meV for the Γ_7 doublet at high-temperature, rising to 71.7 meV in the low-temperature distorted temperature. This amounts to a 38% increase in energy of the crystal field level as the structure distorts. The neutron-scattering data show clearly that there is an increase in the Γ_7 energy accompanying the structural distortion, but the percentage increase between 200 K and 7 K is in fact only 9%. The calculation also estimated a 42% reduction in intensity of this level going from the cubic to the chiral structure. Again, the data show that the intensity does decrease when the distortion occurs, by approximately 40%.

3.3.7   Analysis of $E_i = 80$ meV Data

The $E_i = 80$ meV spectra contain detailed information on the broad band of vibronic scattering, and the possible splitting of the ground-state Γ_8 quartet. Figure 3.11 shows the PrO$_2$ spectra at the nine temperatures measured, after correction for absorption and self-shielding effects and subtraction of the non-magnetic background. The spectrum at 7 K contains a peak centred close to zero energy [8], the broad band of intensity previously attributed to vibronic scattering, and a small peak on top of this broad feature. As the temperature increases the region above 30 meV varies very little, but below 30 meV the spectra are highly temperature dependent: the low-energy peak becomes quasielastic above $T_N = 13.5$ K and decreases in intensity as the temperature increases, the dip in intensity around 10 meV begins to fill up, and the small peak shifts toward lower energies.

Comparison to the Point Charge Calculation

The above analysis of the Γ_7 doublet has confirmed that the energy levels are underestimated by the point-charge calculation. In order to compare the model to the data we therefore linearly scale the calculated levels so that the Γ_7 peaks in

---

[8]In fact the peak peak at 7 K is shifted to 3 meV because of the magnetic splitting (below $T_N = 13.5$ K) described in section 3.1. However, in the analysis presented here we neglect this shift, which is small compared to the instrumental resolution.
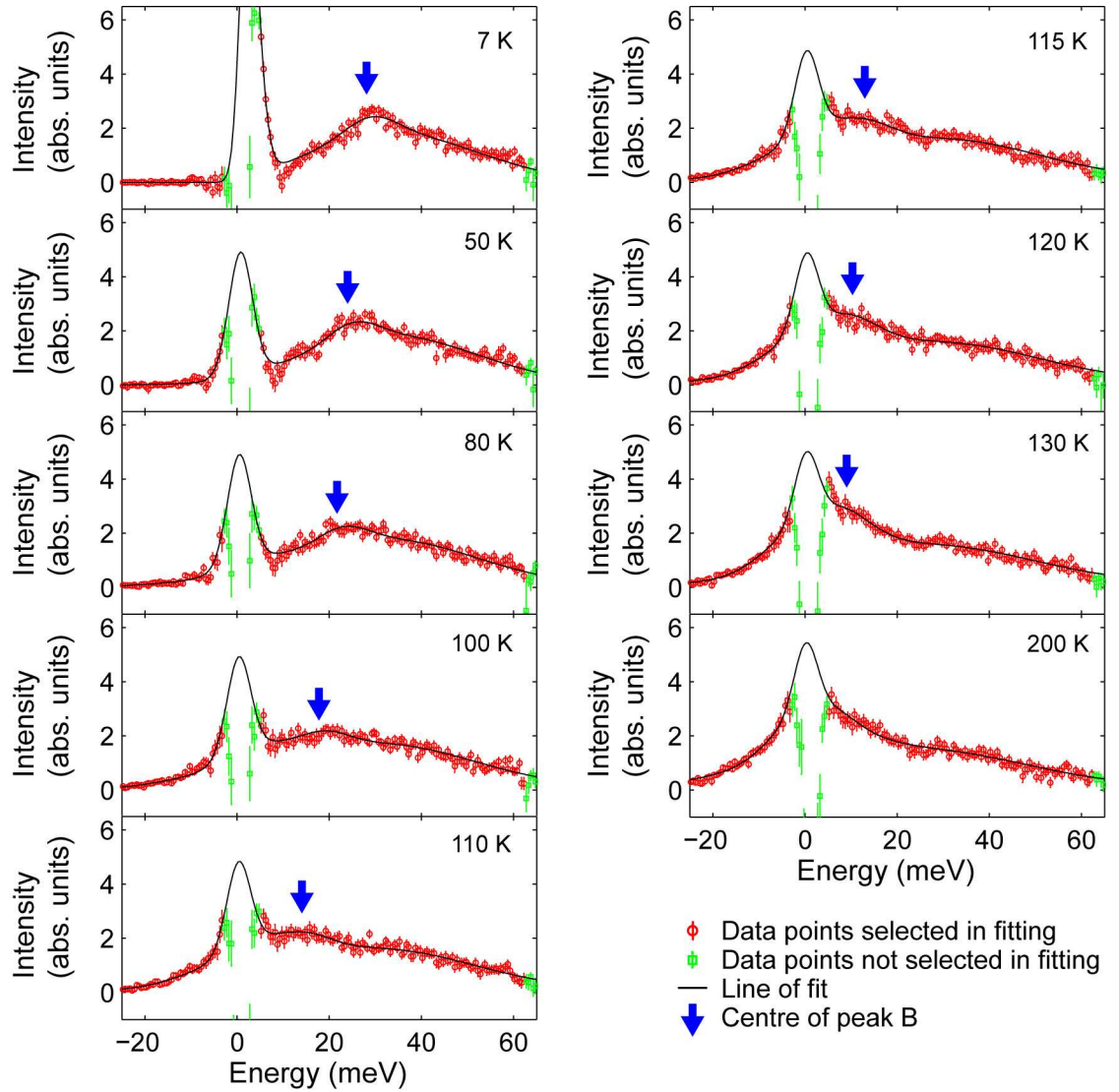
Figure 3.11: Data points are PrO$_2$ data from the low-angle detector banks measured with $E_i = 80$ meV, and corrected for phonons and multiple-scattering by simple subtraction of low-angle CeO$_2$ data. Data are presented for the nine temperatures measured between 7 K and 200 K. Solid black lines depict fits to the model described in the text. Red circles mark data points including in the fitting, while green squares show data points excluded from the fits. Blue arrows mark the centre of the peak labelled B in fig. 3.13.

the cubic and chiral crystal fields match the values measured at 200 K and 7 K respectively. These levels are plotted in figure 3.12, with Lorentzian lineshapes of relative height calculated from eqn. 3.12 to aid comparison with the neutron spectra.
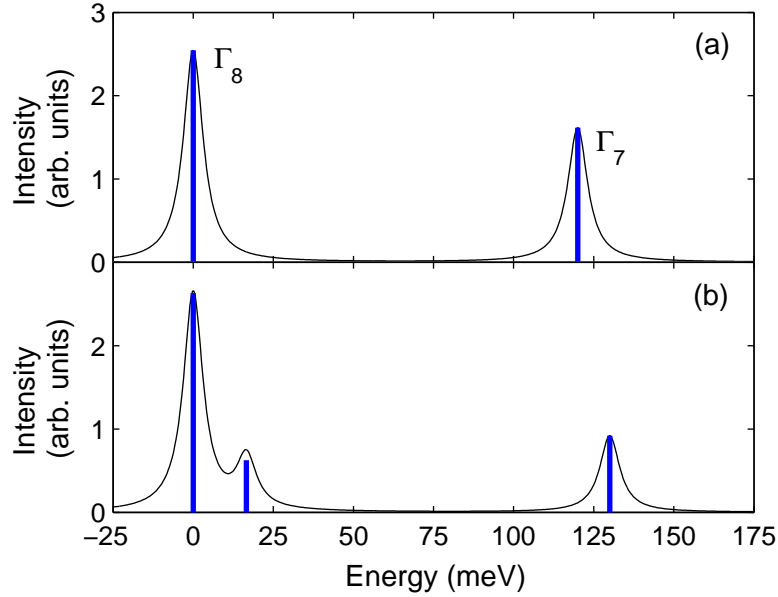
Figure 3.12: (a) Point charge model for the fluorite crystal structure above 120 K. (b) Point charge model for the chiral structure. Different scaling factors are used for the two models to ensure agreement between model and data.

With this scaling the cubic crystal field is estimated to split the ground state quartet by approximately 16 meV. This is sufficiently close to the observed small peak (at approximately 25 meV at 7 K) to justify modelling the peak as the result of this crystal-field splitting.

Model lineshape

We model the system as a three-level system of sharp levels, shown in figure 3.13a. Here levels $|0\rangle$ and $|1\rangle$ are intended to represent the ground state split by the chiral crystal field, as in fig. 3.12b, and level $|2\rangle$ is the vibronic continuum. Since the ground-state splitting goes to zero above $T_D = 120$ K we expect the position of level $|1\rangle$ to be temperature dependent. In this approximation the vibronic level is modelled as a sharp magnetic level, with broadening introduced later. The Γ_7 crystal field level lies outside the energy range of the data measured with $E_i = 80$ meV, and since its thermal population does not vary within this temperature range there is no need to include it in the system.

The lineshape was artificially constructed to describe transitions between these levels, including the correct temperature dependence while satisfying the principle of detailed balance. Since we consider only excitations from the ground level to an excited state we can write the response function $\tilde{S}(E)$ as a sum of that for each of
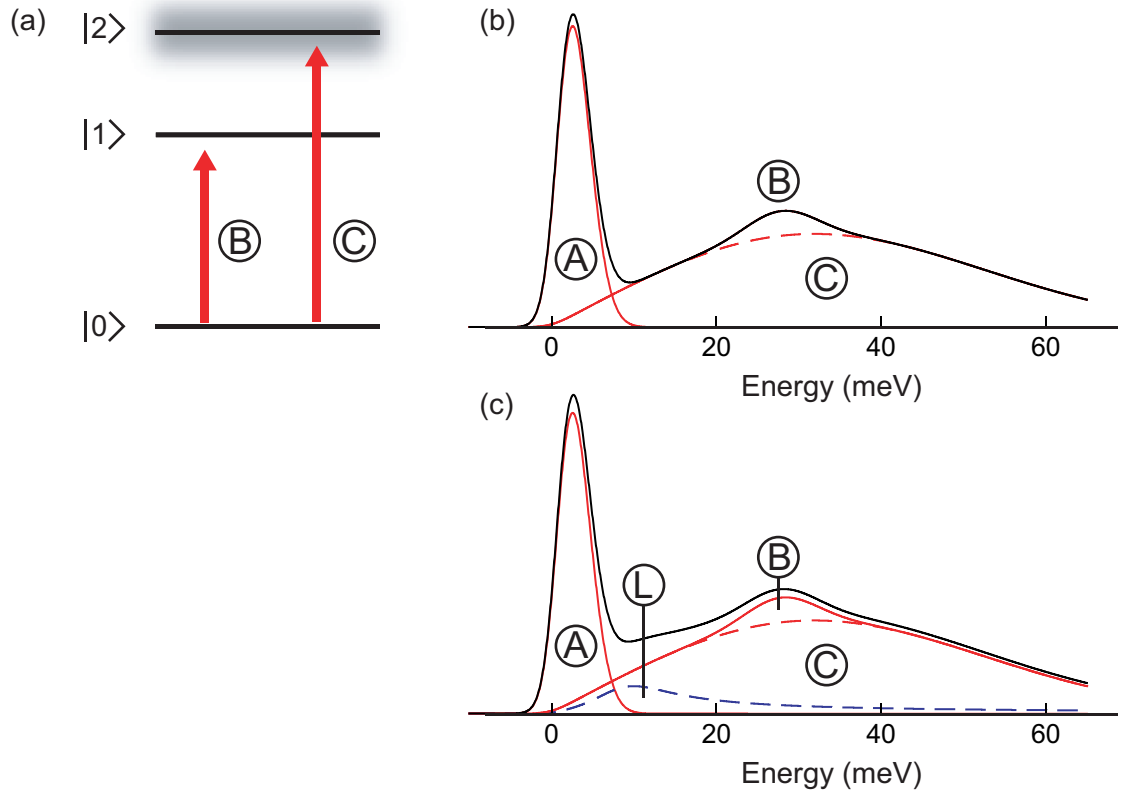
Figure 3.13: (a) Three level system: $|0\rangle$ and $|1\rangle$ represent the first two doublet crystal field levels, while $|2\rangle$ is included to model the vibronic states. (b) Lineshape resulting from the three-level system, using underlying symmetrized Gaussians. (c) Lineshape shown in (b), but with a symmetrized Lorentzian function added (blue dashed line marked L), as described in the text.

the three levels:

$$\tilde{S}(E) = \tilde{S}_0(E) + \tilde{S}_1(E) + \tilde{S}_2(E) \quad , \tag{3.19}$$

with $\tilde{S}_n(E)$:

$$\tilde{S}_n(E) = \rho_0 \, E \, [1 + n(E)] \, D_n \, G_n(E) \quad , \tag{3.20}$$

where $\rho_0 = \frac{\mathrm{e}^{-E_0/k_B T}}{Z}$ is the thermal population factor of the ground state [9]. The justification for constructing eqn. 3.20 in this form is discussed in chapter 2, section 2.2.5. The factor $[1 + n(E)] = (1 - \mathrm{e}^{-E/k_B T})^{-1}$ in eqn. 3.20 is the *detailed balance factor*. We take $G_n(E)$ to be a symmetrized Gaussian function [10]:

$$G_n(E) = A_n \left\{ \exp\left(-\frac{(E - E_{0n})^2}{2\sigma_n^2} \right) + \exp\left(-\frac{(E + E_{0n})^2}{2\sigma_n^2} \right) \right\} \quad , \tag{3.21}$$

---

[9] $Z = \sum_{n=0}^{2} \mathrm{e}^{-E_{0n}/k_B T}$ is the partition function.

[10] A Gaussian function was chosen since it gave a better fit to the data than a Lorentzian function.
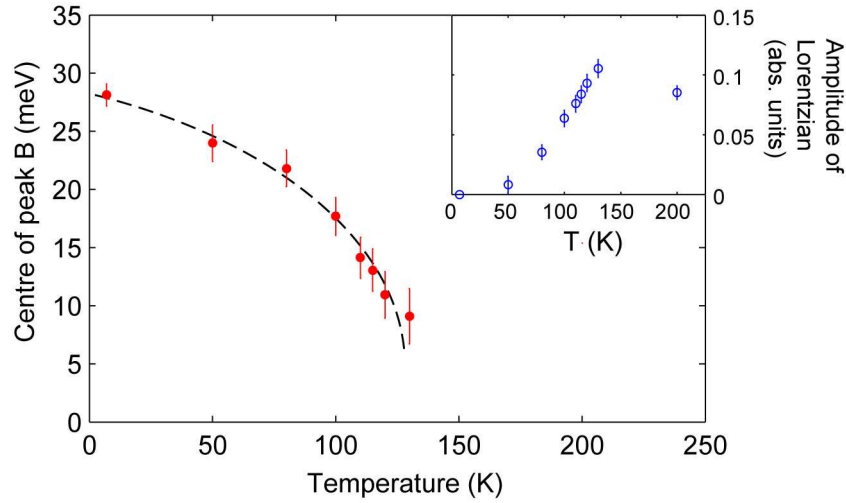
Figure 3.14: Parameters of the fits depicted in figure 3.11. (a) Centre of the peak labelled B in fig. 3.13, and marked with blue arrows in fig. 3.11. (b) Amplitude of the Lorentzian centred on 5.6 meV. Dashed line is a guide to the eye.

with amplitude A_n, width σ_n and centred on E_{0n}, the energy between levels $|0\rangle$ and $|n\rangle$ [11].

The lineshape described by this function at low temperature is shown in fig. 3.13, and has a good shape to fit the data at 7 K. However in order to achieve a good fit to the data at higher temperatures it was necessary to introduce another lineshape, a symmetrized Lorentzian multiplied by the detailed balance factor $[1 + n(E)]$ (see fig. 3.13c). This fits the increase in intensity around ~ 10 meV as the temperature increases above 7 K which could not be replicated using the temperature dependence factors in the above equations alone.

Fitting the data

Data at all nine temperatures were fitted simultaneously. The width of the peak labelled B was fixed by fitting the model to the 7 K data only, prior to fitting all temperatures. The only parameters allowed to vary with temperature were the centre of the peak labelled B in figure 3.13(b,c), and the amplitude of the the Lorentzian. All other changes in the lineshape with temperature derive from the temperature factors included in eqn. 3.19. The fitting was achieved using the *MFit* package for *Matlab* [17]. Figure 3.11 shows the results of the fitting plotted as solid black lines over the data at all nine temperatures [12]. The fits describe the data well. Blue

---

[11]In this case the factor D_n is then given by $D_n = \frac{(1-e^{-\beta E_{0n}})}{E_{0n}}$.

[12]At each temperature the subtraction of two large elastic peaks in the background subtraction routine has resulted in unphysical data points around zero energy transfer. These points were excluded from the fitting and are plotted as green squares to distinguish them from data included.

arrows mark the centre of the small peak (labelled B) which was allowed to move with temperature. The peak moves lower in energy as the temperature is increased. The peak centre is plotted in fig. 3.14a, showing an order-parameter-like decrease in energy from 28.1 ± 0.9 meV at 7 K to 9.1 ± 0.9 meV at 130 K. At 200 K a better fit to the data was achieved by omitting the peak altogether. The curve agrees well with a transition temperature of $T \approx 120$ K, the Jahn-Teller distortion temperature. Figure 3.14b shows the increase in amplitude of the added Lorentzian peak, which was centred at 5.6 meV.

3.4 Discussion and Conclusions

In this chapter we have presented neutron inelastic scattering measurements on polycrystalline PrO$_2$ which provide insights into the effect of a static distortion on a system with a large dynamic Jahn-Teller effect. Accompanying crystal field calculations aided the interpretation of the neutron data.

Making use of precise measurements of the positions of oxygen ions in the cubic and distorted crystal structures in PrO$_2$ above and below T_D we have calculated the positions of the crystal field levels estimated by a simple point charge model. Although the point-charge model grossly underestimates the absolute values of the crystal field splittings as expected, the essential features of the energy spectra were reproduced. These are as follows:

1. The ground state in the cubic structure is the four-fold degenerate Γ_8 level.

2. In the cubic field the first excited state is the Γ_7 doublet. After the chiral distortion this level is predicted by the point-charge model to increase in energy, while decreasing in intensity.

3. The chiral distortion is predicted to split the ground-state Γ_8 level, by approximately 15% of the Γ_8-Γ_7 cubic splitting.

Neutron inelastic scattering measurements on the temperature dependence of the crystal field level at $\approx$ 130 K have confirmed that it does increase in energy as the temperature is lowered below $T_D = 120$ K, *i.e.* as the symmetry distorts from cubic to chiral. In fact, the centre of the peak follows an order parameter-like curve, in strong agreement with the Jahn-Teller transition temperature (see. fig 3.10b), from 121.9 ± 0.3 meV at high temperature to 132.1 ± 0.1 meV at low temperature.

Of particular interest is the predicted splitting of the cubic Γ_8 ground-state by the chiral distortion. Neutron scattering measurements revealed a small peak at low temperatures at 27 meV, approximately 20% of the Γ_8-Γ_7 splitting. The point-charge calculations allowed us to confidently ascribe this peak to the chiral distortion splitting of the cubic ground-state. A simple three-level model of the system allowed us to fit the temperature dependence of this level, which showed an order parameter-like decrease in energy towards the Jahn-Teller distortion temperature, $T_D = 120$ K.

At 7 K then, our three-level model including the two crystal-field levels and vibronic scattering provided a good fit to the data. However, at higher temperatures a Lorentzian lineshape was introduced to account for extra intensity around 10 meV. The temperature dependence of the Lorentzian intensity is shown in fig. 3.14b. The explanation for this extra intensity requires some thought. It is possible that there is a phonon mode around 10 to 20 meV, and in fact evidence to support this is given by a peak in the high-angle data shown in fig. 3.8bii. Extra intensity may result from imperfect alignment of the phonons in CeO$_2$ and PrO$_2$, allowing intensity from phonons to appear in the subtracted data sets. However, the weighted background subtraction method should account for misalignment of the phonons, and no difference

was seen when using this method over simple subtraction. Another possibility is that the broad vibronic mode does not have the temperature dependence of our model, which assumes a magnetic temperature dependence for all three levels. If the vibronic mode has a more phonon-like character the increase in intensity with temperature may be explained. A more complicated model would be required to investigate this possibility.

Finally we comment on the presence of the broad vibronic scattering both above and below the Jahn-Teller distortion temperature, $T_D = 120$ K. This mode was first reported by Boothroyd *et al.* [3], before the chiral distortion had been observed. The explanation given by them for the presence of vibronic excited modes relies on the presence of a highly orbitally-degenerate ground-state, as in a cubic crystal field. Although the ground state is split by the crystal field at low temperatures, since the energy scale of the splitting is small compared to that of the vibronic continuum the vibronic mode is still present. In other words, the dynamic Jahn-Teller effect exists at low temperature despite the existence of a static Jahn-Teller distortion.

References

[1] S. Kern, J. Chem. Phys. **40**, 208 (1964).

[2] S. Kern, C.-K. Loong, J. Faber, Jr, and G. H. Lander, Solid State Commun. **49**, 295 (1984).

[3] A. T. Boothroyd, C. H. Gardiner, S. J. S. Lister, P. Santini, B. D. Rainford, L. D. Noailles, D. B. Currie, R. S. Eccleston, and R. I. Bewley, Phys. Rev. Lett. **86**, 2082 (2001).

[4] C. H. Gardiner, A. T. Boothroyd, P. Pattison, M. J. McKelvy, G. J. McIntyre, and S. J. S. Lister, Phys. Rev. B **70**, 024415 (2004).

[5] J. Jensen, Ørsted Laboratory, Niels Bohr Institute fAPG, Universitetsparken 5, 2100 Copenhagen, Denmark (2004), private communication.

[6] C. H. Gardiner, private communication.

[7] For a review of Ligand Field Theory see for example B. N. Figgis and M. A. Hitchman, *Ligand Field Theory and Its Applications* (Wiley-VCH, New York, U.S., 2000).

[8] B. G. Wybourne, *Spectroscopic Properties of Rare Earths* (Interscience Publishers, John Wiley & Sons Inc., New York, U.S., 1965).

[9] M. T. Hutchings, Solid State Phys. **16**, 227-273 (1964).

[10] A. J. Kassman, J. Phys. Chem. **53**, 4118 (1970).

[11] A. T. Boothroyd, *SPECTRE: A program to calculate the spectra of rare earth ions in crystal fields* (1990-2006).

[12] A. J. Freeman and J. P. Desclaux, J. Magn. Magn. Mat. **12**, 11-13 (1979).

[13] W. Burton Lewis, *Magnetic Resonance and Related Phenomena*, (p717 Proc. XVIth Congress AMPERE, Bucharest, ed. I. Ursu, 1971).

[14] Scattering lengths are listed at http://www.ncnr.nist.gov/resources/n-lengths/, taken from Neutron News, **3**, No. 3, 29-37 (1992).

[15] For an explanation of the *Homer* program used at the ISIS facility, see the HET manual: *http://www.isis.rl.ac.uk/excitations/documents/het.pdf.*

[16] See for example *http://www.ncnr.nist.gov/resourses/n-lengths.*

[17] For the Mfit user guide, see http://www.ill.fr/tas/matlab/doc/mfit4/mfit.html

CHAPTER 4

Magnetic Excitations in Charge Ordered La$_{1.5}$Sr$_{0.5}$CoO$_4$

4.1 Introduction

La$_{2-x}$Sr$_x$CoO$_4$ is a typical doped transition metal oxide, with a tetragonal unit cell consisting of two-dimensional conduction layers of CoO$_2$ separated by lanthanum and strontium spacer layers, as shown in fig. 4.1a. This is the same structure as the so called LSCO cuprate superconductors which are discussed in chapter 1. In order to understand the unique properties of the superconducting compounds it is essential to understand the interactions in isostructural compounds containing transition metals other than Cu, and to this end many studies of La$_{2-x}$Sr$_x$TO$_4$ have been made with T=Mn, Ni and Co. All of these compounds, as well as the cuprates, exhibit forms of spin and charge order.
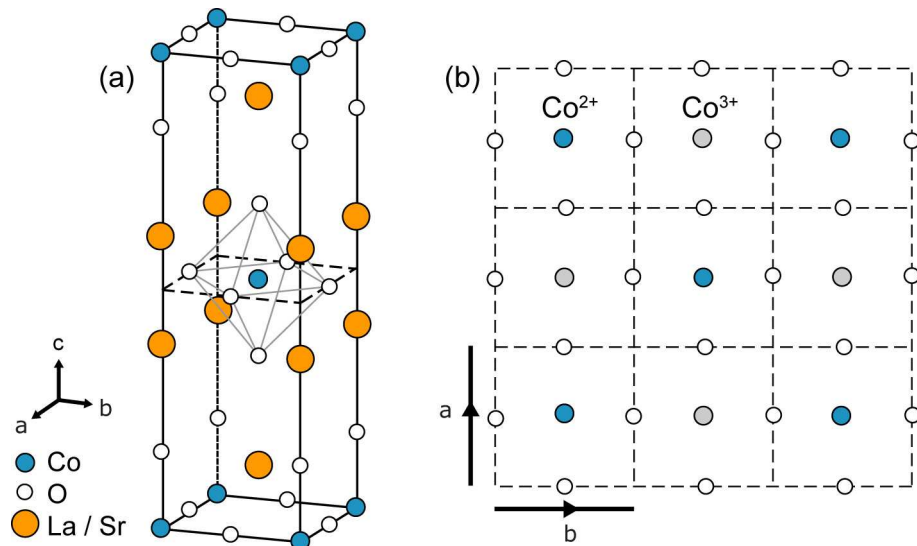
Figure 4.1: (a) Crystal structure of La$_{2-x}$Sr$_x$CoO$_4$. (b) Checkerboard charge ordering within the *ab* planes of the $x = 0.5$ compound. The low temperature lattice parameters are $a = b = 3.83$Å and $c = 12.5$Å
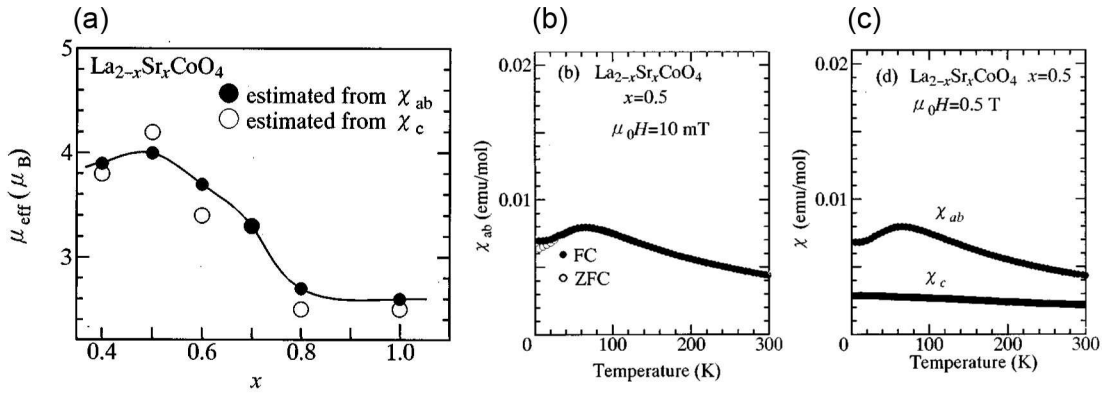
Figure 4.2: (a) Effective magnetic moments μ_{eff} per Co site, estimated from susceptibility measurements. (b) Temperature dependence of the in-plane component of the susceptibility ($\chi = M/H$) of La$_{1.5}$Sr$_{0.5}$CoO$_4$ single crystals. Data measured after cooling to 5 K in zero-field (ZFC) and after cooling in a field of $\mu_0 H = 10$ mT (FC). (c) Anisotropy of the susceptibility of La$_{1.5}$Sr$_{0.5}$CoO$_4$. Data taken from Moritomo *et al.* [4].

This chapter is concerned with investigating the magnetic excitations of the charge-ordered half-doped cobaltate, La$_{1.5}$Sr$_{0.5}$CoO$_4$. The parent compound, La$_2$CoO$_4$ is an insulator with cobalt ions in the Co^{2+} $S = 3/2$ (HS) spin-state, and exhibits antiferromagnetic order below 275 K [22]. Replacing one lanthanum ion in the structure with strontium introduces one excess hole into the material, and the holes reside on the CoO$_2$ layers. At half-doping ($x = 0.5$) Coulomb repulsion between holes is minimized when the holes lose mobility and form a checkerboard lattice on the Co sites, resulting in a charge ordered state of Co^{2+} and Co^{3+} ions [2, 3]. Figure 4.1b shows the checkerboard charge ordering in the *ab* plane in La$_{1.5}$Sr$_{0.5}$CoO$_4$, as determined by Zaliznyak *et al.* using neutron diffraction [2, 3]. The checkerboard ordering is accompanied by breathing-type distortions of the oxygen octahedra surrounding the Co ions, as shown in fig. 4.4(b, c). Neutron diffraction measurements of this effect over a wide temperature range have allowed the charge ordering transition temperature to be estimated as $T_{\text{CO}} \approx 825$ K [3].

Magnetic susceptibility measurements on La$_{1.5}$Sr$_{0.5}$CoO$_4$ by Moritomo *et al.* [4], shown in fig. 4.2(b, c), revealed a broad maximum at ~ 60 K suggestive of a build-up of magnetic correlations. Figure 4.2c compares the in-plane (χ_{ab}) and out-of-plane (χ_c) susceptibilities. The large difference in magnitude between the two curves reveals significant anisotropy in the system, with the *ab* plane as the easy direction for spins. Subsequent neutron diffraction measurements confirmed the presence of magnetic order below $T_{\text{SO}} \approx 30$ K [2]. Magnetic Bragg peaks were observed at slightly incommensurate positions such as $\boldsymbol{Q}_{ab} = (0.258, 0.258)$ in the $\boldsymbol{a}^*\boldsymbol{b}^*$ plane. Neglecting the slight incommensuration, the observation of a magnetic Bragg peak
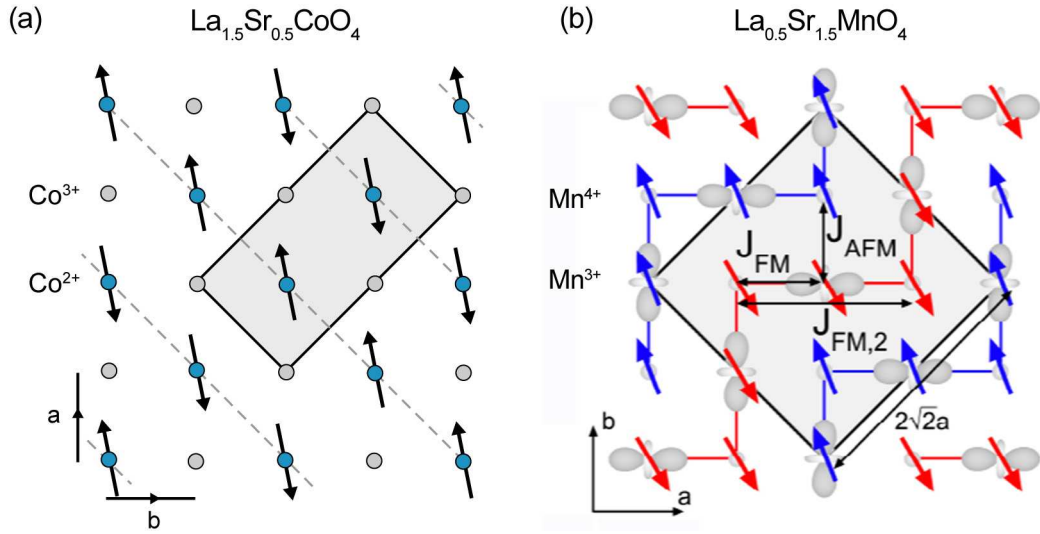
Figure 4.3: Magnetic order in checkerboard charge-ordered compounds. (a)
Antiferromagnetic order in La$_{1.5}$Sr$_{0.5}$CoO$_4$ proposed by Zaliznyak
et al. [2]. (b) Magnetic order in La$_{0.5}$Sr$_{1.5}$MnO$_4$, from Senff *et al.*
[10]. Grey boxes mark the magnetic unit cells in each.

at $\boldsymbol{Q}_{ab} = (0.25, 0.25)$ signifies a doubling of the charge-ordering unit cell in the
$(a, b) = (1, 1)$ direction, as shown by the grey box in fig. 4.3. Zaliznyak *et al.*
concluded that the Co^{2+} ions have $S = 3/2$ and align antiferromagnetically below
T_{SO}, while the the Co^{3+} ions have effectively no moment and do not contribute to the
magnetic Bragg scattering. This ordering pattern is shown in fig. 4.3a. Bragg peaks
at positions such as $\boldsymbol{Q}_{ab} = (0.75, 0.25)$ were also observed, indicating a doubling
of the charge-ordered unit cell in the $(a, b) = (1, -1)$ direction. This implies that
the compound is twinned, with the second set of Bragg peaks corresponding to an
ordering pattern rotated by 90° from that shown in fig. 4.3a.

   As well as La$_{1.5}$Sr$_{0.5}$CoO$_4$, checkerboard charge ordering has also been observed in
La$_{0.5}$Sr$_{1.5}$MnO$_4$ [5] and La$_{1.5}$Sr$_{0.5}$NiO$_4$ [6], and a comparison of the order in the three
compounds is given in ref. [7]. In all three compounds magnetic order (SO) follows
the charge order (CO) at a lower temperature, but the temperatures at which CO and
SO occur vary greatly, reflecting the different relative strengths of the magnetic and
Coulomb interactions. In the nickelate compound the Ni^{2+} and Ni^{3+} ions order into
a commensurate checkerboard at $T_{CO} \approx 480$ K, but there is a transition to slightly
incommensurate charge order at $T_{ICO} \approx 180$ K. The Ni^{2+} spins carry $S = 1$ and
order antiferromagnetically at $T_{SO} \approx 80$ K. Like the charge order, the magnetic order
is also slightly incommensurate. The $S = 1/2$ Ni^{3+} spins do not appear to order
[8]. In La$_{0.5}$Sr$_{1.5}$MnO$_4$ commensurate checkerboard ordering of Mn^{3+} and Mn^{4+}
occurs at $T_{CO} \approx 240$ K. In this compound orbital ordering (OO) develops at the
same temperature as the charge ordering, accompanied by Jahn-Teller distortions [9].

Magnetic ordering follows at $T_{SO} \approx 110$ K, involving spins on both the Mn^{3+} and Mn^{4+} sites, in a more complicated ordering pattern than the nickelate [10] (see fig. 4.3b).

Magnetic excitations have been studied in both La$_{1.5}$Sr$_{0.5}$NiO$_4$ [8] and La$_{0.5}$Sr$_{1.5}$MnO$_4$ [10]. The charge and orbital ordering strongly influence the magnetic excitations. In La$_{1.5}$Sr$_{0.5}$NiO$_4$ features are observed which are not predicted by standard spin-wave theory, and appear to be explained by discommensurations in the charge ordering. In both compounds the excitations are highly two-dimensional, reflecting the layered structure of the crystal lattice. We know of no measurements of the magnetic excitations in La$_{1.5}$Sr$_{0.5}$CoO$_4$ prior to those reported in this chapter.

In La$_{1.5}$Sr$_{0.5}$CoO$_4$ checkerboard charge ordering occurs at a very high temperature, $T_{CO} \approx 825$ K, and the charges are very well localized. Magnetic ordering on the other hand does not occur until $T_{SO} \approx 30$ K [2, 3]. There is currently no experimental evidence of orbital ordering. The huge difference between the two transition temperatures, and the lack of any CO anomaly at the SO temperature, suggests that the magnetic and charge ordering degrees of freedom may be effectively decoupled. This should make it a good compound in which to study the magnetic excitations in a CO system, without the necessity of considering competing degrees of freedom.

As in LaCoO$_3$ [11] and other cobaltate compounds, there has been some debate over the Co spin-state in La$_{2-x}$Sr$_x$CoO$_4$. The magnetization study by Moritomo *et al.* estimated the effective magnetic moment of La$_{2-x}$Sr$_x$CoO$_4$ from susceptibility measurements [1] over the doping range $0.4 \leq x \leq 1.0$, and the results are shown in fig. 4.2a [4]. For $0.4 \leq x \leq 0.6$ there is a large effective moment (3.5-4.2μ_B per Co), but this drops to around 2.6μ_B per Co between $x = 0.7 - 0.8$. Assuming that the Co^{2+} spin remains in the high-spin (HS) state ($S = 3/2$) as in the parent compound, and neglecting the orbital moment, Moritomo *et al.* concluded that it is not possible to produce such a large moment unless the Co^{3+} spins are also magnetic. They interpreted the reduction in magnetic moment at $x = 0.7 - 0.8$ as a spin-state transition of the Co^{3+} ions from the high-spin state (HS, $S = 2$) to an intermediate-spin state (IS, $S = 1$). Subsequent NMR measurements observed a large change in the hyperfine coupling constant in the same region, $x = 0.7 - 0.8$ [12].

As discussed above, neutron diffraction measurements of the magnetic order in La$_{1.5}$Sr$_{0.5}$CoO$_4$ [2] at low temperatures found antiferromagnetic order consistent with ordered Co^{2+} $S = 3/2$ spins and unordered Co^{3+}. Zaliznyak *et al.* argued that the Co^{3+} could be in either the high ($S = 2$), intermediate ($S = 1$) or low ($S = 0$) spin-state, but that the strong planar anisotropy in the compound would lead to quenching of the orbital angular momentum and freezing of any integer spin in a singlet state [2]. For this reason they assumed that the Co^{3+} ions could be modelled as effectively non-magnetic. However, there are in fact three magnetic ordering scenarios that are consistent with the observed magnetic Bragg positions:

---

[1]The effective magnetic moment can be estimated from the susceptibility χ using the Curie-Weiss law: $\chi = C/(T - \theta)$, where θ is the Curie temperature and C is the Curie constant, which is related to the effective magnetic moment μ_{eff} by $C = \mu_{eff}^2 \mu_B^2 g^2$. By fitting a straight line to $1/\chi$ against T it is possible to extract C and therefore μ_{eff}. Moritomo *et al.* assumed a spin-only moment so $g = 2$.

1. Antiferromagnetically ordered Co^{2+} ($S = 3/2$) spins, with no moment on the Co^{3+} ions, which are either (a) in the low-spin state $S = 0$, or (b) in a singlet state with $S = 1$ or 2 and $M_S = 0$. The latter is assumed in references [2, 3] (fig. 4.3a).

2. Antiferromagnetically ordered Co^{2+} ($S = 3/2$) spins, while the Co^{3+} spins have a moment which is paramagnetic [2].

3. Antiferromagnetically ordered Co^{2+} and Co^{3+} sublattices, ordered with the same ordering wavevector.

One ordering scenario that can be ruled out immediately is the pattern observed in $La_{0.5}Sr_{1.5}MnO_4$ (fig. 4.3b). This structure has a different periodicity from that observed in $La_{1.5}Sr_{0.5}CoO_4$, and would not be consistent with experimental data [3]. However, the above options show that the question of the Co^{3+} spin-state is still open.

In order to gain a better understanding of the magnetic ground states of the ions we have performed a simple point-charge calculation of the effect of the crystal field on the energy levels of the Co^{2+} and Co^{3+} ions, in a similar manner to the calculation described in the previous chapter for PrO_2. Crystal field parameters were calculated in the manner described in section 3.2, using the positions of oxygen in the distorted octahedra reported by Zaliznyak *et al.* [3]. These breathing-type distortions are shown in fig. 4.4(b,c). The subsequent calculation of energy levels and eigenvectors was performed by A. T. Boothroyd using a modified version of the SPECTRE program described in section 3.2 [4]. The spin-orbit interaction was included using a value of $\lambda = -20$ meV [5].

First we consider the point-charge calculation for Co^{2+} ions ($L = 3$, $S = 3/2$), the results of which are presented in fig. 4.4a. Including only the crystal field, the ground state is four-fold spin-degenerate, with $M_L = 0$. However, with the inclusion of the spin-orbit interaction the ground-state splits into two doublet states of mixed spin and orbital angular momentum. The lowest doublet is found to be predominantly $M_S = \pm 3/2$. For this ground state (marked *) we find that the g values parallel and perpendicular to the ab planes are $g_\parallel \approx 5.9$ and $g_\perp \approx 2.1$ respectively[6]. The value of $g_\parallel \gg 2$ shows that there is a significant orbital angular momentum

---

[2]This is analogous to the ordering in $La_{1.5}Sr_{0.5}NiO_4$ which has similar magnetic Bragg positions, and where the Ni^{2+} ($S = 1$) sublattice orders, while the Ni^{3+} ($S = 1/2$) sublattice does not [8].

[3]As well as the magnetic Bragg positions $\boldsymbol{Q}_{ab} = (0.25, 0.25)$, $La_{0.5}Sr_{1.5}MnO_4$ also has magnetic Bragg peaks at positions $\boldsymbol{Q}_{ab} = (0.5, 0)$ *etc.* [10]. These reflections are not observed in $La_{1.5}Sr_{0.5}CoO_4$.

[4]For PrO_2 tensor operators were used to include both J multiplets, while here Stevens' operators were sufficient. In the Stevens' operator method only the lowest LSJ term is included, but higher terms are well separated in energy so can be neglected [13].

[5]The spin-orbit parameter λ is defined by the spin-orbit interaction term in the Hamiltonian: $\mathcal{H}_{SO} = \lambda \boldsymbol{L} \cdot \boldsymbol{S}$. For a free ion the value is given by Abragam and Bleaney as $\lambda \approx -180$ cm$^{-1} \approx -20$ meV [13].

[6]The g factor is defined by the Zeeman Hamiltonian $\mathcal{H}_Z = g\mu_B \boldsymbol{B} \cdot \boldsymbol{J}$. $g_\parallel$ and $g_\perp$ are calculated by applying a field B (parallel or perpendicular to the ab planes respectively) and the calculated Zeeman splittings $\Delta E = g\mu_B B$ allow g to be extracted.
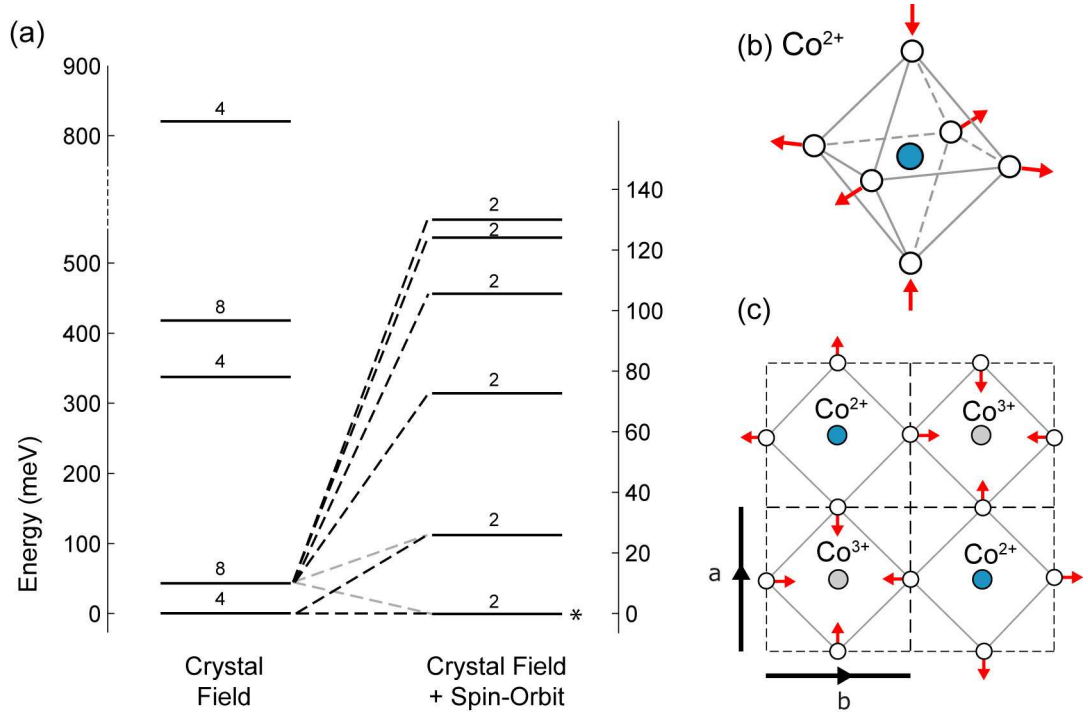
Figure 4.4: (a) Co^{2+} levels in La$_{1.5}$Sr$_{0.5}$CoO$_4$ calculated using a simple point-charge calculation for $L = 3$, $S = 3/2$. The spin-orbit interaction is also included. Numbers label the spin degeneracy of the levels. (b) Distortion of the oxygen octahedra surrounding the Co^{2+} ions [3], and (c) a view of the distortions in the ab plane.

component in the ground state. In addition, the large difference between $g_\parallel$ and $g_\perp$ is evidence for a strong magnetic anisotropy, consistent with the magnetization data (fig. 4.2c). Furthermore, the calculated magnetic moment for the ground state doublet is $\mu_{\text{eff}} = 6.7\mu_B$ per Co^{2+} ion, including both spin and orbital angular momentum [7]. This equates to $3.3\mu_B$ per Co ion in La$_{1.5}$Sr$_{0.5}$CoO$_4$, which is a significant proportion of the effective moment found experimentally by Moritomo *et al.* (see fig. 4.2a) [4]. It is possible then that little or no contribution to the magnetic moment comes from the Co^{3+} sites, and hence that they could either be in the low-spin state $S = 0$, or in a spin singlet state ($M_S = 0$) with $S = 1$ or 2.

Secondly, we investigated the proposal by Zaliznyak *et al.* that the Co^{3+} ions are in a spin-state with $S \neq 0$, but that the strong planar anisotropy leads to a state in which both orbital angular momentum and spin angular momentum are quenched, so that Co^{3+} has effectively no moment at low temperatures. In this scenario the crystal-field split Co^{3+} levels must have a singlet ground state well separated from

---

[7]This is in contrast to $\mu_{\text{eff}} = g\sqrt{S(S+2)}\mu_B = 3.87\mu_B$ per Co^{2+} (or $1.94\mu_B$ per Co) for spin only $S = 3/2$.

the nearest excited states. This was not found to be the case in the point-charge calculations. Starting with the Hund's rule state of Co^{3+} ($L = 2$, $S = 2$), the point charge calculations predict many levels very close to the ground state singlet, each with a large orbital angular momentum. Since there are many levels in close proximity it is very unlikely that the Co^{3+} ions would have quenched spin, even at low temperatures. Also, the large orbital angular momentum of the lowest levels suggests that if the Co^{3+} ions are in the high-spin state they would give a large contribution to the effective magnetic moment. Since most of the experimentally observed moment can be explained by the contribution from Co^{2+} (spin and orbital angular momentum contributions) this is evidence for Co^{3+} being in the low-spin ground state ($S = 0$).

The problem of what happens to the Co^{3+} ions in the magnetic ordered state will be addressed further in the discussion. However, following the points made above, the Co^{3+} ions will be assumed not to contribute to the magnetic order or low energy spin excitations for the analysis presented in the rest of this chapter.

The next section reports magnetization measurements on $La_{1.5}Sr_{0.5}CoO_4$, followed by neutron diffraction measurements to refine the structure, and further elastic neutron scattering studies to characterize the charge and magnetic order. In section 4.5 we present inelastic neutron scattering studies of the magnetic excitations in $La_{1.5}Sr_{0.5}CoO_4$, which are the main result of this chapter. This is followed by analysis of the inelastic neutron data through comparison with spin-wave models in section 4.6.

4.2 Magnetization Measurements

As a preliminary study of $La_{1.5}Sr_{0.5}CoO_4$, magnetization measurements were made using a Superconducting QUantum Interference Device (SQUID) magnetometer. The bulk magnetic properties were studied in order to check consistency with previous measurements [4], and to give an idea of regions of interest for later study with neutrons.

A small single crystal of $La_{1.5}Sr_{0.5}CoO_4$ was cleaved from a rod prepared using the floating zone technique in Oxford to give a sample of mass 0.135 g. X-ray Laue photographs were used to find the orientation of the crystal axes. The sample was then mounted in a plastic capsule, secured in position by cotton wool [8], and mounted in the centre of a plastic straw designed to fit the SQUID sample rod. The straw containing the sample was then mounted in the SQUID magnetometer, with the *ab* plane (or *c*-axis) parallel to the field direction (vertical).

4.2.1 SQUID Magnetometer

The SQUID magnetometer used here has a sample environment consisting of a cryostat with base temperature 1.8 K and maximum temperature 350 K, and a superconducting magnet capable of producing a vertical field up to 7 T (70000 Oe). Operation and data acquisition are controlled by computer. To measure the magnetization of a sample a field must be applied to induce a net magnetic moment in the sample. The moment induces a current in the SQUID's detector coils, and the output voltage is directly proportional to the current induced by the magnetization [9]. Two techniques were used to measure the sample magnetization:

Field-cooled measurements At room temperature a measuring field, typically of about 100 Oe, was applied to the sample, which was then cooled to the base temperature. Measurements were made at increasing temperatures from 1.8 K to 350 K.

Zero-field-cooled measurements The sample was cooled from room temperature to base temperature with no applied field. At 1.8 K a measuring field was applied, and measurements were again made at increasing temperatures up to 350 K.

The resulting magnetization measurements (M) were converted to units of emu/mol, for ease of comparison with previous data. Measurements to discover the hysteresis of the compound were made in fields up to 10000 Oe (1 T), but no evidence of hysteresis was found.

---

[8]Cotton wool has a small diamagnetic signal, but this signal is not temperature dependent over the range studied here [14].

[9]For all measurements within this thesis the 'D.C.' technique was used to take measurements. In this method the sample is moved through the detector coils in steps, measuring the induced voltage at each point. The points are fitted with a theoretical curve, the amplitude of which is recorded as the final reading.

4.2.2 Results

Figure 4.5 depicts the temperature variation of the in-plane FC and ZFC magnetizations, with the inset showing data up to 350 K. Our results agree generally with those of Moritomo *et al.* [4], with a broad maximum in the magnetization centred at about 60 K. However, in addition we see a definite splitting between the ZFC and FC data at low temperatures indicating a glassy ground-state, and an abrupt change in slope at ≈ 30 K.

The inset of fig. 4.5 shows measurements made with $H \parallel ab$ and $H \parallel c$. The difference between them is roughly a factor of two, which shows that there is a large anisotropy in the system. The $H \parallel c$ curve shows a larger temperature dependence than that of Moritomo *et al* [4] (see figure 4.2c), but this is likely to be due to a small misalignment of the sample allowing some of the moment parallel to ab to be measured, since the crystal alignment in our experiment was only accurate to $\sim 10°$.

The broad maximum at 60 K suggests that the magnetic ordering in La$_{1.5}$Sr$_{0.5}$CoO$_4$ has a gradual onset rather than a sharp transition temperature, and we will see from neutron scattering measurements presented later that this is the case. Prompted by the magnetization measurements, the possibility of a reorientation of the spins in the ab plane at ≈ 30 K was also investigated with neutrons, and this is presented in section 4.4.3.
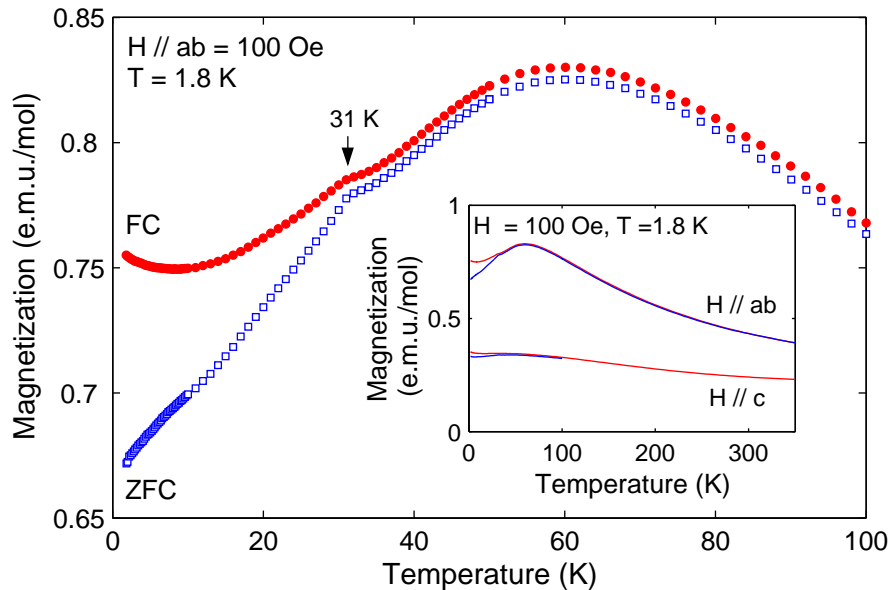
Figure 4.5: Temperature dependence of the susceptibility ($\chi = M/H$) of La$_{1.5}$Sr$_{0.5}$CoO$_4$ with $H \parallel ab$. Measurements were made measuring upward in temperature. Red circles and blue squares show data from field-cooled (FC) and zero-field-cooled (ZFC) measurements respectively. Inset: Data up to $T = 350$ K, showing data with both $H \parallel ab$ and $H \parallel c$.

4.3   Structure Refinement

The samples of La$_{1.5}$Sr$_{0.5}$CoO$_4$ which were studied in this chapter are what are known as 'strontium-doped' samples. This is because strontium is used to replace some of the lanthanum in the parent compound La$_2$CoO$_4$ to introduce holes into the system. Each lanthanum position that is replaced by a strontium ion adds one hole into the cobalt–oxygen layers, and the ratio of La to Sr determines the ratio of Co^{2+} to Co^{3+} ions. However, La$_2$CoO$_4$ can also be doped by adding extra oxygen to the system [16]. If both methods of doping are used the Co^{2+}/Co^{3+} balance is given by

$$\text{La}_{2-x}\text{Sr}_x\text{Co}^{2+}_{1-z}\text{Co}^{3+}_z\text{O}_{4+\delta} \quad z = x + 2\delta \ . \tag{4.1}$$

The properties of compounds such as these are strongly dependent on doping, and it was important to determine the oxygen content of the samples to ascertain whether the nominal doping value x did represent the holes added to the cobalt layer. The oxygen content was therefore determined by refining the crystal structure using Rietveld refinement of neutron diffraction data.

4.3.1   Neutron Powder Diffraction

Neutron powder diffraction measurements were performed on the GEM diffractometer at ISIS at the Rutherford Appleton Laboratory. GEM is a high-resolution powder diffractometer equipped with detector banks covering 1 to 170° in scattering angle. This makes it ideal for structural studies of crystalline powders. A brief description of powder diffractometers is given in chapter 2.

Sample Preparation

The polycrystalline sample of La$_{1.5}$Sr$_{0.5}$CoO$_{4+\delta}$ was prepared by grinding small single crystals of the compounds the day before the experiment. The single crystals were grown in the Clarendon Laboratory image furnace by D. Prabhakaran. The sample comprised of about 6 g of powder, packed into an aluminium can of 8 mm in diameter to a depth of approximately 33 mm. The can was sealed with a screw cap and mounted vertically in a cryostat fitted to the instrument.

Measurements

Each measurement was made by counting for approximately half an hour. For the structural refinement it was important to choose a low temperature to reduce the thermal motion of the oxygen atoms and so improve the refinement. 60 K was chosen as a low temperature that lies just above the magnetic ordering temperature for La$_{1.5}$Sr$_{0.5}$CoO$_4$ to avoid the need to consider the magnetic structure in the refinement. However, the measurement was also repeated at 2, 100, 150, 200 and 300 K [10].

---

[10]These measurements were performed in the following order: 2 K, 60 K, 150 K, 300 K, 200 K, 100 K.

4.3.2 Refinement of Powder Diffraction Data

The data collected on GEM were analysed using GSAS [15], a set of programs designed for Rietveld refinement of neutron or X-ray diffraction data. For each measurement, data in the three highest scattering-angle detector banks (4, 5 and 6) were refined simultaneously. High angle banks were used because the resolution of the powder diffractometer is best at high angles of 2θ.

The structure was refined in the tetragonal $I4/mmm$ space group whose unit cell is shown in figure 4.1. Some studies of La$_{2-x}$Sr$_x$CoO$_4$ have assumed an orthorhombic unit cell, with the a and b axes at $45°$ to those of the tetragonal unit cell used here [2, 3, 16]. However, refinements of our data within the orthorhombic $Fmmm$ space group revealed no orthorhombic distortion [11]. As well as the atoms shown in fig. 4.1 an interstitial oxygen position was included in the refinement, at $(x, y, z) = (0.5, 0, 0.25)$ in the unit cell. Excess oxygen is known to reside in this site in both La$_2$CoO$_{4+\delta}$ [16] and La$_2$NiO$_{4+\delta}$ [17]. In order to achieve convergence in the refinement it was necessary to fix the thermal parameter (U_{iso}) of this third oxygen site to be the same as that of the second oxygen site.

Figure 4.6 shows a typical refined profile. The data shown were taken with the La$_{1.5}$Sr$_{0.5}$CoO$_{4+\delta}$ sample at 60 K, and are averaged over the backscattering detector bank (bank 6, $\langle 2\theta \rangle = 154.5°$), although banks 4 and 5 were also included in the fitting. The line through the data points is the calculated profile, and the difference between this curve and the data points is plotted below. Tick marks show allowed reflections. The parameters of this refinement, as well as those of the other temperatures at which La$_{1.5}$Sr$_{0.5}$CoO$_{4+\delta}$ was measured are given in table 4.2. They are defined as follows

$a = b, c$	lattice constants of the tetragonal unit cell;
V	volume of unit cell $V = a \times b \times c$;
x, y, z	ion position within tetragonal unit cell in lattice units;
n	occupancy, or number of ions per formula unit;
U_{iso}	isotropic thermal parameter, which defines the Debye-Waller factor [15], and quantifies the thermal fluctuations of each ion;
δ	total excess oxygen;
R_{wp}	average weighted profile R values, a measure of the goodness of fit [15];
χ^2	the standard χ^2 value for the fit, for 39 parameters.

At all temperatures the refinements show that $\delta \approx 0$ to within errors, so there is no excess oxygen in the sample of La$_{1.5}$Sr$_{0.5}$CoO$_4$. The refinements are well fitted, although the data at 100 K have a higher value of χ^2 than the others. The reason for this is not known. Values for the lattice constants and atom positions are in good agreement with previously reported values [3]. Values for the ratio of La to Sr differ

---

[11]We note that in using the single tetragonal unit cell shown in figure 4.1 it is not possible to refine breathing type distortions reported by Zaliznyak *et al* due to charge ordering [3]. However, no peak splittings were observed to suggest that these distortions could be refined, and this was not the aim of our study.
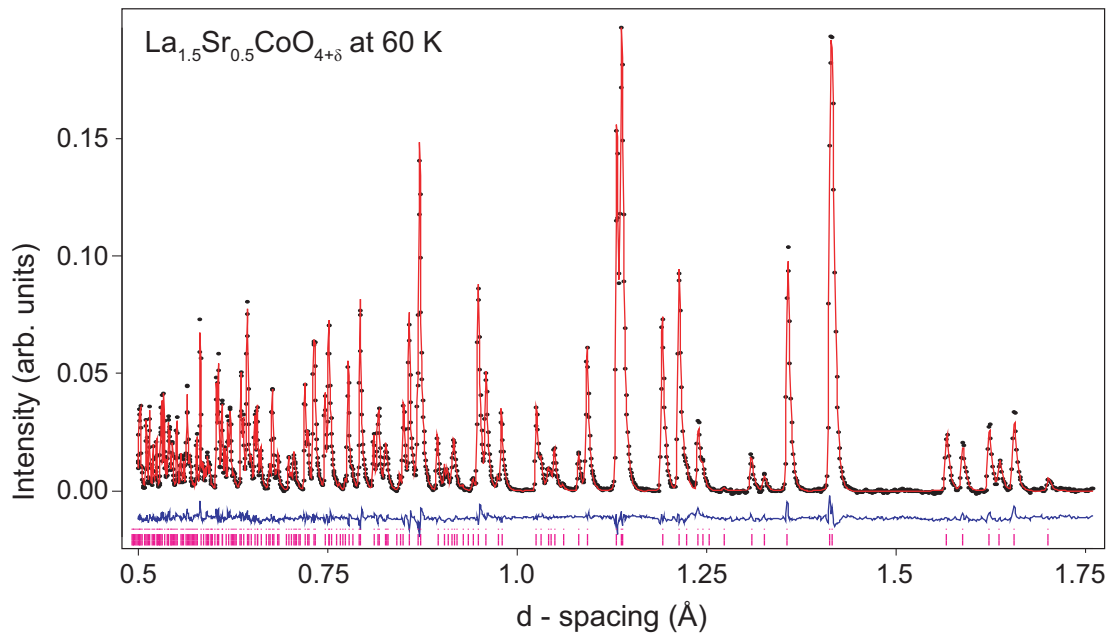
Figure 4.6: Portion of the Rietveld refinement for tetragonal La$_{1.5}$Sr$_{0.5}$CoO$_{4+\delta}$ at 60 K. Circles are data measured in the backscattering detector bank ($\langle 2\theta \rangle = 154.5°$) on GEM at ISIS. The solid (red) line shows the calculated profile fit using GSAS. Tick marks show the positions of allowed reflections, and the solid (blue) line below the data shows the difference between observed data and calculation. The background fitted in the refinement was subtracted prior to plotting. The fit parameters are given in table 4.2.

slightly from the nominal doping level of $x = 0.5$. However, La and Sr have very similar scattering lengths and we do not expect to be able to accurately refine this ratio by neutron powder diffraction.

La$_{1.5}$Sr$_{0.5}$CoO$_{4+\delta}$

T (K)		2	60	100	150	200	300
$a = b$	(Å)	3.83495(2)	3.83537(2)	3.83665(2)	3.83693(2)	3.83959(2)	3.84080(2)
c	(Å)	12.5235(1)	12.5239(1)	12.5277(1)	12.5287(1)	12.5413(1)	12.5481(1)
V	(Å^3)	184.181(2)	184.227(2)	184.406(2)	184.448(2)	184.890(2)	185.107(2)
La/Sr	$x = y$	0	0	0	0	0	0
	z	0.36216(2)	0.36214(2)	0.36216(2)	0.36215(2)	0.36217(3)	0.36216(3)
	n_{La}	1.55(7)	1.59(7)	1.52(7)	1.51(7)	1.49(7)	1.47(7)
	n_{Sr}	0.45(7)	0.41(7)	0.48(7)	0.49(7)	0.51(7)	0.53(7)
	U_{iso}	0.219(7)	0.244(7)	0.300(7)	0.307(7)	0.419(8)	0.480(8)
Co	$x = y$	0	0	0	0	0	0
	z	0	0	0	0	0	0
	n	1	1	1	1	1	1
	U_{iso}	0.24(3)	0.24(3)	0.30(3)	0.29(3)	0.42(3)	0.43(4)
O(1)	x	0.5	0.5	0.5	0.5	0.5	0.5
	y	0	0	0	0	0	0
	z	0	0	0	0	0	0
	n	2.01(1)	2.01(1)	2.00(1)	2.00(1)	2.00(1)	1.99(1)
	U_{iso}	0.50(1)	0.52(1)	0.56(1)	0.57(1)	0.70(1)	0.75(1)
O(2)	$x = y$	0	0	0	0	0	0
	z	0.16967(4)	0.16968(4)	0.16968(3)	0.16967(4)	0.16977(4)	0.16981(4)
	n	1.98(1)	1.99(1)	1.98(1)	1.98(1)	1.98(1)	1.97(1)
	U_{iso}	1.02(1)	1.06(1)	1.11(1)	1.12(1)	1.29(1)	1.37(2)
O(3)	x	0.5	0.5	0.5	0.5	0.5	0.5
	y	0	0	0	0	0	0
	z	0.25	0.25	0.25	0.25	0.25	0.25
	n	0.012(2)	0.008(2)	0.008(2)	0.006(2)	0.004(2)	0.004(2)
	U_{iso}	1.02(1)	1.06(1)	1.11(1)	1.12(1)	1.29(1)	1.37(2)
δ		0.00(2)	0.00(2)	-0.01(2)	-0.02(2)	-0.02(2)	-0.03(2)
R_{wp}	(%)	3.11	3.04	2.85	2.96	2.88	2.85
χ^2		9.31	8.89	41.04	8.33	7.76	7.47

Table 4.2: Refined structural parameters for La$_{1.5}$Sr$_{0.5}$CoO$_{4+\delta}$ at temperatures between 2 K and 300 K. The data are refined in the tetragonal space group $I4/mmm$. Where no error is given in brackets the value was not refined. x, y, z are ion positions in lattice units, n are the number of each ion per formula unit, U_{iso} are the isotropic temperature factors (as percentages). The number of La/Sr ions were constrained such that $n_{La} + n_{Sr} = 1$. R_{wp} is the weighted profile residual function [15], a measure of how well the data was fitted with these parameters.

4.4 Elastic Neutron Scattering Measurements on La$_{1.5}$Sr$_{0.5}$CoO$_4$ Single Crystals

The main focus of this chapter is on the inelastic neutron scattering studies made to investigate the magnetic excitations in La$_{1.5}$Sr$_{0.5}$CoO$_4$. Within these experiments some elastic measurements were also made, and these are descibed in this section. The experimental details for both elastic and inelastic measurements are therefore presented together here.

4.4.1 Experimental Details

Two sets of neutron scattering measurements were made on single crystals of La$_{1.5}$Sr$_{0.5}$CoO$_4$. Firstly, an inelastic neutron scattering study was made on the MAPS spectrometer at the ISIS facility at the Rutherford Appleton Laboratory. MAPS is a time-of-flight chopper spectrometer with a very large pixelated detector bank, and is particularly well suited to studies of two-dimensional systems. Chopper spectrometers are described in chapter 2. The large detector bank allowed us to survey a large area of reciprocal space in a single measurement, including both elastic and inelastic data in a single data set.

Secondly, a series of measurements were made on the triple-axis spectrometers IN20 and IN22 at the Institut Laue-Langevin. For these measurements polarized neutrons were employed, which allowed us to verify the magnetic nature of the features observed on MAPS. Polarization analysis also enabled a temperature dependent study of the direction of the ordered moments.

Sample Preparation

Crystals of La$_{1.5}$Sr$_{0.5}$CoO$_4$ were prepared using the floating-zone method in an image furnace in Oxford by D. Prabhakaran [18]. Sections of the zone-melted rods were cut to give cylindrical single crystals, with the growth direction approximately along the [110] direction.

MAPS Measurements

For the time-of-flight experiment a crystal of mass 35.5 g and length [12] 80 mm was mounted on a goniometer using an aluminium bracket, and adjusted so that the (001) and (110) reciprocal lattice vectors defined the horizontal scattering plane (this left the crystal rod approximately vertical). Cadmium was used to shield the goniometer and an aluminium foil bag was placed over the sample as a heat shield. The sample was then mounted in a closed cycle refrigerator situated within the vacuum chamber containing the detector banks.

Measurements were performed at room temperature and 9.5 K. The incident energy employed was 50 meV, and counting times were approximately 30 hours at an

---

[12]The beam size on MAPS is 55 mm and so the mass of crystal in the beam was estimated to be 24.4 g.
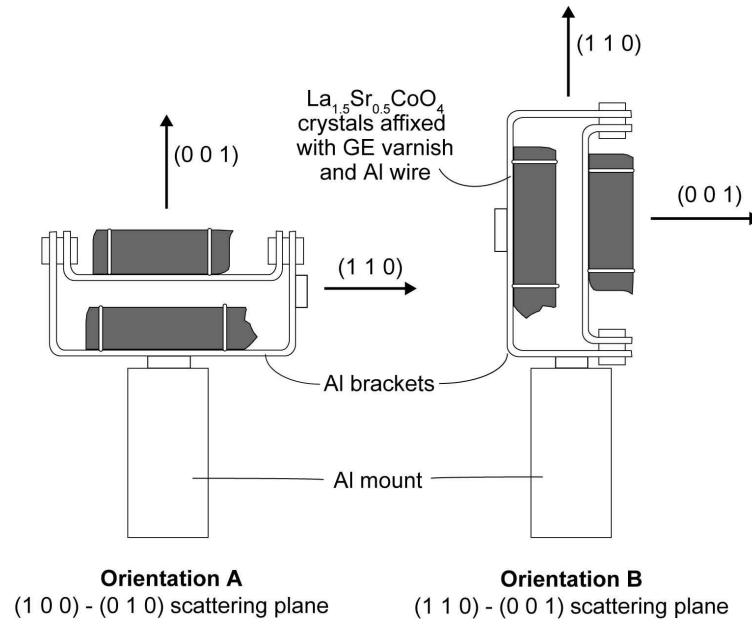
Figure 4.7: The mount for two La$_{1.5}$Sr$_{0.5}$CoO$_4$ crystals used for the experiment on IN20, showing the two possible experimental orientations.

average proton current of 170 μA. Vanadium spectra collected with a white beam and with $E_i = 50$ meV were used to calibrate the detectors, and to convert the intensities to absolute units (see chapter 2).

Triple-axis Measurements

For the polarized neutron experiment on the triple-axis spectrometer IN20 two smaller rod-like crystals of masses 6.5 g and 5.5 g were coaligned using x-rays and mounted on an aluminium mount as shown in fig. 4.7. The mount was designed to allow two experimental configurations with the horizontal scattering plane defined by the reciprocal lattice vectors (A) (100) and (010), or (B) (110) and (001). Further measurements on IN22 were made on the larger of the two crystals, aligned on a new mount in the same orientation as fig. 4.7b. In both triple-axis experiments the base of the mount was shielded with cadmium, and the sample was mounted in a standard helium cryostat.

On both triple-axis instruments we used curved Heusler (111) as both monochromator and analyser and worked with a fixed final energy $E_f = 14.7$ meV, and on both instruments PG (002) filters were used to suppress higher order harmonics. In this section we consider only the elastic measurements, *i.e.* those made with $E_i = E_f = 14.7$ meV. Inelastic measurements are discussed in section 4.5.
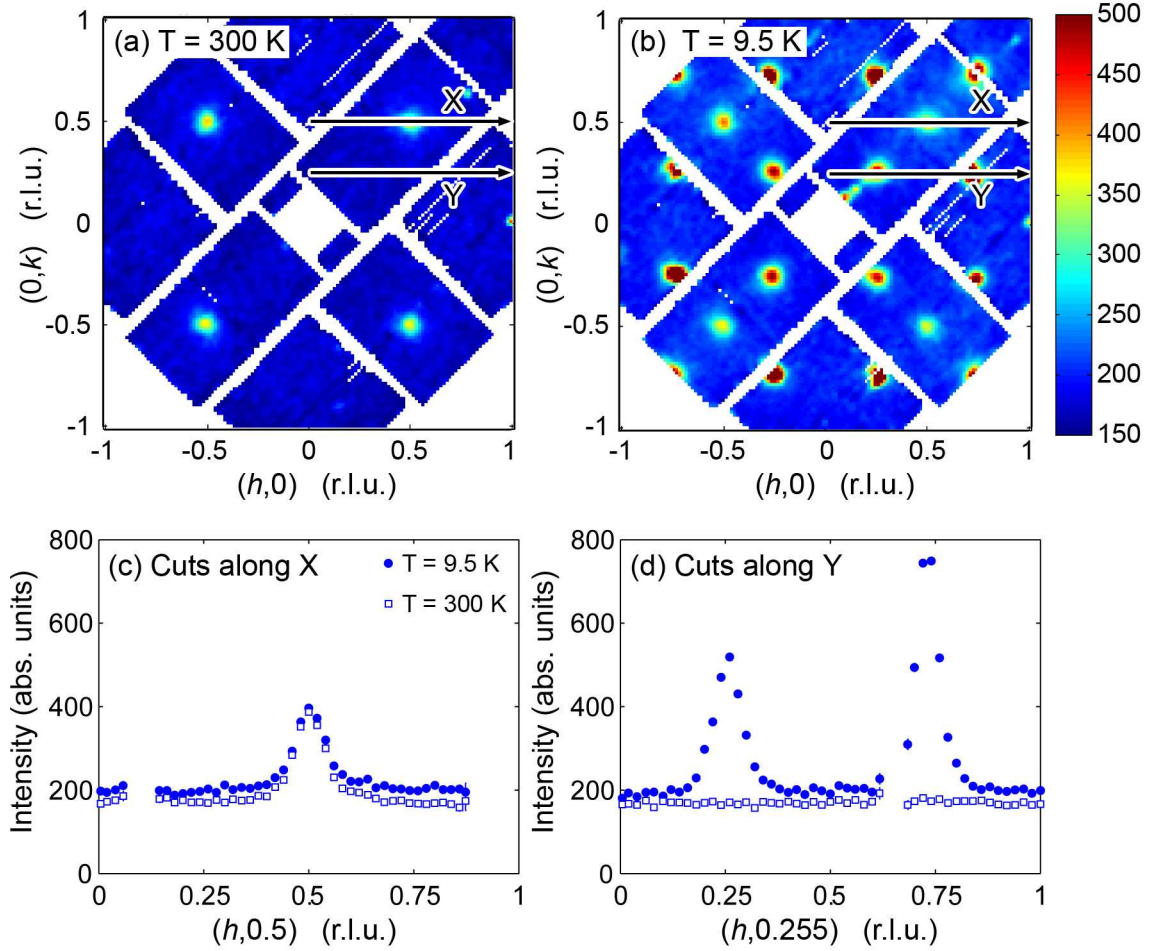
Figure 4.8: Elastic neutron scattering measurements on La$_{1.5}$Sr$_{0.5}$CoO$_4$ made on MAPS with $E_i = 50$ meV. (a) Elastic scattering projected into the (h, k) plane, measured at room temperature. Spots of intensity at $(n/2, m/2)$, where n, m are integers, are charge order Bragg peaks. (b) The same measurement at $T = 9.5$ K. There are now additional spots of intensity at $(n/2 \pm \{0.25 - \delta\}, m/2 \pm \{0.25 - \delta\})$. These are magnetic Bragg peaks. Colourbar shows the intensity of scattering in absolute units (sr^{-1}meV^{-1}Co^{-1}). Within (a,b) l varies from zero at the origin to 1.1 r.l.u at the corners. (c,d) Elastic cuts through both MAPS data sets along the directions X (through the charge peak) and Y (through the magnetic peaks) respectively.

4.4.2 Results

Figure 4.8 is an overview of the elastic neutron scattering measurements made on the MAPS spectrometer. Figure 4.8(a, b) show data measured at (a) 300 K and (b) 9.5 K, averaged over the elastic peak and projected into the (h, k) reciprocal lattice

plane. The colour bar represents intensity in absolute units. Within these plots l varies from zero at the origin to 1.1 r.l.u. at the corners. Figure 4.8(c,d) show cuts through the two sets of data shown in fig. 4.8(a, b) in the directions marked X and Y. The figures confirm the existence of charge ordering Bragg peaks at half integer positions which do not change in intensity between 300 K and 9.5 K, in agreement with previous studies of the compound [2, 3]. At $T = 9.5$ K magnetic order Bragg peaks are also observed at approximately quarter-integer positions, and these are not present in the 300 K data. The magnetic Bragg peaks are in fact found to be slightly incommensurate, occurring at positions $(h, k) = (n/2 \pm \{0.25 - \delta\}, m/2 \pm \{0.25 - \delta\})$ with $\delta = 0.005$, where n, m are integers, as reported previously [13].

The difference in intensity between the peaks at $(0.255, 0.255)$ and $(0.745, 0.255)$ shown in fig. 4.8d is due to their l dependence, and this was further investigated using the triple-axis spectrometer IN20. Some elastic measurements made on IN20 are presented in figure 4.9. Figure 4.9a is a schematic diagram of the magnetic Bragg peak positions (circles) surrounding the charge order Bragg peak at $(h, k) = (0.5, 0.5)$ (crossed circle, A). White and grey circles represent magnetic Bragg peaks from two different domains: white circles from the domain shown in fig. 4.3a; grey circles from the domain with ordering at 90° to this. Figures 4.9(b-e) show both spin-flip (SF) and non-spin-flip (NSF) channels of elastic scans along various $\boldsymbol{Q}$ directions. In scans through the charge order Bragg peak the intensity appears in the non-spin-flip channel, confirming that the peak is structural in origin, whereas in the scans through the magnetic Bragg peaks the intensity appears in the spin-flip channel, as expected for magnetic scattering.

Figures 4.9(bi,bii) and (ci,cii) are $(h, h, 0)$ and $(h, -h, 0)$ scans through the magnetic Bragg peaks marked B (0.745,0.745,0) and C (0.745, 0.255, 0) respectively. In these scans, made at $l = 0$, the magnetic Bragg peak C is roughly ten times as intense as that marked B. The l dependence of the magnetic Bragg peak B is shown in fig. 4.9e, and displays peaked intensity at odd values of l. This fits with the low intensity seen in the (h, h) scans at $l = 0$, and we deduce that the magnetic Bragg peak marked C must have the opposite l-dependence, with intensity peaked at even values of l. The two pairs of magnetic Bragg peaks from the two domains, denoted by white and grey circles, therefore have opposite l dependence, as is found in the nickelate compounds [20]. The l-dependence of the magnetic Bragg peaks gives information on the stacking pattern of the antiferromagnetically ordered cobalt layers [19].

Figure 4.9d shows the l-dependence of the intensity of the charge ordering peak (A): the intensity peaks at $l = 7$, as reported previously [2].

4.4.3 Polarization Analysis

The results presented above characterize the La$_{1.5}$Sr$_{0.5}$CoO$_4$ samples, and show good agreement with previous measurements on the compound. This section describes measurements made to determine the direction of the ordered moments

---

[13]Zaliznyak *et al* found $\delta = 0.008$ [7].
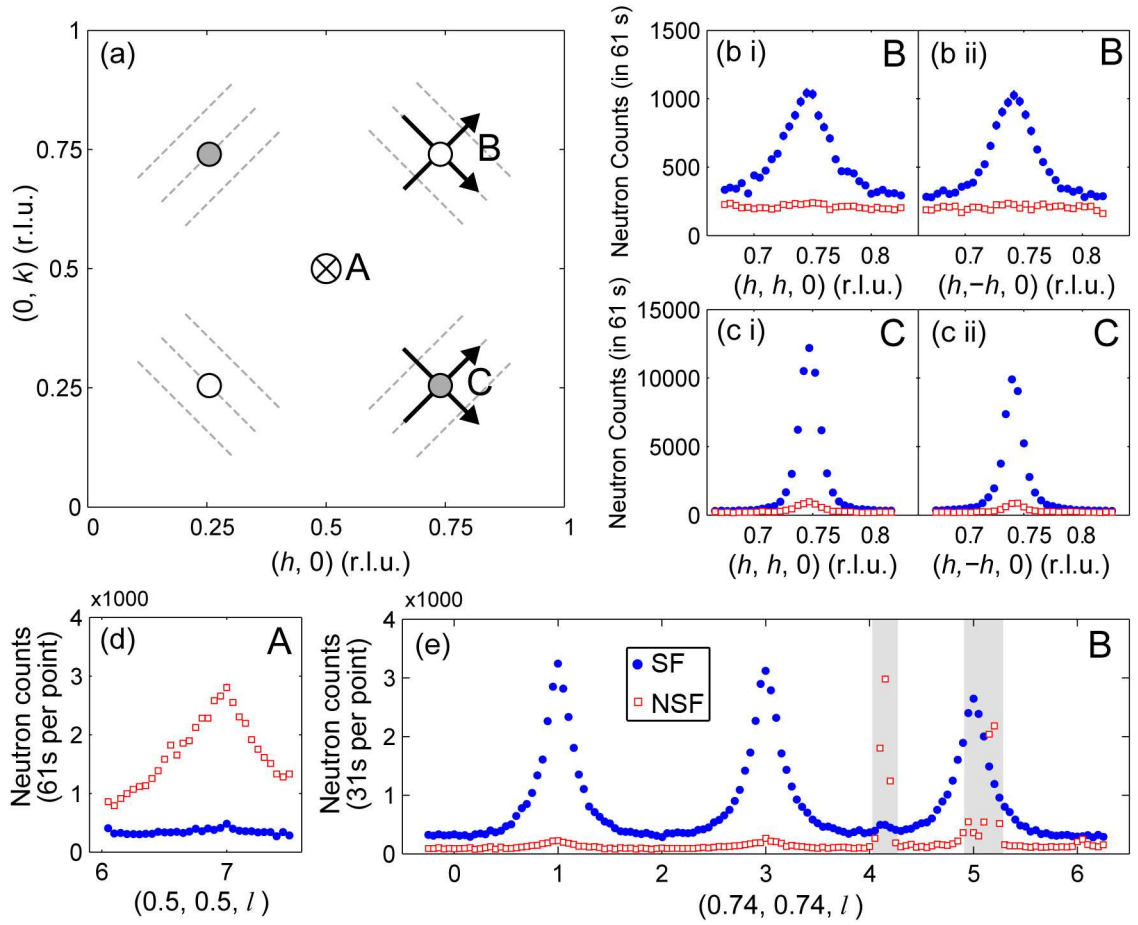
Figure 4.9: (a) Diagram of the magnetic Bragg peaks (two twins, filled and unfilled circles) around the charge order Bragg peak at (h, k)=(0.5, 0.5) (crossed circle, A). (b-e) Polarized neutron elastic scans made on IN20 with $\boldsymbol{P} \parallel \boldsymbol{Q}$: Spin-flip (filled blue circles) channel and non-spin-flip (open red squares) are both shown. (b, c) $(h, h, 0)$ and $(h, -h, 0)$ scans through magnetic Bragg peaks B and C as labelled. (d) l-dependence of the intensity of the charge ordering peak (A) between $l = 6$–7.5. (e) l-dependence of the intensity of the magnetic Bragg peak B, peaking at odd values of l. Shaded grey regions contain points contaminated with aluminium scattering.

in La$_{1.5}$Sr$_{0.5}$CoO$_4$, which has not previously been reported. The polarization analysis reveals a spin-reorientation within the *ab* planes.

The theory of how polarization analysis can be used to determine the relative components of the ordered moments, and from this their direction, is covered in appendix A. The measurement involves recording the spin-flip and non-spin-flip signals at two magnetic Bragg positions using three orthogonal polarization directions.
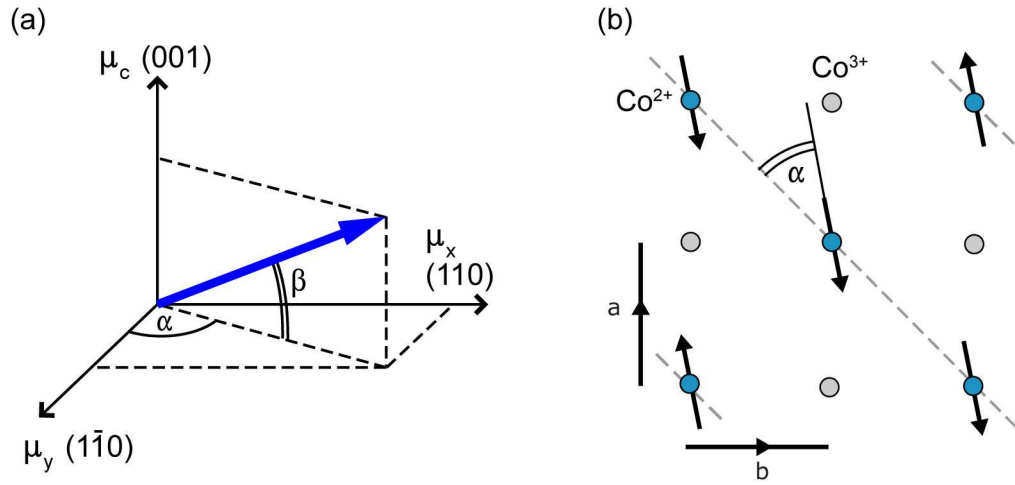
Figure 4.10: (a) The components of the ordered magnetic moment $\boldsymbol{\mu}$: the axes are defined such that $\mu_x = \mu_{110}$, $\mu_y = \mu_{1\bar{1}0}$ and $\mu_c = \mu_{001}$. α is the in-plane angle measured from $(1\bar{1}0)$ and β is the out-of-plane angle as shown. (b) Antiferromagnetic ordering of Co^{2+} spins in $La_{1.5}Sr_{0.5}CoO_4$, also showing the in-plane angle α.

These six measurements allow direct comparison of the *squares* of the components of the ordered magnetic moment $\boldsymbol{\mu}$: μ_x^2, μ_y^2 and μ_c^2. These components are shown in fig. 4.10, defined such that $\mu_x = \mu_{110}$, $\mu_y = \mu_{1\bar{1}0}$ and $\mu_c = \mu_{001}$. The in-plane (α) and out-of-plane (β) angles are also marked in fig. fig. 4.10. Defined in this way for a single domain they are related to the moment components by:

$$\alpha = \arctan\left(\sqrt{\frac{\mu_x^2}{\mu_y^2}}\right) \qquad \text{and} \qquad \beta = \arctan\left(\sqrt{\frac{\mu_c^2}{(\mu_x^2 + \mu_y^2)}}\right) \quad . \tag{4.2}$$

The six polarization-SF combinations were measured at temperatures between 1.5 and 55 K, using either IN20 or IN22. Figure 4.11a shows the relative size of the squares of the moments calculated from the results (see appendix A) [14]. At all temperatures there is almost no component of the magnetic moment out of the plane (μ_c), and we find $\beta = 0 \pm 5°$ (eqn. 4.2). At low temperatures the ratio μ_x^2/μ_y^2 is approximately 0.4. At $T \approx 30$ K this ratio rises until $\mu_x^2 \approx \mu_y^2$ around 50 K. This indicates that there is a spin-reorientation in $La_{1.5}Sr_{0.5}CoO_4$, as is found in the isostructural nickelate compounds [20]. The dashed vertical line in 4.11 marks the feature found in the magnetization data at $T \approx 31$ K (fig. 4.5), and it now seems that this feature does signify a spin-reorientation. For comparison, the temperature

---

[14]Measuring all polarization directions at both magnetic Bragg peaks, $\boldsymbol{Q}_A = (0.25, 0.25, 7)$ and $\boldsymbol{Q}_B = (1.25, 1.25, 1)$ allowed both μ_x^2/μ_y^2 (and therefore α) and $\mu_c^2/(\mu_x^2 + \mu_y^2)$ to be calculated. When only $\boldsymbol{Q}_A$ was measured an approximation was made to allow calculation of μ_x^2/μ_y^2 (and therefore α). This had negligible effect on the result, as shown in fig. 4.11.
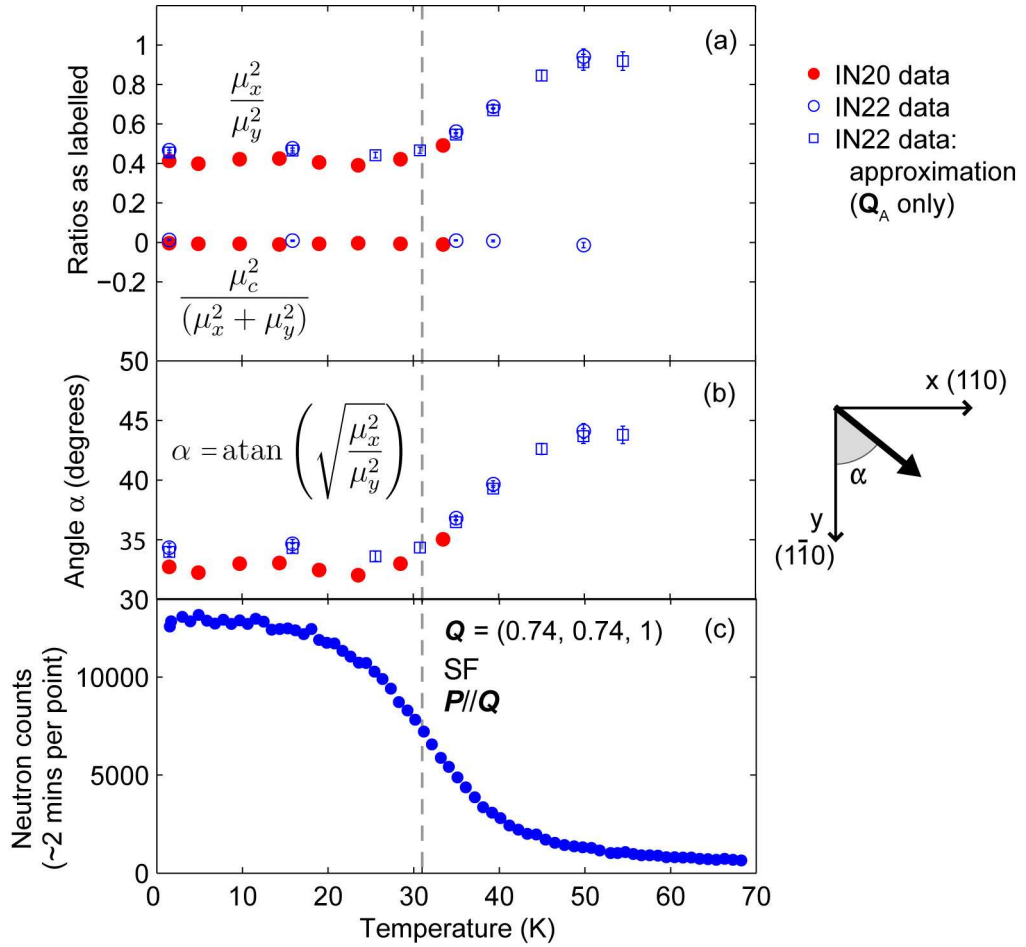
Figure 4.11: (a, b) Results of elastic polarization analysis on $La_{1.5}Sr_{0.5}CoO_4$. (a) Temperature dependence of two ratios of the squared components of the ordered magnetic moment $\boldsymbol{\mu}$: $(\mu_x^2)/(\mu_y^2)$ and $(\mu_c^2)/(\mu_x^2 + \mu_y^2)$. (b) The in-plane angle α, as defined in fig. 4.10. (Note that μ_x is the component of μ in the (110) direction, μ_y is the component of μ in the $(1\bar{1}0)$ direction, see appendix A.) (c) Temperature dependence of the intensity of the magnetic Bragg peak $\boldsymbol{Q} = (0.74, 0.74, 1)$ measured with polarized neutrons, with polarization parallel to $\boldsymbol{Q}$ (spin-flip channel). The dashed grey line shows the position of the kink at 31 K in the magnetization data (see fig. 4.5).

dependence of a magnetic Bragg peak, $\boldsymbol{Q} = (0.74, 0.74, 1)$ is plotted in fig. 4.11c. This gives an indication of the broad magnetic ordering temperature, and the very low intensity above 60 K explains why polarization analysis measurements could not be continued to higher temperatures [15] .

---

[15]It is worth commenting on the very gradual increase in intensity of the magnetic Bragg peak
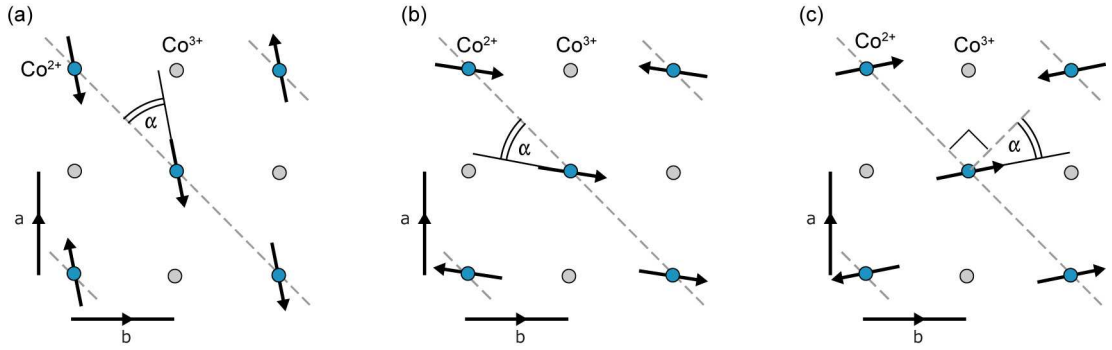
Figure 4.12: (a-c) Three possible domains with the same ordering wavevector.

The interpretation of this reorientation in terms of the in-plane angle α depends on assumptions made about domains in the crystal. For a single domain eqn. 4.2 can be used to calculate α, and this angle is shown in fig. 4.11b. At low temperatures the spins lie at $\sim 33°$ to the $(1\bar{1}0)$ direction. At $T \approx 30$ K the spins start to rotate away from this direction, reaching $\sim 44°$ at 50 K. This is approximately along the Co–O bond direction.

If we consider more than one domain in the crystal the calculation is more complicated (see appendix A). Since the measurements were made at one type of the magnetic Bragg reflections shown in fig. 4.9, we only probe the angles of spins aligned in the domain with ordering wavevector shown in fig. 4.12. However, we cannot rule out the possibility that there are other domains with the same ordering wavevector but spins at different angles within the compound. One possibility is a domain with spins at $-\alpha$ to the diagonal, rather than $+\alpha$ to the diagonal, as shown in fig. 4.12b. Since polarization probes the squares of the magnetic moments it is not possible to distinguish between these two. However, if the spins are aligned 90° away, at $(90 + \alpha)$ to the diagonal, the contribution to the measured components of the magnetic moment is different. Appendix A shows that for two domains at 90° it is in fact not possible to extract both the angle α, and the percentage of spins in each domain, from the measurements.

in La$_{1.5}$Sr$_{0.5}$CoO$_4$ as the temperature is lowered through the ordering temperature (fig. 4.5c). In La$_2$CuO$_4$, which is also an antiferromagnet with spins lying in the *ab* plane, the magnetic Bragg peak intensity shows a much sharper increase at the ordering temperature, with the order parameter fitting a simple power law [21]. The order parameter of La$_2$CoO$_4$, the parent compound of La$_{1.5}$Sr$_{0.5}$CoO$_4$, similarly follows a power law, with only very slight rounding at the transition temperature. The ordering observed in La$_{1.5}$Sr$_{0.5}$CoO$_4$ is shown to be different from these similar systems.

4.5 Inelastic Neutron Scattering Measurements on La$_{1.5}$Sr$_{0.5}$CoO$_4$ Single Crystals

This section describes inelastic neutron scattering measurements made as a continuation of the elastic measurements described in the last section. The measurements were therefore performed on single crystals of La$_{1.5}$Sr$_{0.5}$CoO$_4$ on the MAPS time-of-flight spectrometer and on the triple-axis spectrometers IN20 and IN22. The experimental details were exactly as described previously in section 4.4.1.

4.5.1 Spin-wave Dispersion

The main feature of the inelastic spectrum of La$_{1.5}$Sr$_{0.5}$CoO$_4$ is a strong spin-wave dispersion arising from the magnetic Bragg positions. Figure 4.13 shows slices taken in various directions through the MAPS data set to illustrate the characteristics of the dispersion. On the left hand side (a–c) are three constant energy slices at $\langle E \rangle = 7$, 11 and 17 meV. The intensities have been projected into the (h, k) plane. We see that spots of intensity marking the magnetic Bragg peaks in the elastic data broaden into rings of scattering as the energy increases to 7 and then to 11 meV. By $E = 17$ meV the sharp features in the scattering have disappeared. On the right hand side of figure 4.13 are displayed three energy–$\boldsymbol{Q}$ slices taken along different $\boldsymbol{Q}$ directions in the (h, k) plane. There is clearly a dispersive mode coming out of the magnetic Bragg positions and turning over at the magnetic zone boundaries, with a maximum energy of approximately 15 meV.

In order to interpret the inelastic data we have projected the intensities into the $(h, k, 0)$ plane, ignoring any l dependence of the excitations. This is justified because La$_{1.5}$Sr$_{0.5}$CoO$_4$ is a strongly two dimensional compound, and the excitations are therefore expected to show little l-dependence. Figure 4.14 shows a series of measurements made on the triple-axis spectrometer IN20 to check this assertion: figs. 4.14(a–c) show l-scans through a magnetic Bragg position with three different energy transfers: (a) 0 meV, (b) 2 meV and (c) 4meV. Magnetic correlations along $(0, 0, l)$ are evident in the elastic data (a). At 2 meV weak correlations are still present, but by 4 meV there is no longer any l dependence to the magnetic scattering. It is therefore valid to neglect the l-dependence in the analysis of the inelastic data measured on MAPS for energies above 4 meV.

To facilitate comparison with models, cuts through the MAPS data set were taken along several symmetry directions in the (h, k) plane and fitted to extract data points describing the dispersion. Figures 4.15a and b show typical examples of the two different types of cut taken: (a) constant-energy cut, and (b) constant-$\boldsymbol{Q}$ cut. The cuts were fitted with Lorentzian (or two Lorentzian) lineshapes, and the peak centres of fits such as these provide data points characterizing the dispersion, for example along $(0.255, k)$ (shown in fig. 4.15c).

No information on the dispersion could be gained from the MAPS data below 5 meV due to the width of the elastic peak. However, the position of points around the magnetic zone centre in fig. 4.15c suggested that the excitation might be gapped.
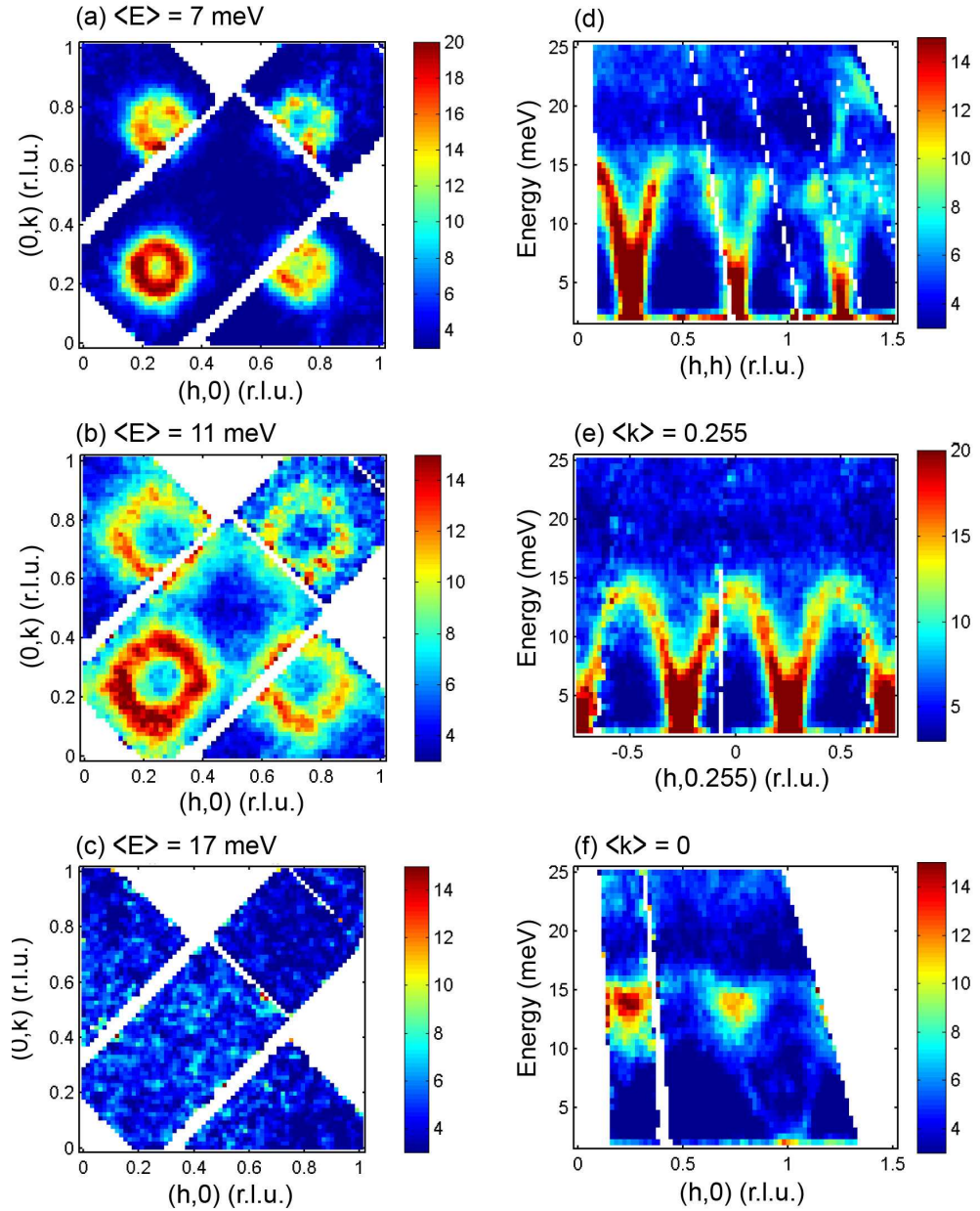
Figure 4.13: Inelastic neutron scattering measurements made at $T = 9.5$ K on La$_{1.5}$Sr$_{0.5}$CoO$_4$ on the MAPS spectrometer: Colour bars show intensity in absolute units (sr^{-1}meV^{-1}Co^{-1}). (a–c) Constant energy slices at energies labelled; data have been projected onto the (h, k) plane. (c–e) $\boldsymbol{Q}$-energy slices: (c) diagonally through the magnetic zone centres; (d) through the magnetic zone centres in the h direction; (e) in between the magnetic zone centres in the h direction.
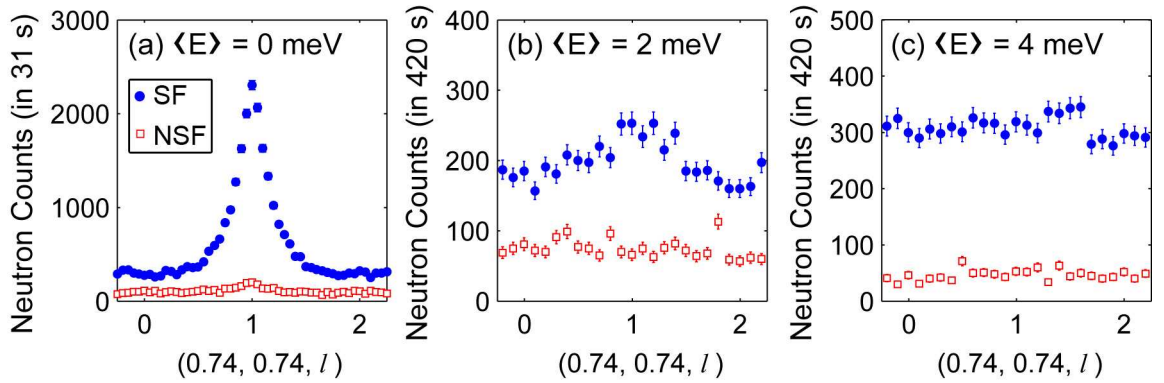
Figure 4.14: Inelastic scans along (0.74, 0.74, l) at $T = 1.5$ K, with energy transfers (a) 0 meV, (b) 2 meV and (c) 4meV. Polarization parallel to $\boldsymbol{Q}$; both spin-flip (SF) and non-spin-flip (NSF) channels shown, as labelled.
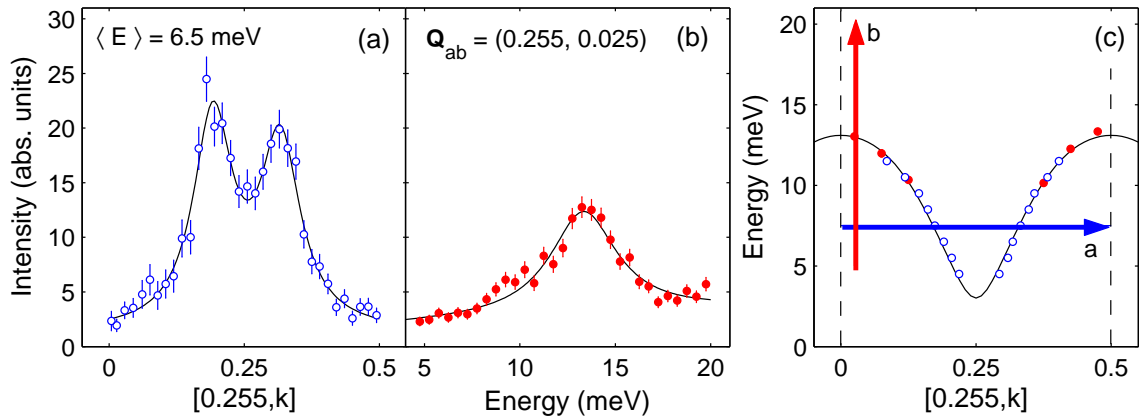
Figure 4.15: (a, b) Example cuts through the MAPS data set taken at $T =$ 9.5 K. (a) Constant-energy cut at $\langle E \rangle = 6.5$ meV, fitted with a double Lorentzian lineshape. (b) Constant-$\boldsymbol{Q}$ cut at $\boldsymbol{Q}$= (0.255, 0.025), fitted with a Lorentzian on a sloping background. (c) Data points show the dispersion relation derived from fits such as those in (a) and (b). The solid curve is a guide to the eye; dashed lines mark the Brillouin zone boundaries; arrows show the directions of the example cuts shown in (a) and (b) as labelled.

Further measurements were therefore made on IN20 to investigate this possibility. Figure 4.16 shows an energy scan made with polarized neutrons at the magnetic zone centre $\boldsymbol{Q}$=(0.75, 0.25, 0). As the energy is lowered from 10 meV the non-spin-flip (NSF) scattering is relatively flat until about 1.5 meV when the intensity rises
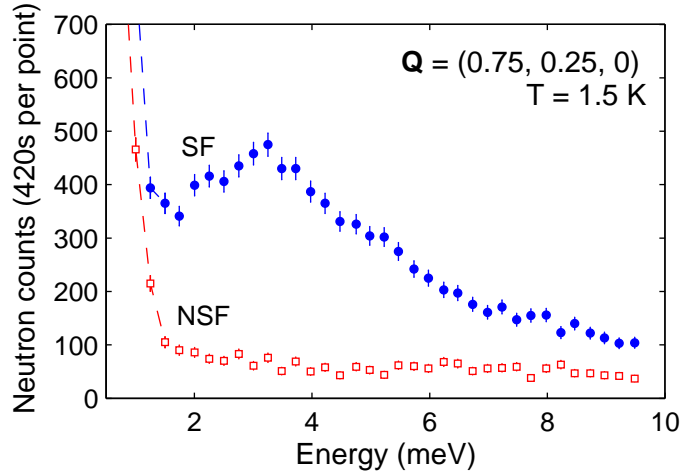
Figure 4.16: Gap at the magnetic zone centre (0.75,0.25,0) measured with polarized neutrons on IN20. Both spin-flip (SF) and non-spin-flip (NSF) channels are plotted ($\boldsymbol{P} \parallel \boldsymbol{Q}$).

sharply into the incoherent elastic peak. In the spin-flip (SF) spectrum, the intensity rises as the energy decreases from 10 meV. This increase in magnetic scattering is due to the resolution ellipsoid moving down into the spin-wave dispersion. For an ungapped mode the intensity would continue to rise until it reached the incoherent peak. Here, however, the intensity peaks at approximately 3 meV, and the intensity drops again before rising sharply below 1.5 meV into the incoherent peak. The spin-wave dispersion in La$_{1.5}$Sr$_{0.5}$CoO$_4$ is therefore gapped at the magnetic zone centre, with a gap of approximately 3 meV.

4.5.2 Higher Mode

The spin-wave dispersion described above has a maximum energy of approximately 15 meV, above which there is a region where the magnetic scattering disappears (see for example fig. 4.13c). However, above this energy the magnetic scattering is observed to increase again, indicating a higher magnetic mode between approximately 20 and 32 meV.

Figure 4.17 displays some plots made to characterize this feature. The scattering is very diffuse in comparison to the lower mode, but does appear to show some dispersion. Figure 4.17a is a slice through the top of the scattering, showing peaked intensity at (h, k) positions $(0, 0)$, $(0.5, 0)$, $(0, 0.5)$ *etc.* Figure 4.17b shows the feature in comparison with the lower dispersion: the higher mode is far less intense than the lower dispersion. In order to display the higher mode scattering it is necessary to shift the intensity scale such that the features of the lower mode cannot be seen. Figures 4.17(c,d) present cuts through the top region of the higher mode (27–30 meV), and reveal the $\boldsymbol{Q}$-dependence of the scattering in this region. Identical cuts made at
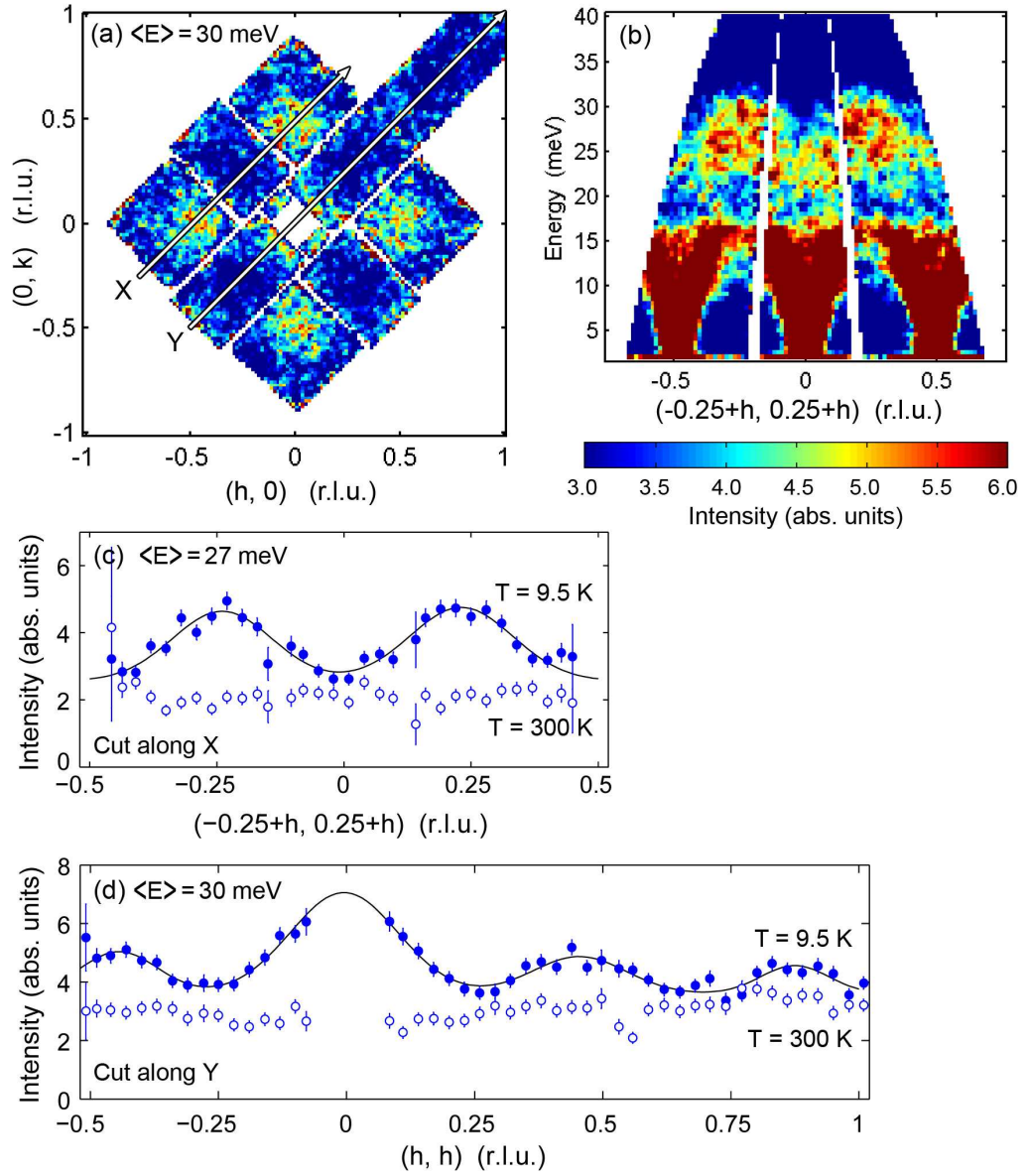
Figure 4.17: Evidence for a magnetic mode in $La_{1.5}Sr_{0.5}CoO_4$ between approximately 20 and 32 meV. (a,b) Slices through the MAPS data set measured at $T = 9.5$ K. (a) Scattering at a constant energy of $\langle E \rangle = 30$ meV projected into the (h, k) plane. (b) An energy–Q slice perpendicular to that in (a), and cutting through the direction marked X. (c,d) Cuts though the data set in the directions marked X and Y respectively, at constant energies $\langle E \rangle$ as labelled. Identical cuts made through the $T = 300$ K data set are also plotted.

Energy E_T	$(\Delta\mu_x)^2/(\Delta\mu_y)^2$	$(\Delta\mu_c)^2/(\Delta\mu_y)^2$
2 meV	1.19 ± 0.07	-0.04 ± 0.06
4 meV	1.00 ± 0.05	-0.02 ± 0.04

Table 4.3: Ratios of components of fluctuations of the ordered magnetic moments, $\boldsymbol{\mu}$, at 2 meV and 4 meV, determined by inelastic polarization analysis at $T = 1.5$ K.

300 K are overplotted, and show no features, indicating that the scattering at 9.5 K is magnetic in origin. We also note that cuts through the higher mode in the region 20–25 meV (not shown) do not display any obvious $\boldsymbol{Q}$-dependence, just diffuse scattering.

4.5.3   Inelastic Neutron Polarization Analysis

Inelastic polarization analysis can be performed in a similar way to the elastic polarization analysis described in section 4.4.3, but the inelastic measurements probe the components of the fluctuations of the moments, rather than their magnitude. The technique of using inelastic polarization analysis to characterize the fluctuations of the moments, $\Delta\boldsymbol{\mu}$ is described in appendix A (section A.2). Measurements were made using the same six polarization-spin-flip combinations as for the elastic measurements, at the same two wavevectors, but with energy transfers of 2 meV and 4 meV. These two energy transfers were chosen as points above and below the gap (see fig. 4.16). Due to the long counting times needed for the inelastic measurements they were only performed at low temperature ($T = 1.5$ K). Defining the components of the fluctuations as $\Delta\mu_x = \Delta\mu_{110}$, $\Delta\mu_y = \Delta\mu_{1\bar{1}0}$ and $\Delta\mu_c$, their relative amplitudes can be extracted (see section A.2).

The ratios $(\Delta\mu_x)^2/(\Delta\mu_y)^2$ and $(\Delta\mu_c)^2/(\Delta\mu_y)^2$ for the two energy transfers are shown in table 4.3. Within errors there is no c component to the fluctuations, so the excitations are in-plane, both below and above the gap. The ratio $(\Delta\mu_x)^2/(\Delta\mu_y)^2$ varies from approximately 1.2 to 1.0 between $E_T = 2$ meV and 4 meV. Assuming isotropic fluctuations within the ab plane, and taking $\alpha = 33°$ as the angle of moments within the ab plane (from section 4.4.3), the ratio $(\Delta\mu_x)^2/(\Delta\mu_y)^2$ is expected to be $(\tan^2\alpha)^{-1} = 2.37$.[16] This is not in agreement with the experimental results, but the reason for this is unclear [17].

---

[16]This expression assumes isotropic fluctuations perpendicular to the moment direction, *i.e.* the assumption is made that the moments do not fluctuate in length, see section 4.4.3.

[17]It is possible that the data at 2 meV may be contaminated by Bragg scattering (see fig. 4.16), which might explain the discrepancy between the 2 meV and 4 meV results.

4.6 Spin-wave Analysis

To understand the magnetic excitations in La$_{1.5}$Sr$_{0.5}$CoO$_4$ observed by inelastic neutron scattering it is informative to compare the data with a model that describes the main features. This enables us to gain information on the interactions in the system. To do so we assume that the excitation spectrum can be modelled with a spin-only Hamiltonian.

As a first approximation we attempt to model the results as a spin-1/2 system using a simple Heisenberg model, presented in section 4.6.1. We will see that the simple Heisenberg model fails to describe the system adequately, and a more complete model which includes the full spin-3/2 physics is considered in section 4.6.2. We will refer to this model as the *exciton* model, to distinguish it from the Heisenberg model.

Throughout the analysis presented in this section we will assume that the Co^{2+} ions carry spin, while the Co^{3+} ions are non-magnetic, and therefore do not contribute to the excitations, as has previously been assumed in the literature (see section 4.1). This issue was discussed in the introduction. The possibility that the Co^{3+} sublattice might play a part in the excitation spectrum will be addressed in the discussion. Since no $\mathbf{Q}_l$-dependence was found in the excitations we consider only the *ab* planes in the models.

4.6.1 Simple Heisenberg Model

In this model we assume that the exchange interactions between Co^{2+} ions are isotropic Heisenberg couplings, that exchange interactions between layers are negligible, and that the spins lie along an in-plane axis (a). The Heisenberg Hamiltonian can be written in terms of the sum of the exchange interactions as

$$\mathcal{H} = \sum_{\langle ij \rangle} J_{ij}\, \mathbf{S}_i \cdot \mathbf{S}_j = \sum_{\langle ij \rangle} J_{ij} \left(S_i^x S_j^x + S_i^y S_j^y + S_i^z S_j^z \right) \quad , \tag{4.3}$$

where i, j are pairs of spins interacting with exchange constant J_{ij} (each pair is counted only once).

Figure 4.18 shows the antiferromagnetic ordering in the *a–b* plane. The dashed grey box represents the magnetic unit cell which contains one spin pointing along the positive a axis (spin 'up', marked A) and one pointing along the negative a axis (spin 'down', marked B). The up and down spins can be considered as two sublattices, A and B. The most likely possible exchange paths are marked J, J_1 and J_2. J and J_1 are inter-sublattice interactions, while J_2 acts between spins in the same sublattice. We expect the strongest coupling to be J because this interaction occurs through superexchange along straight bonds Co–O–Co–O–Co.

Equation 4.3 can now be rewritten explicitly in terms of these exchange parameters, summing over all nearest-neighbouring pairs linked by the three exchanges J, J_1 and J_2. Δ, Δ_1 and Δ_2, the vectors along which the three exchanges act respectively, are Δ={(2,0,0), (0,2,0), (-2,0,0), (0,-2,0)}, Δ_1={(1,1,0), (-1,-1,0)} and Δ_2={(1,-1,0), (-1,1,0)}, as shown in fig. 4.18.
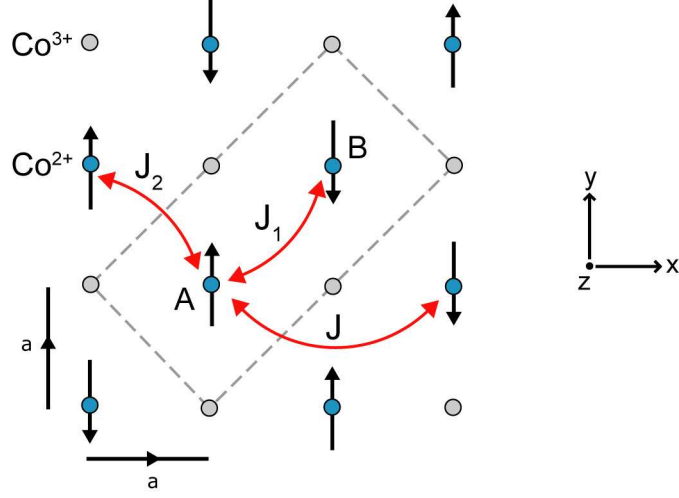
Figure 4.18: Schematic diagram of the magnetic ordering and exchange interactions (J, J_1 and J_2) in $La_{1.5}Sr_{0.5}CoO_4$. Spins are modelled as lying directly along an inplane axis. A and B label the two sublattices of 'up' and 'down' spins, and the grey dashed box indicates the magnetic unit cell.

Linear spin-wave theory was used to calculate the excitation spectrum of this model. First, the Holstein-Primakoff transformations are used to write the spin operator components for the two sublattices in terms of Bose operators, with the quantization direction along the y axis:

$$
\begin{aligned}
S_i^y &= S - a_i^\dagger a_i & S_j^y &= -(S - b_j^\dagger b_j) \\
S_i^z &= \sqrt{S/2}\left(a_i + a_i^\dagger\right) & S_j^z &= \sqrt{S/2}\left(b_j^\dagger + b_j\right) \\
S_i^x &= \frac{1}{i}\sqrt{S/2}\left(a_i - a_i^\dagger\right) & S_j^x &= \frac{1}{i}\sqrt{S/2}\left(b_j^\dagger - b_j\right) \quad ,
\end{aligned}
\tag{4.4}
$$

where $a_i^\dagger$ ($b_j^\dagger$) creates a spin deviation on site i (j) of sublattice A (B). The Hamiltonian (eqn. 4.3) is then rewritten, first in terms of the Bose operators, retaining only terms to second order in the operators, and then in terms of their Fourier transforms:

$$
\begin{aligned}
a_{\boldsymbol{Q}} &= \frac{1}{\sqrt{N}}\sum_i e^{-i\boldsymbol{Q}\cdot\boldsymbol{r}_i}a_i & a_{\boldsymbol{Q}}^\dagger &= \frac{1}{\sqrt{N}}\sum_i e^{+i\boldsymbol{Q}\cdot\boldsymbol{r}_i}a_i^\dagger \\
b_{\boldsymbol{Q}} &= \frac{1}{\sqrt{N}}\sum_i e^{+i\boldsymbol{Q}\cdot\boldsymbol{r}_i}b_i & b_{\boldsymbol{Q}}^\dagger &= \frac{1}{\sqrt{N}}\sum_i e^{-i\boldsymbol{Q}\cdot\boldsymbol{r}_i}b_i^\dagger \quad .
\end{aligned}
\tag{4.5}
$$

The result is an expression for the Heisenberg Hamiltonian for the system in terms of 2nd order products of the operators $a_{\boldsymbol{Q}}$, $a_{\boldsymbol{Q}}^\dagger$, $b_{\boldsymbol{Q}}$ and $b_{\boldsymbol{Q}}^\dagger$ which can be written in matrix form:

$$
\mathcal{H} = H_0 + \sum_{\boldsymbol{Q}} X_{\boldsymbol{Q}}^\dagger H_{\boldsymbol{Q}} X_{\boldsymbol{Q}} \quad ,
\tag{4.6}
$$

where X is the column vector $(a_{\boldsymbol{Q}}, b_{\boldsymbol{Q}}, a_{\boldsymbol{Q}}^\dagger, b_{\boldsymbol{Q}}^\dagger)$, and the matrix $H_{\boldsymbol{Q}}$ is written in general form as:

$$H_{\boldsymbol{Q}} = \frac{1}{2} \begin{pmatrix} A_{\boldsymbol{Q}} & B_{\boldsymbol{Q}} & C_{\boldsymbol{Q}} & D_{\boldsymbol{Q}} \\ B_{\boldsymbol{Q}} & A_{\boldsymbol{Q}} & D_{\boldsymbol{Q}} & C_{\boldsymbol{Q}} \\ C_{\boldsymbol{Q}} & D_{\boldsymbol{Q}} & A_{\boldsymbol{Q}} & B_{\boldsymbol{Q}} \\ D_{\boldsymbol{Q}} & C_{\boldsymbol{Q}} & B_{\boldsymbol{Q}} & A_{\boldsymbol{Q}} \end{pmatrix} \ . \tag{4.7}$$

The general method for deriving the dispersion relations and scattering function from eqn. 4.6 is detailed in Appendix B. For this simple Heisenberg model we have (with $\boldsymbol{Q} = (h, k, l)$):

$$A_{\boldsymbol{Q}} = 4JS + 2J_1 S + 2J_2 S + 2J_2 S \cos(2\pi(h-k)) \tag{4.8}$$
$$D_{\boldsymbol{Q}} = 2JS[\cos(4\pi h) + \cos(4\pi k)] + 2J_1 S \cos(2\pi(h+k))$$
$$B_{\boldsymbol{Q}} = C_{\boldsymbol{Q}} = 0 \ .$$

The $A_{\boldsymbol{Q}}$ and $D_{\boldsymbol{Q}}$ terms originate directly from the Fourier transforms of the exchange couplings J, J_1 and J_2. Diagonalization of the bilinear form of the Bose operators (as described in Appendix B) gives a doubly degenerate mode with dispersion relation:

$$\hbar\omega(\boldsymbol{Q}) = (A_{\boldsymbol{Q}}^2 - D_{\boldsymbol{Q}}^2)^{1/2} \ , \tag{4.9}$$

and the intensities are proportional to the terms $S^{zz}(\boldsymbol{Q}, \omega)$ and $S^{xx}(\boldsymbol{Q}, \omega)$[18].

The dispersion in the (h, h) direction calculated with the simple Heisenberg model is plotted in the left hand column of fig. 4.19, along with $S^{zz}(\boldsymbol{Q}, \omega)$ and $S^{xx}(\boldsymbol{Q}, \omega)$. We see that the doubly degenerate modes have identical intensities: one mode has intensity resulting from $S^{zz}(\boldsymbol{Q}, \omega)$ and the other from $S^{xx}(\boldsymbol{Q}, \omega)$. The intensities peak at the magnetic zone centre positions $(0.25, 0.25)$ *etc.*, as observed experimentally. However, the periodicity of the modes is double that observed experimentally. In the equivalent direction through the data (fig. 4.13d) the dispersion clearly peaks at positions $(0.5, 0.5)$ *etc.* This position is a minimum in the calculated Heisenberg dispersion.

Anisotropy Terms

The system is known to exhibit strong anisotropy, with moments favouring the *ab* plane. This is seen in both the magnetization data (fig. 4.5) and the polarization analysis measurements made to study the ordered moment direction (section 4.4.3). We therefore add to the Heisenberg Hamiltonian an *out-of-plane* anisotropy term, identical for both sublattices:

$$\sum_i D(S_i^z)^2 + \sum_j D(S_j^z)^2 \ , \tag{4.11}$$

---

[18]From appendix B the intensity of each mode is proportional to

$$\sum_{\alpha\beta} \left\langle \left(\delta_{\alpha,\beta} - \hat{Q}_\alpha \hat{Q}_\beta \right) S^{\alpha\beta}(\boldsymbol{Q}, \omega) \right\rangle \ . \tag{4.10}$$

For this model, terms with $\alpha \neq \beta$ are zero, and $S^{yy}(\boldsymbol{Q}, \omega)$ is zero since the spins lie in the y direction. The intensity is therefore proportional to $\left\langle \left(1 - \hat{Q}_z \hat{Q}_z \right) S^{zz}(\boldsymbol{Q}, \omega) + \left(1 - \hat{Q}_x \hat{Q}_x \right) S^{xx}(\boldsymbol{Q}, \omega) \right\rangle$.
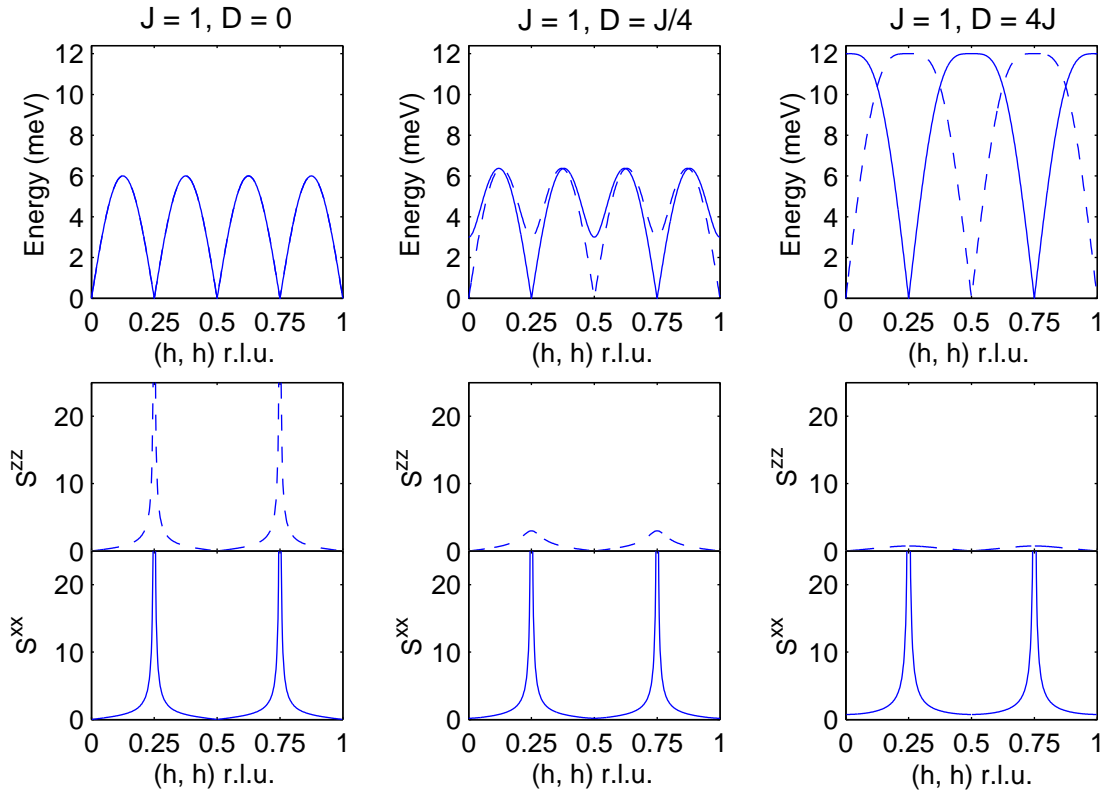
Figure 4.19: Spin-wave dispersions calculated using the simple Heisenberg model, with $S = 3/2$, exchange parameter $J = 1$ ($J_1 = J_2 = 0$) and three values of anisotropy parameter D, as labelled. The lower plots show $S^{zz}(\boldsymbol{Q}, \omega)$ and $S^{xx}(\boldsymbol{Q}, \omega)$ for each mode, dashed line for one mode and solid line for the second.

This term forces the spins to lie preferentially within the *ab* plane, as has been experimentally observed using polarization analysis (see section 4.4.3). With the addition of this term the Hamiltonian can still be expressed in the general form given in eqn. 4.24, with $A_{\boldsymbol{k}}$, $C_{\boldsymbol{k}}$ and $D_{\boldsymbol{k}}$ modified to give

$$A_{\boldsymbol{Q}} = 4JS + 2J_1S + 2J_2S + 2J_2S \cos(2\pi(h - k)) + DS \qquad (4.12)$$
$$B_{\boldsymbol{Q}} = 0$$
$$C_{\boldsymbol{Q}} = DS$$
$$D_{\boldsymbol{Q}} = 2JS[\cos(4\pi h) + \cos(4\pi k)] + 2J_1S \cos(2\pi(h + k)) \ .$$

With the anisotropy term included the two spin-wave modes are no longer degenerate, and their dispersion relations are given by

$$\hbar\omega(\boldsymbol{Q}) = \left[A_{\boldsymbol{Q}}^2 - (C_{\boldsymbol{Q}} \pm D_{\boldsymbol{Q}})^2\right]^{1/2} \ , \qquad (4.13)$$

The centre and right hand columns of fig. 4.19 show the dispersion modes calculated with two different values for the anisotropy parameter D, along with $S^{zz}(\boldsymbol{Q}, \omega)$ and
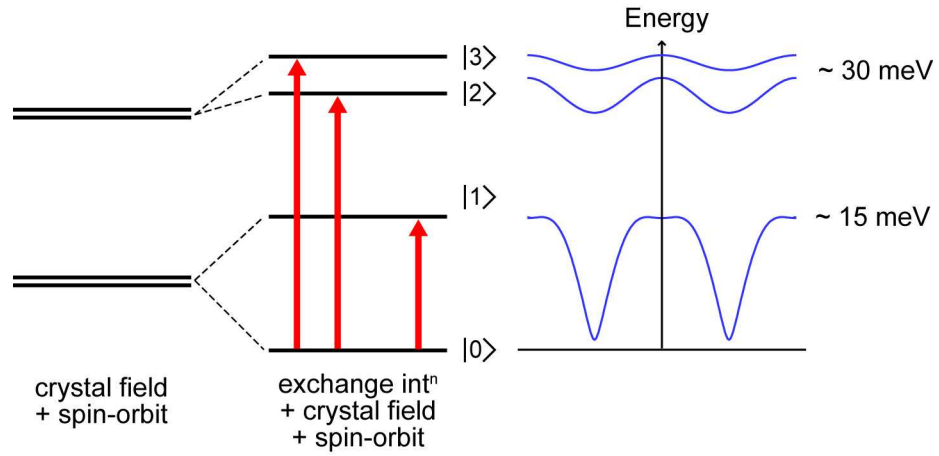
Figure 4.20: Left: Energy levels of Co^{2+} ions split by the crystal field and exchange interactions. Right: Lower dispersion should arise from excitations to first excited state; excitations to levels $|2\rangle$ or $|3\rangle$ may generate a higher mode.

$S^{xx}(\boldsymbol{Q},\omega)$. Increasing D from zero produces gaps at the magnetic zone boundaries ((h,k)=(0.5, 0.5) *etc.*) in one mode, and at the magnetic zone centres ((h,k)=(0.25, 0.25) *etc.*) in the other mode. As D increases, the intensity of the second mode falls, and the first mode begins to resemble the dispersion observed in the data.

However, in order to reproduce the shape of the dispersion observed experimentally, with dispersion maxima at the magnetic zone boundaries ((h,k)=(0.5, 0.5) *etc.*) and intensity peaked at the magnetic zone centres ((h,k)=(0.25, 0.25) *etc.*), the value of the anisotropy parameter D must be much larger than the exchange parameter J. An anisotropy parameter this large represents a significant crystal field, and this would cause splitting of the four-fold spin-3/2 manifold assumed for the Heisenberg model, and mixing of the M_s states. The exchange interaction would further split the levels, as shown in figure 4.20, and the mixed nature of the final levels would allow transitions to higher levels not allowed in the Heisenberg model, providing a possible explanation for the observed higher mode. Together this suggests that it is necessary to include the full spin-3/2 physics of the system, and we do so in the next section.

4.6.2 Exciton Model

In La$_{1.5}$Sr$_{0.5}$CoO$_4$ the Co^{2+} ions are in the free-ion state 3d^7, with spin $T = 3/2$ (we use $\boldsymbol{T}$ to distinguish from the Heisenberg spin operators $\boldsymbol{S}$ used in the last section). The point charge calculation presented in section 4.1 predicts that the crystal field at the Co^{2+} should produce a significant splitting of the ground state. In this model we include the effects of both the crystal field and the exchange interaction in a mean field Hamiltonian which allows a self-consistent calculation of the basis states of the Co^{2+} ions. These states will be mixtures of the $S = 3/2$ states $|-\frac{3}{2}\rangle$, $|+\frac{3}{2}\rangle$, $|-\frac{1}{2}\rangle$

and $|+\frac{1}{2}\rangle$. The spin-wave dispersion emerging from the magnetic zone centres (0.25, 0.25) *etc.* then corresponds to excitations from the new ground state to the first excited level, as shown in fig. 4.20. The higher mode of excitations observed in the data (section 4.5.2) may then be modelled by excitations to higher levels (second and third excited states).

Calculating basis states using the mean field Hamiltonian

The first stage of the calculation is performed to find the basis states, which can be written in general form as

$$|n, A\rangle = a_n^A |-\tfrac{1}{2}\rangle + b_n^A |+\tfrac{1}{2}\rangle + c_n^A |+\tfrac{3}{2}\rangle + d_n^A |-\tfrac{3}{2}\rangle \ , \tag{4.14}$$

for sublattice A where $n = 1$–4, and similarly for sublattice B. This is achieved by diagonalizing the mean field Hamiltonians for each sublattice iteratively to reach a self-consistent solution.

We start with a Hamiltonian containing the exchange interaction J, which is defined as before (see fig. 4.18), and the out-of-plane anisotropy parameter D as in the simple Heisenberg Hamiltonian. We also include an *in-plane anisotropy* term, with parameter E.[19] Although the calculation was initially performed including the two other exchange interactions J_1 and J_2 defined by fig. 4.18, these were not found to be necessary to describe the data, and we omit them from this description for simplicity. Again considering the two sublattices A (spin 'up') and B (spin 'down') (as shown in fig. 4.18), the total Hamiltonian is given by

$$\mathcal{H} = \quad \sum_i \left\{ \sum_\Delta \tfrac{J}{2} \boldsymbol{T}_i^A \cdot \boldsymbol{T}_{i+\Delta}^B + D(T_z^A(i))^2 - E\left[(T_y^A(i))^2 - (T_x^A(i))^2\right] \right\} \tag{4.15}$$
$$+ \sum_i \left\{ \sum_\Delta \tfrac{J}{2} \boldsymbol{T}_i^B \cdot \boldsymbol{T}_{i+\Delta}^A + D(T_z^B(i))^2 - E\left[(T_y^B(i))^2 - (T_x^B(i))^2\right] \right\} \ ,$$

including only nearest neighbour interactions with exchange parameter J, and $\Delta = \{(2,0,0), (0,2,0), (-2,0,0), (0,-2,0)\}$ as before. To solve this Hamiltonian in the mean field approximation we replace the exchange couplings with local mean field terms. The mean field Hamiltonians for the two sublattices can then be written

$$\mathcal{H}_{mf}^A = D(T_z^A)^2 - E[(T_y^A)^2 - (T_x^A)^2] + z_0 J \langle \boldsymbol{T}_{00}^B \rangle \cdot \boldsymbol{T}^A \tag{4.16}$$
$$\mathcal{H}_{mf}^B = D(T_z^B)^2 - E[(T_y^B)^2 - (T_x^B)^2] + z_0 J \langle \boldsymbol{T}_{00}^A \rangle \cdot \boldsymbol{T}^B \ ,$$

where $z_0 = 4$ is the coordination number for the exchange J. The mean field spin terms $\langle \boldsymbol{T}_{00}^{A,B} \rangle$ are solved self-consistently by fixing them to the ground state expectation values of the spin-operators, *i.e.*

$$\langle \boldsymbol{T}_{nm}^A \rangle = \langle n^A | \boldsymbol{T}^A | m^A \rangle = \begin{pmatrix} \langle n^A | T_x^A | m^A \rangle \\ \langle n^A | T_y^A | m^A \rangle \\ \langle n^A | T_z^A | m^A \rangle \end{pmatrix} \ , \tag{4.17}$$

---

[19]The results of the inelastic polarization analysis at the magnetic zone centres presented in section 4.5.3 show that the moments fluctuate in-plane both above and below the gap. This suggests that the small gap at the magnetic zone centres is an in-plane anisotropy gap, while the out-of-plane term serves to raise produce the large gap at the magnetic zone boundaries.

with $n = m = 0$, and similarly for B. The mean field Hamiltonians for sublattices A and B are written in matrix form:

$$\hat{H}_{mf}^{A,B} = \begin{pmatrix} \langle -\frac{1}{2}|\mathcal{H}_{mf}^{A,B}|-\frac{1}{2}\rangle & \langle -\frac{1}{2}|\mathcal{H}_{mf}^{A,B}|+\frac{1}{2}\rangle & \cdots & \langle -\frac{1}{2}|\mathcal{H}_{mf}^{A,B}|-\frac{3}{2}\rangle \\ \langle +\frac{1}{2}|\mathcal{H}_{mf}^{A,B}|-\frac{1}{2}\rangle & & & \vdots \\ \vdots & & & \vdots \\ \langle -\frac{3}{2}|\mathcal{H}_{mf}^{A,B}|-\frac{1}{2}\rangle & \cdots & \cdots & \langle -\frac{3}{2}|\mathcal{H}_{mf}^{A,B}|-\frac{3}{2}\rangle \end{pmatrix} \tag{4.18}$$

Evaluating the determinant $|\hat{H}_{mf}^A - \varepsilon_n^A \hat{I}| = 0$ gives eigenvalues ε_n^A and eigenvectors $v_n^A = (a_n^A, b_n^A, c_n^A, d_n^A)$. Similarly, diagonalization of the matrix $\hat{H}_{mf}^B$ generates ε_n^B and v_n^B. These values specify the states $|n^{A,B}\rangle$, as shown in equation 4.14. The new ground states are used to recalculate the mean field spin terms $\langle \boldsymbol{T}_{00}^{A,B}\rangle$, and the process is repeated iteratively until there is convergence of all the spin terms $\langle \boldsymbol{T}^{A,B}\rangle$ to within 5%.

Calculating spin-wave excitations in the exciton model

Having determined the basis states split by the crystal field and exchange interaction, the spin-wave excitations between the four levels can be calculated using linear spin-wave theory. Pseudo-boson operators are defined that create (or annihilate) local excitations from the new ground state $|0\rangle$ to the excited states $|1\rangle$, $|2\rangle$ and $|3\rangle$. Excitations are created on the A sublattice by the pseudo-boson operators $a_n^\dagger$ and and on the B sublattice by $b_n^\dagger$. In matrix form the creation and annihilation operators $a_{i,n}^\dagger$ and $a_{i,n}$ can be represented as

$$a_{i,1}^\dagger = \begin{pmatrix} 0 & 0 & 0 & 0 \\ 1 & 0 & 0 & 0 \\ 0 & 0 & 0 & 0 \\ 0 & 0 & 0 & 0 \end{pmatrix} \quad a_{i,1} = \begin{pmatrix} 0 & 1 & 0 & 0 \\ 0 & 0 & 0 & 0 \\ 0 & 0 & 0 & 0 \\ 0 & 0 & 0 & 0 \end{pmatrix} \text{ etc. ,} \tag{4.19}$$

and $b_{i,n}^\dagger$ and $b_{i,n}$ can be written similarly. The spin-operators can be expressed in terms of these operators in a general form [23]: [20]

$$\boldsymbol{T}_i^A = \langle \boldsymbol{T}_{00}^A\rangle + \sum_{n=1}^{3} \left[\langle \boldsymbol{T}_{nn}^A\rangle - \langle \boldsymbol{T}_{00}^A\rangle \right] a_{i,n}^\dagger a_{i,n} + \sum_{n=1}^{3} \left[\langle \boldsymbol{T}_{n0}^A\rangle a_{i,n}^\dagger + \langle \boldsymbol{T}_{0n}^A\rangle a_{i,n} \right] \tag{4.20}$$

$$\boldsymbol{T}_i^B = \langle \boldsymbol{T}_{00}^B\rangle + \sum_{n=1}^{3} \left[\langle \boldsymbol{T}_{nn}^B\rangle - \langle \boldsymbol{T}_{00}^B\rangle \right] b_{i,n}^\dagger b_{i,n} + \sum_{n=1}^{3} \left[\langle \boldsymbol{T}_{n0}^B\rangle b_{i,n}^\dagger + \langle \boldsymbol{T}_{0n}^B\rangle b_{i,n} \right] ,$$

where the matrix elements $\langle \boldsymbol{T}_{nm}^{A,B}\rangle$ are defined by eqn. 4.17.

The mean field Hamiltonians have been solved to give energy levels ε_n^A and ε_n^B, and we can now write

$$\sum_i \left\{ \mathcal{H}_{mf}^A(i) + \mathcal{H}_{mf}^B(i) \right\} = \sum_i \sum_{n=0}^{3} \varepsilon_n^A a_{i,n}^\dagger a_{i,n} + \varepsilon_n^B b_{i,n}^\dagger b_{i,n} , \tag{4.21}$$

---

[20]This expression is approximate, and neglects excitations from levels other than the ground-state. It is justified if the ground state is significantly separated from other levels.

in terms of the pseudo-boson operators $a_n^\dagger$ and $b_n^\dagger$ that create excitations to energy levels ε_n^A or ε_n^B respectively. By substituting this expression into the original Hamiltonian (eqn. 4.15) we can rewrite it as

$$
\begin{aligned}
\mathcal{H} = \quad & \sum_i \Big\{ \sum_{n=0}^3 \varepsilon_n^A a_{i,n}^\dagger a_{i,n} + \varepsilon_n^B b_{i,n}^\dagger b_{i,n} \\
& + \sum_\Delta \tfrac{J}{2} \left(\boldsymbol{T}_i^A \cdot \boldsymbol{T}_{i+\Delta}^B + \boldsymbol{T}_i^B \cdot \boldsymbol{T}_{i+\Delta}^A \right) \\
& - z_0 J \langle \boldsymbol{T}_{00}^B \rangle \cdot \boldsymbol{T}_i^A - z_0 J \langle \boldsymbol{T}_{00}^A \rangle \cdot \boldsymbol{T}_i^B \Big\} \quad .
\end{aligned}
\tag{4.22}
$$

The Hamiltonian above is then rewritten in terms of Bose operators using eqn. 4.20, neglecting terms higher than second order. Solving this full Hamiltonian would require diagonalization of a 16×16 matrix. In order to reduce the problem to a 4×4 matrix we neglect terms that mix different excited states (products of Bose operators such as $a_{i,n}^\dagger a_{i,m}$ with $n \neq m$). This is justified if the ground state is significantly separated from higher levels. Making this approximation allows each excitation to be calculated independently, by writing the Hamiltonian as a sum of three Hamiltonians for excitations to each of the three excited states:

$$
\mathcal{H} = \sum_{n=1}^3 \mathcal{H}_n = \sum_{n=1}^3 \sum_{\boldsymbol{Q}} X_n^\dagger(\boldsymbol{Q}) H_n(\boldsymbol{Q}) X_n(\boldsymbol{Q}) \ ,
\tag{4.23}
$$

where $X_n^\dagger$ is the column vector $(a_{\boldsymbol{Q}}, b_{\boldsymbol{Q}}, a_{-\boldsymbol{Q}}^\dagger, b_{-\boldsymbol{Q}}^\dagger)$, and the matrices $H_n(\boldsymbol{Q})$ can each be written in the general form as before:

$$
H_n(\boldsymbol{Q}) = \frac{1}{2} \begin{pmatrix} A_n(\boldsymbol{Q}) & B_n(\boldsymbol{Q}) & C_n(\boldsymbol{Q}) & D_n(\boldsymbol{Q}) \\ B_n(\boldsymbol{Q}) & A_n(\boldsymbol{Q}) & D_n(\boldsymbol{Q}) & C_n(\boldsymbol{Q}) \\ C_n(\boldsymbol{Q}) & D_n(\boldsymbol{Q}) & A_n(\boldsymbol{Q}) & B_n(\boldsymbol{Q}) \\ D_n(\boldsymbol{Q}) & C_n(\boldsymbol{Q}) & B_n(\boldsymbol{Q}) & A_n(\boldsymbol{Q}) \end{pmatrix} \ .
\tag{4.24}
$$

In the exciton model the elements of this matrix are given by

$$
\begin{aligned}
A_n(\boldsymbol{Q}) &= (\varepsilon_n^A - \varepsilon_0^A) = (\varepsilon_n^B - \varepsilon_0^B) \\
B_n(\boldsymbol{Q}) &= 2J[\cos(4\pi h) + \cos(4\pi k)] \langle \boldsymbol{T}_{n0}^A \rangle \langle \boldsymbol{T}_{0n}^B \rangle \\
C_n(\boldsymbol{Q}) &= 0 \\
D_n(\boldsymbol{Q}) &= 2J[\cos(4\pi h) + \cos(4\pi k)] \langle \boldsymbol{T}_{n0}^A \rangle \langle \boldsymbol{T}_{n0}^B \rangle \ ,
\end{aligned}
\tag{4.25}
$$

where $\boldsymbol{Q} = (h, k, l)$. The solution for the Hamiltonian in this form is outlined in appendix B, and leads to two non-degenerate modes for excitations to each level n:

$$
\hbar \omega_n(\boldsymbol{Q}) = \left[(A_n(\boldsymbol{Q}) \pm B_n(\boldsymbol{Q}))^2 - (D_n(\boldsymbol{Q}))^2 \right]^{1/2}
\tag{4.26}
$$

The intensities of each mode are calculated as described in appendix B, with the element $S^{\alpha\alpha}$ defined in terms of the true spin operators $\boldsymbol{T}$:

$$
S_n^{\alpha\alpha}(\boldsymbol{Q}, \omega) = \sum_{\boldsymbol{Q}'} \left| \langle \lambda_{n,\boldsymbol{Q}'} | T_n^\alpha(\boldsymbol{Q}) | 0 \rangle \right|^2 \delta(\hbar\omega - \hbar\omega_{n,\boldsymbol{Q}'}) \ .
\tag{4.27}
$$
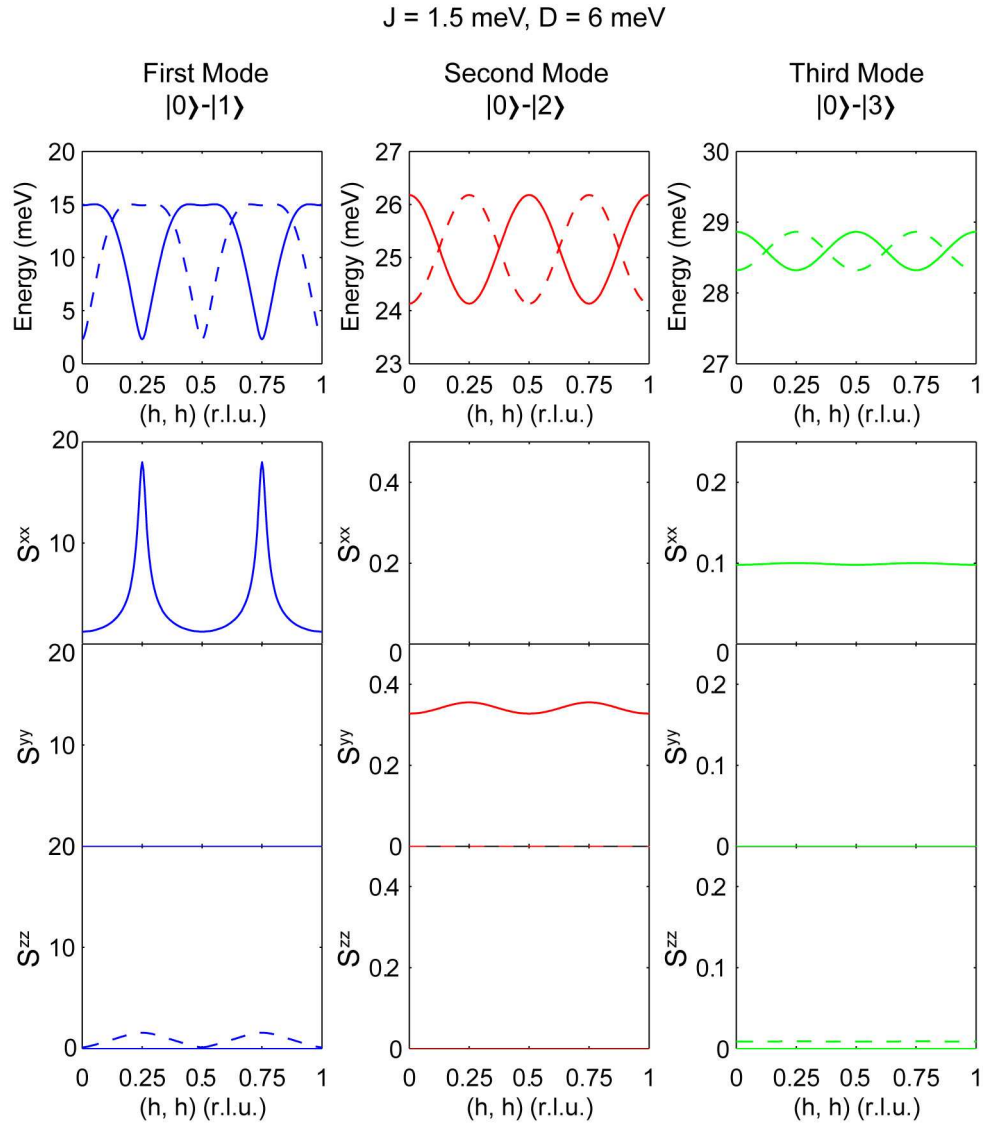
Figure 4.21: Spin-wave dispersion calculated from exciton model with parameters J and D as marked. The top row shows excitations from the ground state to levels $|1\rangle$, $|2\rangle$ and $|3\rangle$ from left to right. The two modes given by eqn. 4.26 are shown as solid and dashed lines. $S^{xx}(\boldsymbol{Q},\omega)$, $S^{yy}(\boldsymbol{Q},\omega)$ and $S^{zz}(\boldsymbol{Q},\omega)$ are plotted below for each mode (solid or dashed relating to the mode with the same line-style).

Figure 4.21 shows the results of the exciton model calculation, with example parameter values of $J = 1.5$ and $D = 6$. Excitations from the ground-state $|0\rangle$ to the three excited levels $|1\rangle$, $|2\rangle$ and $|3\rangle$ are shown from left to right. The two modes of the dispersion relation given by eqn. 4.26 are plotted as solid and dashed lines,

with the $S^{xx}(\boldsymbol{Q}, \omega)$, $S^{yy}(\boldsymbol{Q}, \omega)$ and $S^{zz}(\boldsymbol{Q}, \omega)$ functions plotted below in the linestyle corresponding to each mode.

We first consider the lower modes. The two lower modes show the right periodicity, with most of the intensity in the mode arising from the zone centres at (0.25, 0.25) *etc.*, and we note that to achieve this it is still necessary to use a large value of D, the out-of-plane anisotropy parameter. We should also point out that these plots have the in-plane anisotropy parameter E set to zero. The effect of increasing E is to raise the solid mode at the zone centres ((0.25, 0.25) *etc.*), and the dashed mode at the zone boundaries ((0.5, 0.5) *etc.*). With E set to zero we expect the modes to be gapless at these points, since gaps at these points should not be generated from the out-of-plane anisotropy term, but this is shown not to be the case. One possible explanation is that the gap is generated from the omission of terms mixing between excited states, but this is not certain, and the full 16×16 Hamiltonian would need to be solved to check this.

The excitations to levels $|2\rangle$ and $|3\rangle$, shown in the centre and right hand columns of fig. 4.21 produce modes in the right region to describe the upper mode seen in the data (see section 4.5.2). In both cases only one of the two modes has intensity, and the intensities of these higher modes are relatively flat over the Brillouin zone, and are approximately two orders of magnitude lower than that of the lower dispersion at the zone centre.

Fitting the exciton model to the observed dispersion

To achieve a better comparison between the model and data the lower mode of the dispersion calculated from the exciton model was fitted to data points taken from fits of constant-energy and constant-$\boldsymbol{Q}$ cuts through MAPS data, as shown in figure 4.15, along several symmetry directions simultaneously. Only the lower mode was fitted, since the higher mode in the data is too diffuse to extract points in the same manner, and only the dispersion relation was fitted (not the intensities). The fitting was performed by iteratively recalculating the basis states, as described above, each time the parameters J and D were varied, to find the best fit. The final values were $J = 1.41 \pm 0.02$ meV and $D = 7.3 \pm 0.4$ meV. It was not possible to fit the value for the in-plane anisotropy E since the model with $E = 0$ already produces gaps at the magnetic zone centres, as discussed earlier.

The basis states corresponding to the final J and D values are shown in table 4.4, bottom row (for comparison we also show basis states achieved for exchange interaction only ($D = 0$), and for crystal-field only ($J = 0$).) The ground state for the fitted values of $J = 1.4$ meV and $D = 7.3$ meV is mostly $|+\frac{3}{2}\rangle$ [21] but, there is some mixing. Figure 4.22 shows the results of the fit with these parameters, plotted along three symmetry directions within the first Brillouin zone, along with data points extracted from fits of constant-energy and constant-$\boldsymbol{Q}$ cuts through the MAPS data. Below this is a plot of the intensities calculated with these fitted values [22], scaled to

---

[21] In fact the ground state is mostly $|+\frac{3}{2}\rangle$ for sublattice A and $|-\frac{3}{2}\rangle$ for sublattice B since the spins point in opposite directions on the two sublattices.

[22] These intensities are simply the sum of S^{xx}, S^{yy} and S^{zz}. The full formula for the intensity

J (meV)	D (meV)	n	ε_n (meV)	$\lvert n, A\rangle$	$\lvert n, B\rangle$
1	0	0	0	$\lvert+\tfrac{3}{2}\rangle$	$\lvert-\tfrac{3}{2}\rangle$
		1	6.0	$\lvert+\tfrac{1}{2}\rangle$	$\lvert-\tfrac{1}{2}\rangle$
		2	12.0	$\lvert-\tfrac{1}{2}\rangle$	$\lvert+\tfrac{1}{2}\rangle$
		3	18.0	$\lvert-\tfrac{3}{2}\rangle$	$\lvert+\tfrac{3}{2}\rangle$
0	1	0,1	0	$+\frac{\sqrt{3}}{2}\lvert+\tfrac{3}{2}\rangle - \tfrac{1}{2}\lvert-\tfrac{1}{2}\rangle$ $-\frac{\sqrt{3}}{2}\lvert-\tfrac{3}{2}\rangle + \tfrac{1}{2}\lvert+\tfrac{1}{2}\rangle$	$+\frac{\sqrt{3}}{2}\lvert+\tfrac{3}{2}\rangle - \tfrac{1}{2}\lvert-\tfrac{1}{2}\rangle$ $-\frac{\sqrt{3}}{2}\lvert-\tfrac{3}{2}\rangle + \tfrac{1}{2}\lvert+\tfrac{1}{2}\rangle$
		2,3	2	$+\frac{\sqrt{3}}{2}\lvert+\tfrac{1}{2}\rangle + \tfrac{1}{2}\lvert-\tfrac{3}{2}\rangle$ $-\frac{\sqrt{3}}{2}\lvert-\tfrac{1}{2}\rangle - \tfrac{1}{2}\lvert+\tfrac{3}{2}\rangle$	$+\frac{\sqrt{3}}{2}\lvert+\tfrac{1}{2}\rangle + \tfrac{1}{2}\lvert-\tfrac{3}{2}\rangle$ $-\frac{\sqrt{3}}{2}\lvert-\tfrac{1}{2}\rangle - \tfrac{1}{2}\lvert+\tfrac{3}{2}\rangle$
1.41	7.33	0	0	$+0.97\lvert+\tfrac{3}{2}\rangle - 0.25\lvert-\tfrac{1}{2}\rangle$	$-0.97\lvert-\tfrac{3}{2}\rangle + 0.25\lvert+\tfrac{1}{2}\rangle$
		1	13.2	$+0.88\lvert+\tfrac{1}{2}\rangle - 0.48\lvert-\tfrac{3}{2}\rangle$	$-0.88\lvert-\tfrac{1}{2}\rangle + 0.48\lvert+\tfrac{3}{2}\rangle$
		2	20.1	$-0.97\lvert-\tfrac{1}{2}\rangle - 0.25\lvert+\tfrac{3}{2}\rangle$	$+0.97\lvert+\tfrac{1}{2}\rangle + 0.25\lvert-\tfrac{3}{2}\rangle$
		3	26.3	$+0.88\lvert-\tfrac{3}{2}\rangle + 0.48\lvert+\tfrac{1}{2}\rangle$	$-0.88\lvert+\tfrac{3}{2}\rangle - 0.48\lvert-\tfrac{1}{2}\rangle$

Table 4.4: Basis states calculated as described in section 4.6.2, for three sets of J, D values.

match the data points. The fitted dispersion provides a good description of the lower mode, including the $\boldsymbol{Q}$-dependence of the intensities.

Although the higher mode was not including in the fit, fixing the values of J and D from the lower mode fit fully specifies the upper mode dispersions, and the intensities of all modes. These are also plotted in fig. 4.22. It is clear that this model can produce a mode in the right region in $\boldsymbol{Q}$–energy space. Since the upper mode in the data is very diffuse and much weaker than the lower mode it is difficult to compare the dispersions.

As a further comparison between model and data the intensity for each point in the MAPS data set was calculated, including the magnetic form factor, orientation factor and twinned domains, using the fitted values $J = 1.41$ meV and $D = 7.3$ meV. This resulted in a simulated MAPS data set from which slices could be taken to compare directly with slices through the experimental data. In the simulation broadening was simulated using a Gaussian broadening of the dispersion relation in energy, with width set to 2 meV to give agreement with the lower mode.

(see appendix B), including form factor and orientation factor is employed for the simulations in fig. 4.23 and fig. 4.24.

Figure 4.23 displays slices through the simulated data set which can be compared directly with the slices though the experimental data set shown in fig. 4.13. These slices compare the lower mode simulated using the model with the measured intensities. The model gives good agreement with the experimental data. Figure 4.24 plots two slices though the simulated data set displaying the higher mode, which can be compared directly with fig. 4.17(a,b). The slice through the top of the mode (fig. 4.23a) does show intensity with the correct wavevector dependence. However, the simulated upper mode (which is calculated from excitations to both levels $|2\rangle$ and $|3\rangle$ in the model) is much sharper than the observed scattering. This suggests that there is some broadening mechanism that has not been considered in this model, or that some or all of the observed scattering has a different origin. For instance it is possible that there is non-magnetic scattering contaminating the magnetic signal.
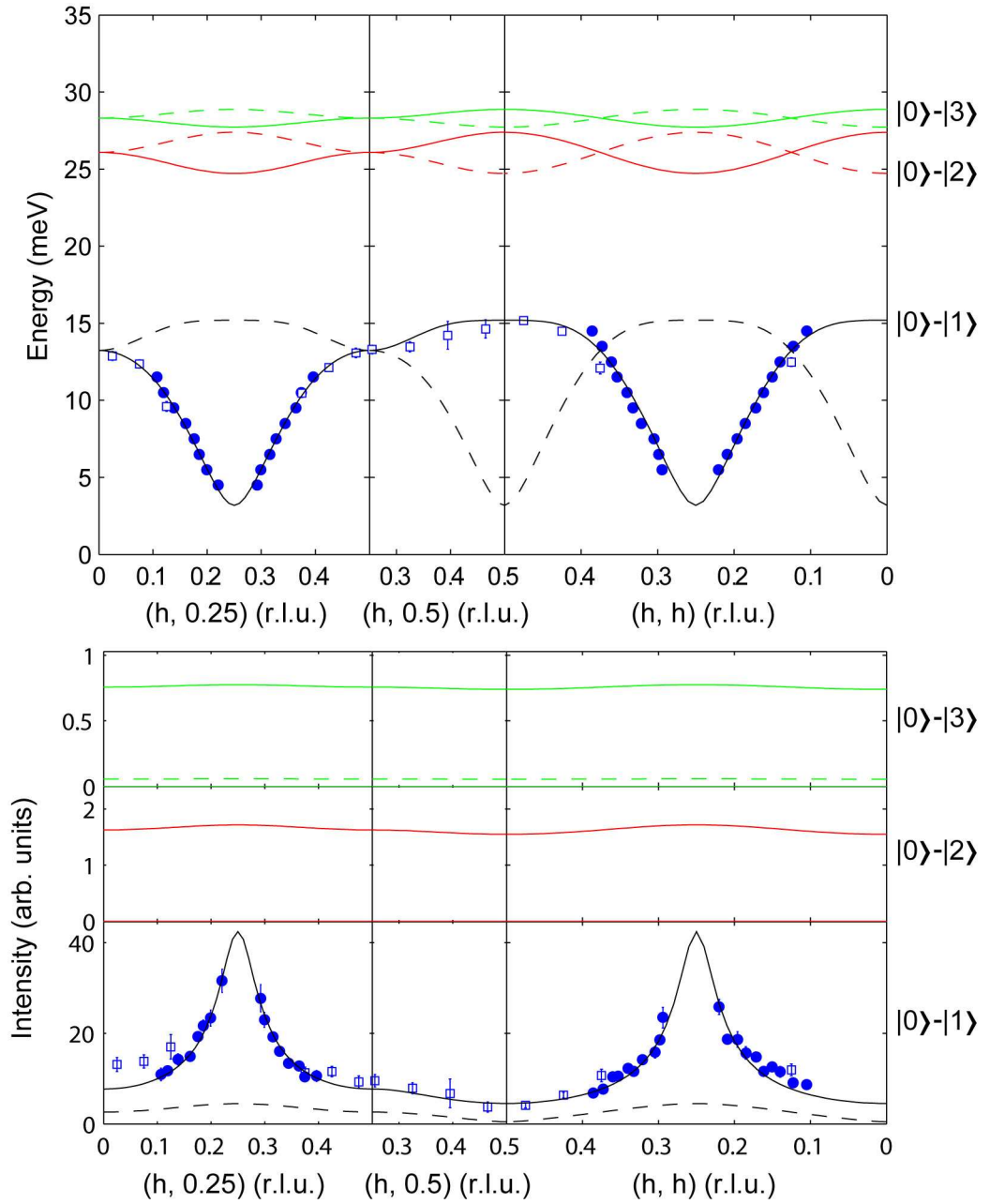
Figure 4.22: Top: Spin-wave dispersion fitted with the exciton model described in section 4.6.2, with $J = 1.4$ meV, $D = 7.3$ meV and $E = 0$ meV. Solid circles and open squares are data points taken from fits of constant-energy and constant-Q cuts through MAPS data along the symmetry directions marked, as shown in fig. 4.15. Bottom: Intensities calculated with the above parameters, scaled to match the intensity of the lower mode. Data points are extracted from the same fits of constant-energy and constant-Q cuts.
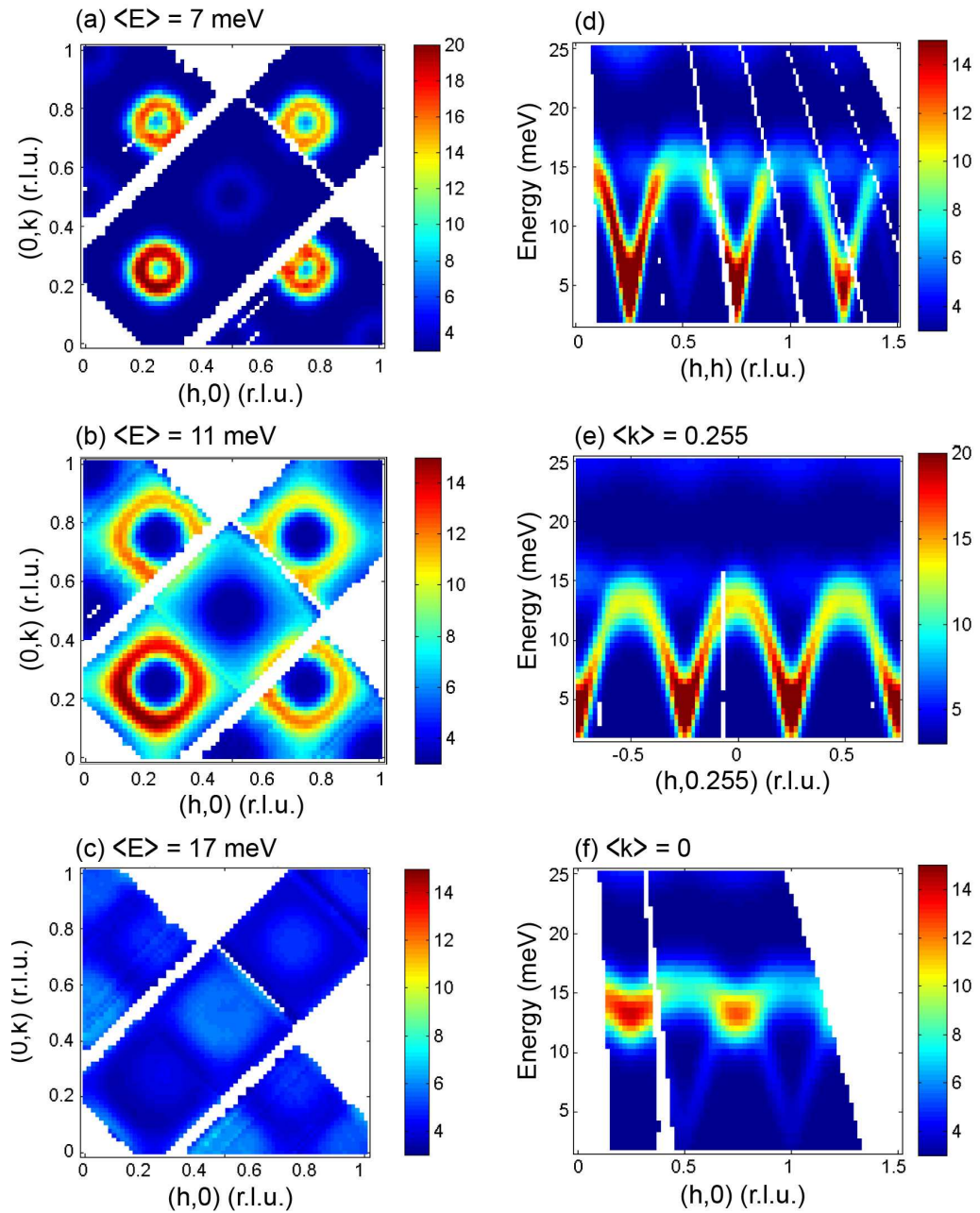
Figure 4.23: Slices through the simulated inelastic neutron scattering data set calculated with the exciton model, with $J = 1.41$ meV and $D = 7.3$ meV. (a–f) Slices showing the lower mode, directly comparable to slices through the experimental data set shown in fig. 4.13.
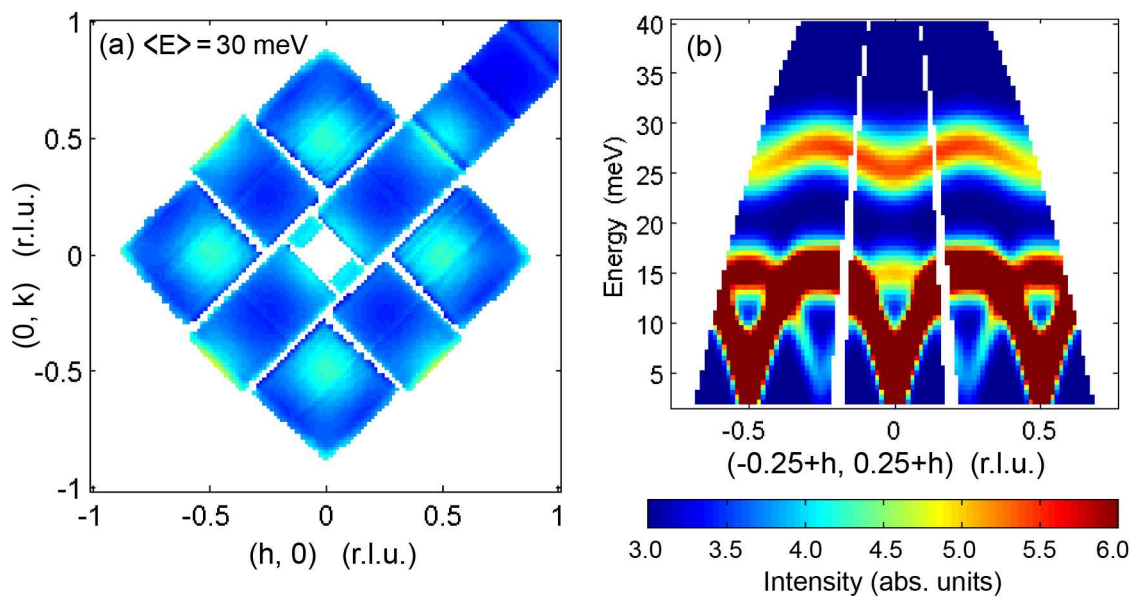
Figure 4.24: Slices through the simulated inelastic neutron scattering data set calculated with the exciton model, with $J = 1.41$ meV and $D = 7.3$ meV. (a,b) Slices showing the upper mode, directly comparable to slices through the experimental data set shown in fig. 4.17(a,b).

4.7   Discussion and Conclusions

In this chapter we have reported elastic neutron scattering measurements of the charge and magnetic order in single crystals of La$_{1.5}$Sr$_{0.5}$CoO$_4$, consistent with previous measurements. Using polarized neutron analysis we have confirmed that the magnetic moments lie within the ab plane, and revealed a spin-reorientation between 30 K and 50 K, which corresponds to a rotation of spins from 33° to 44° away from the ($1\bar{1}0$) direction in a single domain model.

The inelastic neutron scattering measurements reported in this chapter have characterized the spin-wave dispersions in La$_{1.5}$Sr$_{0.5}$CoO$_4$. We have shown that there is a two dimensional dispersive mode with a maximum energy of ~ 15 meV arising from the magnetic Bragg positions, and that this mode is gapped at the magnetic zone centres. Both above and below the gap the spin fluctuations seem to be restricted to the ab planes. Above this mode there is further magnetic scattering, between approximately 20 and 32 meV. This higher mode is much more diffuse than the lower one, but is shown to have some wavevector dependence.

To model the dispersions we first employed a simple Heisenberg Hamiltonian, based on nearest neighbouring interactions between antiferromagnetically aligned Co^{2+} ions, assuming a $S = 3/2$ ground-state. It is not possible to obtain a higher mode with this simple model. Furthermore, the periodicity of the lower mode can only be reproduced by including a large out-of-plane anisotropy term. We concluded that it is necessary to include the full spin-3/2 physics of the system, with crystal-field splitting of the ground state, in order to model the system correctly. This was achieved using a self-consistent calculation of the ground-state energy levels, including the exchange interaction as well as in-plane and out-of-plane anisotropy terms. In this model the $S = 3/2$ levels split into four levels of mixed M_S values, allowing neutron induced excitations to all three excited states. Excitations to the first excited state were found to reproduce the lower mode of the dispersion very well, and by fitting the model to the experimentally obtained dispersion relation for this mode the exchange and out-of-plane anisotropy parameters were obtained as $J = 1.41 \pm 0.02$ meV and $D = 7.3 \pm 0.4$ meV. Other possible exchange parameters were found to be unnecessary.

The parameters extracted by fitting the lower mode fully determine the upper mode dispersions in this model. We found that the modes resulting from transitions to the second and third excited states occurred at approximately the right energy, although quantitative comparisons were difficult because of the diffuse nature of the observed higher mode. The higher mode is much more diffuse than expected from simulations, which assume the same energy broadening on all modes. It is possible that there is a reason for this extra broadening within the current model, or that the extra scattering has a different origin, possibly non-magnetic. Further polarized neutron measurements are needed to investigate this.

One inconsistency in the model is that a gap is generated at the magnetic zone centres without the need to include the in-plane anisotropy term. By including only the exchange and out-of-plane anisotropy the lower mode should be gapless at the magnetic zone centre (a Goldstone mode). Inelastic polarization analysis performed

at this point above and below the gap confirmed that the gap is not an out-of-plane anisotropy gap. We do not know why the gap is generated in this model, but speculate that it stems from terms neglected in the calculation. In order to check this it would be necessary to repeat the calculation keeping the entire 16×16 matrix Hamiltonian, and avoiding the approximations. We note that the presence of a gap when only J and D are included has prevented us from fitting a value for the in-plane anisotropy parameter E, but that in-plane anisotropy clearly exists in the compound.

Although this inconsistency needs addressing, we have successfully shown that both the lower and higher mode can be generated by considering only excitations of the antiferromagnetically aligned Co^{2+} lattice. This brings us back to the question of the Co^{3+} spin state in La$_{1.5}$Sr$_{0.5}$CoO$_4$. In the introduction we discussed three possibilities for the Co^{3+} ions that would be consistent with the observed magnetic ordering. Point-charge calculations favoured the low-spin $S = 0$ state for Co^{3+}. We now consider whether the magnetic excitations can give any more clues as to the Co^{3+} spin-state. If the Co^{3+} ions carry ordered moments we would expect to see excitations arising from this sublattice. This was not the case. The only possibility for ordered Co^{3+} moments consistent with both the observed magnetic Bragg positions and the excitation spectrum is that the Co^{3+} sublattice orders with the same wavevector as the Co^{2+} sublattice, but without interactions between the two sublattices. As well as this, the exchange and anisotropy parameters for the two sublattices would have to be identical to generate the sharp lower dispersion mode that is observed. This seems unlikely. Another possibility is that the Co^{3+} ions have moments, but that the Co^{3+} sublattice is paramagnetic. The point-charge model described in the introduction suggests that in this scenario there would be many energy levels close to the Co^{3+} ground state. In this case we would expect to see a large amount of quasi-elastic scattering in the neutron scattering measurements, but again this was not seen. Although not conclusive, the excitation spectrum of La$_{1.5}$Sr$_{0.5}$CoO$_4$ does appear to be consistent with a low spin-state for Co^{3+}.

The main conclusion for this chapter is that the excitation spectrum of La$_{1.5}$Sr$_{0.5}$CoO$_4$ can be successfully modelled with a spin-only Hamiltonian for the Co^{2+} sublattice. The spin and charge ordering degrees of freedom appear to be uncoupled. As discussed in the introduction, this is not the case for other similar transition metal oxides. The isostructural nickelate compounds exhibit features that cannot be explained without coupling of spin and charge order, and complex excitation modes are observed in the cuprate compounds. La$_{1.5}$Sr$_{0.5}$CoO$_4$ is therefore an ideal system for studying uncoupled magnetic excitations. It would be interesting to investigate other compounds in the La$_{2-x}$Sr$_x$CoO$_4$ family to see if this behaviour extends to other doping levels or is a feature of the stability of the checkerboard charge ordering.

References

[1] K. Yamada, M. Matsuda, Y. Endoh, B. Keimer, R. J. Birgeneau, S. Onodera, J. Mizusaki, T. Matsuura and G. Shirane, Phys. Rev. B **39**, 2336 (1989).

[2] I. A. Zaliznyak, J. M. Tranquada, R. Erwin and Y. Moritomo, Phys. Rev. Lett. **85**, 4353 (2000).

[3] I. A. Zaliznyak, J. P. Hill, J. M. Tranquada, R. Erwin and Y. Moritomo, Phys. Rev. B **64**, 195117 (2001).

[4] Y. Moritomo, K. Higashi, K. Matsuda and A. Nakamura, Phys. Rev. B **55** R14725 (1997).

[5] B. J. Sternlieb, J. P. Hill, U. C. Wildgruber, G. M. Luke, B. Nachumi, Y. Moritomo and Y. Tokura, Phys. Rev. Lett. **76**, 2169 (1995).

[6] R. Kajimoto, K. Ishizaka, H. Yoshizawa, and Y. Tokura, Phys. Rev. B **67**, 014511 (2003).

[7] I. A. Zaliznyak, J. M. Tranquada, G. Gu, R. W. Irwin and Y. Moritomo, J. Appl. Phys. **95**, 7369 (2004).

[8] P. G. Freeman, A. T. Boothroyd, D. Prabhakaran, C. D. Frost, M. Enderle and A. Hiess, Phys. Rev. B **71**, 174412 (2005).

[9] S. B. Wilkins, P. D. Spencer, P. D. Hatton, S. P. Collins, M. D. Roper, D. Prabhakaran and A. T. Boothroyd, Phys. Rev. Lett. **91**, 167205 (2003).

[10] D. Senff, F. Krüger, S. Scheidl, M Benomar, Y. Sidis, F. Demmel and M. Braden, Phys. Rev. Lett. **96**, 257201 (2006).

[11] See for example: M. Abbate, J. C. Fuggle, A. Fujimori, L. H. Tjeng, C. T. Chen, R. Potze, G. A. Sawatzky, H. Eisaki and S. Uchida, Phys. Rev. B **47**, 16124 (1993), and references contained therin.

[12] M. Itoh, M. Mori, Y. Moritomo and A. Nakamura, Physica B **259-261**, 997 (1999).

[13] A. Abragam and B. Bleaney, *Electron Paramagnetic Resonance of Transition Ions* (Dover Pulications, Inc., New York, U.S.A., 1986).

[14] P. G. Freeman, *Magnetism and the Magnetic Excitations of Charge Ordered La$_{2-x}$Sr$_x$NiO$_{4+\delta}$*, D.Phil Thesis, University of Oxford (2005).

[15] See the GSAS manual:
http://www.ncnr.nist.gov/programs/crystallography/software/gsas.html

[16] R. Le Toquin, W. Paulus, A. Cousson, G. Dhalenne and A. Revcolevschi, Physica B **350**, e269 (2004).

[17] J. D. Jorgensen, B. Dabrowski, Shiyou Pei, D. R. Richard and D. G. Hinks, Phys. Rev. B **40**, 2187 (1989).

[18] Private communications with D. Prabhakaran.

[19] P. Wochner, J. M. Tranquada, D. J. Buttrey and V. Sachan, Phys. Rev. B **57**, 1066 (1998).

[20] P.G. Freeman, A.T. Boothroyd, D. Prabhakaran, D. Gonzalez, and M. Enderle, Phys. Rev. B **66**, 212405 (2002).

[21] M. A. Kastner, R. J. Birgeneau, G. Shirane and Y. Endoh, Rev. Mod. Phys. **70**, 897 (1998).

[22] K. Yamada, M. Matsuda, Y. Endoh, B. Keimer, R. J. Birgeneau and S. Onodera, Phys. Rev. B **39**, 2336 (1989).

[23] S. J. Allen, Jr. and H. J. Guggenheim, Phys. Rev. B **4**, 950 (1971); C. J. Mukherjee, *Neutron Scattering Studies on Low-Dimensional Quantum Magnets*, D.Phil Thesis, University of Oxford (2005).

CHAPTER 5

Magnetic Excitations in Metallic Na$_x$CoO$_2$

5.1 Introduction

Na$_x$CoO$_2$ is a layered transition metal oxide which is composed of layers of CoO$_2$ spaced with layers of sodium, see fig. 5.1. The crystal structure is hexagonal, so the cobalt ions form a two-dimensional triangular lattice within the ab planes, each surrounded by an octahedron of oxygen atoms. Na$_x$CoO$_2$ is metallic [1], and the metallic behaviour is achieved by doping the Mott-insulating CoO$_2$ layers with electrons donated by sodium atoms. The exception is at $x = 0.5$ where an insulating state exists. Each cobalt ion has an average charge Co$^{(4-x)+}$, and in an ionic picture this corresponds to x non-magnetic Co^{3+} ions (with $S = 0$) in a background of Co^{4+} ions carrying spin $S = 1/2$. The sodium ions are mobile, and for many doping levels they order into ion-vacancy superlattices at around room temperature [2]. A current unresolved issue is whether the ordering of the Na$^+$ ions causes a spatial
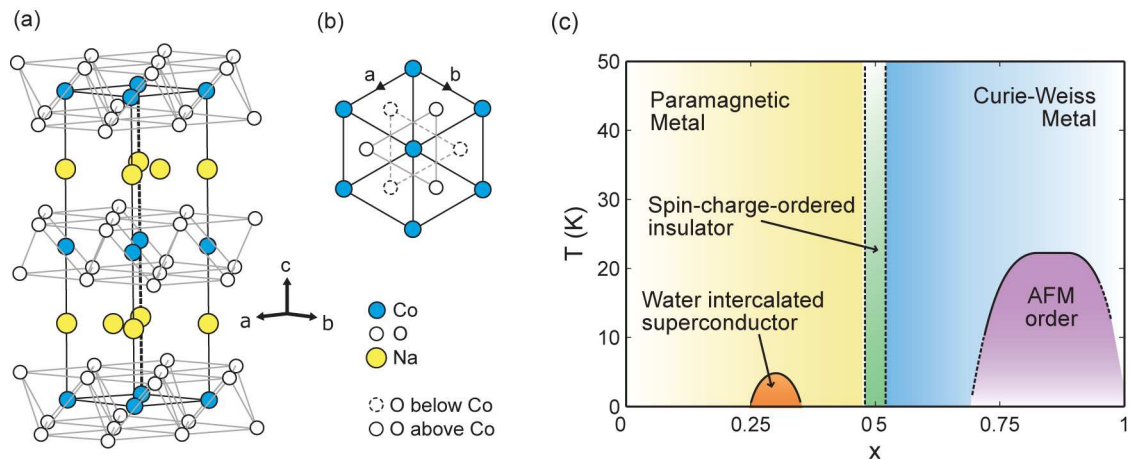
Figure 5.1: (a) Crystal structure of Na$_x$CoO$_2$: CoO$_2$ layers are spaced by Na. (b) The hexagonal lattice of Co in the a–b planes, showing the orientation of the oxygen tetrahedron around the central Co ion. (c) The phase diagram of Na$_x$CoO$_2$.
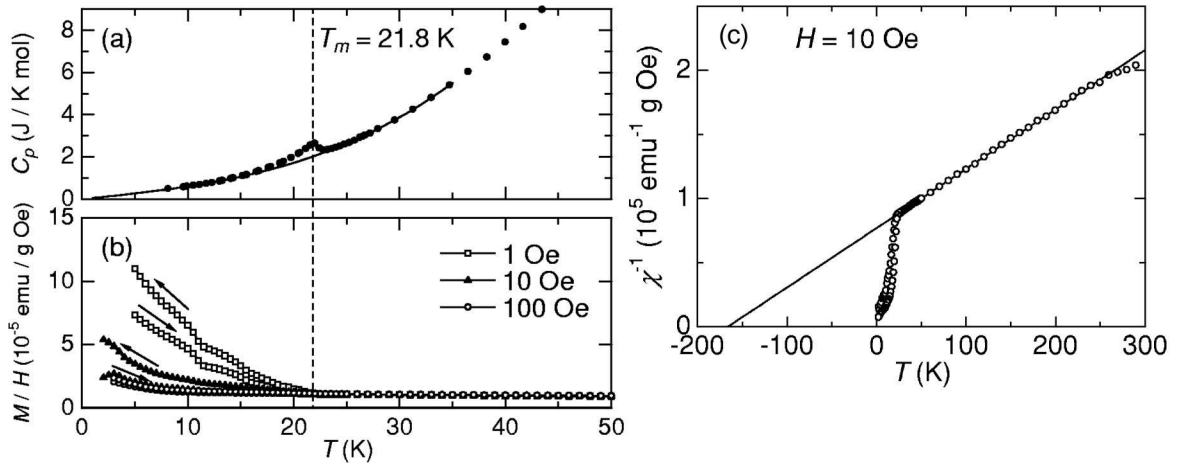
Figure 5.2: Temperature dependences of bulk properties of polycrystalline Na$_{0.75}$CoO$_2$ measured by Motohashi *et al.* [12]. (a) Specific heat (C_p), (b) magnetic susceptibility ($\chi = M/H$), (c) inverse susceptibility (χ^{-1}). The solid line shows the best fit to the Curie-Weiss law above $T_m = 22$ K.

disproportionation of charge on the Co layer, *i.e.* whether it drives ordering of the Co^{3+}/Co^{4+} charges through the Coulomb interaction. Density function (LDA) calculations for $0.3 \leq x \leq 0.7$ found that the electronic structure is highly two-dimensional, and suggested a weak itinerant ferromagnetic ground state [3].

In chapter 2 we discussed the renewed interest in sodium cobaltate precipitated by the recent discovery of superconductivity in the hydrated compound (Na$_x$CoO$_2$ · yH$_2$O, $x \approx 0.3$, $y \approx 1.3$) [4]. Much of the discussion is focussed on the mechanism of superconductivity. There is strong support from both experiment [5] and theory [6, 7] for an unconventional pairing state, the origin of which derives from the triangular geometry of the Co lattice and the existence of strong spin and charge fluctuations.

Before the discovery of a superconducting phase, the unhydrated parent compound Na$_x$CoO$_2$ was already attracting interest due to its large thermopower coupled with low resistivity, making it a promising candidate for technological applications [8]. The large thermoelectric effect has been observed in the sodium doping range $0.5 \leq x \leq 0.9$ [8, 9]. Both the thermopower and resistivity were found to be highly dependent on the doping level [10], with thermopower increasing at higher values of x. A recent investigation into the enhanced thermopower found evidence to show that it originates from a large spin-entropy due to strong electron correlations in the CoO$_2$ layers [11].

The importance of the spin degrees of freedom, both to explain the large thermoelectric effect, and to aid discrimination between proposed mechanisms of superconductivity, provides a strong incentive for characterizing the magnetic order and excitations of Na$_x$CoO$_2$. This chapter and the following chapter are concerned

with the weakly magnetic phase found for $x \approx 0.7-0.95$. Although the sodium doping value x in this region is very different from the superconducting value ($x \sim 0.3$), there is experimental evidence to suggest that the Co valence in the hydrated superconductor in fact corresponds to $x \approx 0.6$ - 0.75, due to the presence of H$_3$O$^+$ ions. The magnetic phase studied here may therefore represent the true 'parent' of the superconducting phase, and the magnetic order in this phase may have real relevance to the mechanism of superconductivity.

In the $x \approx 0.7-0.95$ region, the susceptibility data shows a sharp magnetic transition which occurs at $T_m \approx 22$ K [12, 13], first observed in Na$_{0.75}$CoO$_2$ by Motohashi *et al.* whose data is reproduced in figure 5.2. The magnetic transition is seen as an upturn in the low temperature susceptibility, and a sharp jump in the specific heat data. A Curie-Weiss fit to the high temperature susceptibility (fig. 5.2c) gives a negative value for the Curie-Weiss constant, which is indicative of antiferromagnetic interactions. Further information is gained from magnetization measurements of single crystals. Figure 5.3 shows magnetization measurements made by D. Prabhakaran on a single crystal of Na$_{0.7}$CoO$_2$ [13], and we note the main

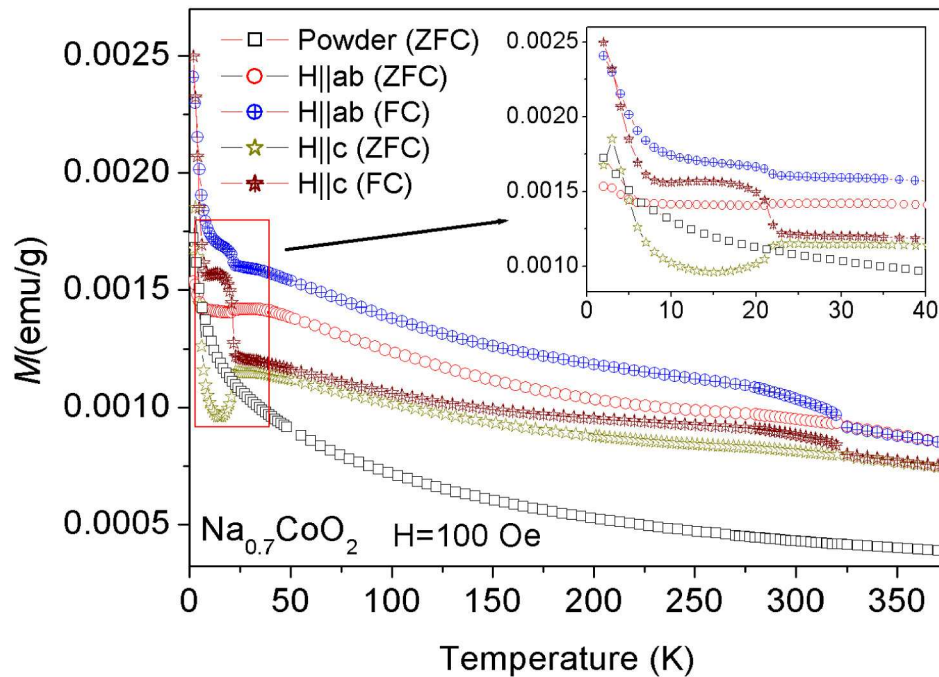**Figure 5.3**: Temperature dependence of the dc magnetization of a single crystal of Na$_{0.7}$CoO$_2$ measured with $H \parallel ab$ and $H \parallel c$, and both zero-field cooled (ZFC) and field cooled (FC). There are transitions at $T_m \approx 22$ K and around room temperature (270K and 320K). The inset illustrates the sharp transition at 22 K, and the steep rise below 8 K. Data measured by D. Prabhakaran [13].

features:

- The $H \parallel ab$ magnetizations are consistently larger than $H \parallel c$, until the curves cross over below ~ 7 K. This suggests that the ab plane is the easy direction for magnetic moments for $T > 7$ K.

- The features at $T \sim 300$ K correspond to sodium ordering temperatures, revealing that the sodium order does have some effect on the magnetic order.

- The magnetic transition at $T_m \approx 22$ K is marked by a dramatic change in gradient in the magnetization parallel to c. This suggests that the magnetic ordering below T_m has ordered moments along c.

There is a conflict between the first and last points made above. Measurements performed using μSR also revealed static order below $T_m \approx 22$ K in Na$_{0.75}$CoO$_2$ [14], and estimated a magnetic moment of $\sim 0.18\mu_B$ per Co at 2.5 K. The μSR measurements also concluded that the magnetic moments point along the c-axis in the ordered phase [15], in conflict with the single crystal magnetization measurements.

In order to consolidate these pieces of experimental evidence, to determine the magnetic ground state below T_m and to gain information on the magnetic correlations, the most direct experimental method is neutron scattering. This chapter presents inelastic neutron scattering measurements made on single crystals of Na$_x$CoO$_2$ with $x \approx 0.75$. The magnetic excitations observed are consistent with an A-type antiferromagnetically ordered ground state, with ferromagnetic alignment within the ab plane and antiferromagnetic alignment between planes. By modelling the excitations with a linear spin-wave model we go on to extract magnetic exchange parameters, and to gain information on the anisotropy in the compound.

Sample characterization

Before presenting the results we briefly discuss the samples that were studied, both in this chapter and in chapter 6. All the neutron scattering measurements were made on single crystals of Na$_x$CoO$_2$, which are notoriously difficult to grow. They were grown by D. Prabhakaran, as described in reference [13]. The crystals studied in this chapter were nominally $x = 0.75$, while the one studied in chapter 6 was nominally $x = 0.85$. The nominal values are those calculated from the starting materials, which should give a good indication of the final doping. The samples were characterized by magnetization studies, and the presence of the $T_m \sim 22$ K transition confirmed that they lie in the $x \approx 0.7 - 0.95$ phase.

Recent electron probe micro-analysis (EPMA) measurements on one of the $x = 0.75$ samples, and the $x = 0.85$ sample, gave values of $x_E = 0.79 \pm 0.03$ and $x_E = 0.80 \pm 0.03$ respectively, where the errors are calculated from variation of the result between measurements over an area of the sample surface.[1] There may

---

[1]The measurements were made on small single crystals taken from the same zone-melted rods from which the neutron scattering samples were cleaved.

therefore not be as much difference between the samples studied in the two chapters as is suggested by the nominal doping values. However, EPMA is a surface probe, and there may be differences in sodium doping on the surface, so we do not rely too heavily on these values of x. We therefore use the nominal values of x when referring to Na$_x$CoO$_2$ samples throughout the thesis.

The EPMA measurements were performed by N. R. Charnley, and a description of the method is given in reference [13].

5.2   Measurement of Excitations in $Na_{0.75}CoO_2$

In this section we describe inelastic neutron scattering measurements made to characterize the spin excitations in single crystals of $Na_{0.75}CoO_2$. Usually the magnetic structure of a system is established before embarking on measurements of its magnetic excitations, giving a good indication of where to look for excitations in reciprocal space. However, the magnetic structure of sodium cobaltate was not known when we began investigations into the magnetic excitations of $Na_{0.75}CoO_2$. For this reason the first measurements were made on the MAPS spectrometer at the ISIS facility. The MAPS spectrometer is a time-of-flight instrument equipped with a large pixellated detector, and provided a good overview of a large area of reciprocal space in one measurement. Having determined the wavevectors of the excitations, this study was followed up by measurements made on the triple-axis spectrometers IN8 and IN20 at the Institut Laue-Langevin (ILL), which allowed more precise characterization of the excitations perpendicular to the *ab*-planes. Details of the instruments are given in chapter 2.

The MAPS results were first published in reference [16], and the preliminary analysis presented there was performed by R. Coldea. Subsequent analysis performed as part of this thesis, including analysis of the triple-axis data and further analysis of the MAPS data, has been published in references [17] and [18].

5.2.1   MAPS Measurements

Experimental details

A single crystal of $Na_{0.75}CoO_2$ was grown by the floating-zone method in the Clarendon laboratory image furnace by D. Prabhakaran [13]. A crystal of size $\sim 10 \times 8 \times 3$ mm^3 and mass 1.25 g was cleaved from the zone-melted rod. Samples were taken from adjacent parts of the same rod for magnetization and powder X-ray diffraction measurements and showed no impurity phases within the detectable limit of $\sim 2\%$.

The crystal was attached to a copper rod using a small amount of G.E. varnish, copper foil and copper wire, so that the (001) and (100) reciprocal lattice vectors defined the horizontal scattering plane, see fig. 5.4. The top of the copper rod was painted with gadolinium paint, which shields against neutrons, to reduce background scattering from the copper. The sample was then mounted on a closed-cycle cooler to allow measurements to be performed at temperatures between 6 K and room temperature. Counting times were typically ~ 36 hours at an average proton current of 170 μA. An initial examination by neutron Laue diffraction showed that the crystal contained several grains with an overall mosaic spread of $\sim 10°$.

MAPS is a time-of-flight chopper spectrometer equipped with a large pixellated detector array covering 20 m^2. Chopper spectrometers are described in chapter 3, where there is also a drawing of the MAPS spectrometer (fig. 2.3). To maintain good $\boldsymbol{Q}$ resolution relatively low incident energies ($E_i = 40$ meV and 60 meV) were employed, and the measurements were restricted to small scattering angles.
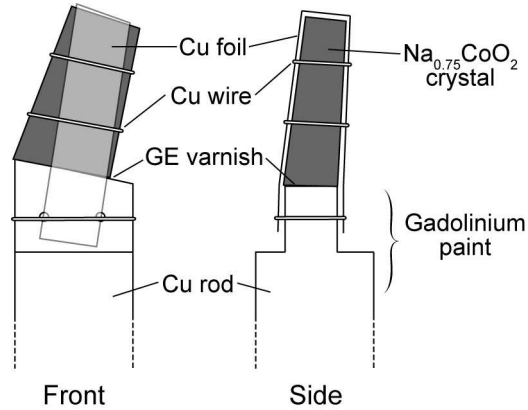
Figure 5.4: Diagram of the $Na_{0.75}CoO_2$ sample mounted for the experiment on MAPS. The c axis is perpendicular to the face shown on the left ('Front').

Measurements and results

It was initially assumed that the magnetic correlations between the CoO_2 layers would be weak, given the highly two-dimensional (2D) physical properties of Na_xCoO_2, and so likely that the magnetic scattering would be relatively insensitive to the component of $\boldsymbol{Q}$ parallel to the crystal c axis. Therefore, for an initial survey, the crystal was aligned with the c axis parallel to the incident neutron beam. In this configuration the area detector recorded the energy spectrum over a large region of 2D reciprocal space (defined by the $\boldsymbol{a}^*$ and $\boldsymbol{b}^*$ reciprocal lattice basis vectors of the triangular lattice in the CoO_2 plane). Measurements were made in this orientation with an incident energy of 40 meV at two temperatures, room temperature and 6 K. By taking a series of constant energy slices of the 6 K data we made a search of $(\boldsymbol{Q}_{2D}, E)$ space, where $\boldsymbol{Q}_{2D} = h\boldsymbol{a}^* + k\boldsymbol{b}^* \equiv (h, k)$ is the in-plane component of the scattering vector. The only signal we found that was clearly in excess of the background in this energy range was distributed symmetrically around the unscattered beam, i.e. $\boldsymbol{Q}_{2D} = (0,0)$. In particular there was no observable signal at wave vectors corresponding to antiferromagnetic correlations between adjacent Co sites. The signal seen at 6 K was found not to be present in the room temperature measurement, indicating that it is magnetic in origin.

Figure 5.5 shows the signal at 6 K. The intensity has been averaged over the energy range 8-12 meV and projected onto the a^*b^* plane. The crystal orientation with c parallel to $\boldsymbol{k}_i$ means that the region of interest around $\boldsymbol{Q}_{2D} = (0,0)$ lies along the direction of the unscattered beam, where there is a gap in the detector bank. In this orientation much of the signal is lost in the gap, and there is the possibility that the scattering is a detector-edge effect and not real. Therefore, to investigate the signal further, the crystal was rotated by 30° so that more of the scattering would be recorded in the detector bank adjacent to the unscattered beam. Again,

Figure 5.5: Neutron inelastic scattering from $Na_{0.75}CoO_2$ recorded in the MAPS spectrometer pixellated detector with $\boldsymbol{k}_i \parallel c$ and $E_i = 40$ meV at $T = 6$ K. This slice shows scattering with $\langle E \rangle = 10$ meV projected into the ab plane, and intensity is in absolute units of $\mathrm{mb\,sr^{-1}\,meV^{-1}\,f.u.^{-1}}$. The dashed hexagon shows the 2D Brillouin zone boundaries.

measurements were taken at two temperatures: 6 K and 200 K.

Figure 5.6 shows the neutron intensity averaged over the energy range 8-12 meV and projected onto the a^*b^* plane, for both (a) $T = 6$ K and (b) $T = 200$ K. The unscattered beam passes through the blank rectangle where there are no detectors. At 6 K the map shows an enhanced signal roughly twice the background, again centred on $\boldsymbol{Q}_{2D} = (0, 0)$, but this time shifted right into the detector bank due to the rotation of the crystal. At 200 K there is no evidence of the signal.

In order to look at the energy dependence of the signal, cuts were made through the data set, averaging over the rectangular boxes marked A and B in figure 5.6. The cut averaged over A shows the energy dependence of the signal of interest, and the cut averaged over B represents a background signal for comparison, both plotted in fig. 5.7. The signal around $\boldsymbol{Q}_{2D} = (0, 0)$ is high at low energies, and decreases in intensity around 12 meV. There is a further small peak in the intensity around 20 meV, but comparisons of this signal in the high and low temperature data showed an increase in intensity at high temperature, suggesting that the 20 meV feature is due to an optic phonon (see ref. [16]). Conversely, the low energy feature disappears at high temperature, as shown in fig. 5.6, which implies a magnetic origin.

The fact that the scattering is localized around $\boldsymbol{Q}_{2D} = (0, 0)$ suggests that the spin correlations within the ab plane are ferromagnetic (see chapter 1). In order to investigate the dispersion of this signal, constant-cuts were taken through the 6 K MAPS data along a symmetry direction within the ab plane, marked X in fig. 5.6.
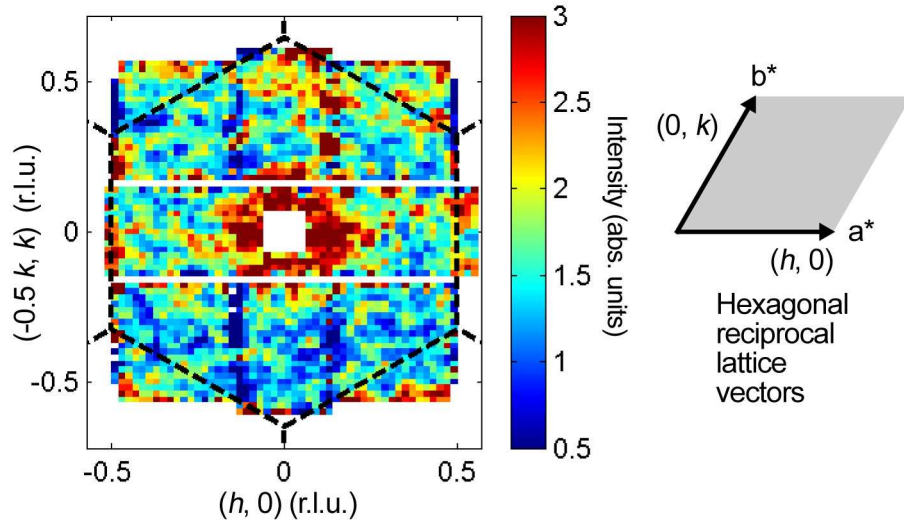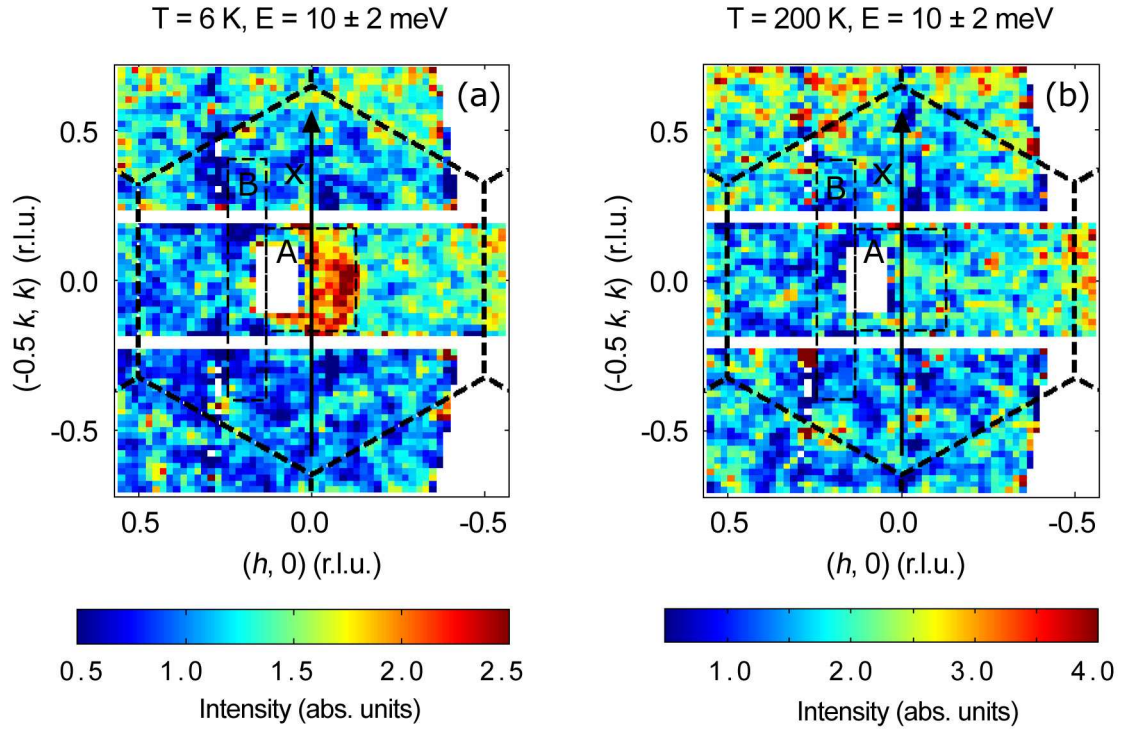
Figure 5.6: Neutron inelastic scattering from Na$_{0.75}$CoO$_2$ recorded in the MAPS spectrometer pixellated detector with $E_i = 60$ meV at (a) $T = 6$ K and (b) $T = 200$ K (k_i 30° from c). Each image is a plot of intensity averaged between energies of 10 ± 2 meV and projected into the (h, k) plane in reciprocal space. The dashed hexagonal grid shows the 2D Brillouin zone boundaries.

Figure 5.8 shows three such cuts with average energies $\langle E \rangle = 6.5$, 10 and 14 meV. The horizontal bar indicates the instrumental resolution [2]. The 6.5 meV cut shows a single peak centred at $(0, 0)$, but at higher energies the peak broadens and decreases in amplitude. The shape off the peaks at 10 and 14 meV suggests that these cuts are through two almost-resolved peaks on either side of $(0, 0)$. At higher energies the signal is weak, and but it is highly dispersive, and extends into the range where the optic phonon contaminates the scattering (around 20 meV) [3].

---

[2]This estimate of the resolution was made by calculating the spread in $\boldsymbol{Q}$ due to beam divergence $\Delta\theta$ using $\Delta Q = k_i \Delta\theta$. We note that it does not take into account the way in which the resolution ellipsoid scans through the dispersion curve.

[3]We note that the cuts shown in fig. 5.8 are not truly cuts through the dispersion in the ab plane, since l varies with energy, as shown in the top axis of fig. 5.7. This prevents us being able to directly extract the in-plane exchange parameters, as was done in chapter 4 for La$_{1.5}$Sr$_{0.5}$CoO$_4$.
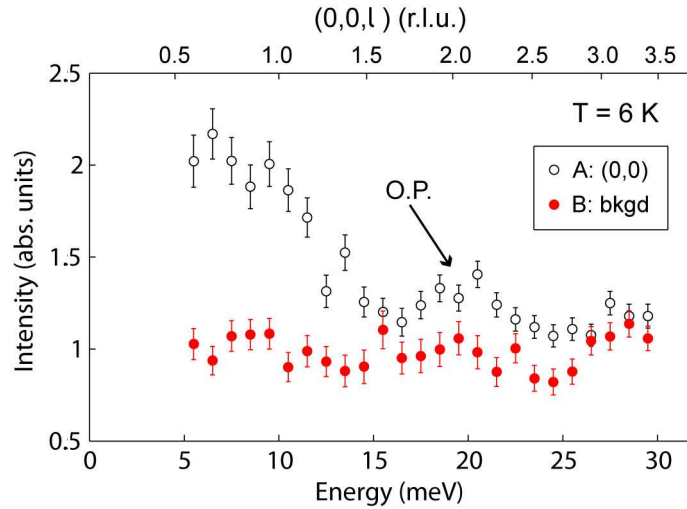
Figure 5.7: Energy dependence of the signal measured on MAPS at 6 K. Open circles are data averaged over the box marked A in fig. 5.6 centred on $\boldsymbol{Q}_{2D} = (0,0)$. Filled circles show the background signal, estimated from the region marked B in fig. 5.6. The out-of-plane wave vector component $l\mathbf{c}^*$ is marked on the upper axis in reciprocal lattice units for scan A. The peak marked 'O.P.' is probably an optic phonon.

5.2.2 Triple-axis Measurements

The measurements made on MAPS showed conclusively that strong ferromagnetic in-plane correlations exist in Na$_{0.75}$CoO$_2$. However, the measurements did not probe the $(0,0,l)$ direction, and at this point the full nature of the magnetic order was not established. Full 3D ferromagnetic order was excluded by the magnetization data [12]. However, a spin-density-wave (SDW) order along the c-axis would be compatible with the MAPS data, one example being an A-type antiferromagnetic structure (with in-plane ferromagnetic order and antiferromagnetic stacking along the c axis). In order to probe the magnetic fluctuations perpendicular to the ab planes, and to investigate the nature of the magnetic order below T_m, further measurements were made using triple-axis spectrometers at the Institut Laue-Langevin.

Experimental details

The triple-axis measurements were made on a single crystal of Na$_{0.75}$CoO$_2$ grown in Oxford by the floating-zone method, as before [13]. For the neutron studies a crystal of mass ~ 1.5 g was cleaved from a zone-melted rod. Smaller crystals from the same rod were examined by x-ray diffraction, magnetometry and electron microscopy. The analysis revealed the presence of small inclusions of cobalt oxides (CoO and Co$_3$O$_4$) consistent with previous reports for melt-grown crystals [19]. These impurity phases, which amounted to a few per cent of the total, were found by neutron diffraction to
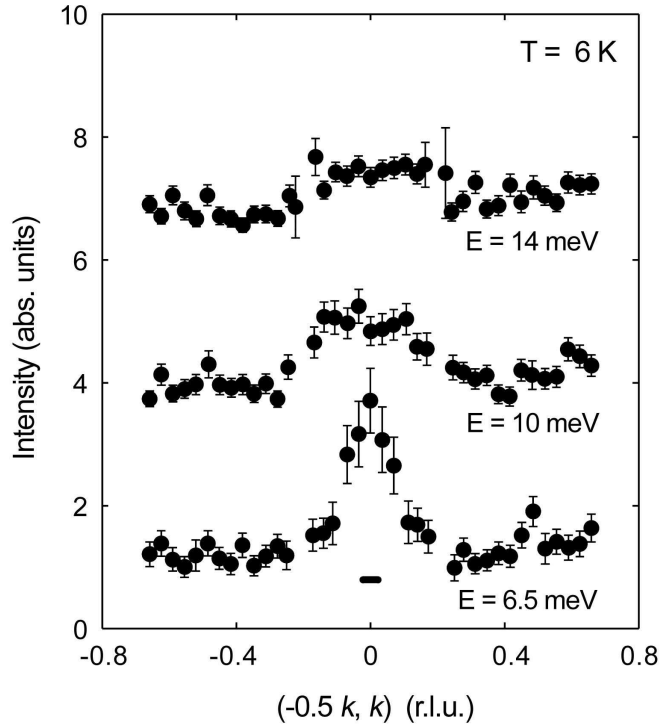
Figure 5.8: Constant energy cuts taken along the line marked X in fig. 5.6. Filled circles show neutron data points: the 10 meV and 14 meV data have been displaced vertically by 3 and 6 units, respectively. The horizontal bar indicates the instrumental resolution.

grow epitaxially on the host lattice. Once the orientation of the impurity crystallites had been determined it was straightforward to distinguish the impurity signal from that of the host. The anisotropic magnetic susceptibility of the crystals exhibited an anomaly at $T_m \approx 22$ K for fields applied parallel to the c axis, consistent with the magnetic transition observed previously [12]. The crystal was mounted on a copper bracket using a small amount of G.E. varnish, copper foil and copper wire, and attached to an aluminium mount. Different aluminium pieces allowed several orientations of the crystal, but the majority of the measurements were made with the horizontal plane defined by $(100) - (001)$, as shown in fig. 5.9. Cadmium shielding was wrapped around the aluminium mount to reduce background scattering, and the crystal was mounted in a standard helium cryostat.

Unpolarized- and polarized-neutron scattering measurements were performed on the thermal triple-axis spectrometers IN8 and IN20, respectively. On IN8 we employed a Si (111) monochromator and a pyrolytic graphite (002) analyser, and worked with a fixed final energy $E_f = 14.7$ meV. To increase the count rate both monochromator and analyser were curved horizontally and vertically for optimum focussing. For the polarized-neutron measurements on IN20 we used curved Heusler (111) as both monochromator and analyser, and $E_f = 34.8$ meV. On both instruments

a graphite filter was placed in the scattered beam to suppress higher order harmonics.

Measurements and results

To probe the out-of-plane wave-vector of the magnetic fluctuations two types of scan were performed, as shown in fig. 5.10 (right): constant-energy scans parallel to the (00l) direction, and constant-Q scans at points along (00l). Figure 5.10a shows an example scan parallel to the (00l) direction performed on IN8 at a fixed energy transfer of 7 meV. Two peaks can be seen symmetrically either side of $l = 3$. Figure 5.10b displays the same scan but this time performed on IN20 with the neutron polarization maintained parallel to the scattering vector during the scan. In this configuration the spin-flip (SF) scattering is purely magnetic, and the non-spin-flip scattering is non-magnetic. The two peaks are clearly present in the SF channel and absent from the NSF channel. The peaks are essentially resolution-limited, as indicated, but are less well resolved in fig. 5.10b than in fig. 5.10a because of the larger neutron energy used on IN20. We conclude that the peaks arise from magnetic excitations.

The scan shown in fig. 5.10a was repeated for different fixed energies between 3 meV and 10 meV. Each scan contained two peaks symmetric about (003), with the peak separation increasing with increasing energy. In addition, energy scans were made at several fixed points along the line (00l). Figure 5.10c shows one such scan, made at $l = 2.5$, the zone boundary in the out-of-plane direction. The scan was performed at 1.5 K and then repeated at 70 K. The prominent peak at $\sim$12 meV in the low temperature scan has disappeared by 70 K. This again confirms the magnetic
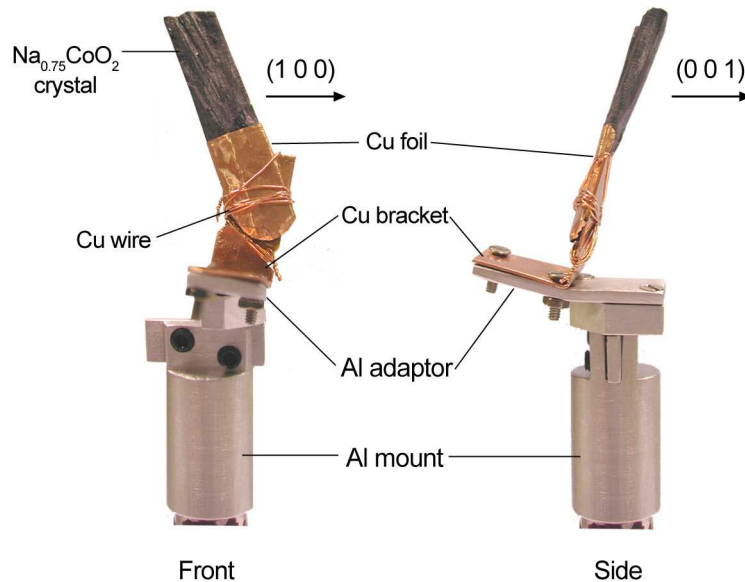
Figure 5.9: A single crystal of Na$_{0.75}$CoO$_2$ mounted for the experiment on IN20 with the horizontal scattering plane defined as (001)-(100).
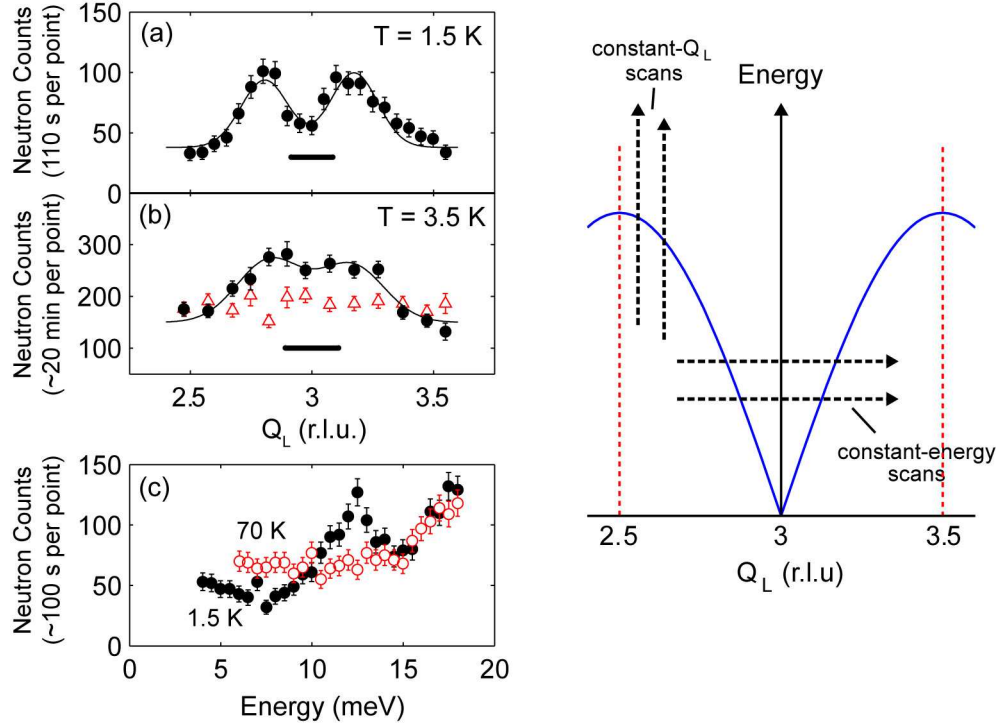
Figure 5.10: Triple-axis measurements of the magnetic scattering from Na$_{0.75}$CoO$_2$. Right: Diagram showing directions of the scans made to map out the dispersion in the $(0,0,l)$ direction. Left: (a) constant-energy scan at 7 meV along $(0,0,l)$ measured with unpolarized neutrons on IN8; (b) the same scan made on IN20 with polarized neutrons (spin-flip (SF) and non-spin-flip (NSF) channels measured with the polarization $\boldsymbol{P} \parallel \boldsymbol{Q}$ are both plotted); (c) constant-$\boldsymbol{Q}_l$ scan made at the Brillouin zone boundary $l = 2.5$ with unpolarized neutrons at two temperatures. In (a, b) the horizontal bar represents the experimental resolution.

origin of the scattering since magnetic correlations are destroyed with increasing temperature.

By fitting Gaussian functions to the peaks in both types of scan we constructed the magnon dispersion relation. This is displayed later in fig. 5.12. There is clearly a mode dispersing from (003) with a maximum energy of approximately 12 meV. The crystal structure of Na$_x$CoO$_2$ is such that no structural Bragg peaks are allowed for positions (00l) with odd l. As expected, therefore, no structural Bragg peak was observed at (003), but scans made at different temperatures revealed no magnetic Bragg peak at this point either [4].

---

[4]Magnetic Bragg peaks could not be observed at other expected positions either, but these were contaminated with relatively strong nuclear elastic scattering which probably swamped the weak magnetic Bragg scattering.

5.3 Spin-wave Analysis

In order to extract quantitative information on the magnetic correlations it was necessary to fit the data with a theoretical model of the excitations. This section presents a simple spin-wave model which allows the exchange parameters to be extracted. Linear spin-wave theory assumes localized spins coupled through isotropic Heisenberg exchange interactions, although we note that the system is actually metallic, and the true magnetic couplings may be more complex. Nevertheless, our model provides an estimate of the strength of the inter-plane and intra-plane coupling.

5.3.1 Model

The simplest spin arrangement consistent with the observations described above is the A-type antiferromagnet shown in fig. 5.11, in which the spins are ordered ferromagnetically within the layers and the layers are coupled antiferromagnetically along the c axis. Each cobalt ion is taken to have the same spin. For no magnetic Bragg peak to appear at (003) the spins must be parallel or antiparallel to the c axis, since neutrons do not couple to spin components parallel to the scattering vector.

To analyze the three-dimensional dispersion in more detail we compare the experimental results with a spin-wave model containing the minimum number of exchange parameters. The Heisenberg Hamiltonian is

Figure 5.11: (a) The A-type antiferromagnetic structure on which the spin-wave model is based, showing the two exchange constants J_{ab} and J_c. (b) The a–b planes, showing the orientation of the oxygen tetrahedron around a central Co ion.

$$\mathcal{H} = J_{ab} \sum_{\langle i,i' \rangle} \mathbf{S}_i \cdot \mathbf{S}_{i'} + J_c \sum_{\langle i,j \rangle} \mathbf{S}_i \cdot \mathbf{S}_j, \tag{5.1}$$

where J_{ab} and J_c are intra- and inter-layer exchange parameters, respectively, as indicated in fig. 5.11. Only nearest-neighb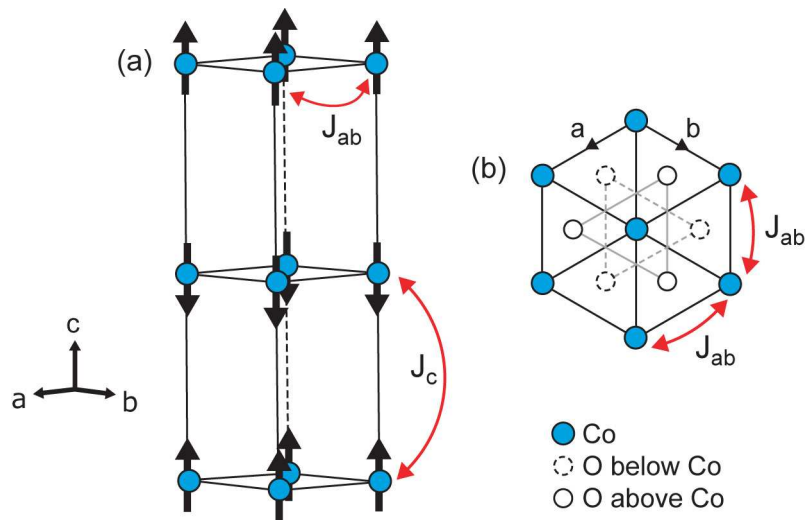our interactions are included in the summations, and $\langle i, i' \rangle$ and $\langle i, j \rangle$ denote spin pairs within the same layer and on adjacent layers, respectively.

To derive the spin-wave dispersion and scattering cross-section standard linear spin-wave theory was used. As in the La$_{1.5}$Sr$_{0.5}$CoO$_4$ calculation (chapter 4), we consider the system as two sublattices A and B containing the 'up' and 'down' spins respectively. Holstein-Primakoff transformations are used to write the spin operator components for the two sublattices in terms of Bose operators, with the quantization direction along the z-axis (parallel to the crystal c axis):

$$\begin{aligned} S_i^z &= S - a_i^\dagger a_i & S_j^z &= -(S - b_j^\dagger b_j) \\ S_i^x &= \sqrt{S/2}\left(a_i + a_i^\dagger\right) & S_j^x &= \sqrt{S/2}\left(b_j^\dagger + b_j\right) \\ S_i^y &= \frac{1}{i}\sqrt{S/2}\left(a_i - a_i^\dagger\right) & S_j^y &= \frac{1}{i}\sqrt{S/2}\left(b_j^\dagger - b_j\right) \quad, \end{aligned} \tag{5.2}$$

where $a_i^\dagger(b_j^\dagger)$ creates a spin deviation on site $i(j)$ of sublattice A(B), and we take $S = 1/2$. The Hamiltonian (eqn. 5.1) is then rewritten in terms the Fourier transforms of these operators:

$$\begin{aligned} a_{\boldsymbol{Q}} &= \frac{1}{\sqrt{N}} \sum_i e^{-i\boldsymbol{Q}.\boldsymbol{r}_i} a_i & a_{\boldsymbol{Q}}^\dagger &= \frac{1}{\sqrt{N}} \sum_i e^{+i\boldsymbol{Q}.\boldsymbol{r}_i} a_i^\dagger \\ b_{\boldsymbol{Q}} &= \frac{1}{\sqrt{N}} \sum_i e^{+i\boldsymbol{Q}.\boldsymbol{r}_i} b_i & b_{\boldsymbol{Q}}^\dagger &= \frac{1}{\sqrt{N}} \sum_i e^{-i\boldsymbol{Q}.\boldsymbol{r}_i} b_i^\dagger \quad. \end{aligned} \tag{5.3}$$

In this way the Hamiltonian is expressed in terms of the 2nd order products of the operators $a_{\boldsymbol{Q}}$, $a_{\boldsymbol{Q}}^\dagger$, $b_{\boldsymbol{Q}}$ and $b_{\boldsymbol{Q}}^\dagger$, and can be written in the general matrix form:

$$\mathcal{H} = H_0 + \sum_{\boldsymbol{Q}} X_{\boldsymbol{Q}}^\dagger H_{\boldsymbol{Q}} X_{\boldsymbol{Q}} \quad, \tag{5.4}$$

where X is the column vector $(a_{\boldsymbol{Q}}, b_{\boldsymbol{Q}}, a_{\boldsymbol{Q}}^\dagger, b_{\boldsymbol{Q}}^\dagger)$. The matrix $H_{\boldsymbol{Q}}$ is written in general form as:

$$H_{\boldsymbol{Q}} = \frac{1}{2} \begin{pmatrix} A_{\boldsymbol{Q}} & B_{\boldsymbol{Q}} & C_{\boldsymbol{Q}} & D_{\boldsymbol{Q}} \\ B_{\boldsymbol{Q}} & A_{\boldsymbol{Q}} & D_{\boldsymbol{Q}} & C_{\boldsymbol{Q}} \\ C_{\boldsymbol{Q}} & D_{\boldsymbol{Q}} & A_{\boldsymbol{Q}} & B_{\boldsymbol{Q}} \\ D_{\boldsymbol{Q}} & C_{\boldsymbol{Q}} & B_{\boldsymbol{Q}} & A_{\boldsymbol{Q}} \end{pmatrix} \quad, \tag{5.5}$$

and the method for solving this form of the Hamiltonian is given in appendix B. For the Hamiltonian above the matrix elements of eqn. 5.5 are

$$\begin{aligned} A_{\boldsymbol{Q}} &= 2J_{ab}S\left[\cos(2\pi h) + \cos(2\pi k) + \cos(2\pi(h+k)) - 3\right] + 2J_cS \tag{5.6} \\ D_{\boldsymbol{Q}} &= 2J_cS\cos(\pi l) \\ B_{\boldsymbol{Q}} &= C_{\boldsymbol{Q}} = 0 \quad, \end{aligned}$$

where $\boldsymbol{Q} = (h, k, l)$. The method of calculating the dispersion relation is given in appendix B, and we find one doubly degenerate mode described by

$$\hbar\omega_{\boldsymbol{Q}} = (A_{\boldsymbol{Q}}^2 - D_{\boldsymbol{Q}}^2)^{1/2} \quad . \tag{5.7}$$

5.3.2 Fitting the Interlayer Exchange Parameter, J_c

Along the direction $\boldsymbol{Q} = (0, 0, l)$ the expression for the dispersion relation can be simplified to

$$\hbar\omega_{\boldsymbol{Q}=(0,0,l)} = 2J_c S \left|\sin(\pi l)\right| \quad . \tag{5.8}$$

The dispersion relation along the $(0, 0, l)$ direction does not depend on J_{ab}, so by comparing the spin-wave dispersion to the data in fig. 5.12 we can immediately obtain a value for J_c. The best fit is shown by the solid curve on fig. 5.12, which is calculated with $J_c = 12.2\,\text{meV}$. At low energies the data points lie systematically above the fitted curve, suggesting the presence of a small gap of 1–2 meV. Apart from this, the model provides a good description of the data.

5.3.3 Fitting the In-plane Dispersion

The analysis described so far characterises only the inter-plane correlations. To continue the analysis and gain quantitative information on correlations within the
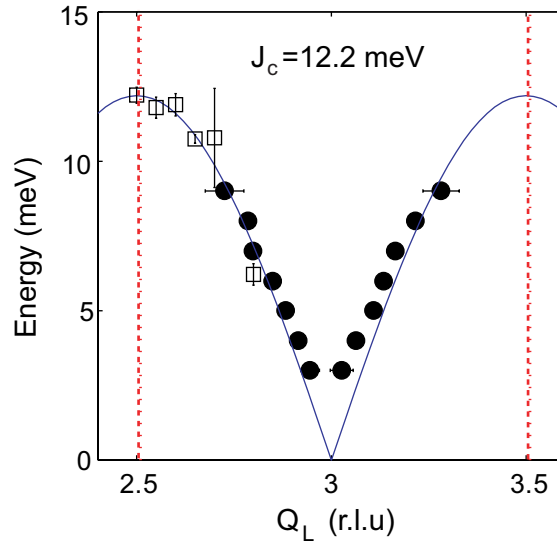
Figure 5.12: The magnon dispersion of Na$_{0.75}$CoO$_2$ parallel to $(00l)$. Data points are derived from fits of scans such as those shown in fig. 5.10: filled circles from constant-E scans and open squares from constant-$\boldsymbol{Q}$ scans. The solid curve is calculated from the spin-wave dispersion eqn. 5.8 with exchange constant $J_c = 12.2\,\text{meV}$. Dotted lines show the Brillouin zone boundaries.

planes we apply the model to the results obtained using MAPS. As described in chapter 2, on MAPS the energy transfer is coupled to the component of wavevector perpendicular to the detector bank. For a system with two-dimensional excitations, such as $La_{1.5}Sr_{0.5}CoO_4$, there is no dependence on one component of wavevector, and it is possible to take cuts through the data set to map out the dispersion relation, as described in section 4.5. For three-dimensional excitations this is not possible, and the analysis is more complicated. A MAPS-style data set was simulated from the model to allow direct comparison with the MAPS data. The MAPS data set is an intensity array in $(\boldsymbol{Q}, E)$ space, so for each data point in this space the simulated intensity was calculated, including the magnetic form-factor and orientation factor [20]. For the calculation, J_c was fixed to the value 12.2 meV determined from the inter-layer dispersion, while J_{ab} was varied until good agreement between simulation and experiment was achieved.

Following this procedure we determined that $J_{ab} = -6 \pm 2$ meV. Figure 5.13a shows the central section of the MAPS data at $T = 6$ K presented earlier in fig. 5.6. Figure 5.13b shows a similar slice through the simulated data for $J_{ab} = -6$ meV and $J_c = 12.2$ meV to give direct comparison with fig. 5.13a. The distribution of scattering within the plane is well reproduced by the model. Figure 5.13c shows constant-energy cuts through both real and simulated data sets along the line marked X in fig. 5.13(a, b), at three different energies. To fit the data each mode was broadened in energy by a Gaussian function with $\sigma = 1.7$ meV.[5] The model does not include the variation of the background with energy, so a flat background was fitted for each energy independently. In addition, the overall scattering amplitude had to be systematically reduced with increasing energy to fit the data satisfactorily. This reduction, which was nearly a factor of 2 over the energy range 6.5 meV to 14 meV, is not predicted by the spin wave model.

---

[5]This corresponds to a full width at half maximum of 4 meV.
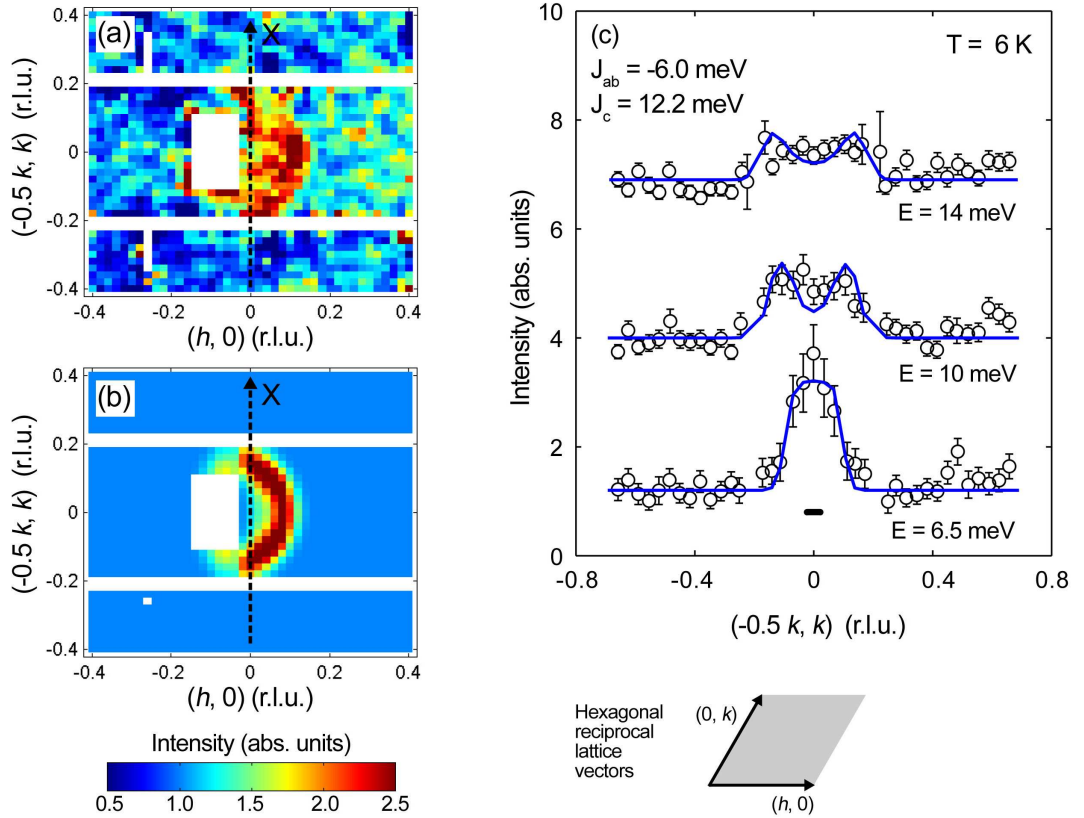
Figure 5.13: (a) Neutron inelastic scattering from Na$_{0.75}$CoO$_2$ recorded on the MAPS spectrometer at 6 K with an incident energy of 60 meV. The map contains data averaged over energy transfers of 8–12 meV, and is projected onto the (h, k) reciprocal lattice plane of the crystal. (b) Simulated intensity using the model described in the text with $J_{ab} = -6$ meV and $J_c = 12.2$ meV. The axis labels correspond to the hexagonal reciprocal axes drawn in the figure. (c) Constant energy cuts taken along the line marked X in (a,b). Open circles show neutron data points, while the solid lines are from the simulation. The 10 meV and 14 meV data have been displaced vertically by 3 and 6 units, respectively. The horizontal bar indicates an estimate of the instrumental resolution.

5.4 Characterising the Spin Gap

The measurements and analysis described above have established that the magnetic order and dynamics in Na$_{0.75}$CoO$_2$ are consistent with an A-type antiferromagnetic structure, and that the magnetic interactions are three-dimensional despite the two-dimensional character of the crystal lattice and electronic structure. The measured c-axis dispersion, shown in fig. 5.12, found evidence of a small excitation gap at the antiferromagnetic zone centre. To investigate the nature of this possible gap we decided to perform further measurements to investigate the spin-wave dispersion in Na$_{0.75}$CoO$_2$ at lower energies. The motivation for this was to gain important information on the magnetic ground state of Na$_{0.75}$CoO$_2$, such as whether itinerant effects are important.

5.4.1 Low-energy Measurements

Experimental details

Inelastic neutron measurements were performed on the cold-neutron triple-axis spectrometer IN14 at the Institut Laue-Langevin. This instrument was chosen to allow investigation of the excitations in Na$_{0.75}$CoO$_2$ at lower energies than previously studied. We employed a pyrolytic graphite (PG) (002) monochromator and a PG (002) analyzer, which were curved vertically and horizontally respectively, to maximize the count rate. The majority of measurements were made with a fixed final energy of $E_\mathrm{f} = 4$ meV. A Beryllium filter was placed in the scattered beam to suppress higher-order harmonics.

The inelastic neutron measurements were performed on the same crystal of Na$_{0.75}$CoO$_2$ as used for our previous triple-axis experiments, see fig. 5.9. The single crystal of mass ~ 1.5 g was mounted on a copper mount and aligned to allow measurements to be made within the (100)–(001) scattering plane.

Since the previous measurements above revealed strong spin-wave scattering around (0,0,1) and (0,0,3), the inelastic measurements here concentrate on spin waves dispersing from the magnetic zone center at (0,0,1), where the inelastic scattering is most intense.

Measurements and results

Figures 5.14 and 5.15 present examples of inelastic neutron scattering data collected on IN14. Each scan was performed by measuring the intensity of scattered neutrons as a function of energy transfer up to ~ 3 meV at the wavevector $\boldsymbol{Q} = (0,0,1)$. Scans were made at ten temperatures between 1.5 K and 24.4 K.

Figure 5.14a shows measurements made of the energy spectrum at low temperature ($T = 1.5$ K). The spectrum consists of an intense peak due to incoherent nuclear elastic scattering centered on $E = 0$ meV, and a broad signal centered around 2 meV which is attributed to magnetic scattering as the scan cuts through the spin-wave dispersion. There is clearly a gap where the intensity falls to background below ~ 1 meV, revealing that the magnetic excitations in Na$_{0.75}$CoO$_2$ are separated from

the ordered ground state by a clean gap. To determine the non-magnetic scattering an energy scan was also made at $\boldsymbol{Q} = (0, 0, 1.25)$. The scan, which is plotted in fig. 5.14a, contains the nuclear incoherent peak together with a small constant background signal.

Figure 5.14b displays $\boldsymbol{Q}_l$ scans performed at three constant energy transfers of $E_T = 0.5$, 1.0 and 1.6 meV. The peak present at higher energies has clearly disappeared at 0.5 meV, confirming that the intensity of the spin-wave dispersion really does fall to background in the 'gap', and the remaining intensity at this point seen in fig. 5.14a is simply due to the tail of the incoherent peak.

Figure 5.15 shows the scan in fig. 5.14a along with the same scan at the remaining
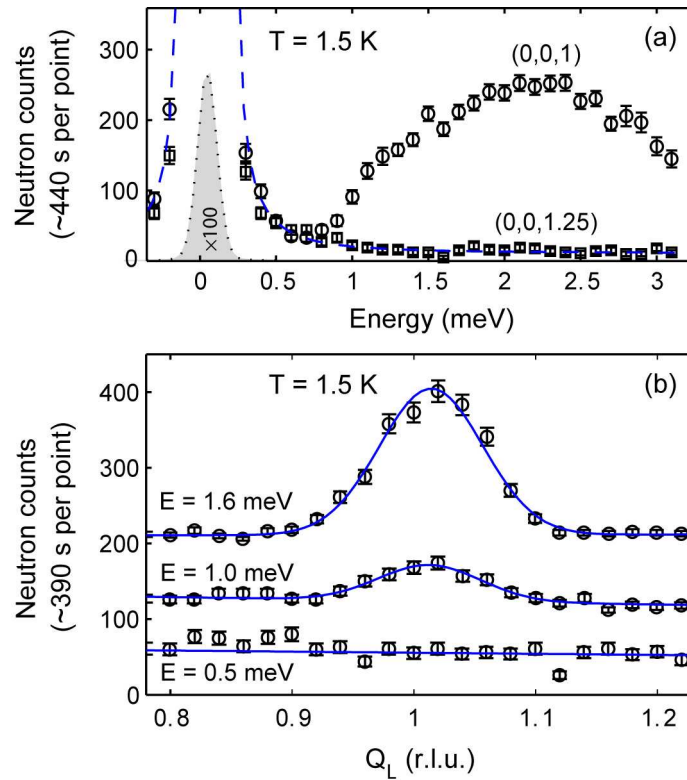
Figure 5.14: Neutron inelastic scattering from Na$_{0.75}$CoO$_2$ measured at $T = 1.5$ K. (a) Energy scan at constant $\boldsymbol{Q} = (0, 0, 1)$, compared with the same scan at a background position $\boldsymbol{Q} = (0, 0, 1.25)$. The dashed curve represents the contribution of the incoherent peak and background, fitted to the data at $\boldsymbol{Q} = (0, 0, 1.25)$. The shaded peak shows the incoherent peak contribution scaled down by a factor of 100, as an indication of the instrumental resolution. (b) $\boldsymbol{Q}_l$ scans with constant energy transfers of 0.5 meV, 1.0 meV and 1.6 meV. Data at 1.0 meV and 1.6 meV have been shifted up by 100 and 200 counts respectively for clarity.
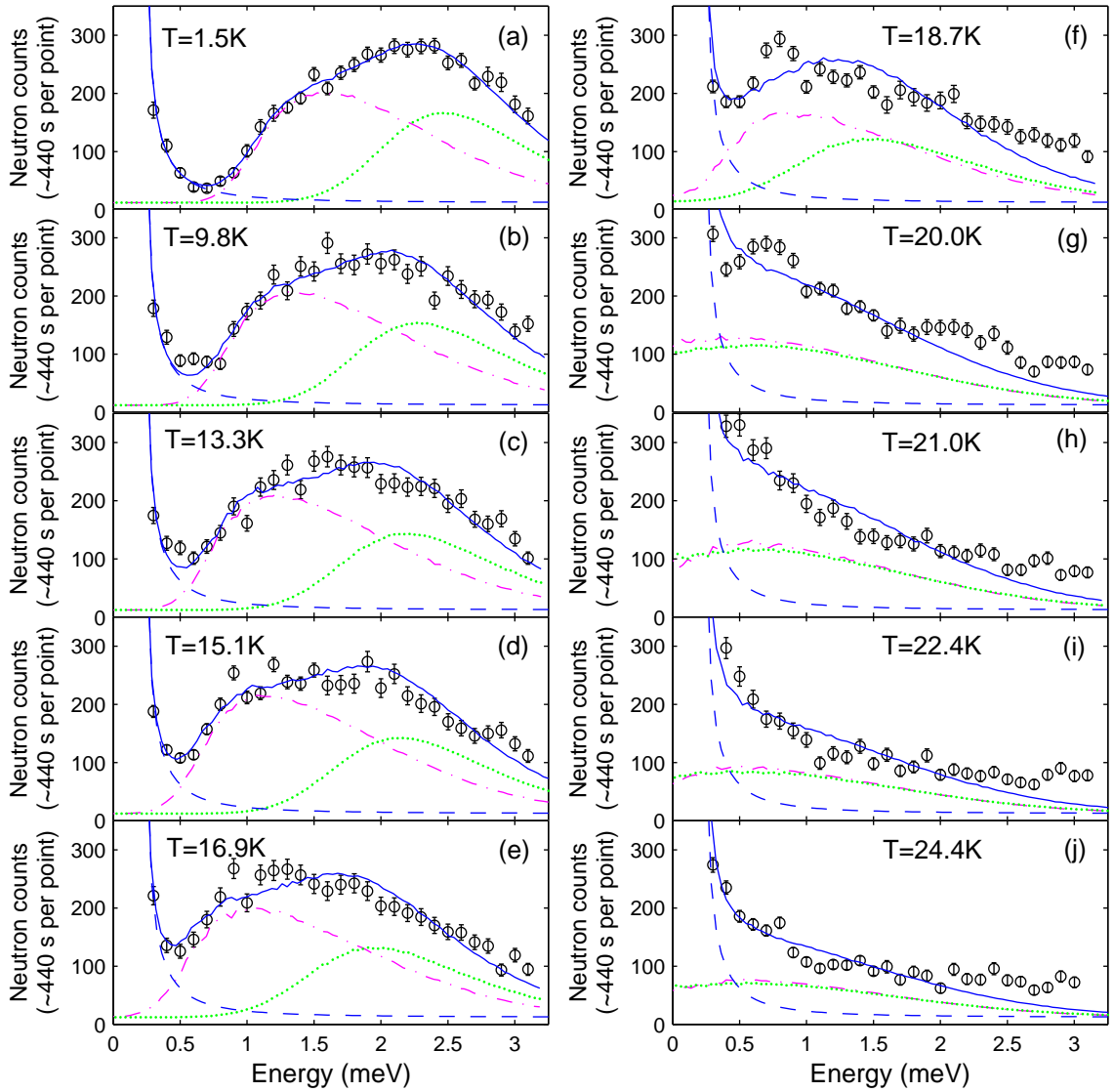
Figure 5.15: (a)-(j) Energy scans at $\boldsymbol{Q} = (0, 0, 1)$ at temperatures between $T = 1.5$ K and 24.4 K. Solid curves represent the best fit of the model described in the text, plus an incoherent peak to the data. The dashed line shows the contribution of the incoherent peak and background, while the pink (dash-dotted) and green (dotted) curves represent the intensities of each mode.

temperatures we measured, below and above the magnetic transition temperature $T_m \approx 22$ K. It appears that the magnetic scattering intensity moves lower in energy as the temperature increases. Somewhere above 20 K the gap seems to disappear, moving into the incoherent peak.

5.4.2 Extension of Spin-wave Model

To determine whether the gap is in fact decreasing with temperature, or whether what we see is simply the mode broadening and decreasing in intensity, we compare the experimental results with a model of the excitations. The spectrum observed at 1.5 K (fig. 5.14a) is suggestive of a two-peak lineshape. In order to extend the spin-wave model introduced in eqn. 5.1 to allow two non-degenerate gapped modes at $\boldsymbol{Q} = (0,0,1)$ we include two anisotropy terms. The Hamiltonian of this refined model is then:

$$
\begin{aligned}
\mathcal{H} \;=\; & J_{ab} \sum_{\langle i,i' \rangle} \mathbf{S}_i \cdot \mathbf{S}_{i'} + J_c \sum_{\langle i,j \rangle} \mathbf{S}_i \cdot \mathbf{S}_j \\
& - D \sum_i (S_i^z)^2 - E \sum_i [(S_i^x)^2 - (S_i^y)^2] \;,
\end{aligned}
\tag{5.9}
$$

where J_{ab} and J_c are intra- and inter-layer exchange parameters, respectively, as before (see fig. 5.11). The anisotropy constant D quantifies the tendency of the spins to lie along the c axis [6], while the term $E \sum_i [(S_i^x)^2 - (S_i^y)^2]$, which has two-fold symmetry in the plane, is the simplest way to introduce in-plane anisotropy. The inclusion of this term is discussed in section 5.5. We define x parallel to a, z parallel to c, and y perpendicular to x and z so as to make a right-handed set.

The spin-wave dispersion resulting from this Hamiltonian can be calculated using the same notation as before (see appendix B) to give two modes:

$$
\hbar\omega_{\boldsymbol{Q}}^{\pm} = \sqrt{A_{\boldsymbol{Q}}^2 - (C_{\boldsymbol{Q}} \pm D_{\boldsymbol{Q}})^2} \;,
\tag{5.10}
$$

where $\hbar\omega$ is the energy transfer, S is the spin (here assumed to be $S = 1/2$), $\boldsymbol{Q} = (h,k,l)$ is the wavevector, and the elements $A_{\boldsymbol{Q}}$, $C_{\boldsymbol{Q}}$ and $D_{\boldsymbol{Q}}$ are redefined for this Hamiltonian as

$$
A_{\boldsymbol{Q}} = 2S \left\{ J_{ab} \left[\cos(2\pi h) + \cos(2\pi k) + \cos(2\pi(h+k)) - 3 \right] + J_c + D \right\}
\tag{5.11}
$$
$$
C_{\boldsymbol{Q}} = -2SE
$$
$$
D_{\boldsymbol{Q}} = 2S J_c \cos(\pi l) \;.
$$

Note that D (the anisotropy parameter) is not the same as $D_{\boldsymbol{Q}}$. The magnitudes of the gaps at the magnetic zone center are then related to the exchange and anisotropy parameters as follows:

$$
\hbar\omega_{gap}^{\pm} = 2S \sqrt{(J_c + D)^2 - (J_c \pm E)^2} \;.
\tag{5.12}
$$

Note that if $E = 0$ only one gap results.

---

[6]We should note that Bayrakci *et al.* introduced a similar term $-D \sum_i (S_i^z)$ (with the sign of D alternating from layer to layer) to describe a single anisotropy gap, in their paper on Na$_{0.82}$CoO$_2$. However they were unable to determine definitively the existence of the gap, fitting a value for $|D|$ of 0.05 ± 0.05. [21]

For the case when $\boldsymbol{Q}$ lies parallel to the ordered moment direction, such as at $\boldsymbol{Q} = (0, 0, 1)$ here, the inelastic neutron intensity is proportional to $S^{xx}(\boldsymbol{Q}, \omega) + S^{yy}(\boldsymbol{Q}, \omega)$ [20], where

$$S^{xx}(\boldsymbol{Q}, \omega) = 2S^2 \frac{\{A_{\boldsymbol{Q}} - (C_{\boldsymbol{Q}} - D_{\boldsymbol{Q}})\}}{\hbar\omega_{\boldsymbol{Q}}^-} G^-(\omega - \omega_{\boldsymbol{Q}}^-) f^2(\boldsymbol{Q})[n(\omega) + 1] \quad (5.13)$$

$$S^{yy}(\boldsymbol{Q}, \omega) = 2S^2 \frac{\{A_{\boldsymbol{Q}} - (C_{\boldsymbol{Q}} + D_{\boldsymbol{Q}})\}}{\hbar\omega_{\boldsymbol{Q}}^+} G^+(\omega - \omega_{\boldsymbol{Q}}^+) f^2(\boldsymbol{Q})[n(\omega) + 1] \,, \quad (5.14)$$

where $[n(\omega) + 1]$ is the Bose factor, and $f(\boldsymbol{Q})$ is the form factor (which is a constant here since all our energy scans were made at one fixed value of $\boldsymbol{Q}$). $G(\omega - \omega_{\boldsymbol{Q}}^\pm)$ are normalized Gaussian functions which replace the usual Delta functions to allow inclusion of intrinsic broadening of the two modes.

The triple-axis spectrometer has a three-dimensional ellipsoid-shaped resolution, and therefore does not probe the dispersion relation at an infinitely sharp point in reciprocal space. In order to fit the spin-wave model to the experimental data it was therefore necessary to convolute the calculated spectrum (eqns. 5.13 and 5.14) with the IN14 spectrometer resolution. This was achieved using RESCAL, a set of programs integrated into Matlab which calculates the resolution function of the neutron triple-axis spectrometer [22]. It allows simulation of scans using a 4D Monte-Carlo convolution of the resolution function with the specified spectrum, and the simulation can then be fitted to the data in order to extract the parameters.

In this way the anisotropy parameters were extracted, while fixing the exchange parameters J_{ab} and J_c to the values obtained previously in section 5.3 (-6 meV and 12.2 meV respectively). This assumption is valid if D and E are small compared to J_{ab} and J_c, which is later shown to be the case. The relative amplitudes of the two modes were fixed by the spin-wave model, with an overall amplitude fitted, and the values for the intrinsic widths of the dispersion modes were fitted independently. The incoherent peak and background were included as a fixed Voigtian peak plus a constant.

At $T = 1.5$ K the values for D and E were found to be 0.096 ± 0.005 and 0.059 ± 0.005 meV, corresponding to two modes with gaps of 0.95 ± 0.15 and 1.95 ± 0.15 meV. To achieve a good fit the intrinsic widths of the two modes were found to be different: 0.37 and 0.74 meV for the lower and higher modes. The fitted curve is displayed on fig. 5.16a, with the two lower curves representing the contribution of each of the gapped modes. The dashed line shows the contribution of the incoherent peak, which is also plotted scaled down by a factor of 100 (shaded peak) as an indication of the instrumental resolution.

The model appears to fit the data well. For comparison fig. 5.16b shows the same data fitted with a 'one-mode' dispersion, by fixing the value of E to zero. In this fit the value of D was found to be 0.082 ± 0.015 meV ($E = 0$), and the intrinsic width of the mode is much larger than before (1.21 meV). It is clear that the model with two modes fits the data better than that with one, yielding a value of $\chi^2 = 1.2$ compared to $\chi^2 = 3.7$ with $E = 0$. In fig. 5.17 we plot the two dispersion modes parallel to $\boldsymbol{Q}_l$
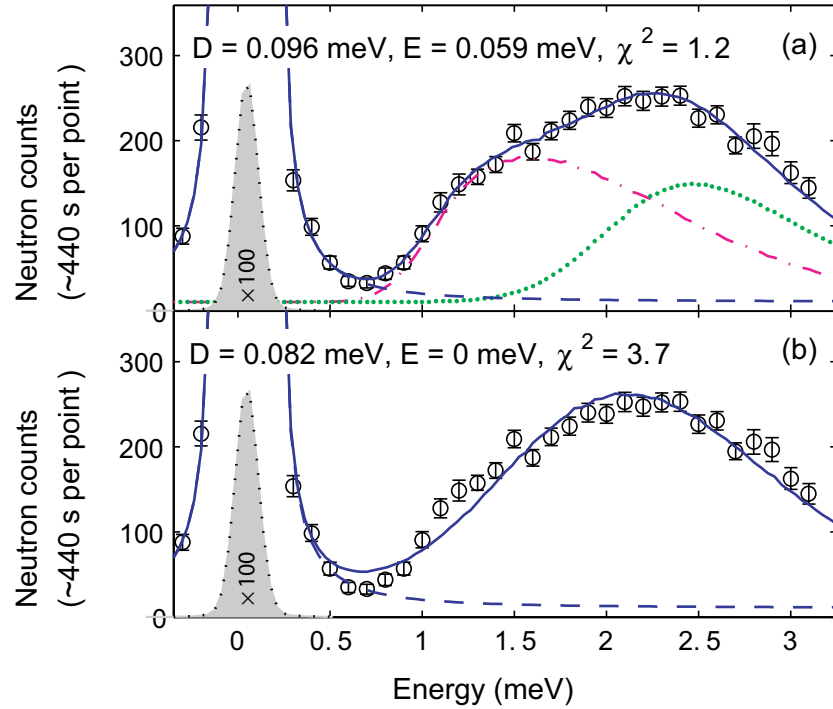
Figure 5.16: Fits to the neutron inelastic scattering from Na$_{0.75}$CoO$_2$ measured at $T = 1.5$ K, as shown in fig. 5.14a: an energy scan at constant $\boldsymbol{Q} = (0, 0, 1)$. Fitted (solid line) with (a) a two-mode dispersion, and (b) one mode only (with $E = 0$), as described in the text. The two peaks (dotted, dash-dotted) under the data in (a) show the contribution of each mode to the total intensity. Dashed curves in both (a) and (b) represent the contribution of the incoherent peak and background; shaded peaks show the incoherent peak contribution scaled down by a factor of 100, as an indication of the instrumental resolution.

(calculated from eqn. 5.10 using the fitted parameters for D and E), together with the data previously measured around $\boldsymbol{Q} = (0, 0, 3)$ (from fig. 5.12). The fitted modes are also in good agreement with the experimental data in the $\boldsymbol{Q}_l$ direction.

The fitting procedure was repeated for data at all temperatures, restricted only by fixing the intrinsic widths of the two modes to the values at 1.5 K. We also assumed that the incoherent peak and background are temperature independent. Figures 5.15a–j are overplotted with fits to each data set, with the contributions from each mode as solid lines underneath, and the contribution from the incoherent peak denoted by the dashed line. The fitted lines provide a reasonable description of the data, reproducing the shift of the intensity towards zero energy with increasing temperature, although clearly the lineshapes fit less well as the temperature increases. The gap energies extracted from these fits are plotted as a function of temperature in
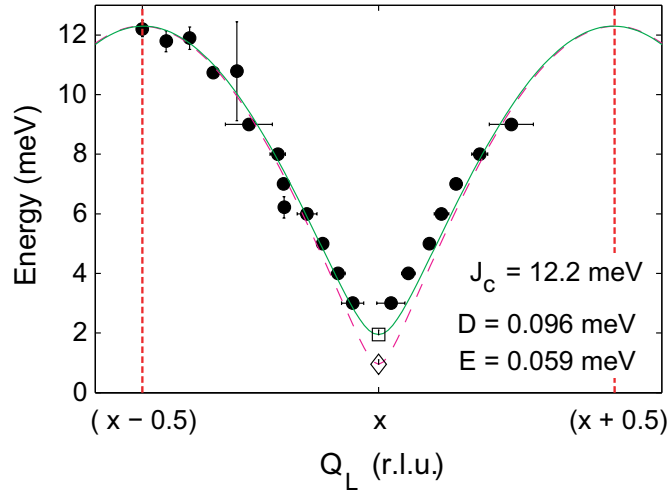
Figure 5.17: Filled circles: Magnon dispersion parallel to $(0,0,l)$ centered on $(0,0,x)=(0,0,3)$, measured previously [17]. Open square/diamond: Fits to 1.5 K energy scan at $(0,0,x)=(0,0,1)$ shown in fig. 5.16a. Solid and dashed curves are modes calculated from the spin-wave dispersion eqn. 5.10 with the constants given, while dotted lines represent the zone boundaries.
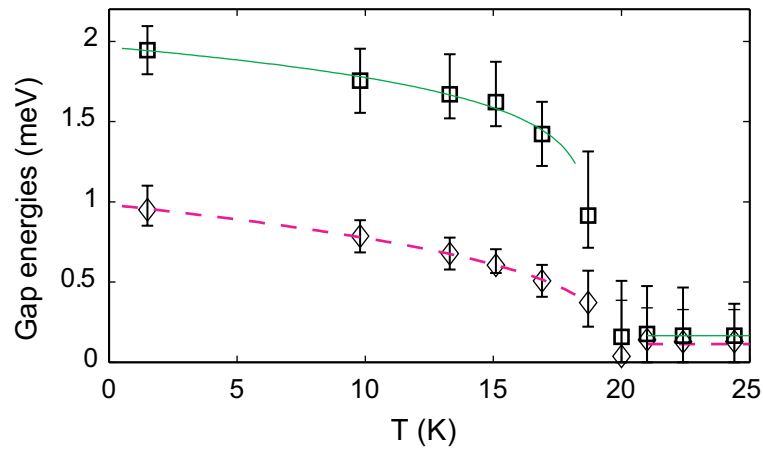
Figure 5.18: The magnitudes of the two gaps as a function of temperature. Data points calculated from eqn. 5.12 using the values of J_c, D and E derived from fits shown in fig. 5.15. Solid and dashed curves are guides for the eye. Error bars were estimated by varying the two gap energies separately until the fit was no longer acceptable.

fig. 5.18. Both gaps decrease with temperature, falling to near zero at ≈ 20 K. Above 20 K the fitted gaps are relatively constant and close to zero.

Attempts were made to fit the spectra with the 'one-mode' dispersion ($E = 0$), but up to 20 K a better fit was achieved with the two-mode lineshape ($E \neq 0$), although improvement was marginal for several of the scans.

5.5 Discussion and Conclusions

In this chapter we have reported measurements and calculations which reveal that the magnetic correlations in $Na_{0.75}CoO_2$ are of a three-dimensional (3D) nature, despite its highly 2D physical properties. In fact, the inter-plane exchange constant J_c is found to be roughly double the intra-plane constant J_{ab}. The spin wave modes propagating along the c-axis are found to be relatively sharp, indicating a well correlated ground state. The in-plane modes exhibit broadening greater than instrumental resolution, as indicated on fig. 5.13c.

Comparisons have been made between Na_xCoO_2 and other layered superconducting families, such as the copper oxides. The strong 2D nature of the cuprates is thought to be important for their superconductivity, and contrasts with the 3D magnetic interactions found here for $Na_{0.75}CoO_2$. It is likely that the c-axis magnetic coupling is weakened in hydrated Na_xCoO_2, due to the large inter-layer spacing, and it is tempting to speculate that this coupling actually inhibits superconductivity. This possibility is especially pertinent given evidence for the presence of H_3O^+ ions in the hydrated compound, which would make Co valence for superconductivity similar to that in $Na_{0.75}CoO_2$ [23].

Since publication of our results, the three-dimensionality of the magnetism in Na_xCoO_2 has been discussed by Johannes *et al.*, in conjunction with theoretical models of the exchange paths [24]. In this paper, first principles calculations were used to analyse the exchange mechanisms. Many different paths between Co ions on adjacent layers were identified by considering hopping mechanisms, both along Co-O-Na-O-Co and Co-O-O-Co paths. By including both nearest and next-nearest Co ions on adjacent planes they concluded that the individual exchange interactions along c should be scaled down by a factor of nine compared to those fitted with our model, *i.e.* $J'_c = J_c/9$. In this scenario, $J'_c \ll J_{ab}$ and the individual exchange paths reflect the two-dimensional nature of the layered compound. However, three-dimensional magnetism is observed because of the multiple exchange paths along the c axis.

We have seen that the spin-wave dispersion in $Na_{0.75}CoO_2$ is clearly gapped, and our analysis indicates that there are probably two gaps. The analysis we have presented in section 5.4 has been performed with a Hamiltonian including two anisotropy terms. While including a term to describe a uniaxial anisotropy (D) seems logical given that the spins do lie along the c axis, the need to introduce also an in-plane anisotropy term, with two-fold symmetry, deserves some comment. Taking into account only the nearest-neighboring oxygen ions, the Co environment has 3-fold symmetry within the planes, as shown in fig. 5.11b. With the quantization direction parallel to the c axis, an anisotropy term with 3-fold symmetry does not lift the two-fold degeneracy of the spin-wave dispersion, so such a term would not generate an in-plane gap. [7] The existence of such a gap therefore implies a lowering of the symmetry in plane.

One possible mechanism by which the 3-fold symmetry within the plane could

---

[7]In fact any term containing only products of S^x and S^y higher than order two will not generate a gap when the spins lie along the z-direction.

be broken is from the distribution of Na atoms. The Na atoms are known to order in various patterns dependent on doping level x, many of which break the 3-fold in-plane symmetry [2]. The distribution of Na atoms could influence the magnetic anisotropy either through the crystal field or through exchange anisotropy. Another possibility is charge disproportionation on Co atoms [25]. At present there is no direct evidence for this, except at $x = 0.5$, but Co charge ordering could also generate crystal or exchange anisotropy.

By fitting the same model to data measured at various temperatures up to 24.4 K we have shown that both gaps vanish within experimental error at approximately 20 K. From the proximity of this temperature to the bulk magnetic transition at $T_m \approx 22$ K found in magnetization studies we infer that the spin waves have the same origin as the T_m transition. This may seem obvious, but the strength of the spin-wave scattering in comparison to the small size of the ordered moment made it important to confirm that the observed spin excitations were really associated with the magnetic order.

There is in fact another possible way of generating two gaps at the magnetic zone centre. The same energy spectrum might be observed if there were two domains in the crystal, each with a slightly different value for the easy-axis anisotropy parameter D, and negligible in-plane anisotropy. While this seems unlikely, it is possible to distinguish between the two scenarios using polarized neutrons. If there are two modes from in-plane and out-of-plane anisotropy gaps the intensity in one mode will come from one component of $S(\boldsymbol{Q}, \omega)$ ($S^{xx}(\boldsymbol{Q}, \omega)$), while the intensity in the other mode will come from $S^{yy}(\boldsymbol{Q}, \omega)$. Using the right polarization setup it would be possible to 'turn off' one mode while measuring the other, and therefore verify that they have different origins. If instead, both observed modes stem from an out-of-plane anisotropy gap, but with slightly different anisotropy parameters, it would not be possible to separate the intensities of the two. This would be a worthwhile extension to the work presented in this chapter.

The spin excitation spectrum observed here is not easily reconciled with the usual picture of localized Co^{4+} and Co^{3+} ions carrying spins $S = 1/2$ and $S = 0$, respectively. If localized Co^{4+} spins were distributed at random then a very broad magnetic excitation spectrum would be expected, unlike the sharp modes observed experimentally. One possibility is that there is a phase separation into ferromagnetic in-plane clusters of Co^{4+} ions in a matrix of non-magnetic Co^{3+}. However, the Coulomb penalty would be considerable, and to obtain consistency with the observed sharp spin modes along the c-axis these clusters would have to be aligned vertically above each other over many layers. There is also evidence that Na$_x$CoO$_2$ is a good metal, which would suggest that an itinerant picture might be more appropriate [26]. A weakly itinerant ground state with strong spin fluctuations would be consistent with both the small ordered moment ($\leq 0.2\mu_B$) and the fact that the energy scale of the magnetic excitations is much greater than the magnetic ordering temperature.

In this vein, the clean gap we have observed in the spin-wave dispersion points towards a system of local moments with a small symmetry-breaking anisotropy field, which is supported by our successful description of the data using a simple spin-

wave model based on localized Co spins. However, the large intrinsic widths are not consistent with a model of purely localized Co ions, and can be taken as evidence of more metallic behavior. These features of the magnetism of Na$_x$CoO$_2$ need to be taken into consideration when assessing theories of the metallic state of this material.

A similar study of excitations was made by Bayrakci *et al.* on Na$_{0.82}$CoO$_2$, at the same time as our investigations into Na$_{0.75}$CoO$_2$. They employed a similar spin-wave model to extract exchange parameters, although a factor of two exists between the exchange parameter definitions in their model compared to ours. In our notation their exchange parameters for Na$_{0.82}$CoO$_2$ are $J_{ab} = -9 \pm 0.6$ meV and $J_c = 6.6 \pm 0.6$ meV, compared to our values of $J_{ab} = -6 \pm 2$ meV and $J_c = 12.2 \pm 0.5$ meV for Na$_{0.75}$CoO$_2$. Figure 5.19 shows a comparison between the two dispersions. The in-plane exchange parameters are fairly good agreement in the two studies, considering that measurements of the dispersion relation in this direction have not reached the zone boundary in either compound. However, in the c direction there is almost a factor of two difference between the energies of the dispersions at the zone boundary, and hence in the extracted exchange parameter J_c. As yet we have no clear explanation for this discrepancy. One possibility is that there is a different pattern of sodium ordering in the two compounds. Theoretical calculations suggest that the Na exchange pathways are important in determining the magnitude of the interlayer coupling [24].
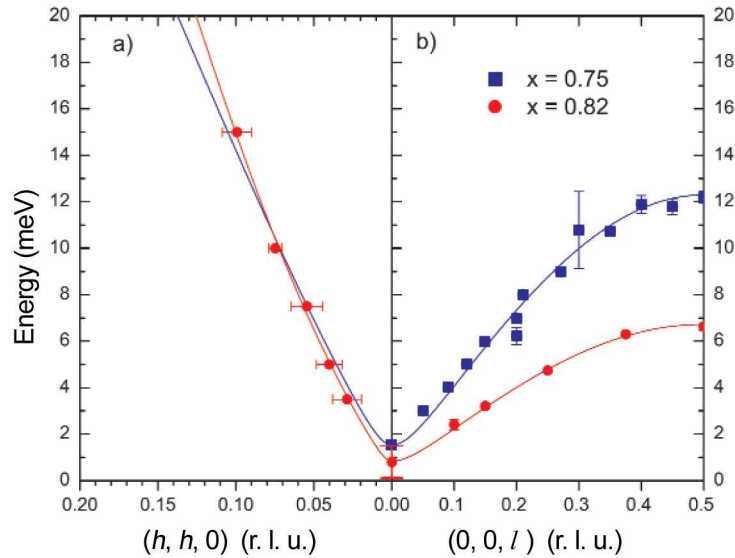
Figure 5.19: Comparison between the dispersions in Na$_x$CoO$_2$ for $x = 0.75$ (determined in this chapter, and reported in ref. [17]), and for $x = 0.82$ (measured by Bayrakci *et. al* [21]). Solid curves show fitted dispersion relations with exchange parameters J_{ab}=-6 meV and J_c =12.2 meV for $x = 0.75$ and J_{ab}=-9 meV and J_c=6.6 meV for $x = 0.82$ in our notation.

Another possibility is that charge disproportionation, which has been observed in this doping region by NMR studies [27], might alter the magnetic ordering and affect the excitations. It is important to note that the sodium contents of both samples are not known very precisely. To investigate the c-axis dispersion further, measurements at other doping levels would be informative, and accurate determination of the sodium content is crucial.

Finally, we comment on some of the remaining puzzles in the bulk magnetization measurements of Na$_x$CoO$_2$ with $x \approx 0.75$–0.85. The magnetic excitation spectrum is clearly consistent with a magnetically ordered A-type antiferromagnetic structure, with spins pointing along the c-axis. However, magnetization measurements on single crystals show that the magnetization M parallel to ab is larger than $M \parallel c$, which would make the ab plane the easy direction. The observation that $M \parallel c$ and $M \parallel ab$ cross over at low temperatures, below ~ 7 K is also still unexplained. As well as this, Curie Weiss fits to the susceptibility give negative values for Θ_W, which indicate dominant antiferromagnetic interactions within the compounds, while the sum of the exchange interactions derived from the magnetic excitation spectrum shows that the ferromagnetic interactions are dominant.

References

[1] T. Tanaka, S. Nakamura and S. Iida, Jpn. J. Appl. Phys. **33**, L581 (1994).

[2] H. W. Zandbergen, M. Foo, Q. Xu, V. Kumar, and R. J. Cava, Phys. Rev. B **70**, 024101 (2004); P. Zhang, R. B. Capaz, M. L. Cohen, and S. G. Louie, Phys. Rev. B **71**, 153102 (2005).

[3] D. J. Singh, Phys. Rev. B **68**, R020503 (2003).

[4] K. Takada, H. Sakurai, E. Takayama-Muromachi, F. Izumi, R. A. Dilanian and T. Sasaki, Nature **422**, 53 (2003).

[5] M. Kato, C. Michioka, T. Waki, Y. Itoh, K. Yoshimura, K. Ishida, H. Sakurai, E. Takayama-Muromachi, K. Takada, and T. Sasaki, J. Phys.: Condens. Matter **18**, 669 (2006). Y. Kobayashi, H. Watanabe, M. Yokoi, T. Moyoshi, Y. Mori and M. Sato, J. Phys. Soc. Japn. **74**, 1800 (2005); H. D. Yang, J.-Y. Lin, C. P. Sun, Y. C. Kang, C. L. Huang, K. Takada, T. Sasaki, H. Sakurai, and E. Takayama-Muromachi, Phys. Rev. B **71**, 020504(R) (2005); W. Higemoto, K. Ohishi, A. Koda, S. R. Saha, R. Kadono, K. Ishida, K. Takada, H. Sakurai, E. Takayama-Muromachi, and T. Sasaki, Phys. Rev. B **70**, 134508 (2004); A. Kanigel, A. Keren, L. Patlagan, K. B. Chashka, and P. King, Phys. Rev. Lett. **92**, 257007 (2004); M. Yokoi, H. Watanabe, Y. Mori, T. Moyoshi, Y. Kobayashi, and M. Sato, J. Phys. Soc. Japn. **73**, 1297 (2004); Y. J. Uemura, P. L. Russo, A. T. Savici, C. R. Wiebe, G. J. MacDougall, G. M. Luke, M. Mochizuki, Y. Yanase, M. Ogata, M. L. Foo, and R. J. Cava , cond-mat/0403031; T. Fujimoto, G. Zheng, Y. Kitaoka, R. L. Meng, J. Cmaidalka, and C. W. Chu, Phys. Rev. Lett. **92**, 047004 (2004); K. Ishida, Y. Ihara, Y. Maeno, C. Michioka, M. Kato, K. Yoshimura, K. Takada, T. Sasaki, H. Sakurai, and E. Takayama-Muromachi, J. Phys. Soc. Japn. **72**, 3041 (2003); Y. Kobayashi, M. Yokoi and M. Sato, J. Phys. Soc. Japn. **72**, 2453 (2003).

[6] I. I. Mazin and M. D. Johannes, Nature Physics **1** 91 (2005).

[7] Y. Yanase, M. Mochizuki, and M. Ogata, J. Phys. Soc. Japn. **74**, 430 (2005); T. Watanabe, H. Yokoyama, Y. Tanaka, J. I. Inoue, and M. Ogata, J. Phys. Soc. Japn. **73**, 3404 (2004); D. Sa, M. Sardar, and G. Baskaran, Phys. Rev. B **70**, 104505 (2004); M. D. Johannes, I. I. Mazin, D. J. Singh, and D. A. Papaconstantopoulos, Phys. Rev. Lett. **93**, 097005 (2004); K. Kuroki, Y. Tanaka, and R. Arita, Phys. Rev. Lett. **93**, 077001 (2004); O. I. Motrunich and P. A. Lee, Phys. Rev. B **69**, 214516 (2004).

[8] I. Terasaki, Y. Sasago and K. Uchinokura, Phys. Rev. B **56**, R12685 (1997).

[9] M. Mikami, M. Yoshimura, Y. Mori, T. Sasaki, R. Funahashi and M. Shikano, Jpn. J. Appl. Phys. **42**, 7383 (2003).

[10] T. Motohashi, E. Naujalis, R. Ueda, K. Isawa, M. Karppinen and H. Yamuchi, Appl. Phys. Lett. **79**, 1480 (2001).

[11] Y. Wang, N. S. Rogado, R. J. Cava and N. P. Ong, Nature **423**, 425 (2003).

[12] T. Motohashi, R. Ueda, E. Naujalis, T. Tojo, I. Terasaki, T. Atake, M. Karppinnen and H. Yamauchi, Phys. Rev. B **67**, 064406 (2003).

[13] D. Prabhakaran, A. T. Boothroyd, R. Coldea and N. R. Charnley, J. Crystal Growth **271**, 74 (2004).

[14] J. Sugiyama, H. Itahara, J. Brewer, E. Ansaldo, T. Motohashi, M. Karppinen and H. Yamauchi, Phys. Rev. B **67**, 214420 (2003).

[15] J. Sugiyama, J. H. Brewer, E. J. Ansaldo, H. Itahara, T. Tani, M. Mikami, Y. Mori, T. Sasaki, S. Hébert and A. Maignan, Phys. Rev. Lett. **92**, 017602 (2004).

[16] A. T. Boothroyd, R. Coldea, D. A. Tennant, D. Prabhakaran, L. M. Helme and C. D. Frost, Phys. Rev. Lett. **92**, 197201 (2004).

[17] L. M. Helme, A. T. Boothroyd, R. Coldea, D. Prabhakaran, D. A. Tennant, A. Hiess, and J. Kulda, Phys. Rev. Lett. **94**, 157206 (2005).

[18] L. M. Helme, A. T. Boothroyd, R. Coldea, D. Prabhakaran, A. Stunault, G. J. McIntyre, and N. Kernavanois, Phys. Rev. B **73**, 054405 (2006).

[19] F. C. Chou, E. T. Abel, J. H. Cho and Y. S. Lee, cond-mat/0405158.

[20] G.L. Squires, *Introduction to the Theory of Thermal Neutron Scattering* (Cambridge University Press, Cambridge, U.K., 1978).

[21] S. P. Bayrakci, I. Mirebeau, P. Bourges, Y. Sidis, M. Enderle, J. Mesot, D. P. Chen, C. T. Lin, and B. Keimer, Phys. Rev. Lett. **94**, 157205 (2005).

[22] 'RESCAL for MATLAB: a computational package for calculating neutron TAS resolution functions'. Written by D. A. Tennant and D. F. McMorrow. http://www.ill.fr/tas/matlab/doc/rescal5/rescal.htm

[23] C. J. Milne, D. N. Argyriou, A. Chemseddine, N. Aliouane, J. Veira, S. Landsgesell and D. Alber, Phys. Rev. Lett. **93**, 247007 (2004).

[24] M. D. Johannes, I. I. Mazin and D. J. Singh, Phys. Rev. B **71**, 214410 (2005).

[25] C. Bernhard, A. V. Boris, N. N. Kovaleva, G. Khaliullin, A. V. Pimenov, Li Yu, D. P. Chen, C. T. Lin, and B. Keimer, Phys. Rev. Lett. **93**, 167003 (2004).

[26] D. J. Singh, Phys. Rev. B **61**, 13397 (2000).

[27] I. R. Mukhamedshin, H. Alloul, G. Collin, and N. Blanchard, Phys. Rev. Lett. **93**, 167601 (2004); I. R. Mukhamedshin, H. Alloul, G. Collin, and N. Blanchard, Phys. Rev. Lett. **94**, 247602 (2005).

CHAPTER 6

Spin-flop Transition in $\mathrm{Na}_x\mathrm{CoO}_2$

6.1 Introduction

In this chapter we present a way to investigate the magnetic structure of $\mathrm{Na}_x\mathrm{CoO}_2$ ($x \approx 0.7-0.95$) and also to gain information about spin anisotropy in the compound.

In the accepted A-type antiferromagnetic structure (fig. 6.1a) the moments are ferromagnetically aligned within the layers and stacked antiferromagnetically along the c axis. [1, 2]. The ordering wavevector for this structure is $(0,0,1)$. We saw in the previous chapter that strong spin-wave scattering is observed emerging from $(0,0,l)$ positions with odd l, which are zone centres for the A-type antiferromagnetic order, but no magnetic Bragg peaks have been observed at these positions using
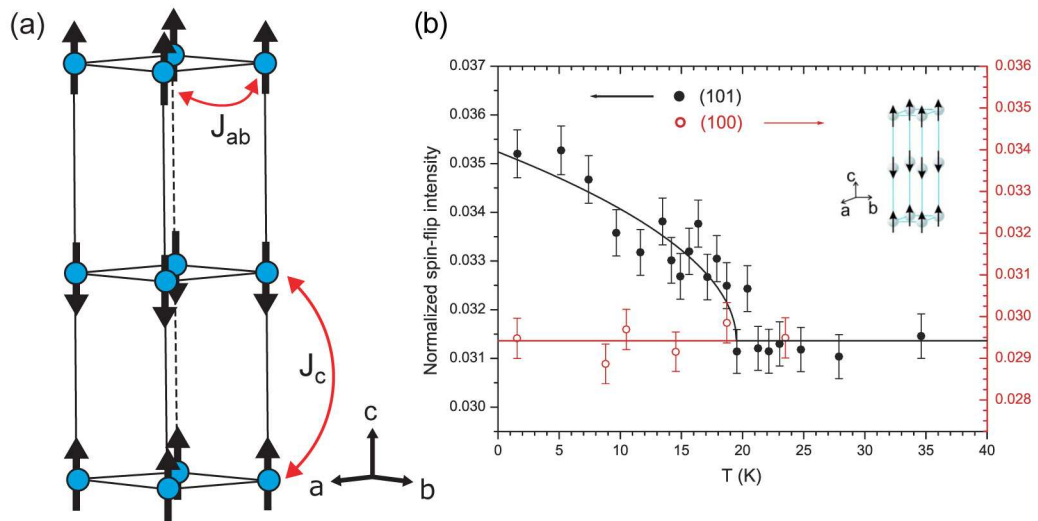
Figure 6.1: (a) The accepted A-type antiferromagnetic ground state of $\mathrm{Na}_x\mathrm{CoO}_2$ with $x \sim 0.7-0.9$. (b) Polarized neutron measurements of a magnetic Bragg peak in $\mathrm{Na}_{0.82}\mathrm{CoO}_2$ measured by Bayrakci *et al* [2]. Normalized intensity (equal to spin-flip intensity divided by non-spin-flip intensity) as a function of temperature measured with polarization $\boldsymbol{P} \parallel \boldsymbol{Q}$ at two reciprocal lattice points: $\boldsymbol{Q} = (1,0,1)$ and $\boldsymbol{Q} = (1,0,0)$.

neutrons [1]. On this basis it was deduced that the ordered moments point along the c direction since neutrons scatter from the component of the moments perpendicular to the scattering vector. This moment direction is consistent with what has been inferred from the uniform susceptibility and from μSR data [3]. Moreover, Bayrakci *et al.* did succeed recently in observing magnetic Bragg reflections at a few (h, k, l) positions with h, $k \neq 0$ and odd l using polarized neutrons [2]. Figure 6.1b shows polarized neutron measurements made at the position $\boldsymbol{Q} = (1, 0, 1)$ compared with the same measurements at the forbidden reflection $\boldsymbol{Q} = (1, 0, 0)$. Again, these are consistent with the accepted magnetic structure. Polarized neutrons were required because the ordered moment is small and strong non-magnetic scattering is observed at all positions where magnetic Bragg peaks are expected. Up to now no magnetic Bragg peaks have been observed with unpolarized neutrons.

The experiment we describe here was originally designed to confirm the proposed magnetic structure by a method that employs unpolarized neutrons but avoids the problem of having to separate the weak magnetic scattering from the strong non-magnetic background signal. Our approach was motivated by measurements of the magnetization of $Na_{0.85}CoO_2$ in applied fields up to 14 T by Luo *et al.* [4]. These measurements are reproduced in figure 6.2. The magnetization data with $H \parallel c$ show a clear anomaly at 8 T at low temperatures, with no such transition seen for $H \perp c$. The authors interpreted this as a spin-flop transition in which the ordered moments rotate by $\sim$90 degrees while preserving the A-type antiferromagnetic arrangement. After the transition the spins lie approximately in the hexagonal plane, but the magnetic structure has a small ferromagnetic component along the c axis. Assuming this explanation to be correct we induced the spin-flop transition in a neutron diffraction experiment and searched for magnetic Bragg peaks along $\boldsymbol{Q} = (0, 0, l)$, since now the ordered moment should be perpendicular to the scattering wavevector and should scatter neutrons. Our experimental results are in excellent accord with the predicted behavior. Encouraged by this, we go on to show that the size of the spin gap in the magnetic excitation spectrum is in agreement with the observed spin-flop field. This quantitative analysis provides the link between the static magnetic properties studied in this chapter and dynamic magnetic properties explored in the previous chapter.

---

[1]There is strong spin-wave scattering around $\boldsymbol{Q} = (0, 0, l)$ with $l =$ odd because the spin fluctuations are perpendicular to $\boldsymbol{Q}$.
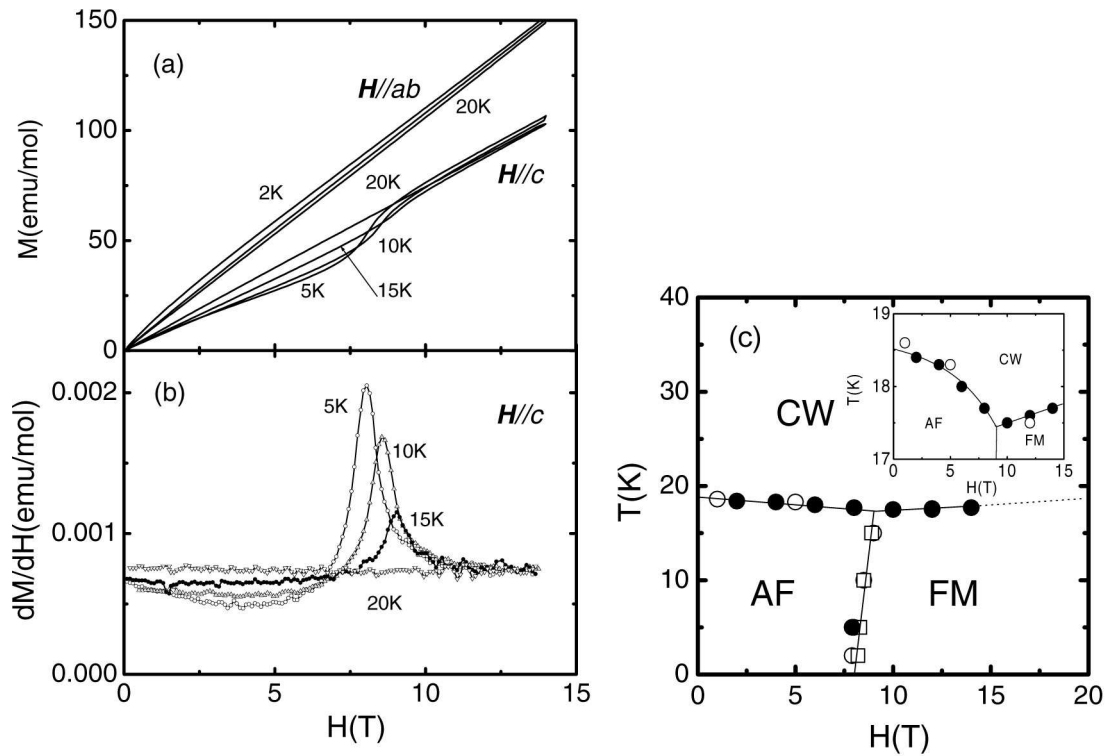
Figure 6.2: (a) The magnetization M versus field H of Na$_{0.85}$CoO$_2$ at $H \parallel c$ and $H \parallel ab$ for various temperatures $2 \le T \le 20$ K as marked. (b) dM/dH versus H at 5, 10, 15, and 20 K for $H \parallel c$. (c) The phase diagram of Na$_{0.85}$CoO$_2$ determined from susceptibility (open circle), specific heat (solid circle), and magnetoresistance (open square) measurements. CW, AF, and FM represent a Curie-Weiss, an antiferromagnetically ordered and a spin ferromagnetically polarized state, respectively. All figures from Luo *et al.* [4].

6.2 Diffraction Studies of $Na_{0.85}CoO_2$

6.2.1 Experimental Details

Neutron diffraction measurements were performed on the hot-neutron diffractometer D3 at the Institut Laue-Langevin. The instrument was used in unpolarized-neutron mode with a neutron wavelength of 0.84 Å. The single crystal of $Na_{0.85}CoO_2$ used for these measurements was cleaved from a rod grown in Oxford by the floating-zone method [5]. The crystal had a mass of 0.3 g and a mosaic spread of ~ 2 degrees.

In the introduction to chapter 5 we discussed the sodium content of the Na_xCoO_2 studied in this thesis. EPMA measurements on the $Na_{0.85}CoO_2$ crystal studied here suggest that the sodium level is nearer to $x = 0.80$. EPMA is a surface probe, so the accuracy of this measurement as a characterization of the whole sample is not known, and we refer to the sample using the nominal value throughout the chapter.

The crystal was pre-aligned on the neutron Laue diffractometer Orient Express at the ILL and mounted on an aluminium pin using ceramic glue, as shown in fig. 6.3. The ideal setup for this experiment would be to align the c axis vertically, applying a vertical field, with the incident and scattered beams inclined at the Bragg angle to the horizontal in order to access the $(0, 0, 3)$ reflection. An alternative setup, with a fixed horizontal incident beam, would require the cryomagnet holding the sample to be tilted by the Bragg angle (θ_B), with the detector lifted out of the plane (by $2\theta_B$), allowing access to the $(0, 0, 3)$ reflection while still applying the field directly along the c axis. However, on D3 we were restricted to using a horizontal incident beam (ruling out the first setup), and also unable to tilt the cryomagnet (ruling out the second). In order to access the $(0, 0, 3)$ reflection we tilted the crystal c axis 7 degrees away from vertical, corresponding to the $(0, 0, 3)$ Bragg angle for 0.84 Å neutrons, and lifted the detector out of the horizontal plane by 14 deg. The 10 Tesla
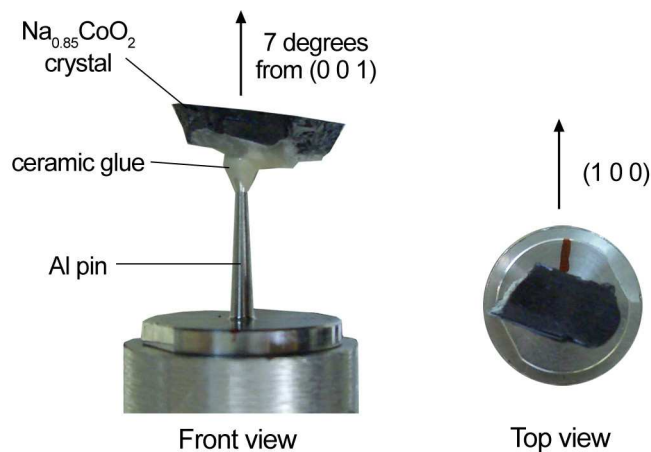
Figure 6.3: Single crystal of $Na_{0.85}CoO_2$ (0.3 g) mounted for measurements on D3.

vertical-field cryomagnet in which the crystal was mounted then allowed application of a field almost parallel to the c axis (though actually 7 degrees away from it). The field-induced $(0,0,1)$ magnetic Bragg peak is expected to be larger than that at $(0,0,3)$ due to the magnetic form factor, but with 0.84 Å neutrons the scattering angle for $(0,0,1)$ was too small to access with our setup.

6.2.2 Measurements and Results

Figure 6.4 shows the main results of the diffraction studies of $Na_{0.85}CoO_2$. All the measurements were made by scanning either field or temperature with the other external variable fixed. For ideal Na_xCoO_2 no structural Bragg peak is allowed at this position and no magnetic Bragg peak is allowed if the moments point along the c axis.

Figure 6.4a shows three field scans at $\boldsymbol{Q} = (0,0,3)$, performed at constant temperatures of $T = 1.8$, 10 and 30 K. The data at 10 K and 1.8 K have been shifted up by 500 and 1000 counts respectively for clarity.

At $T = 1.8$ K there is a large increase in the intensity of scattering at $(0,0,3)$ between $\sim$6 T and 9 T as the field increases, with the intensity appearing to flatten off between 9 and 10 T. At $T = 10$ K the increase in intensity has shifted up in field to start at $\sim$8 T, and at $T = 30$ K the intensity remains constant with field.
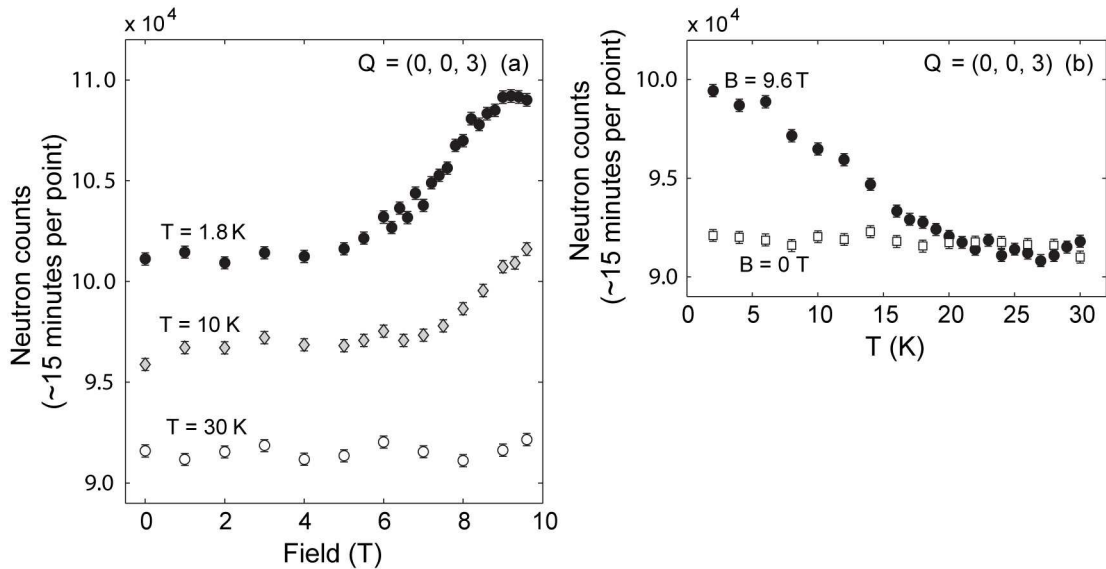
Figure 6.4: Diffraction studies of $Na_{0.85}CoO_2$. (a) Field scans at $\boldsymbol{Q} = (0,0,3)$ at constant temperatures of $T = 1.8$, 10 and 30 K. Data at $T = 10$ K and 30 K are shifted up by 500 and 1000 counts respectively. (b) Temperature scans at $\boldsymbol{Q} = (0,0,3)$, with zero applied field (open circles), and with $H = 9.6$ T applied at 7 degrees to the c-axis (filled circles).

The increase in intensity with field at 1.8 K is consistent with the expected spin-flop transition because once the spins have rotated away from the c direction magnetic Bragg scattering is allowed at $(0, 0, 3)$, provided that the ordering wavevector remains $(0, 0, 1)$.

With increasing temperature two effects are at work: (1) the field at which the spin-flop transition occurs shifts up slowly with T [4], and (2) the ordered magnetic moment μ decreases with T. Both effects would result in the reduction of intensity with increasing temperature. However, the effect of (1) is too small to explain the disappearance of the signal by 30 K (see Luo *et al.* [4]), so we deduce that the signal disappears due to the reduction of the ordered magnetic moment to zero above the magnetic ordering temperature T_m.

In fig. 6.4b we plot the temperature dependence of the scattering at $\boldsymbol{Q} = (0, 0, 3)$, in both zero applied field and 9.6 T. We confirm that the signal induced by application of the magnetic field decreases to zero as the temperature is raised to ~ 20 K.

6.3 Analysis of the Spin-Flop Transition

Figure 6.5 shows the magnetic structure of the low-field A-type antiferromagnetic (AF) phase (a), along with that of the spin-flop (SF) phase (b). As discussed above, the large increase in Bragg intensity at $Q = (0, 0, 3)$ that occurs between ~ 6 T and 9 T (fig. 6.4a) appears to support the idea that a phase transition from an AF to a SF phase occurs at this field. In order to further investigate this interpretation of the data it is constructive to compare the observed spin-flop transition field with that calculated from a model based on the exchange and anisotropy parameters extracted in the previous chapter.

6.3.1 Spin-wave Analysis

To model the spin-flop transition we extend the spin-wave model to include an external magnetic field applied along the c axis. We begin by calculating the effect
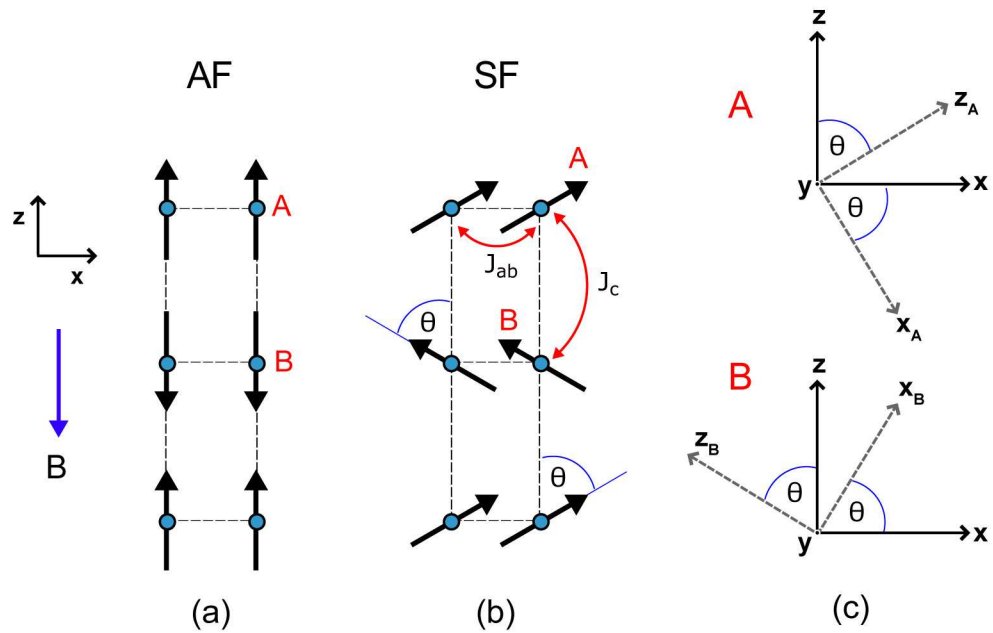
Figure 6.5: (a) The ordered A-type antiferromagnetic structure in the a–c plane, with an external magnetic field **B** applied parallel to the spins. (b) Above a critical field B_{sf} the system undergoes a spin-flop transition, to a phase with spins at an angle θ to the c-axis. We take the spins to lie in the xz plane. A and B label the two sublattices of the antiferromagnet in both cases. (c) Transformation of coordinates for the A and B sublattices in the spin-flop phase, from (x, y, z) to (x_A, y, z_A) and (x_B, y, z_B) respectively.

of the field on the spin-wave modes of the AF phase. This enables us to calculate the critical field at which a phase transition would be expected to occur. A term is added to the original Hamiltonian (eqn. 5.9) to represent a vertical applied magnetic field, giving a new Hamiltonian:

$$\mathcal{H}' = \mathcal{H} + g\mu_B B \sum_i S_i^z \tag{6.1}$$

$$= J_{ab} \sum_{\langle i,i' \rangle} \mathbf{S}_i \cdot \mathbf{S}_{i'} + J_c \sum_{\langle i,j \rangle} \mathbf{S}_i \cdot \mathbf{S}_j$$

$$- D \sum_i (S_i^z)^2 - E \sum_i [(S_i^x)^2 - (S_i^y)^2] + g\mu_B B \sum_i S_i^z , \tag{6.2}$$

where B is the magnitude of the applied magnetic field, we take the spin as $S = 1/2$ and we assume $g = 2$.

The spin-wave dispersion was derived from $\mathcal{H}'$ using the method described in the previous chapter. The Hamiltonian can again be written to second order in the form

$$\mathcal{H}_{\text{2nd order}} = \sum_{\boldsymbol{Q}} X_{\boldsymbol{Q}}^\dagger H_{\boldsymbol{Q}} X_{\boldsymbol{Q}} , \tag{6.3}$$

where X is the column vector $(a_{\boldsymbol{Q}}, b_{\boldsymbol{Q}}, a_{\boldsymbol{Q}}^\dagger, b_{\boldsymbol{Q}}^\dagger)$. However, in the AF phase the applied field B alters the symmetry of the matrix $H_{\boldsymbol{Q}}$, which can be expressed slightly differently to the general form in appendix B:

$$H_{\boldsymbol{Q}} = \frac{1}{2} \begin{pmatrix} A_{\boldsymbol{Q}} + \Delta_{\boldsymbol{Q}} & 0 & C_{\boldsymbol{Q}} & D_{\boldsymbol{Q}} \\ 0 & A_{\boldsymbol{Q}} - \Delta_{\boldsymbol{Q}} & D_{\boldsymbol{Q}} & C_{\boldsymbol{Q}} \\ C_{\boldsymbol{Q}} & D_{\boldsymbol{Q}} & A_{\boldsymbol{Q}} + \Delta_{\boldsymbol{Q}} & 0 \\ D_{\boldsymbol{Q}} & C_{\boldsymbol{Q}} & 0 & A_{\boldsymbol{Q}} - \Delta_{\boldsymbol{Q}} \end{pmatrix} , \tag{6.4}$$

where

$$A_{\boldsymbol{Q}} = 2J_{ab}S\left[\cos(2\pi h) + \cos(2\pi k) + \cos(2\pi(h+k)) - 3\right] + 2J_cS + 2DS \tag{6.5}$$

$$\Delta_{\boldsymbol{Q}} = g\mu_B B$$

$$C_{\boldsymbol{Q}} = -2ES$$

$$D_{\boldsymbol{Q}} = 2J_cS\cos(\pi l) .$$

The diagonalization of this matrix gives two modes:

$$\hbar\omega_{\boldsymbol{Q}}^\pm = \left[(A_{\boldsymbol{Q}}^2 + \Delta_{\boldsymbol{Q}}^2) - (C_{\boldsymbol{Q}}^2 + D_{\boldsymbol{Q}}^2) \pm 2\sqrt{(A_{\boldsymbol{Q}}\Delta_{\boldsymbol{Q}})^2 - (\Delta_{\boldsymbol{Q}}C_{\boldsymbol{Q}})^2 + (C_{\boldsymbol{Q}}D_{\boldsymbol{Q}})^2}\right]^{1/2}$$
$$\tag{6.6}$$

In zero applied magnetic field $\Delta_{\boldsymbol{Q}} = 0$, and eqn. 6.6 reduces to the expression derived in chapter 6, eqn. 5.10. Applying a field further splits the two modes, *i.e.* the lower mode moves down in energy, and the higher mode moves up in energy, as

the field is increased. The magnitude of the gaps at the magnetic zone center as a function of field, B, are then given by

$$\hbar\omega_{gap}^{\pm}(B) = 2S\left[\beta^2 + (2J_cD + D^2 - E^2) \pm 2\sqrt{\beta^2D(2J_c + D) + J_c^2E^2}\right]^{\frac{1}{2}} , \quad (6.7)$$

where $\beta = g\mu_B B/2S$.

As the field is increased to a critical field, B_{c1}, a local instability occurs when the energy of the lower mode falls to zero and then becomes imaginary, and the system can no longer remain in the low-field AF phase (fig. 6.5a) [6]. Figure 6.6a shows the evolution of the gap energies of the two modes with increasing field (solid lines) for the exchange and anisotropy values derived in chapter 6. The critical field is determined by setting $\hbar\omega_{gap}(B_{c1}) = 0$ for the lower mode, resulting in the expression

$$B_{c1} = \frac{2S}{g\mu_B}\sqrt{(D - E)(2J_c + D - E)} . \quad (6.8)$$

B_{c1} is the critical field at which we would expect the system to 'flop' out of the A-type antiferromagnetic phase (fig. 6.5a) into the spin-flop phase (fig. 6.5b) based on the closing of the gap with increasing field.

A similar calculation can be performed by considering the spin-wave modes in the SF phase. In this phase there are two modes at high field, and as the field is decreased there exists a critical field B_{c2} at which the lower mode vanishes and the SF phase is no longer stable. At this field, B_{c2}, the system returns to the AF phase.

In order to carry out the spin-wave calculation in the SF phase it is necessary to transform the coordinate system for the two sublattices as shown in fig. 6.5c, so that the spin quantization directions for the two sublattices A and B lie along z_A and z_B respectively. The Holstein-Primakoff transformations used to transform the spin operators to Bose operators (see eqn. 5.2, chapter 6) can then be written as

$$
\begin{array}{ll}
S_i^{z_A} = S - a_i^{\dagger}a_i & S_j^{z_B} = -(S - b_j^{\dagger}b_j) \qquad (6.9) \\
S_i^{x_A} = \sqrt{S/2}\left(a_i + a_i^{\dagger}\right) & S_j^{x_B} = \sqrt{S/2}\left(b_j^{\dagger} + b_j\right) \\
S_i^{y} = \frac{1}{\mathrm{i}}\sqrt{S/2}\left(a_i - a_i^{\dagger}\right) & S_j^{y} = \frac{1}{\mathrm{i}}\sqrt{S/2}\left(b_j^{\dagger} - b_j\right) ,
\end{array}
$$

where $a_i^{\dagger}(b_j^{\dagger})$ creates a spin deviation on site $i(j)$ of sublattice A(B), and we take $S = 1/2$ as before. The Hamiltonian (eqn. 6.1) is rewritten first in the new coordinate systems using the transformations

$$
\begin{array}{ll}
S_i^{z} = S_i^{z_A}\cos\theta - S_i^{x_A}\sin\theta & S_j^{z} = S_i^{z_B}\cos\theta + S_i^{x_B}\sin\theta \qquad (6.10) \\
S_i^{x} = S_i^{x_A}\cos\theta + S_i^{z_A}\sin\theta & S_j^{x} = S_i^{x_B}\cos\theta - S_i^{z_B}\sin\theta ,
\end{array}
$$

and then in terms of the Bose operators using eqns. 6.9. All terms greater than second order in the Bose operators $a^{\dagger}$, a, $b^{\dagger}$, b are neglected, so we obtain a Hamiltonian involving only zero, first and second order terms in the Bose operators:

$$\mathcal{H} = \mathcal{H}_0 + \mathcal{H}_{\text{1st order}} + \mathcal{H}_{\text{2nd order}} . \quad (6.11)$$
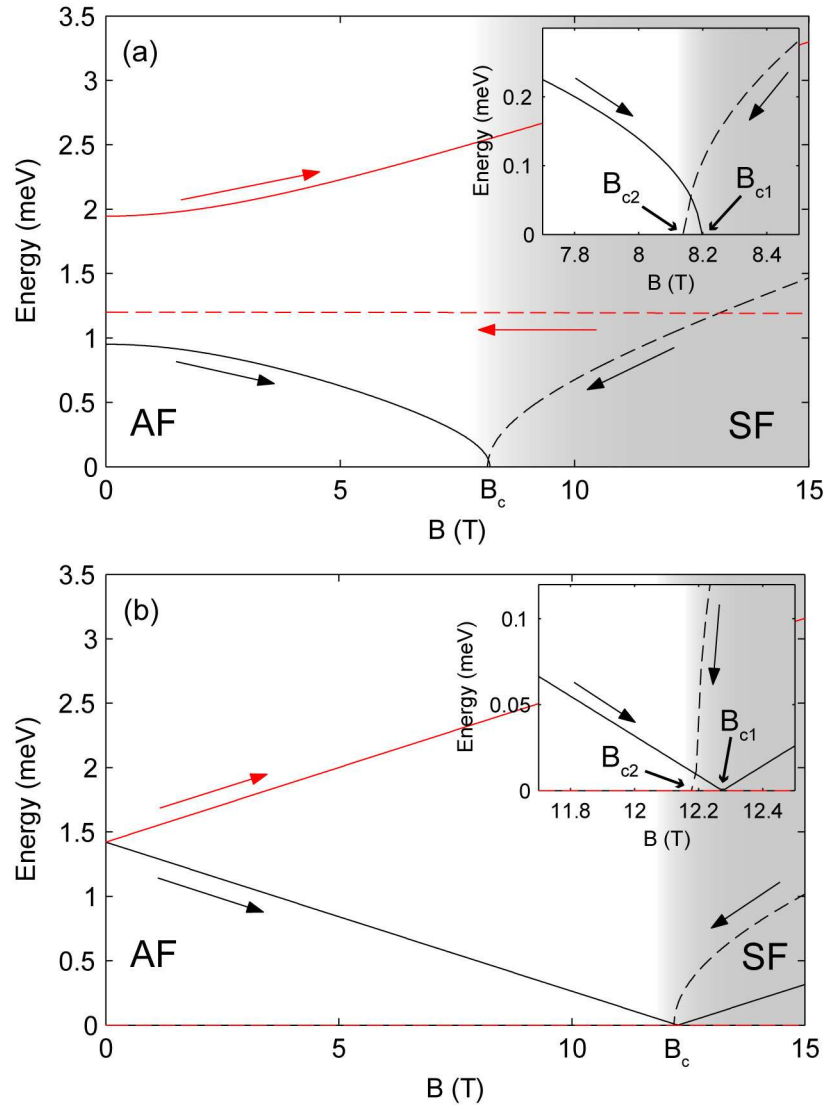
Figure 6.6: Calculated gap energies at antiferromagnetic zone centre of the two modes as a function of applied field **B**. J_c=12.2, J_{ab}=6 and (a) D=0.096 and E=0.059, (b) D=0.082 and E=0. Solid lines show two modes as field increases from 'AF' structure (fig. 6.5a); dashed lines show two modes as field decreases from 'SF' structure (fig. 6.5b). Insets: close-ups of region around the critical field.

$\mathcal{H}_0$ does not contribute to the excitations and is neglected. The spin-flop angle θ, defined by figure 6.5b, is determined by the condition that the first order terms in the Hamiltonian vanish, *i.e.* $\mathcal{H}_{1st\,order} \equiv 0$ [6]. From this condition we derive the expression

$$\theta = \arccos\left(\frac{g\mu_B B}{2S(2J_c - D + E)}\right) .$$ (6.12)

The second order terms in the Hamiltonian describe the spin-wave excitations, and using Fourier transforms (as given in eqn. 5.3), $\mathcal{H}_{\text{2nd order}}$ can be written in the standard form (see appendix B):

$$\mathcal{H}_{\text{2nd order}} = \sum_{\boldsymbol{Q}} X_{\boldsymbol{Q}}^{\dagger} H_{\boldsymbol{Q}} X_{\boldsymbol{Q}} \ , \tag{6.13}$$

where X is the column vector $(a_{\boldsymbol{Q}}, b_{\boldsymbol{Q}}, a_{\boldsymbol{Q}}^{\dagger}, b_{\boldsymbol{Q}}^{\dagger})$. The matrix $H_{\boldsymbol{Q}}$ is written in general form as:

$$H_{\boldsymbol{Q}} = \frac{1}{2} \begin{pmatrix} A_{\boldsymbol{Q}} & B_{\boldsymbol{Q}} & C_{\boldsymbol{Q}} & D_{\boldsymbol{Q}} \\ B_{\boldsymbol{Q}} & A_{\boldsymbol{Q}} & D_{\boldsymbol{Q}} & C_{\boldsymbol{Q}} \\ C_{\boldsymbol{Q}} & D_{\boldsymbol{Q}} & A_{\boldsymbol{Q}} & B_{\boldsymbol{Q}} \\ D_{\boldsymbol{Q}} & C_{\boldsymbol{Q}} & B_{\boldsymbol{Q}} & A_{\boldsymbol{Q}} \end{pmatrix} \ , \tag{6.14}$$

and here the matrix elements are given by

$$A_{\boldsymbol{Q}} = 2J_{ab}S \left[\cos(2\pi h) + \cos(2\pi k) + \cos(2\pi(h+k)) - 3\right] - 2J_c S \cos(2\theta) \tag{6.15}$$
$$+ DS(2\cos^2\theta - \sin^2\theta) + ES(2\sin^2\theta - \cos^2\theta) + g\mu_B B\cos\theta$$
$$B_{\boldsymbol{Q}} = 2J_c S \cos(\pi l) \cos^2\theta$$
$$C_{\boldsymbol{Q}} = -DS\sin^2\theta - ES\cos^2\theta$$
$$D_{\boldsymbol{Q}} = -2J_c S \cos(\pi l) \sin^2\theta \ \ ,$$

where J_{ab}, J_c, D and E are again the exchange and anisotropy parameters derived in the previous chapter, B is the applied magnetic field and $S = 1/2$. θ is the spin-flop angle, given by eqn. 6.12. The dispersion is calculated as in appendix B, giving two modes:

$$\hbar\omega_{\boldsymbol{Q}}^{\pm} = \left[(A_{\boldsymbol{Q}} \pm B_{\boldsymbol{Q}})^2 - (C_{\boldsymbol{Q}} \pm D_{\boldsymbol{Q}})^2\right]^{1/2} \tag{6.16}$$

The energies of the two modes at the magnetic zone centre ($\boldsymbol{Q} = (0,0,1)$ *etc.*) are plotted in fig. 6.6a (dashed lines) as a function of field. At high fields the system is in the spin-flop (SF) phase. As the field decreases the critical field B_{c2} occurs when the lower of the two modes vanishes, and using this condition we find an expression for B_{c2}:

$$B_{c2} = \frac{2S}{g\mu_B} \sqrt{\frac{(D-E)(2J_c - D - E)^2}{(2J_c + D - 3E)}} \ . \tag{6.17}$$

This is the field at which the SF (spin-flop) phase is no longer stable when the field is decreased from high fields, and the spins flip into the AF phase.

We now evaluate the expressions for B_{c1} and B_{c2} to compare these values with the field at which the spin-flop transition is observed to occur in $Na_{0.85}CoO_2$. The values of the parameters J_c, D and E have not been measured for this sample, so we use values obtained in the previous chapter from $Na_{0.75}CoO_2$ (see fig. 5.16a). These are $J_c = 12.2$ meV, $D = 0.096$ meV and $E = 0.059$ meV, and with these we obtain $B_{c1} = 8.19 \pm 1.1$ T and $B_{c2} = 8.15 \pm 1.1$ T (hereafter written together as $B_c = 8.2 \pm 1.1$ T) (see fig. 6.6a). These values are in strong agreement with the spin-flop transition field obtained experimentally (fig. 6.4a and by Luo *et al.* [4]).

When the spins 'flop' into the SF phase we calculate $\theta = 87.8 \pm 0.5$ degrees (from eqn. 6.12), so the spins lie almost antiferromagnetically perpendicular to the applied magnetic field.

We note that it is likely that J_c, D and E do vary with doping x. The level of agreement of the spin-flop transition observed with that calculated above is greater than can reasonably be expected, given the assumptions made. Figure 6.6b shows the field dependence of modes calculated with parameter values obtained in the 'one-mode' fit shown in fig. 5.16b. In this fit the in-plane anisotropy parameter is set to zero so that the two modes of the dispersion are degenerate in zero field. The parameters for this fit are $J_c = 12.2$ meV, $D = 0.082$ meV and $E = 0$, and with these we obtain $B_c = 12.2 \pm 1.1$ T, which is also in reasonable agreement with the observed transition.

6.3.2 Mean-field Approximation

The calculated and experimental values for the transition field are in strong agreement, supporting the interpretation of the data as a spin-flop transition. However, the spin-wave calculation makes the assumption that the magnetic field is applied parallel to the c axis, although experimentally the field was tilted slightly, at $7°$ to the c axis. In order to check that this tilt does not make a large difference to the above calculation we now calculate the critical field and angle with a mean-field approximation. In this simple calculation it is straightforward to include the field tilt angle. The mean field energies are calculated from the Hamiltonian eqn. 6.1, but since the field is no longer parallel to z we replace the last term with $+g\mu_B \sum_i \boldsymbol{B} \cdot \boldsymbol{S}_i$. The mean field energy for the two spin magnetic unit cell (containing one spin on sublattice A and one on sublattice B) is then given by:

$$
\begin{aligned}
\varepsilon_{\text{Mean field}} = &\frac{J_{ab}}{2}\left(6\boldsymbol{S}_A \cdot \boldsymbol{S}_A + 6\boldsymbol{S}_B \cdot \boldsymbol{S}_B\right) + \frac{J_c}{2}\left(2\boldsymbol{S}_A \cdot \boldsymbol{S}_B + 2\boldsymbol{S}_B \cdot \boldsymbol{S}_A\right) \\
&- D\left[(\boldsymbol{S}_A^z)^2 + (\boldsymbol{S}_B^z)^2\right] - E\left[(\boldsymbol{S}_A^x)^2 + (\boldsymbol{S}_B^x)^2\right] \\
&+ g\mu_B\left(\boldsymbol{B} \cdot \boldsymbol{S}_A + \boldsymbol{B} \cdot \boldsymbol{S}_B\right) \quad,
\end{aligned} \tag{6.18}
$$

where we assume spins lie in the x–z plane so that $\boldsymbol{S}_A^y = \boldsymbol{S}_B^y = 0$.

We again begin with the low-field AF phase. When a field B is applied at an angle β to the vertical (c-axis), the component of the field perpendicular to c causes the vertically aligned spins to tilt slightly, so that they are no longer perfectly antiferromagnetic aligned. This is shown in fig. 6.7a (left). The two sublattices of 'up' (A) and 'down' (B) spins are tilted away from the c axis by an angle γ in different directions (see fig. 6.7a, right). From eqn. 6.18 the mean-field energy in the AF phase is given by

$$
\begin{aligned}
\varepsilon_{\text{AF}} = &6J_{ab}S^2 - 2J_cS^2\cos(2\gamma) - 2DS^2\cos^2(\gamma) - 2ES^2\sin^2(\gamma) \\
&- g\mu_BBS\left[\cos(\beta - \gamma) - \cos(\beta + \gamma)\right].
\end{aligned} \tag{6.19}
$$
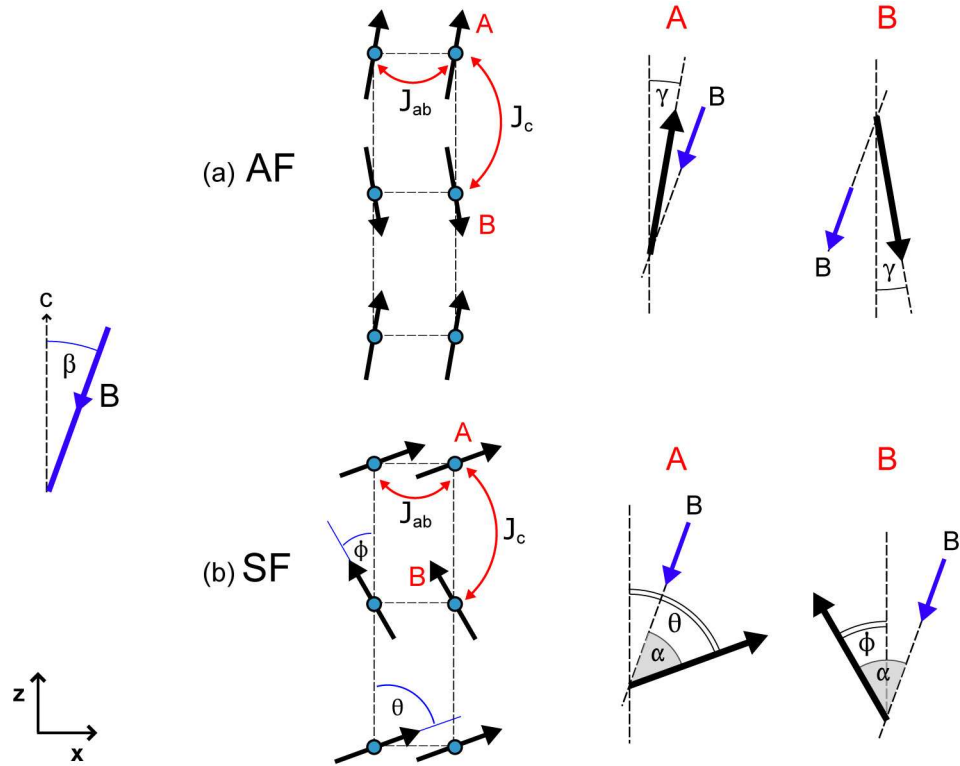
Figure 6.7: (a) AF and (b) SF phases in a magnetic field $\boldsymbol{B}$ applied at an angle β to the vertical (c-axis). Right: spins on each sublattice A and B. In the AF phase spins lie at an angle γ to the c-axis. In the SF phase spins on the A and B sublattices lie at ϕ and θ to the vertical respectively, with $\phi \neq \theta$ (both at α to the field).

The angle γ is dependent on the field, and is calculated by minimizing the energy, *i.e.* setting $(d\varepsilon_{\mathrm{AF}}/d\gamma) = 0$. This results in an expression for γ:

$$\gamma = \arcsin\left(\frac{g\mu_B B \sin(\beta)}{2S\left[2J_c + (D - E)\right]}\right) \quad . \tag{6.20}$$

Next we consider the energy of the spin-flop (SF) phase in the tilted field, which occurs as shown in fig. 6.7b. The spins make an angle α to the magnetic field, but the angle of spins from the vertical differs between layers (θ for sublattice A and ϕ for sublattice B). From eqn. 6.18 the mean-field energy in the SF phase can be written

$$\varepsilon_{\mathrm{SF}} = 6J_{ab}S^2 + 2J_cS^2\cos(2\alpha) - DS^2\left[\cos^2(\alpha - \beta) + \cos^2(\alpha + \beta)\right] \tag{6.21}$$
$$- ES^2\left[\sin^2(\alpha - \beta) + \sin^2(\alpha + \beta)\right] - 2g\mu_B BS\cos(\alpha) \quad .$$

The angle α is calculated by minimizing the energy, as for γ, resulting in the expression

$$\alpha = \arccos\left(\frac{g\mu_B B}{2S\left[2J_c - (D - E)\cos(2\beta)\right]}\right) \quad . \tag{6.22}$$

At zero field $\varepsilon_{\mathrm{AF}} < \varepsilon_{\mathrm{SF}}$ so it is more energetically favourable for the system to be in the AF phase. At high fields $\varepsilon_{\mathrm{AF}} > \varepsilon_{\mathrm{SF}}$ so the system is in the spin-flop phase. To find the crossover point, or critical field, we equate $\varepsilon_{\mathrm{AF}}$ and $\varepsilon_{\mathrm{AF}}$ and solve for $B_c = B(\varepsilon_{\mathrm{AF}} = \varepsilon_{\mathrm{SF}})$:

$$B_c = \frac{2S}{g\mu_B} \sqrt{\frac{(D-E)(2J_c + (D-E))(2J_c - (D-E)\cos(2\beta))}{2(2J_c + (D-E)) - (2J_c + (D-E)\cos(2\beta))}} \ . \tag{6.23}$$

Evaluating this expression with zero angle β using the parameters fitted in chapter 6, we find that for the 'two mode' parameters ($J_c = 12.2 \pm 0.5$ meV, $D = 0.096 \pm 0.005$ meV, $E = 0.059 \pm 0.005$ meV) the critical field $B_c(\beta = 0) = 8.2 \pm 1.3$ T, and for the 'one mode' parameters ($J_c = 12.2 \pm 0.5$ meV, $D = 0.082 \pm 0.015$ meV, $E = 0$) the critical field $B_c(\beta = 0) = 12.2 \pm 1.4$ T. These values are in strong agreement with the values obtained by spin-wave analysis. When β is set to 7°, as in the experimental setup, B_c rises, but the change is negligible compared to the errors due to the parameter errors, and we get the same values: $B_c(\beta = 7°) = 8.2 \pm 1.3$ T for the 'two mode' parameters and $B_c(\beta = 7°) = 12.2 \pm 1.4$ T for the 'one mode' parameters. We conclude that the tilt of the applied magnetic field away from the c axis by 7° does not make a difference to the critical field.

6.4   Discussion and Conclusions

We have successfully observed the magnetic Bragg peak at $\boldsymbol{Q} = (0,0,3)$ in Na$_{0.85}$CoO$_2$ with unpolarized neutrons by inducing a spin-flop transition in a large vertical magnetic field. The transition occurred at a field of $B_{sf} \approx 8$ T, but was broad, with a width of approximately 3 T. It is possible that the broadening of the transition may be due to disorder in the structure, which would lead to a spread of values of the interlayer exchange constant J_c and in turn lead to a range of values for B_{sf}.

We have presented a simple calculation of the spin-flop transition field that would be expected based on the anisotropy parameters derived from the measurement of the spin gap in Na$_{0.75}$CoO$_2$ in the previous chapter. The calculated value for this critical field of 8.2 ± 1.1 T is in strong agreement with the observed value for Na$_{0.85}$CoO$_2$ of $B_{sf} \approx 8$ T. A mean-field approximation to the calculation, including the tilt of the applied magnetic field away from vertical, also gives very good agreement.

We caution, however, that the calculation has assumed J_c, D and E to be the same for the nominal doping levels $x = 0.75$ and $x = 0.85$, which is unlikely to be the case. [2] The agreement is therefore better than can reasonably be expected, given the assumptions made. It is possible that the real sodium contents of the $x = 0.75$ and $x = 0.85$ samples are in fact very close to the same value, which would explain the excellent agreement between the observed and calculated B_{sf}. This is supported by the EPMA measurements reported in the introduction to the previous chapter. We stress, however, that these measurements are in no way conclusive. With more time, we would like to repeat the measurements of both the magnetic excitations and spin-flop transition on one single crystal of known sodium content.

---

[2]At present the exchange parameters have only been measured for $x = 0.75$ (presented in this work), and $x = 0.82$ by Bayrakci *et al.* [2]. A factor of two exists between our notation for the exchange parameters J_{ab} and J_c and that of Bayrakci *et al.* In our notation their parameters for Na$_{0.82}$CoO$_2$ are $J_{ab} = -9$ meV and $J_c = 6.6$ meV, compared to our values of $J_{ab} = -6$ meV and $J_c = 12.2$ meV for Na$_{0.75}$CoO$_2$.

References

[1] L. M. Helme, A. T. Boothroyd, R. Coldea, D. Prabhakaran, D. A. Tennant, A. Hiess, and J. Kulda, Phys. Rev. Lett. **94**, 157206 (2005).

[2] S. P. Bayrakci, I. Mirebeau, P. Bourges, Y. Sidis, M. Enderle, J. Mesot, D. P. Chen, C. T. Lin, and B. Keimer, Phys. Rev. Lett. **94**, 157205 (2005).

[3] J. Sugiyama, H. Itahara, J. H. Brewer, E. J. Ansaldo, T. Motohashi, M. Karppinen, and H. Yamauchi, Phys. Rev. B **67**, 214420 (2003); S. P. Bayrakci, C. Bernhard, D. P. Chen, B. Keimer, R. K. Kremer, P. Lemmens, C. T. Lin, C. Niedermayer, and J. Strempfer, Phys. Rev. B **69**, 100410(R) (2004).

[4] J. L. Luo, N. L. Wang, G. T. Liu, D. Wu, X. N. Jing, F. Hu, and T. Xiang, Phys. Rev. Lett. **93**, 187203 (2004).

[5] D. Prabhakaran, A. T. Boothroyd, R. Coldea, and N. R. Charnley, J. Crystal Growth **271**, 74 (2004).

[6] Y. Wang and H. B. Callen, J. Phys. Chem. Solids **25**, 1459 (1964).

CHAPTER 7

Conclusions and Further Work

In this thesis three correlated electron systems, each exhibiting different forms of complex behaviour, were investigated though neutron scattering studies and modelling of the results. The experimental work highlights the diversity of neutron scattering techniques currently available for the study of condensed matter systems, and the importance of selecting the right instrument to investigate each problem.

The study of magnetic excitations in $La_{1.5}Sr_{0.5}CoO_4$, for example, was ideally suited to the MAPS time of flight spectrometer. For two-dimensional excitations MAPS allows measurements of a large area of reciprocal space over a wide range of energy transfers, and we were therefore able to map out the whole dispersion in one measurement, including the diffuse upper mode which has very low intensity. Had a triple-axis spectrometer been employed for the first measurements instead, it is unlikely that we would have found the upper mode. Conversely, in $Na_{0.75}CoO_2$, where the magnetic excitations are unexpectedly three-dimensional, the interdependence of wavevector and energy on MAPS makes it difficult to interpret the signal. Triple-axis measurements offer the most straightforward way to characterize a three-dimensional dispersion, and in this way the dispersion along c in $Na_{0.75}CoO_2$ was followed up to the Brillouin zone boundaries. Furthermore, choosing the IN14 cold neutron spectrometer allowed low energy measurements of the anisotropy gap.

Polarized neutron scattering is another important technique, and is fast becoming more powerful as neutron fluxes increase. It is invaluable in separating magnetic and nuclear scattering, and we have shown how it can be used to directly probe the orientation of ordered moments, and the components of their fluctuations.

Each of the results chapters 3–6 contains a section of discussion and conclusions, but here we will reiterate some of the more important and interesting points made, and discuss further work that might be undertaken.

The investigations into PrO_2 reported in chapter 3 were motivated by new measurements of a Jahn-Teller structural distortion below $T_D \sim 120$ K. It was hoped that the distortion might help to explain a broad feature in the low-temperature inelastic neutron scattering spectrum centred at ~ 30 meV. To this end, point charge calculations were performed to estimate the ground state splitting expected from the Jahn-Teller distortion. At the same time, inelastic neutron scattering spectra were measured at temperatures above and below T_D. A feature in the low temperature data at ~ 25 meV was identified as the right order of magnitude to correspond to the ground-state splitting. By fitting the evolution of this peak's position with temperature we confirmed that it showed an order-parameter-like behaviour

consistent with T_D. However, the crystal field splitting did not account for all the intensity in the broad feature at low temperature. In fact, vibronic scattering was present both above and below the distortion temperature T_D. This suggests that, even when the static Jahn-Teller distortion splits the crystal field levels, the dynamic Jahn-Teller effect is still present.

Chapter 4 reported experimental measurements and modelling of the magnetic order and excitations in charge-ordered $La_{1.5}Sr_{0.5}CoO_4$. Overall, a good description of the whole excitation spectrum was achieved with a spin-wave model containing only Co^{2+} ions, and a spin-only Hamiltonian (although the anisotropic crystal field and the exchange interaction were taken into account in calculating the basis states). It was not necessary to include interactions between the spins and charge order, and we concluded that the spin and charge degrees of freedom are uncoupled in $La_{1.5}Sr_{0.5}CoO_4$. Still assuming that only the Co^{2+} ions order, polarization analysis revealed a spin-reorientation corresponding to a rotation within the ab plane.

Two puzzles remain after these analyses. Firstly, the direction of the ordered moments calculated using elastic polarization analysis is inconsistent with the components of the fluctuating moment derived from inelastic polarization analysis. There is also the issue of whether domains with different spin orientations exist in the same sample, and we cannot resolve this using the existing measurements. It would be interesting to see whether performing polarization analysis in another scattering plane would allow the domains to be distinguished. The second puzzle is the issue of the spin-state of the Co^{3+} ions, which remains unresolved. No evidence for an ordered Co^{3+} moment was observed in the excitation spectrum of $La_{1.5}Sr_{0.5}CoO_4$, but further work needs to be done to definitively identify the spin-state. One option would be to use a local probe such as NMR, which should be able to distinguish the Co^{2+} and Co^{3+} sites, and determine the moment on each.

To further the studies of $La_{1.5}Sr_{0.5}CoO_4$ it would also be informative to perform neutron scattering measurements on $La_{2-x}Sr_xCoO_4$ with different doping levels. Although bulk measurements of $La_{2-x}Sr_xCoO_4$ at various dopings have been published, we are not aware of any neutron scattering studies for $x \neq 0.5$, and there has been no measurement of charge or magnetic ordering patterns for other values of x. In the isostructural nickelate compounds, $La_{2-x}Sr_xNiO_4$, a number of doping levels have been characterized, and anomalous behaviour has been discovered in some compounds, such as the resonance peak found in the $x \approx 1/3$ excitation spectrum. It would be interesting to discover whether similar effects are present in third-doped $La_{2-x}Sr_xCoO_4$. By measuring magnetic excitations in doping levels with different charge ordering patterns it would be possible to investigate whether the decoupling of charge and spin is a feature of this family of cobaltates, or due to the particular stability of the checkerboard charge ordering in $La_{1.5}Sr_{0.5}CoO_4$.

Chapters 5 and 6 present investigations of the magnetic order and excitations in Na_xCoO_2 ($x \sim 0.75$). The magnetic excitations were found to be highly three-dimensional, despite the two-dimensional layered lattice structure, and were well modelled with a spin-wave Hamiltonian assuming spin-1/2 on every Co site. The spin-flop transition reported in chapter 6 confirmed the A-type antiferromagnetic

magnetic ordering with spins lying along the c direction.

These results leave some remaining ambiguities. Firstly, the neutron scattering measurements show that the spins lie along c, while bulk magnetization measurements are consistent with an easy axis lying in the ab plane. Secondly, the spin-wave analysis assumes that all Co sites have localized spins ($S = 1/2$) and are ordered. For a doping level of $x = 0.75$, in an ionic picture, only 25% of the cobalt sites are Co^{4+} ($S = 1/2$), while the remaining 75% are Co^{3+}. The magnetic ordering pattern is not consistent with localized spins on only a quarter of the Co sites, in a charge ordered picture, or with an ordering pattern involving two very different sized spins. Also, the large intrinsic widths of the dispersion modes at the zone centre indicate an itinerant nature, consistent with the bulk metallic behaviour. It is important to resolve the issue of whether charge disproportionation is present in these samples, and it is possible that this might be achieved through resonant x-ray studies.

To extend the study of Na_xCoO_2 it is crucial that we have better samples, in particular larger single crystals with better mosaics, and accurately determined doping levels. Especially in the low x region, and hydrated phase, progress is being severely hindered by the lack of samples. Solving this problem would allow many more neutron scattering measurements to be undertaken. Firstly, we would like to continue the measurements of the in-plane dispersion relation up to the magnetic zone boundary. This would give more detailed information on the exchange interactions and itinerant effects. Currently measurements only reach 16 meV, while the top of the dispersion is estimated at ~ 40 meV. Secondly, it would be interesting to study other doping levels using neutron scattering. Some neutron scattering measurements have already been carried out on magnetic excitations in the $x = 0.5$ compound, but for the relevance to superconductivity it is important to extend measurements of the magnetic order and excitations to $x = 0.3$, and ideally to the hydrated compound.

APPENDIX A

Polarization Analysis

A.1 Elastic Measurements: Direction of the Ordered Moments

The elastic neutron scattering data collected using the six different polarization and spin-flip configurations (described in chapter 4) were used to perform an analysis of the direction of the spins of the ordered Co^{2+} ions in $La_{1.5}Sr_{0.5}CoO_4$.

Measurements were made at two magnetic reflections in the $(hh0) - (00l)$ plane, $\boldsymbol{Q}_A$ and $\boldsymbol{Q}_B$, which are shown in figure A.1a. Wavevectors $\boldsymbol{Q}_A = (0.25, 0.25, 7)$ and $\boldsymbol{Q}_B = (1.25, 1.25, 1)$ were chosen to make the angles θ_A and θ_B small.

Expressions for the relative intensities of measurements at each $\boldsymbol{Q}$ point for each
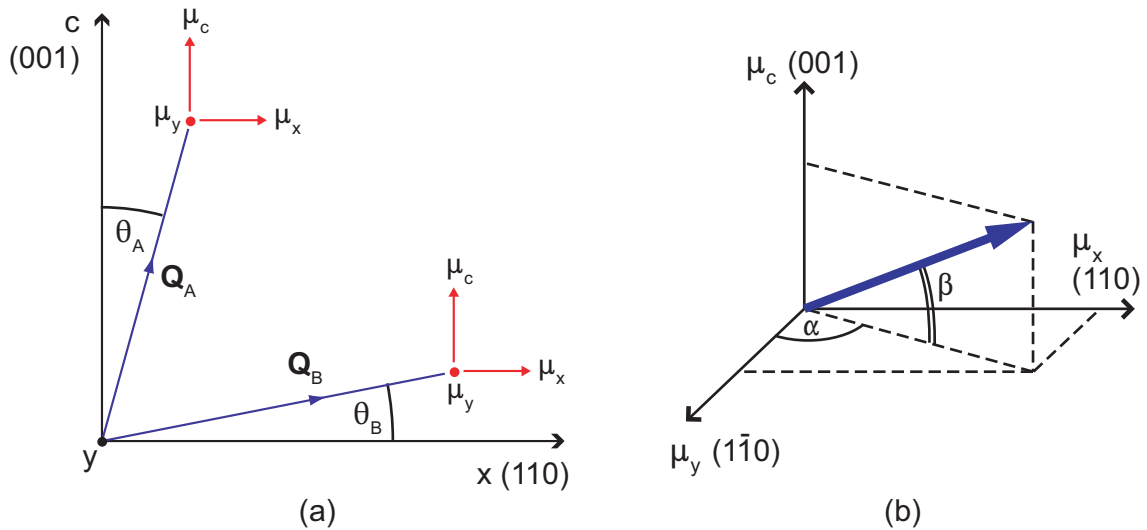
Figure A.1: (a) Diagram of the $(hh0)-(00l)$ plane in reciprocal space, showing the two wavevectors $\boldsymbol{Q}_A$ and $\boldsymbol{Q}_B$ at which measurements were made for polarization analysis. The orthogonal axes (110) and $(1\bar{1}0)$ have been labelled as x and y for ease of reference. (b) The ordered moment μ with respect to the crystallographic axes, showing the angle out of the horizontal plane (β), and the angle within the plane (α, measured from the diagonal $(1\bar{1}0)$).

configuration were derived using three facts about neutron scattering from spins:

- magnetic neutron scattering measures components of the magnetic moment $\vec{\mu}$ perpendicular to $\boldsymbol{Q}$;

- the component of $\vec{\mu}$ perpendicular to the polarization $\boldsymbol{P}$ contributes to spin-flip scattering;

- the component of $\vec{\mu}$ parallel to the polarization $\boldsymbol{P}$ contributes to non-spin-flip scattering.

These expressions are given in table A.1, in terms of the components of the ordered moment μ, as shown in figure A.1, and the angles $\theta_{A,B}$ defined by figure A.1 as:

$$\theta_A = \arctan\left(\frac{\sqrt{h_A^2 + k_A^2} \times (2\pi/a)}{l_A \times (2\pi/c)}\right) \text{ and } \theta_B = \arctan\left(\frac{l_B \times (2\pi/c)}{\sqrt{h_B^2 + k_B^2} \times (2\pi/a)}\right),$$
(A.1)

where $\boldsymbol{Q}_A = (h_A, k_A, l_A)$ and $\boldsymbol{Q}_B = (h_B, k_B, l_B)$, and a and c are the lattice constants for $La_{1.5}Sr_{0.5}CoO_4$.

	$\boldsymbol{P}$		$\boldsymbol{Q}_A$: intensity proportional to	$\boldsymbol{Q}_B$: intensity proportional to
I_1	$\parallel \boldsymbol{Q}$	SF	$\mu_x^2 \cos^2 \theta_A + \mu_y^2 + \mu_c^2 \sin^2 \theta_A$ $+ B_{SF}^A$	$\mu_x^2 \sin^2 \theta_B + \mu_y^2 + \mu_c^2 \cos^2 \theta_B$ $+ B_{SF}^B$
I_2	$\parallel \boldsymbol{Q}$	NSF	B_{NSF}^A	B_{NSF}^B
I_3	$\perp \boldsymbol{Q}$	SF	$\mu_y^2 + B_{SF}^A$	$\mu_y^2 + B_{SF}^B$
I_4	$\perp \boldsymbol{Q}$	NSF	$\mu_x^2 \cos^2 \theta_A + \mu_c^2 \sin^2 \theta_A + B_{NSF}^A$	$\mu_x^2 \sin^2 \theta_B + \mu_c^2 \cos^2 \theta_B + B_{NSF}^B$
I_5	$\parallel \vec{y}$	SF	$\mu_x^2 \cos^2 \theta_A + \mu_c^2 \sin^2 \theta_A + B_{SF}^A$	$\mu_x^2 \sin^2 \theta_B + \mu_c^2 \cos^2 \theta_B + B_{SF}^B$
I_6	$\parallel \vec{y}$	NSF	$\mu_y^2 + B_{NSF}^A$	$\mu_y^2 + B_{NSF}^B$

Table A.1: Expressions for the scattering intensities at the two wavevectors $\boldsymbol{Q}_A$ and $\boldsymbol{Q}_B$ with the six different polarization and spin-flip configurations. μ_x, μ_y and μ_c are components of the magnetic moment (as shown in fig. A.1a), and $B_{SF}^{A,B}$ and $B_{NSF}^{A,B}$ represent the background scattering in the spin-flip and non-spin-flip channels. ($B_{NSF}^{A,B}$ includes all non-magnetic scattering).

From figure A.1(b) we can write expressions for the angle of the ordered moment

out of the plane (β) and in the plane (α), in terms of its components (μ_c, μ_x, μ_y):

$$\alpha = \arctan\left(\frac{\mu_x}{\mu_y}\right) = \arctan\left(\sqrt{\frac{\mu_x^2}{\mu_y^2}}\right) , \tag{A.2}$$

$$\beta = \arctan\left(\frac{\mu_c}{\sqrt{\mu_x^2 + \mu_y^2}}\right) = \arctan\left(\sqrt{\frac{\mu_c^2/\mu_y^2}{(\mu_x^2/\mu_y^2 + 1)}}\right) .$$

Expressions for ratios of the squares of the ordered moment components in the x, y and c directions are then written in terms of the intensities in each configuration measured (I_i) by rearranging the expressions in table A.1. These expressions are:

$$\frac{\mu_x^2}{\mu_y^2} = \frac{1}{T}\left\{\cos^2\theta_B \frac{(I_1^A - I_3^A)}{(I_1^A - I_5^A)} - \sin^2\theta_A \frac{(I_1^B - I_3^B)}{(I_1^B - I_5^B)}\right\} , \tag{A.3}$$

$$\frac{\mu_c^2}{\mu_y^2} = \frac{1}{T}\left\{\cos^2\theta_A \frac{(I_1^B - I_3^B)}{(I_1^B - I_5^B)} - \sin^2\theta_B \frac{(I_1^A - I_3^A)}{(I_1^A - I_5^A)}\right\} ,$$

where $T = \cos(\theta_A + \theta_B)\cos(\theta_A - \theta_B)$ [1]. Since θ_A and θ_B are chosen to be small angles (here $\theta_A = 9.4^o$ and $\theta_B = 9.8^o$), and $(I_1^B - I_3^B)$ is also small [2] we can make the approximation:

$$\frac{\mu_x^2}{\mu_y^2} \approx \frac{1}{\cos^2\theta_A}\frac{(I_1^A - I_3^A)}{(I_1^A - I_5^A)} . \tag{A.4}$$

A.1.1 Flipping Ratio Correction

Due to the finite flipping ratio of the polarized neutron spectrometer a correction must be made to the neutron counts measured in each configuration before applying the formulae above. This corrects for a small leaking of spin-flip neutrons into the non-spin-flip measurements and *vice versa*. If c_i represent the actual counts measured for each configuration shown in table A.1, and I_i are the corrected intensities corresponding to the expressions in the same table:

$$I_i = \frac{f}{f-1}c_i - \frac{1}{f-1}c_j \quad \text{and} \quad I_j = \frac{f}{f-1}c_j - \frac{1}{f-1}c_i , \tag{A.5}$$

where (i, j) are pairs of indices (1,2), (3,4) or (5,6), and f is the flipping ratio.

Error analysis

To calculate the errors on the angles, full error analysis was performed to take into account the errors on neutron counts in each channel ($c_{1-6}^{A,B}$) and the error on the flipping ratio. Details of the method are given in reference [1].

---

[1] We note that equations A.3 are written here in terms of the spin-flip intensities (I_1, I_3, I_5), but can equally be written in terms of the non-spin-flip intensities (I_2, I_4, I_6) simply by substituting $1 \rightarrow 2$, $3 \rightarrow 4$, $5 \rightarrow 6$ throughout.

[2] This is true when the spins lie approximately in the a–b plane, as is found to be the case here.

A.1.2 Two Domains

The scattering intensities measure the squares of the components of the magnetic moment (table A.1). It is therefore not possible to distinguish between positive and negative angles either within (α) or out of (β) the a–b plane. However, two domains at 90° to each other within the plane would produce a different result, and we briefly consider the this case (in plane angle only).

Figure A.2 shows the possible setup. We consider a proportion ζ of the spins to be in the first domain and $(1 - \zeta)$ to be in the second domain. The magnitudes of components of the ordered moments in the two domains are related: $|\mu_x|_{\mathrm{domain1}} = |\mu_y|_{\mathrm{domain2}}$, $|\mu_y|_{\mathrm{domain1}} = |\mu_x|_{\mathrm{domain2}}$ and $|\mu_c|_{\mathrm{domain1}} = |\mu_c|_{\mathrm{domain2}}$. Is is
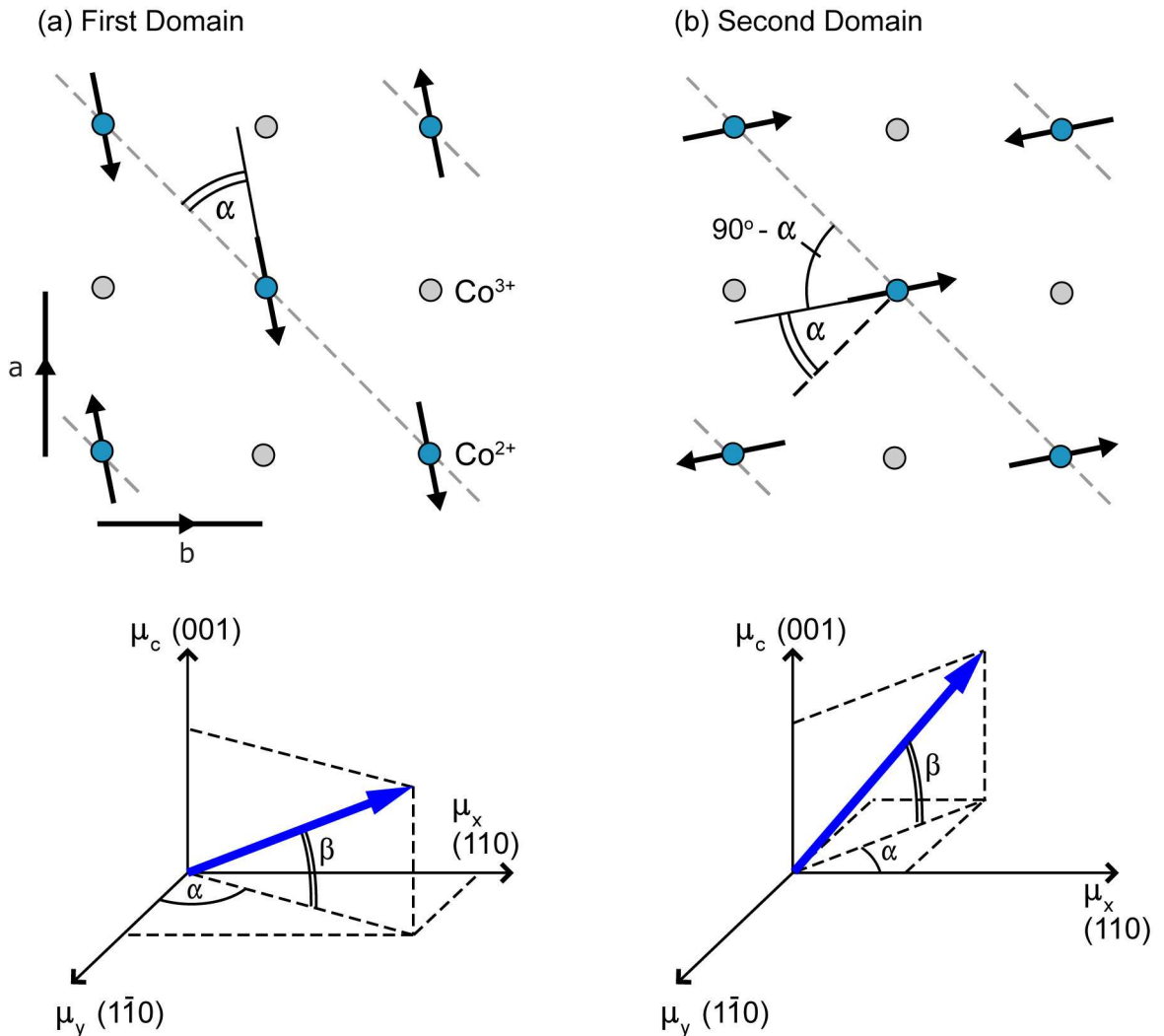

Figure A.2: Two possible spin domains: (a) as assumed for a single domain, and (b) with spins at 90° to those in the first domain.

straightforward to rewrite the equations for the scattering intensities measured at $\boldsymbol{Q}_A$ given in table A.1. For example:

$$I_1^A \propto \quad \zeta \left\{ \mu_x^2 \cos^2 \theta_A + \mu_y^2 + \mu_c^2 \sin^2 \theta_A \right\} \tag{A.6}$$
$$+ (1 - \zeta) \left\{ \mu_y^2 \cos^2 \theta_A + \mu_x^2 + \mu_c^2 \sin^2 \theta_A \right\} + B_{SF}^A \quad .$$

Since there are now two unknowns, the ratio of spins in two domains ζ and the angle of spins in the domains α, we can rearrange for either ζ or α, using the same approximations as made to reach eqn. A.4:

$$\zeta = \quad \frac{\left(I_1^A - I_5^A \right) \cos^2 \theta_A - \tan^2 \alpha}{(1 - \tan^2 \alpha) \left[\left(I_1^A - I_5^A \right) \cos^2 \theta_A + \left(I_1^A - I_3^A \right) \right]} \quad , \tag{A.7}$$

$$\alpha = \quad \arctan \left(\sqrt{\frac{(1 - \zeta) \left(I_1^A - I_5^A \right) \cos^2 \theta_A - \zeta \left(I_1^A - I_3^A \right)}{(1 - \zeta) \left(I_1^A - I_3^A \right) - \zeta \left(I_1^A - I_5^A \right) \cos^2 \theta_A}} \right) \quad . \tag{A.8}$$

This shows that the polarization measurements made may be interpreted using a model with two domains, which would give a different in-plane angle α. However, to determine the angle it is necessary to know the proportion of spins in each domain, and equally it is possible to determine the proportion of spins in each domain if their direction is known.

A.2 Inelastic Measurements: Relative Components of the Spin Fluctuations

Inelastic measurements were also made using the six polarization and spin-flip configurations shown in table A.1. In the case of inelastic scattering, polarization analysis can be used to calculate the relative components of the fluctuations of the moments, and it is therefore an important tool in identifying anisotropy gaps.

The equations which describe the scattering intensity in each of the six configurations are analogous to those for elastic scattering shown in table A.1 but the components of the moments (μ_x, μ_y, μ_c) are replaced by components of the fluctuations of the moments $(\Delta\mu_x, \Delta\mu_y, \Delta\mu_c)$. We can therefore write expressions for the components in an analogous way to eqn. A.3:

$$\frac{(\Delta\mu_x)^2}{(\Delta\mu_y)^2} = \frac{1}{T} \left\{ \cos^2 \theta_B \frac{\left(I_1^A - I_3^A \right)}{\left(I_1^A - I_5^A \right)} - \sin^2 \theta_A \frac{\left(I_1^B - I_3^B \right)}{\left(I_1^B - I_5^B \right)} \right\} \quad , \tag{A.9}$$

$$\frac{(\Delta\mu_c)^2}{(\Delta\mu_y)^2} = \frac{1}{T} \left\{ \cos^2 \theta_A \frac{\left(I_1^B - I_3^B \right)}{\left(I_1^B - I_5^B \right)} - \sin^2 \theta_B \frac{\left(I_1^A - I_3^A \right)}{\left(I_1^A - I_5^A \right)} \right\} \quad ,$$

where $T = \cos(\theta_A + \theta_B) \cos(\theta_A - \theta_B)$, $\theta_{A,B}$ are the angles of the positions $\boldsymbol{Q}_{A,B}$, as defined in fig. A.1, and $I_n^{A,B}$ are the intensities measured at these scattering vectors (with the same polarization-spin-flip configurations as defined in table A.1, but with a fixed non-zero energy transfer).
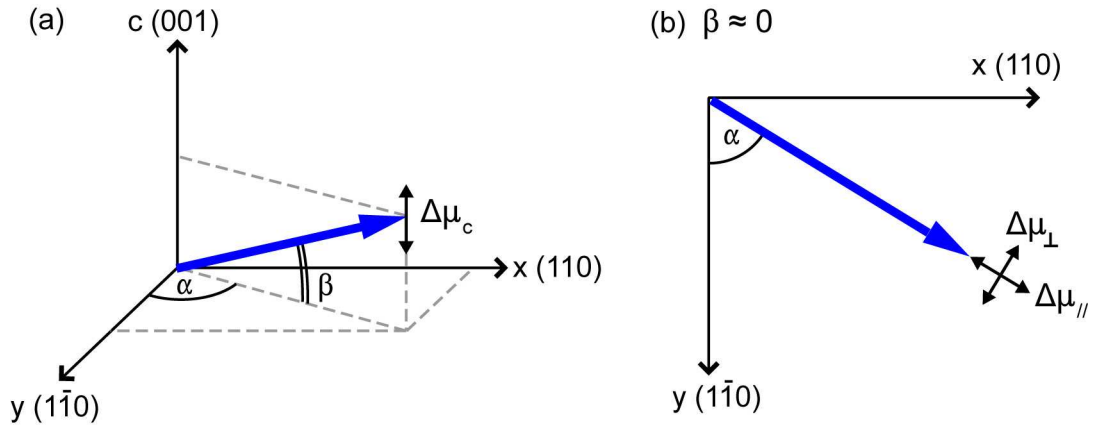
Figure A.3: Components of the fluctuations of the magnetic moment $\boldsymbol{\mu}$: $\Delta\mu_{\parallel}$, $\Delta\mu_{\perp}$ and $\Delta\mu_c$.

Although $\Delta\mu_x$, $\Delta\mu_y$ and $\Delta\mu_c$ are the components of the fluctuations probed by the measurements made in this configuration it is conceptually easier to consider the components of the fluctuations parallel and perpendicular to the ordered moment direction. If we consider only ordered moments within the *ab* plane, *i.e.* with angle $\beta = 0$, we can write $\Delta\mu_{\parallel}$ as the fluctuation of the moment along the ordered moment direction, $\Delta\mu_{\perp}$ as the component of the fluctuation perpendicular to the ordered moment within the *ab* plane, and the component of the fluctuation along *c* ($\Delta\mu_c$) is also perpendicular to the ordered moment direction. This is shown in fig. A.3. In this case we can write:

$$\frac{(\Delta\mu_x)^2}{(\Delta\mu_y)^2} = \frac{(\Delta\mu_{\parallel})^2 \sin^2\alpha + (\Delta\mu_{\perp})^2 \cos^2\alpha - 2\Delta\mu_{\parallel}\Delta\mu_{\perp}\sin\alpha\cos\alpha}{(\Delta\mu_{\parallel})^2 \cos^2\alpha + (\Delta\mu_{\perp})^2 \sin^2\alpha + 2\Delta\mu_{\parallel}\Delta\mu_{\perp}\cos\alpha\sin\alpha} \quad \text{(A.10)}$$

$$\frac{(\Delta\mu_x)^2}{(\Delta\mu_y)^2} = \frac{(\Delta\mu_c)^2}{(\Delta\mu_{\parallel})^2 \cos^2\alpha + (\Delta\mu_{\perp})^2 \sin^2\alpha + 2\Delta\mu_{\parallel}\Delta\mu_{\perp}\cos\alpha\sin\alpha}$$

If we assume that the spins do not have fluctuating lengths then $\Delta\mu_{\parallel} = 0$ and these equations reduce to

$$\frac{(\Delta\mu_x)^2}{(\Delta\mu_y)^2} = \frac{1}{\tan^2\alpha} \quad \text{(A.11)}$$

$$\frac{(\Delta\mu_x)^2}{(\Delta\mu_y)^2} = \frac{1}{\sin^2\alpha}\frac{(\Delta\mu_c)^2}{(\Delta\mu_{\perp})^2} \ ,$$

which are easily compared to the measured components give in equation A.9. If the moment fluctuations are isotropic (but with no length change) then $\Delta\mu_c = \Delta\mu_{\perp}$, and $(\Delta\mu_c)^2/(\Delta\mu_y)^2 = 1/\sin^2\alpha$. If the moments fluctuate solely within the *ab* plane then $\Delta\mu_c = 0$, and $(\Delta\mu_c)^2/(\Delta\mu_y)^2 = 0$.

References

[1] D. S. Sivia, *Data Analysis : A Bayesian Tutorial* (Clarendon Press, Oxford, U.K., 1996).

APPENDIX B

Diagonalization of the Spin-wave Hamiltonian

This appendix outlines the method of diagonalizing a general spin-wave Hamiltonian written in bilinear Bose operators to calculate the magnon dispersion relations. The method of calculating the intensities of the modes is also covered briefly.

B.1 Calculating Dispersion Relations

Any Hamiltonian which is quadratic in Bose operators can be expressed in matrix form as

$$\mathcal{H} = \sum_{\boldsymbol{Q}} X^{\dagger}_{\boldsymbol{Q}} H_{\boldsymbol{Q}} X_{\boldsymbol{Q}} \ , \tag{B.1}$$

where X is the column vector whose components are Bose operators, and $X^{\dagger}$ is the transposed Hermitian adjoint of X. For the problems encountered in this thesis it is possible to write X as a vector of magnon creation and annihilation operators for two sublattices, and the matrix $H_{\boldsymbol{Q}}$ in a general form, $i.e.$

$$X_{\boldsymbol{Q}} = \begin{pmatrix} a_{\boldsymbol{Q}} \\ b_{\boldsymbol{Q}} \\ a^{\dagger}_{\boldsymbol{Q}} \\ b^{\dagger}_{\boldsymbol{Q}} \end{pmatrix} \quad \text{with} \quad H_{\mathbf{Q}} = \frac{1}{2} \begin{pmatrix} A_{\boldsymbol{Q}} & B_{\boldsymbol{Q}} & C_{\boldsymbol{Q}} & D_{\boldsymbol{Q}} \\ B_{\boldsymbol{Q}} & A_{\boldsymbol{Q}} & D_{\boldsymbol{Q}} & C_{\boldsymbol{Q}} \\ C_{\boldsymbol{Q}} & D_{\boldsymbol{Q}} & A_{\boldsymbol{Q}} & B_{\boldsymbol{Q}} \\ D_{\boldsymbol{Q}} & C_{\boldsymbol{Q}} & B_{\boldsymbol{Q}} & A_{\boldsymbol{Q}} \end{pmatrix} \ . \tag{B.2}$$

Diagonalizing the Hamiltonian $\mathcal{H}$ consists of rewriting eqn. B.1 in a new basis, so that

$$\mathcal{H} = \sum_{\boldsymbol{Q}} X'^{\dagger}_{\boldsymbol{Q}} H'_{\boldsymbol{Q}} X'_{\boldsymbol{Q}} \ , \tag{B.3}$$

where X' is a column vector of the normal mode operators, and H' is the diagonalized matrix:

$$X'_{\boldsymbol{Q}} = \begin{pmatrix} \alpha_{\boldsymbol{Q}} \\ \beta_{\boldsymbol{Q}} \\ \alpha^{\dagger}_{\boldsymbol{Q}} \\ \beta^{\dagger}_{\boldsymbol{Q}} \end{pmatrix} \quad \text{with} \quad H'_{\mathbf{Q}} = \frac{1}{2} \begin{pmatrix} \Omega_1(\boldsymbol{Q}) & 0 & 0 & 0 \\ 0 & \Omega_2(\boldsymbol{Q}) & 0 & 0 \\ 0 & 0 & \Omega_3(\boldsymbol{Q}) & 0 \\ 0 & 0 & 0 & \Omega_4(\boldsymbol{Q}) \end{pmatrix} \ . \tag{B.4}$$

The transformation from the old basis to the new basis is given by

$$X = \mathcal{S} X' \ , \tag{B.5}$$

where $\mathcal{S}$ is a transformation matrix, and is usually nonunitary. The operators contained in X obey Bose commutation relations, and their operator nature may be specified by the commutator

$$\left[X, X^\dagger\right] \equiv X(X^*)^T - (X^* X^T)^T = g \quad \text{where} \quad g = \begin{pmatrix} 1 & 0 & 0 & 0 \\ 0 & 1 & 0 & 0 \\ 0 & 0 & -1 & 0 \\ 0 & 0 & 0 & -1 \end{pmatrix} . \quad \text{(B.6)}$$

It can be shown, see for example the paper by White *et al.* [1], that the transformation matrix $\mathcal{S}$ is found by solving the eigenvalue problem

$$gH\mathcal{S} = \mathcal{S}gH' \; , \quad \text{(B.7)}$$

where the eigenvalues of the matrix gH are the elements of the diagonal matrix gH', and the columns of $\mathcal{S}$ are the corresponding eigenvectors. The normalization condition for $\mathcal{S}$ is derived from the condition that the transformation must preserve the commutation relations between operators, *i.e.* the condition given for X in eqn. B.6 also holds for X'. This leads to the normalization condition

$$\mathcal{S}g\mathcal{S}^\dagger = g \; . \quad \text{(B.8)}$$

For H and H' defined as above we find expressions for the diagonal elements of H':

$$\Omega_1(\boldsymbol{Q}) = \ \Omega_3(\boldsymbol{Q}) = \ \frac{1}{2}\left[(A_{\boldsymbol{Q}} + B_{\boldsymbol{Q}})^2 - (C_{\boldsymbol{Q}} + D_{\boldsymbol{Q}})^2\right]^{1/2} \quad \text{(B.9)}$$

$$\Omega_2(\boldsymbol{Q}) = \ \Omega_4(\boldsymbol{Q}) = \ \frac{1}{2}\left[(A_{\boldsymbol{Q}} - B_{\boldsymbol{k}})^2 - (C_{\boldsymbol{Q}} - D_{\boldsymbol{Q}})^2\right]^{1/2} \; .$$

This means there are two modes, with spin-wave dispersion relations given by $\hbar\omega_1 = 2\Omega_1$, and $\hbar\omega_2 = 2\Omega_2$.

B.2 Calculating Intensities of the Magnon Modes

From chapter 3, section 3.2.3, we know that the intensity measured in magnetic inelastic scattering can be written:

$$Intensity \propto f^2(\boldsymbol{Q})\frac{k_f}{k_i}\sum_{\alpha\beta}\left\langle\left(\delta_{\alpha,\beta} - \hat{Q}_\alpha\hat{Q}_\beta\right)S^{\alpha\beta}(\boldsymbol{Q},\omega)\right\rangle \; , \quad \text{(B.10)}$$

where $\boldsymbol{Q} = \boldsymbol{k}_i - \boldsymbol{k}_f$, $f^2(\boldsymbol{Q})$ is the magnetic form factor. Often only terms with $\alpha = \beta$ are needed, and then $S^{\alpha\alpha}(\boldsymbol{Q},\omega)$ can be written

$$S^{\alpha\alpha}(\boldsymbol{Q},\omega) = \sum_{\boldsymbol{Q}'}\left|\langle\lambda_{\boldsymbol{Q}'}|S^\alpha(\boldsymbol{Q})|0\rangle\right|^2\delta(\hbar\omega - \hbar\omega_{\boldsymbol{Q}'}) \; , \quad \text{(B.11)}$$

where α is x, y, z. The spin operators S^x, S^y and S^z are defined in terms of the original Bose operators that make up X. The state $|\lambda_{\boldsymbol{Q}}\rangle$ corresponds to the creation

of one excitation, and is defined in terms of the normal mode operators that make up X': $|\lambda_{\boldsymbol{Q}}\rangle = \alpha^\dagger_{\boldsymbol{Q}}|0\rangle$ for one mode and $|\lambda_{\boldsymbol{Q}}\rangle = \beta^\dagger_{\boldsymbol{Q}}|0\rangle$ for the second. Using eqn. B.5 to convert between the original operators $(a,\, b)$ and the normal mode operators $(\alpha,\, \beta)$ allows the evaluation of eqn. B.11 and therefore the calculation of the intensities for each mode.

References

[1] R. M. White, M. Sparks and I. Ortenburger, Phys. Rev. **139**, A450 (1965).